SANDIA REPORT

SAND2000–8661
Unlimited Release
Printed March 2001

From Atoms to Autos
A New Design Paradigm Using Microstructure-Property Modeling Part 2: Cyclic Fatigue

Mark F. Horstemeyer, David L. McDowell, Jinghong Fan

Prepared by
Sandia National Laboratories
Albuquerque, New Mexico 87185 and Livermore, California 94550

Sandia is a multiprogram laboratory operated by Sandia Corporation, a Lockheed Martin Company, for the United States Department of Energy under Contract DE-AC04-94AL85000.

Issued by Sandia National Laboratories, operated for the United States Department of Energy by Sandia Corporation.

Available to DOE and DOE contractors from
Office of Scientific and Technical Information
P.O. Box 62
Oak Ridge, TN 37831

Prices available from (703) 605-6000
Web site: http://www.ntis.gov/ordering.htm

Available to the public from
National Technical Information Service
U.S. Department of Commerce
5285 Port Royal Rd
Springfield, VA 22161

NTIS price codes
Printed copy: A12
Microfiche copy: A01

SAND2000-8661
Unlimited Release
Printed March 2001

From Atoms to Autos
A New Design Paradigm Using Microstructure-Property Modeling
Part 2: Cyclic Fatigue

Mark F. Horstemayer
Sandia National Laboratories
P.O. Box 969
Livermore, CA 94551-0969

David L. McDowell
Georgia Institute of Technology
The George W. Woodruff School of Mechanical Engineering
Atlanta, GA 30332-0405

Jinghong Fan
Division of Mechanical Engineering
Alfred University
Saxon Drive
Albany, NY 14802

Abstract

The work in this report was a five year effort to foster fundamental advances in microstructure-property fatigue relations of a cast A356-T6 aluminum alloy. We identified and quantified microstructure-property relations and then developed a mathematical tool for fatigue analysis of a cast A356-T6 aluminum alloy that is used in automotive structural components. We focused on three main areas of research: a wide variety of cyclic experiments in which specimens were examined with scanning electron microscopic imaging, finite element micromechanical modeling, and the development of a macroscale microstructure-property model for fatigue. Collaborations with Lawrence Livermore National Laboratory (LLNL) and Oak Ridge National Laboratory (ORNL) were important to this work. LLNL provided quantitative data for casting pore size, distribution, volume fraction, and nearest neighbor distance using nondestructive methods. ORNL performed solidification modeling of the casting process and provided insight into the silicon particle size, distribution, and volume fraction; the pore size, distribution, volume fraction, and nearest neighbor distance; and the dendrite cell size.

This page intentionally blank

From Atoms to Autos
A New Design Paradigm Using Microstructure-Property Modeling
Part 2: Cyclic Fatigue

EXECUTIVE SUMMARY

The work in this report, performed by Sandia National Laboratories (SNL) in collaboration with Georgia Institute of Technology, was a five year effort to foster fundamental advances in microstructure-property fatigue relations of a cast A356-T6 aluminum alloy. The goal was to identify and quantify microstructure-property relations and then develop mathematical tools for fatigue analysis of a cast A356-T6 aluminum alloy that is used in automotive structural components. This comprehensive experimental-computational fatigue study was conducted in parallel with developing microstructure-property relations for monotonic loading conditions, covered in a companion report (Microstructure-Property Relations for a Cast A356 Aluminum Alloy). We focused on three main areas of research: a wide variety of cyclic experiments in which specimens were examined with scanning electron microscopic imaging, finite element micromechanical modeling, and the development of a macroscale microstructure-property model for fatigue. Collaborations with Lawrence Livermore National Laboratory (LLNL) and Oak Ridge National Laboratory (ORNL) were important to this work. LLNL provided quantitative data for casting pore size, distribution, volume fraction, and nearest neighbor distance using nondestructive methods. ORNL performed solidification modeling of the casting process and provided insight into the silicon particle size, distribution, and volume fraction; the pore size, distribution, volume fraction, and nearest neighbor distance; and the dendrite cell size.

The mechanical, physical, and casting properties of this A356 aluminum alloy make it attractive for use in cheaper and lighter engineering components. However, to successfully use cast A356 in long life components, it is necessary to understand its resistance to fatigue. The standard method in determining failure locations is to perform finite element analysis to obtain the highest stresses/strains in a particular region of the material. Some material from that region is then extracted and small coupons are extracted for uniaxial, completely reversed tension-compression fatigue tests. These results are used to estimate the life of the component. Other material typically adjacent to the coupons is extracted for microstructure/inclusion analysis. Unfortunately, regions that may be important from the stress analysis may not be important to the microstructural analysis. More importantly, it is the combination of the microstructure/inclusion content with the stress analysis that is needed to determine a precise location for fatigue failure. Figure 1.1. illustrates the point. In this figure, Region D illustratively shows the highest stressed region. If finite element analysis alone were used to determine the failure location during design, then Region D would be the region of interest. However, Region B shows the most severe inclusion. If microstructural analysis alone were used to determine the failure location during design, then Region B would be the region of interest. A relationship that demonstrates the clear connection between the microstructure/inclusion content and mechanical properties are necessary, because neither of these locations may in fact be the location of the failure region. Figure 1.1 shows that the relationship between microstructure/inclusion content combined with the stress/strain state would induce failure in Region A, where neither the highest

stresses nor most severe inclusion exists. Our work clearly demonstrates the relationship between the microstructure/inclusion content and the fatigue properties of a cast A356 aluminum alloy.

The cast A356 aluminum alloy is a highly heterogeneous ductile matrix composite materials with several dominant *types of inclusions* that dictate fatigue resistance. We use the term *inclusion* as distinctly different from a *crack*, as the former occur naturally as products of the casting process, while the latter are usually a result of applied loading. Silicon particles are much

Stress (from highest to lowest)	Inclusion (from most severe to less severe)	Damage (from most severe to less severe)
D	B	A
A	E	D
C	A	E
E	D	C
B	C	B

Figure 1. Illustration of control arm showing locations of the highest stress, worst inclusion, and most severe damage location showing that the combination of stress state and inclusion type both matter to where final failure will occur.

stiffer than the surrounding eutectic aluminum rich matrix and deform elastically, reinforcing the matrix. The matrix is an elastic-plastic material with a low work hardening behavior and is therefore subject to plastic shear strain localization; aluminum exhibits wavy slip behavior (extensive cross slip) and is well approximated using an initially isotropic yield surface with nonlinear kinematic hardening, notwithstanding mild rate sensitivity at room temperature. The extent of reinforcement and the nucleation of crack-like defects depend on the interface strength between the particles and matrix. The microporosity levels engendered by entrapped hydrogen

gas in the melt, which grow in concert with the dendrite cell size (secondary dendrite arm spacing) as microstructure coarsens with solidification, also contribute significantly to the localization of cyclic plastic shear strain in the interdendritic regions under fatigue loading. Both gas pores and shrinkage pores affect the local intensification of cyclic plastic strain and fatigue/fracture resistance of the alloy. Large shrinkage pores are especially potent in degrading the fatigue resistance; they serve as sites for formation of particularly large cracks that then propagate to premature failure. Finely distributed intermetallics and oxides in the matrix affect the rate of crack propagation of small fatigue cracks and overall ductility. Large scale oxide films are highly prone to forming large fatigue cracks that then propagate rapidly to premature failure. Advances in casting technology have continuously improved control of the largest pore size and have minimized the introduction of oxide films into the pour in order to enhance ductility and fracture/fatigue resistance. Nevertheless, our task was to develop a macroscale microstructure-property model for fatigue that includes all of these types of inclusions.

For the microstructure-property fatigue model, we designate the inclusions in descending order of deleterious effect as the following: (1) When pores/oxides are larger than 200 microns, (2) pores/oxides larger than 100 microns near the free surface, (3) pores/oxides between 60-90 microns with a large volume fraction of porosity, (4) small pores/oxides below 60 microns with a large volume fraction of porosity, and (5) small pores/oxides with a low volume fraction of porosity. These categories signify when different casting features dominate the fatigue life, and they are included in the macroscale microstructure-property fatigue model. In fact, Figure 1.2 illustrates the model's calibrated predictions for each type of inclusion. Note that the final number of cycles decreases with increasing level of inclusion severity.

The microstructure-property fatigue model was developed with the following loading environments in mind:

1. Low cycle fatigue
2. High cycle fatigue
3. Mean stress effects
4. Periodic overloads
5. Multiaxial stress effects

In order to capture the responses arising from these various cyclic loading environments, we compartmentalize the fatigue life into four stages. First, we model the incubation stage of fatigue crack growth. Incubation is defined as the number of cycles to initiate a fatigue crack. This is typically not included in fatigue modeling. Most models assume an initial crack size. The second stage is the Microstructurally Small Crack (MSC) in which the crack initiates on the order of a micron. The crack will then grow until it reaches a Physically Small Crack (PSC) stage. This occurs on the order of up to several dendrite cell sizes. It has been noted in the literature that 60-80% of the life is spent in these three domains. In fact, some researchers have combined these three stages into one and called it crack initiation. We separate these stages, because mathematically they differ. The crack will then grow into a Long Crack (LC) in which Paris Law type of analyses will work. The microstructure-property model is used for several different

initial inclusion sizes. We should mention that although we focus on a cast A356 aluminum alloy, other materials and alloys could be analyzed with this same modeling framework.

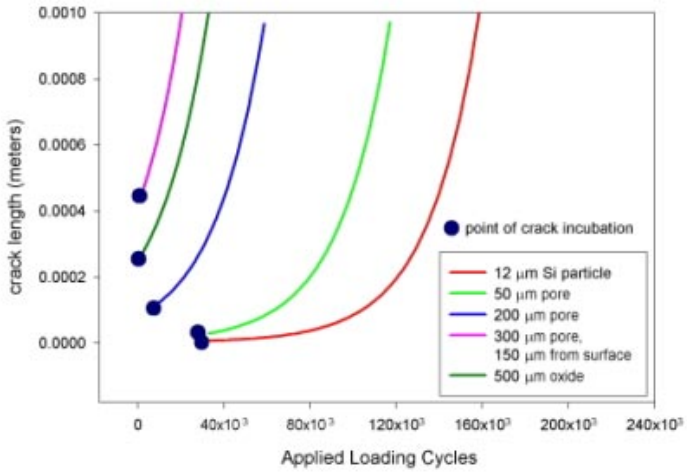

Figure 2. Plot of crack length versus number of cycles for different dominant inclusion types that drive the final fatigue failure.

In order to understand the microstructure/inclusion content on the fatigue life of each stage of this material, we conducted a comprehensive experimental program. Out intent for the experiments was to explore and quantify the small and long crack behaviors for different strain amplitudes, mean stresses, and loading sequences. Furthermore, scanning electron microscope (SEM) analyses were performed on many of these experimental specimens so that correlation between the microstructure and fatigue stage could be ascertained. The following type of experiments were conducted:

1. Smooth specimen, strain-life and stress-life experiments
2. Multiaxial fatigue
3. Small crack experiments
4. Long crack experiments
5. Mean stress experiments
6. Sequence experiments

Of importance here was the quantification of different stages of fatigue cracks as a function of the dendrite cell size, porosity volume fraction, inclusion size that induced final failure fatigue crack, nearest neighbor distance, distance to free surface, and applied strain level. Cast plates were meticulously made in which these microstructures/inclusions were quantified upon testing.

With such a myriad of heterogeneities and factors that contribute to fatigue resistance, it is easily understood why separation of these attributes is difficult from an experimental viewpoint. Due to the large range of length scales and types of inclusions, which may be present in a given casting, two important observations are worth mentioning. First, the fatigue life for a given loading condition may vary substantially over a range of specimens obtained from nominally the same casting (a factor of ten variation is not uncommon) even under Low Cycle Fatigue (LCF) conditions, quite distinct from wrought alloys. Second, experiments can lead to ambiguous outcomes with regard to controlling mechanisms of fatigue crack formation and propagation through the microstructure because cracks can form at unknown locations within the bulk and propagate undetected by surface inspection through much of the fatigue life, especially in High Cycle Fatigue (HCF); it is difficult to perform enough experiments to obtain sufficient quantitative observations of fatigue crack *formation and early propagation* through the microstructure for each inclusion type to formulate truly interpolative or extrapolative empirical fatigue life estimation schemes that contain microstructure parameters. Furthermore, artificially introduced inclusions (e.g. machined surface cracks) do not behave in like manner to naturally occurring cracks, particularly for lower scale inclusion types.

What the experiments did not provide (even with scanning electron microscopy imaging of the failure surfaces), the micromechanical finite element simulations did. Because quantification of the crack incubation and small crack formation stage experimentally is extremely difficult, micromechanical finite element simulations were used to help clarify our understanding of the microstructure-property relations and provide the needed information for the development of the microstructure-property fatigue model. Since quantification of the local cyclic plastic strain in the microstructure is essential in driving fatigue crack initiation, we focused on that aspect in the micromechanical finite element analyses using both idealized geometries and realistic geometries for the microstructure/inclusion morphology. In particular, we examined the effects of applied stress amplitude, microstructure-inclusion content on the maximum plastic shear strain for crack incubation and the cyclic crack tip opening displacement for MSC/PSC crack propagation. For the MSC/PSC crack propagation regimes, we also analyzed the effects of particle shape, particle size, particle nearest neighbor dimension, particle distribution, dendrite cell size, pore size, pore shape, pore nearest neighbor distance, and pore distribution. In this context we examined such characteristics as crack driving force and crack closure behavior. These analyses were based on sophisticated constitutive laws with experimentally determined material constants for the Al 1% Si dendritic matrix region and A356 aluminum alloy under cyclic loading. The results showed excellent agreement with experimental observations and gave insight into the microstructural behavior for LCF and HCF regimes.

In summary, a synergistic program that included experiments, micromechanical finite element modeling of local microstructures, and macroscale modeling of the microstructure-property relations in fatigue gave definitive results for optimizing the design of structural cast components. We developed relations that contain explicit treatment of each inclusion type in order to offer a link between quantitative characterization of inclusion populations and fatigue life estimates, including the variability of fatigue life. Such relations provide a link to the foundry to help guide the selection of section thickness, impurity and gas level controls, solidification rates, and other parameters, especially when used in concert with predictive models for pouring, mixing, and microstructure evolution during solidification which have been developed in the ORNL part of the USCAR program. A shown in Figure 3, this type of modeling effort has proven successful here an increase in load-bearing capacity (by 40%) was exhibited with the optimized, lightweight design (25% lighter) and the fatigue life was lengthened.

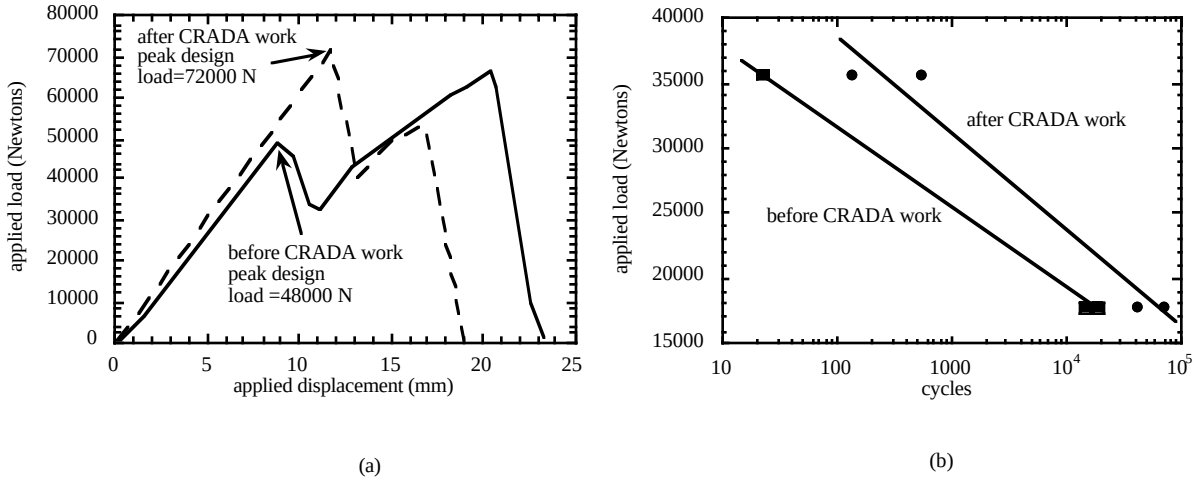

Figure 3. (a) Load-displacement and (b) load-life curves of control arms before and after CRADA work.

This five year effort was performed under the DOE USCAR-USAMP CRADA including collaborations with LLNL, ORNL, and Georgia Tech. An American Foundrymen's Society award for technical excellence and an R&D 100 award were received as a result of this work.

ACKNOWLEDGMENTS

For all the work represented in this report, we certainly cannot take all the credit. First, we need to recognize that the work of Mark F. Horstemeyer was sponsored by the U.S. Department of Energy, Sandia National Laboratories under contract DE-AC04-94AL85000 and that of David L. McDowell and Jinghong Fan was sponsored by the American Foundry Society. Many CRADA partners need to be acknowledged for their support, encouragement, and advice. The leadership of Dick Osborne (GM) and Don Penrod (AFS) representing the USCAR Lightweight Metals Group is greatly appreciated along with their encouragement. Gerry Shulke (Chrysler) provided many cast A356 aluminum plates. The work of Ken Gall (Sandia post-doc) was instrumental in developing the microstructure-property fatigue model. Nancy Yang (Sandia National Labs) and Arun Gokhale (Georgia Tech) were instrumental in performing microstructural/stereological analyses on many different specimens to help provide the motivation for the modeling effort. Ken Dolan (Lawrence Livermore National Lab) provided xray tomography results for the control arm specimens. Paul Nielan (Sandia National Labs) provided the management oversight of the CRADA for Sandia. Jim Sudy and Michele Rhody at Westmoreland Mechanical Testing and Research are to be commended for their oversight of machining and testing all the specimens for the modeling effort. Brett Degner (UC Berkeley) helped by performing finite element analyses of the control arm and helped reduce the weight of the control arm. Fruitful discussions with Srinath Viswanathan (Oak Ridge National Labs) were necessary in understanding the mechanisms involved in the casting process that bring about the microstructural state. Technical reviews and encouragement throughout the program from Vijey Shende (AMCAST), James Burg (ALCOA), Fred Major (ALCAN), and Yi-shin Sheu (GM) are also greatly appreciated. Jay Foulk, Patrick Klein, and Karrolynne Tumacder graciously helped in finalizing this product by their careful reviews and attention to detail. Finally, the sacrifices of our family members during our travels of the many meetings required for this program cannot be ignored as they always have been very gracious and supportive of our work.

1. INTRODUCTION

The Partnership for New Generation Vehicles (PNGV) has mandated that a mid-size automobile be developed in mass production mode in order to achieve greater gas mileage (80 mpg). This is motivated by greater emission requirements and less reliance on foreign oil sources. To achieve this unprecedented milestone in a mass produced automobile, weight reduction is a necessity. Of particular interest are the chassis components, which have been chosen to be a focal point of weight reduction by the USCAR-USAMP Lightweight Metals Group. This group has identified the cast A356 aluminum alloy to be the material of choice for the chassis components.

Different methods exist to manufacture cast A356 components, and each of the methods introduces a different level of casting porosity. The modeling effort described in this report must account for all the possible scenarios of microstructure/inclusion sizes, distributions, and nearest neighbor distances. As such, it is worth briefly describing the different casting processes for context. Castings with the least amount of porosity typically come from squeeze casting. Like all the other casting processes considered here, squeeze casting uses fully liquid metal as the feed material. Squeeze casting is characterized by slow filling rates, minimum turbulence, and high pressure throughout solidification thus lowering the amount of shrinkage porosity. High pressure die casting is popular because it can produce thin walls, great detail, and good dimensional control at a fairly low cost. High pressure die casting is characterized by high pressure during casting compacting trapped pores to small sizes. In vacuum die casting, the dies are evacuated and sealed before the gate is open. The molten metal is forced in by atmospheric pressure. Shrinkage porosity is generally occurs in isolated regions of the casting. In semi-solid metal castings, a partially solidified alloy is introduced into the die and is agitated during flow to produce a rounded, global microstructure. It is used to produce thin sections and high integrity structural components, although this method is a bit expensive. Tilt Pour mold castings are characterized by a gravity pour into a permanent (or semi-permanent sand core). Vacuum riserless castings is a low pressure casting process that has been used for automotive chassis and suspension components. Lost foam castings come from another low pressure method that uses foam for the mold. This inexpensive process can give significantly large porosity levels than the others. All of these processes are used depending on the necessary design requirements and cost constraints.

Aluminum castings have a rich history of successful use in the automotive and aircraft industry in that they are lightweight, fairly inexpensive, and are well tested. However, because of their complex microstructure, understanding the mechanical response has been elusive and thus greater safety factors in design are needed. Unfortunately, increased safety factors mean increased weight. The typical method to design a component under fatigue. Finite element analyses are typically performed to determine the highly stressed regions and then microstructure analysis and experiments are performed in those regions. However, other regions that have worse inclusions could fail sooner than the expected higher stressed region. Alternatively, if only the worst microstructural regions were analyzed, the critical failure location could also be missed since the stresses from the finite element analyses are not considered. Hence, the goal of this work is twofold: to understand the microstructure-property cause-and-effect relationships and to develop a microstructure-property fatigue model. Hence, a chassis designer could use the

microstructure-property fatigue model to more precisely design components without such large safety factors. Consequently, a lighter, safer component could be designed.

1.1. MODELING PHILOSOPHY

In recent years there has been a strong research initiative by the automotive industry to improve the performance of cast aluminum components. One critical aspect of optimizing design is to understand and quantify damage progression under fatigue loading conditions. Developing the ability to predict cyclic damage progression is imperative for the design of components that will experience overloads during service due to impacts, rough ground, and crash environments. The ability to predict fatigue damage is rooted in the ability to understand the inclusion content and microstructure's influence on the mechanical response.

Cast Al-Si-Mg alloys are highly heterogeneous ductile matrix composite materials with several *types of inclusions* that dictate fatigue resistance. We use the term inclusions to distinguish them from cracks, as the former are naturally occurring constituents of the casting process, while the latter are usually a result of applied loading. First, eutectic Si particles are much stiffer than the surrounding eutectic Al-rich matrix and deform elastically, reinforcing the matrix. The matrix is an elastic-plastic material with a low work hardening behavior, and is therefore subject to plastic shear strain localization; aluminum exhibits wavy slip behavior (extensive cross slip) and is well-approximated using an initially isotropic yield surface with nonlinear kinematic hardening, notwithstanding mild rate-sensitivity at room temperature. The extent of reinforcement and the nucleation of crack-like defects depends on the interface strength between the particles and matrix. Second, the microporosity levels engendered by entrapped hydrogen gas in the melt, which grow in concert with the dendrite cell size (secondary dendrite arm spacing) as microstructure coarsens with solidification time (cf. Major, 1994; Tynelius *et al*., 1993), also contributes significantly to the localization of cyclic plastic shear strain in the eutectic regions under fatigue loading conditions. Both gas pores and shrinkage pores affect the local intensification of cyclic plastic strain and fatigue/fracture resistance of the alloy. Large shrinkage pores are especially potent in degrading the fatigue resistance, as they serve as sites for formation of particularly large cracks which then propagate to premature failure. Third, finely distributed intermetallics (cf. Gall *et al*, 2000b) and small oxides (Wang *et al*., 1998) in the matrix affect the rate of crack propagation of small fatigue cracks and overall ductility. Finally, large scale oxide films offer high potential to form fatigue cracks of the same length scale which then propagate rapidly to premature failure. Clearly, advances in casting technology have continuously improved control of the largest pore size and have minimized the introduction of oxide films into the pour in order to enhance ductility and fracture/fatigue resistance.

With such a myriad of heterogeneities and factors that contribute to fatigue resistance, it is easily understood why separation of these variables is difficult from an experimental viewpoint. Due to the large range of length scales and types of inclusions, which may be present in a given casting, there are two relevant observations:

- The fatigue life for a given loading condition may vary substantially over a range of specimens obtained from nominally the same casting (a factor of 10 variation is

not uncommon), *even* under Low Cycle Fatigue (LCF) conditions, quite distinct from wrought alloys.

- Experiments often lead to ambiguous outcomes with regard to controlling mechanisms of fatigue crack formation and propagation through the microstructure because cracks can form at unknown locations within the bulk and propagate undetected by surface inspection through much of the fatigue life, especially in High Cycle Fatigue (HCF); it is difficult to perform enough experiments to obtain sufficient quantitative observations of fatigue crack *formation and early propagation* through the microstructure for each inclusion type to formulate truly interpolative or extrapolative empirical fatigue life estimation schemes that contain microstructure parameters. Furthermore, artificially introduced defects (e.g. machined surface cracks) do not behave in like manner to naturally occurring cracks, particularly for smaller inclusion types.

The last point is important. We desire microstructure-property fatigue model that contain explicit treatment of each inclusion type in order to offer a link between quantitative characterization of inclusion populations and fatigue life estimates, including the variability of fatigue life. Such a treatment also may provide a link to the foundry to help guide the selection of section thickness, impurity and gas level controls, solidification rates, etc., especially when used in concert with predictive models for pouring, mixing and microstructure evolution during solidification.

Because of the cooperative synergism of the microstructure and stresses/strains from the loading conditions, it is important to include microstructures/inclusions in an analysis. This can be illustrated in Figure 1.1. Figure 1.1 clearly illustrates that in one location, A, the highest stress may result, and in another location, B, the most deleterious inclusion may result. Yet, the critical location for failure may be neither as the combination of lesser values for both at location C would be the critical location for failure. As such, a hierarchical classification of inclusion severity on fatigue life is introduced here. Five inclusion types and associated range of length scales are listed as follows, according to the order of ascending level of severity:

Type	Inclusion
A	Distributed microporosity and silicon particles: no significant pores or oxides
B	High levels of microporosity: no large pores or oxides (length scale < 60 μm)
C	Large Pores (length scale > 60-90 μm)
D	Large Pores near the free surface; no large oxides (length scale < 100 μm)
E	Large oxides (length scale greater than 200 μm)

Figure 1.2 illustrates the microstructure-property fatigue model's calibrated predictions for each type of inclusion. Note that the final number of cycles decreases with increasing level of inclusion severity and the character of the function changes with inclusion type.

Stress (from highest to lowest)	Inclusion (from most severe to less severe)	Damage (from most severe to less severe)
D	B	A
A	E	D
C	A	E
E	D	C
B	C	B

Figure 1.1. Illustration of control arm showing locations of the highest stress, worst inclusion, and most severe damage location Illustrating that the combination of the stress state and inclusion type both matter to where final failure will occur.

1.2. MATERIAL: CAST A356 ALUMINUM ALLOY

The cast A356 aluminum alloy has a work hardenable aluminum matrix with the major second phase being silicon particles in the eutectic region. The aluminum alloy comprises 7% Si, 0.4% Mg, 0.01% Fe, 0.01% Cu, 0.01% Mn, 0.01% Sr, 0.01% Ti, and 0.01% Zn. The material used for this study was retrieved mainly from cast horizontal plates, although we also used data from actual automotive cast components and data from the literature. All of these A356 castings had a T6 annealing. In the eutectic regions, large silicon particles and clusters form a dendritic substructure while the Si remains solutionized in the proeutectic phase. Solidification rate, modification, and heat treatment all dictate the morphology and size of the Si substructures. Faster solidification rates decrease the average dendrite arm spacing (DAS) or equivalently the dendrite cell size (DCS) (Spear, 1963). The controlled addition of modifiers such as pure strontium has little effect on dendrite arm spacing, but can spherodize elongated Si particles (Hess and Blackman, 1975). Prolonged exposure to a solutionizing temperature (~ 800 K) after casting modifies the Si particle morphology (Meyers, 1986). The aforementioned microstructural alterations have a strong influence on the mechanical properties.

The plates of A356 aluminum (20 cm by 14 cm by 5 cm) were cast in iron chill molds on the top, bottom, and end of the casting cavity to simulate a permanent mold. A no-bake silica sand was used to create the sides of the plate, the riser, and the down sprue. A ceramic foam filter was used between the down sprue and the riser. A356.2 ingot was melted in an induction furnace.

The melt was grain refined with titanium-boron, modified with strontium, and degassed using a rotary degasser. The castings were poured between 950 K and 977 K, and then cooled over a 16 hour period. The plates were removed from the mold and then heat treated to a T6 anneal (solutionized at 810.8 K for 16 hrs, quenched in hot water at 344 K, and then aged for 4 hours at 492.7 K). The microstructure contained aluminum rich dendrite cells, equiaxed fine silicon particles distributed within the eutectic regions, and submicron intermetallics.

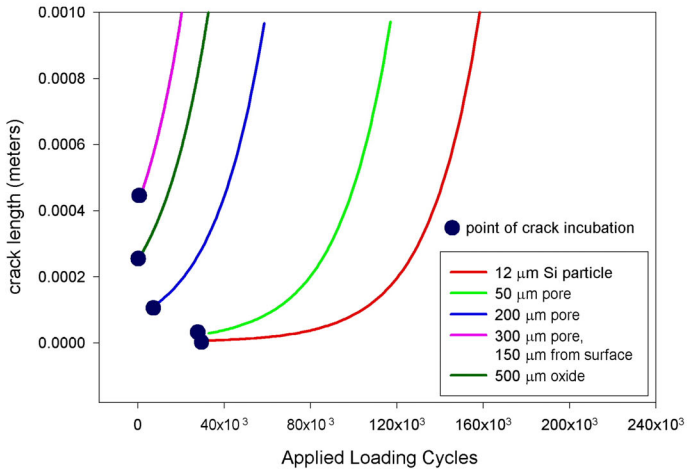

Figure 1.2. Plot of crack length versus number of cycles for different dominant inclusion types that drive the final fatigue failure.

This page intentionally blank

2 Microstructure-Based Fatigue Model for Cast A356-T6 Alloy

2.1 Mechanisms of Fatigue of Casting Alloys

Fracture mechanics, particularly Linear Elastic Fracture Mechanics (LEFM), has been used rather extensively in the literature to formulate fatigue life estimation schemes for the various types of inclusions in cast Al alloys. The logic of doing so derives from the observed dependence of the fatigue life corresponding to a given crack size or critical fracture condition on the inclusion type at which the crack formed. In contrast to conventional strain-life or stress-life approaches for fatigue crack *initiation* (in this case defined as formation and early propagation to a defect size on the order of ½ to 1 mm) as outlined in the round robin SAE program on cast A356-T6 (Stephens et al., 1988a, 1988b), the application of LEFM offers a means of introducing microstructure into the correlation/prediction of fatigue life since the dimension of the identified life-limiting inclusion type serves as the initial size of the crack for the propagation analysis. For example, based on the work by Murakami and Endo (1994), Shiozawa et al. (1997) have developed an algorithm based on defining the maximum projected area on a plane perpendicular to the maximum principal stress range of the largest inclusion within a critically stressed volume as the initial crack length for an LEFM analysis for subsequent propagation life and have obtained sensible correlations for a wide range of casting alloys, when combined with an "initiation" criteria for the formation of the crack at the inclusion. The number of cycles to crack initiation (formation in this case) is assumed to depend on the maximum value of the stress intensity factor for a pseudo-crack with length on the order of the maximum inclusion diameter. The application of LEFM is also appealing, especially in the HCF regime, because the behavior of the cast material appears to be that of a brittle material, with propagation nominally mode-I dominated. Cordes et al. (1988) found that the Smith-Watson-Topper (SWT) parameter (product of the maximum stress and cyclic strain range) appeared to correlate mean stress effects within the context of a strain-life algorithm relatively well for A356-T6; the SWT parameter is well-known to describe normal stress-dominated early growth of fatigue cracks in alloys (cf. Socie, 1993; McDowell, 1996a).

There is no question that LEFM is a useful and valid tool for analysis of the propagation of long fatigue cracks in heterogeneous cast alloys, under standard conditions for which LEFM itself is valid. However, there are serious limitations of LEFM that must be understood when attempting to use it as more of a quantitative tool for injecting microstructure dependence into microstructure-property relations. Since the matrix is ductile, the local behavior at inclusions where cracks are formed and at tips of growing fatigue cracks is elastic-plastic. Hence, it is necessary to consider both the scale of crack tip plasticity relative to crack length and the scale relative to inclusion sizes and spacings in order to assert the validity of singularity-based fracture mechanics concepts (for a review of related issues see McDowell, 1996b). In particular, for LEFM to be valid, the scale of the cyclic plastic zone at the crack tip must be small relative to crack length, as must the scale of the damage process zone which governs the advance of the crack.

Further, for *homogeneous material* solutions for the mode I stress intensity factor, K_I, to be valid, the cyclic plastic zone must enclose a sufficient number of lower scale inclusions that control the rate of crack advance in order for homogeneity to offer a good approximation; this is typically much more demanding than the LEFM requirements on cyclic plastic zone size relative to crack

length. This issue remains even if Elastic-Plastic Fracture Mechanics (EPFM) is employed. Another issue: even if detailed LEFM solutions are used for local geometries of cracks forming at lower scale inclusions and growing away from them (cf. DeBartolo and Hillberry, 1998; Laz and Hillberry, 1998; Ting & Lawrence, 1993), the ductile nature of the matrix material calls into question the validity of the LEFM treatment since the local cyclic plastic strains at the notch root are often substantial, even in the HCF regime. In fact, this point likely renders an overly detailed analysis of stress intensity factors for cracks growing from Si particles or moderate gas or shrinkage pores more of academic than practical value, even if interaction effects of the crack with other adjacent inclusions are considered (i.e. heterogeneity accounted for), because it is based on linear elasticity.

The same comments apply to the treatment of crack closure effects, whether due to either plasticity or roughness (in reality a combination of these for casting alloys) which are essential to include within the LEFM framework in order to capture R-ratio effects in fatigue crack propagation. These effects may be directly experimentally quantified using conventional LEFM for long cracks which sample sufficient microstructure within the damage and closure process zones at the crack tip, although alternative interpretations and treatments based on intrinsic factors have been argued (cf. Sadananda and Vasudevan, 1995) which favor a dependence of da/dN on both K_{max} and ΔK rather than on ΔK_{eff} as in closure models. For small fatigue cracks which are on the order of 10-500 μm, a simple quantitative treatment of closure effects within the context of a simple approach such as ΔK_{eff} is difficult to justify for cast alloys in view of the heterogeneity of the material on the scale of the closure phenomena combined with the strongly heterogeneous elastic-plastic nature of plasticity ahead of and in the wake of the crack. It is almost impossible to unambiguously experimentally measure these closure effects for cracks from 10-500 μm in length other than inferring them from a dependence on the crack growth rate (in a few cases) or the total life of smooth specimens (majority of cases) on the R-ratio. In some sense, closure can be introduced as a means to correct intrinsic shortcomings of the treatment of microstructure heterogeneity in the LEFM formulation, and perhaps this is common in existing works that address propagation from microstructure-scale inclusions, particularly for heterogeneous composites such as cast Al alloys. This objection may not be as strong for crack growth from isolated fractured inclusions in wrought Al alloys, because the scales of heterogeneity (other than grain size) in the Al matrix are smaller than the cyclic plastic zone size for all conceivable stress amplitudes in the HCF range (Newman, 1994).

Consider some examples. For plane strain, the cyclic plastic zone size (Bannantine et al., 1990) is on the order of $1/(12\pi)(\Delta K_I/S_y)^2$, where S_y is the cyclic yield strength (about 160 MPa for horizontally cast A356-T6 plate based on deviation from linearity); therefore for an applied stress amplitude on the order of the yield strength, the maximum cyclic plastic zone size for a crack length of ½ mm is on the order of 30-40 μm, assuming $\Delta K_I = (2/\pi)\Delta\sigma\sqrt{\pi a} = (2/\pi)2S_y\sqrt{\pi a}$ for R = -1, where a is the crack length. This is only slightly larger than the largest Si particles within the distribution, and on the order of the typical dendrite cell size. Certainly, this cyclic plastic zone does not encompass a statistically significant set of microstructural obstacles. For higher applied stress levels, the interdendritic microplasticity transitions towards extensive plasticity conditions and large scale yielding and damage process zones are likely to not amenable to LEFM. For lower applied stresses, the cyclic plastic zone

size drops as the square of the stress amplitude; at ½ S_y, for example, the cyclic plastic zone size is on the order of only the Si particle diameters among the distribution, about 7-10 μm for a crack length of ½ mm. Hence, the concept of homogeneous material fracture mechanics really doesn't make sense for stress amplitudes in the HCF region for crack lengths below about ½ mm. Nor do concepts of plasticity-induced closure based on homogeneous material assumptions. For more details on crack closure, see micromechanics sections 4.3.1.2.7-9. The crack grows through and around fields of obstacles (Si particles) that serve to intensify the local plastic strain ahead of the tip and further change the nature of the crack tip plasticity.

On the other hand, an EPFM model (e.g. crack tip opening displacement) which accounts for heterogeneity and plasticity is most rigorously acceptable; unfortunately, the computational effort involved is substantial, even for just a few geometries and loading levels of interest, because of the strong gradients of cyclic plasticity and contact conditions across the crack faces. Moreover, the results are instructive but not particularly amenable to simple generalization. However, as shown by Shiozawa et al. (1997), the propagation of small cracks (in the range of 0.1mm to 1 mm) in two squeeze cast Al-Si alloys (Si particle nucleation controlled, minimum porosity) for $R = \sigma_{min}/\sigma_{max} = -1$ followed a type of elastic-plastic law which has been found to be valid for steels as well (Nisitani, 1987; Wang and Miller, 1992)

$$\frac{da}{dN} = A\left(\frac{\Delta\sigma}{2S_u}\right)^n a \propto \Delta CTD \qquad \text{Equation 2.1}$$

where S_u is the ultimate strength and A, n are constants, with n = 4.8. The range of crack tip displacement at some distance behind the crack tip (say a few μm) is denoted by ΔCTD. McDowell and Bennett (1999) argued that this type of relation may be expected based on shear strain localization ahead of the crack tip with the cyclic crack tip opening displacement regime as the governing parameter for crack extension (see also McClintock, 1999), even under nominally high cycle fatigue conditions for small cracks.

Of course, for large pores, say greater than ½ mm or so in diameter, the validity requirements of LEFM are easier to satisfy. Ting and Lawrence (1993) clearly state the limits of applicability of their hybrid stress-life (for nucleation)/LEFM-based treatment of nucleation and growth of cracks from large (> ½ mm) pores near the surface in polished specimens, which includes the effect of the decay of the stress intensity factor as the crack grows away from the notch until it extends beyond the influence of the notch. Notwithstanding the scale effects, for cracks growing within elastic-plastic notch root fields (as are most small cracks in cast alloys from small pores or particles), large scale yielding must be considered (cf. Lalor and Sehitoglu, 1987). In contrast, Dugdale type models for plasticity-induced closure for cracks growing from inclusions in wrought Al alloys (cf. Newman, 1994) ignore any other sources of heterogeneity such as grain boundaries and are especially unsuitable for interdendritic particle interactions of microstructurally small fatigue cracks in cast alloys. Anyway, the constraint offered by particles on bulk cracks in the A356-T6 alloy likely induces more of a plane strain condition at the crack front, on average, than plane stress (Sehitoglu and Sun, 1991).

There are two types of notches of interest in fatigue life prediction for cast alloys. First, for cast structures there are typically higher length scale notches such as fillet radii or holes which arise as part of the component geometry. This type of notch dictates *structural* stress concentration. Typically, stress concentration factors or elastic finite element analyses are conducted to quantify the intensification of local stresses at these macronotches. The second type of a notch is a micronotch such as a fractured Si particle or a 100 μm shrinkage pore. This type of inclusion or micronotch dictates the level of *microstructural* stress concentration, in rough terms. Hence, the micronotches dictate *material fatigue resistance* while the macronotches engender *structural fatigue driving forces*. Provided that the volume over which the concentrated stress field acts is sufficiently large compared to microstructure, we can use the material model with micronotch effects as a life prediction tool based on elastic or elastic-plastic stress analysis of the structure, or using Neuber notch root analysis, as appropriate. Of course, for very large casting pores, the distinction of a structural notch and microstructural notch may become blurred. Acting in concert, this combination is extremely potent in decreasing fatigue life.

We may summarize the philosophy of our approach as follows. LEFM is rigorously valid and useful as a crack propagation framework for cracks beyond a certain length scale, typically on the order of about ½ to 1 mm. It is an engineering algorithm for cracks below this scale, perhaps useful for post-mortem failure analysis to ascertain the initial flaw size or help to understand the nature of the failure, but of little use in understanding microstructure-property relations. It is already well-known that 800 μm shrinkage pores or 1 mm trapped oxide films are very severe inclusions with severe reductions in fatigue strength for a given life. Of course, homogeneous material LEFM concepts handle these cases very well. As foundry practice improves for ever increasing demands on reliability and the defect sizes are controlled to lower levels, the convenience of LEFM must be foregone in favor of a characterization of microstructural scale plasticity or so-called *microplasticity* at various inclusions using computational micromechanics, as well as detailed cyclic elastic-plastic analyses of small cracks interacting with particles in eutectic regions. These computational micromechanics results serve as input to a microstructure-based fatigue model developed in this work which, while still an engineering model, provides a more firmly justified foundation for treating fatigue mechanisms occurring at inclusions below scales or extremely large pores or folded oxides. This model can serve as a means of connecting microstructure to fatigue life estimates, including variability arising from populations of different size inclusions. Since the treatment of long fatigue cracks using LEFM is well-documented and understood for its purposes, we focus here on the problem of cracks which form at inclusions in high quality castings, which is not so well understood. Moreover, the fraction of lifetime spent in forming and propagating small cracks in HCF at these lower scale inclusions completely dominates the fraction spent in LEFM-governed propagation in the long crack regime in many cases, so this kind of focus is of considerable practical importance. In the following sections we will summarize the microplasticity phenomena for different inclusions at different levels of applied loading and provide details of the incorporation of computational micromechanics as well as EPFM-based small crack growth calculations and experimental observations into this “first-generation” model.

2.2 Multiple Regimes of Fatigue Crack Development and Growth

Our computational micromechanics studies are reported in Chapter 4 of this report and are based on a substantial range of inclusion geometries (pores and Si particles), size distributions, nearest neighbor distances, distance to the free surface, and shapes. In some cases, multiple scale analyses of actual cast (digitized) microstructures were performed to determine local cyclic plasticity in eutectic regions as affected by long range stress fields of large pores, arrangement of particles, and so forth. The matrix elastoplasticity conforms to experimental cyclic stress-strain behavior of Al-1%Si specimens at room temperature and a frequency on the order of 1-10 Hz. Nonlinear kinematic hardening plasticity theory of Armstrong-Frederick (1966) type is employed (cf. McDowell, 1994).

The micromechanical studies in Chapter 4 provide insight into the nature of fatigue processes for cast alloys with fine scale heterogeneity. Figure 2.1 shows a schematic of three distinct regions of the constant amplitude, completely reversed uniaxial strain- and stress-life plots for a low porosity A356-T6 alloy based on our studies. In this plot, the length scale 'D' pertains to the diameter of either a typical Si particle or a gas pore for the case of significant microporosity. The length scale ℓ pertains to the size of the plastic zone at the notch root, defined as the scale over which the local plastic shear strain exceeds or meets 0.01% (see Figure 2.2). Given that particle spacing is on the order of particle diameter in the eutectic regions, for $\ell / D <$ about 0.3, the local plasticity at cracked or debonded particles or gas pores is confined to the vicinity of the inclusion and does not interact strongly with neighboring inclusions. Hence, we term this as the constrained microplasticity regime. Interestingly, for pores or debonded Si particles, the value of $\ell / D = 0.3$ approximately corresponds to the macroscopic cyclic yield strength of the alloy, so we can make the connection that macroscopic plasticity (hysteresis in the global stress-strain curve) is apparent when the local microplasticity develops past the constrained state – we term this as the domain of unconstrained microplasticity. Hence, we may regard $\ell / D = 0.3$ as a sort of percolation limit for microplasticity through the microstructure. Eventually, as ℓ / D approaches unity, the plasticity becomes extensive and the macroscopic state of cyclic plasticity as measured on test specimens is virtually indistinguishable from the connected microplasticity – we term this as the regime of limit plasticity. It is essential to point out that constrained microplasticity exists even below the macroscopic yield point, which in fact leads to the formation and growth of fatigue cracks. The applied uniaxial strain amplitude for the yield point is well-approximated as 0.0023 ($\ell / D \approx 0.3$), which corresponds to the percolation limit for microplasticity and the point of demarcation between LCF and HCF for this class of materials. For applied strain amplitudes less than 0.0023, the micronotch root cyclic plastic strain amplitude (averaged over a length scale on the order of D/4 as discussed later) is less than the notch root elastic strain amplitude. Above an applied strain amplitude of 0.0023 but below about 0.005 to 0.007, the micronotch root cyclic plastic strain amplitude is greater than the remote cyclic elastic strain amplitude, so this is a kind of transition regime to LCF. In the limit plasticity region the remote plastic strain amplitude becomes on the order of the micronotch plastic strain amplitude, and both eventually exceed the remote applied elastic strain amplitude at an applied strain amplitude of about 0.008. This distinction from the conventional definition of HCF and LCF in wrought alloys (where applied elastic and plastic strain amplitudes are equal) is important. For A356-T6, the HCF region according to our definition is beyond about 5×10^4

cycles, whereas according to the conventional definition it is approximately 100 cycles, an untenable result.

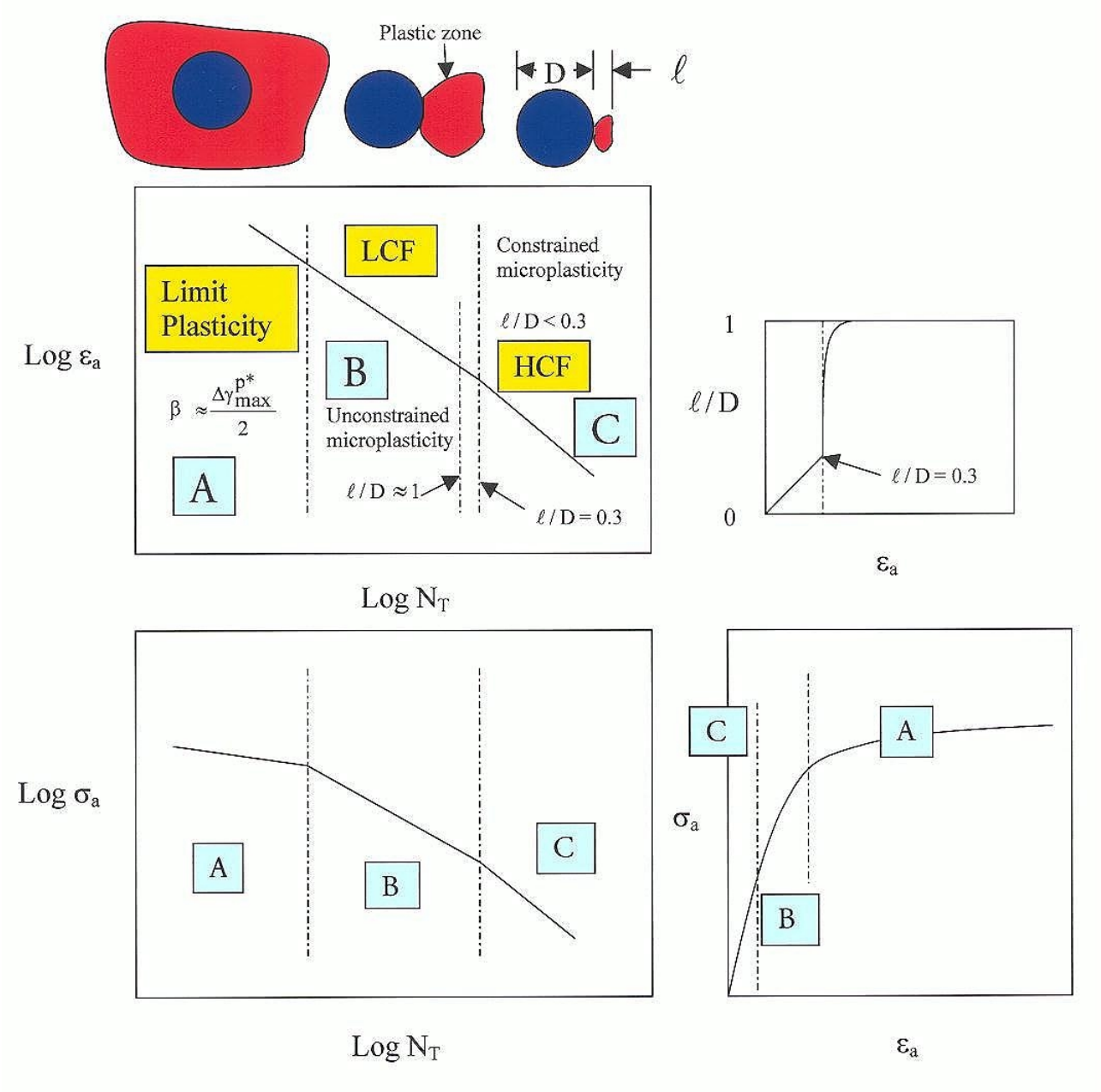

Fig. 2.1 – Regimes characterizing cyclic microplasticity at Si particles and casting pores: (A) EPFM propagation-dominated, (B) transition regime, (C) incubation-dominated. Here, D is the inclusion diameter and ℓ is the cyclic plastic zone size.

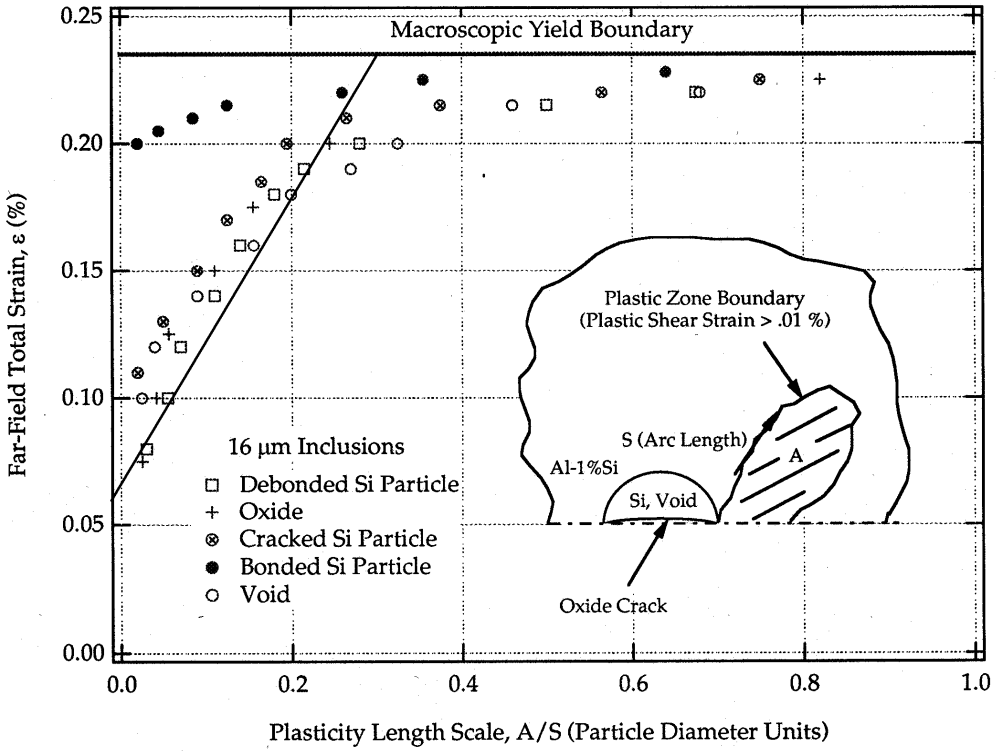

Fig. 2.2 – Computational micromechanics results for ℓ / D (plasticity length scale) as a function of applied total strain (Horstemeyer et al., 1999).

We identify three kinds of thresholds, in ascending order in terms of applied stress or strain amplitude level:

- microplasticity threshold for crack nucleation – corresponding to absence of cyclic microplasticity at debonded or cracked particles or at pores; a shakedown or lower bound fatigue limit associated with a microplasticity threshold.
- ΔCTD threshold for small crack propagation – corresponding to nonzero cyclic microplasticity below the percolation limit which is sufficient to nucleate cracks at inclusions, but insufficient to propagate the small crack away from the influence of the notch root field, leading to arrested or nonpropagating cracks with length on the order of the inclusion size. Small MSC/PSC cracks incubate in this case but do not continue to propagate out of the influence of the inclusion notch root field.
- long crack da/dN versus ΔK_{eff} threshold, which corresponds to an arrest of the development or coalescence of cooperative elastic-plastic deformation and separation processes that contribute to crack extension for a long crack which samples a statistically homogeneous set of Si particles.

In cast alloys, it is essential to take a hierarchical approach to the modeling of the fatigue damage process for several reasons. First, the formation of fatigue cracks is highly sensitive to both

stress amplitude and initial casting defects such as microporosity or gas pores, shrinkage porosity, intermetallics and large brittle second phase particles. So cracks can form at different length scales, with larger defects leading to cracks that can bypass stages of growth observed for cracks which form at much smaller defects. Second, the propagation behavior of fatigue cracks depends on their scale relative to microstructure. Cracks of length on the order of the secondary dendrite arm spacing (denoted as the dendrite cell size, DCS) are observed to propagate in irregular fashion through the microstructure; these interactions tend to dominate the total lifetime under high cycle fatigue (HCF) conditions which are targets for most casting design applications. The total fatigue life is modeled as the sum of numbers of cycles spent in four fatigue regimes as follows:

$$N_T = N_{inc} + N_{MSC} + N_{PSC} + N_{LC} \qquad \text{Equation 2.2}$$

- **N_{inc}** is the number of cycles to incubation of a microstructurally small crack, with initial length, a_i, on the order of ½ the maximum Si particle diameter, $\hat{D}_{part}$, or pore size, $\hat{D}_p$. This component of life is the related principally to the magnitude of cyclic microplasticity in the vicinity of microstructural notches or casting inclusions and the scale of the inclusion relative to the microstructure, with a secondary dependence on details such as defect shape. The nucleation of naturally occurring cracks at casting inclusions is related to the local cyclic plastic shear strain through a Coffin-Manson relation for the matrix material (Al-1% Si for A356), as has been derived for the mechanism of matrix/persistent slip band nanometer-scale void nucleation and coalescence (cf. Venkataraman et al., 1991a, 1991b). Once nucleated, the small cracks (typically on the order of a fraction of one μm) must then propagate through an enclave involving a significant gradient of cyclic stress and plastic strain away from the inclusion, typically losing driving force for fatigue crack growth as it grows, until the crack effectively leaves behind the influence of the notch and behaves as a crack with a physical length that includes the inclusion diameter (cf. Dowling, 1979; Ting and Lawrence, 1993). The zone of cyclic plastic deformation at the defect scales with inclusion size, as does the length scale over which the decelerative effect of the notch root stress/plastic strain concentration acts. The *crack incubation* life, as defined here, is neither the conventional "nucleation life" in the sense of fundamental studies of PSB/matrix decohesion of Venkataraman et al. (1991b) nor the "initiation life" as employed extensively in stress-life or strain-life correlations of fatigue experiments conducted on smooth specimens. Rather, it is the number of cycles required to nucleate a crack at an inclusion and then grow the crack away from the inclusion to the point where some type of EPFM crack growth law can be applied, essentially an incubation period for giving birth to a propagating MSC/PSC crack. As discussed by Bathias (1998), for hard particle-reinforced ductile matrix alloys, the case of a $100\,\mu m$ machined defect exhibits only about 1% of the total HCF life of that associated with an inclusion of the same size for a given applied loading condition; hence, incubation is a significant part of HCF life even for fairly large inclusions.

- **N_{MSC}** is the number of cycles required for propagation of a microstructurally small crack (MSC) with length $a_i < a < kDCS$, with DCS defined as the dendrite cell spacing/diameter, and k is a non-dimensional factor which is representative of the saturation limit for the encountering of the 3-D crack front with sets of Si particles. For $a < k$ DCS, a significant

portion of the the three-dimensional crack front may propagate through Al-rich matrix in dendrite cells. Since cracked or debonded particles amplify local cyclic plasticity, there is a tendency for cracks to form there or to be attracted towards them because of the intensification of local cyclic plastic strain - however, the crack opening displacement is reduced during encounters with debonded particles largely due to crack deflection around particles. Hence, particle encounters represent a rate-limiting step for crack advance. In A356-T6, propagation through the Al-1%Si dendrite cells or α-aluminum eutectic matrix material is impeded much less by comparison. Experimental observations show that the crack front may become pinned at low stress amplitudes at triple points of dendrite cells (Plumtree and Schafer, 1986), such that one may expect k to be on the order of a few DCS. Si particle debonding is predominant for MSC crack growth through eutectic regions. At higher stress amplitudes, the MSC crack is engulfed in extensive cyclic plasticity in the interdendritic regions, a condition far from applicability of conventional singularity-based fracture mechanics. At low stress amplitudes, the highly heterogeneous field of obstacles renders conventional LEFM solutions for homogeneous materials and growth constants based on large laboratory specimens invalid.

- $\mathbf{N_{PSC}}$ is the number of cycles required for propagation of a physically small crack (PSC) (~1-2DCS < a < O(10DCS)) during the transition from microstructurally small crack status to that of a dominant, long crack. Since the dendrite cell size is typically on the order of 30 to 100 μm, depending upon the solidification rate, the PSC regime may conservatively extend to 300-800 μm. The primary distinction of the PSC and long crack (LC) regimes is defined as follows: the microstructurally small crack at the onset of the PSC regime has a crack front that is largely engaged in Si particle encounters, advancing intermittently along segments that propagate through cell interiors. However, the crack is sufficiently small that the stress concentration and cyclic plastic zone ahead of the crack extends only over a fraction of the adjacent cell, e.g. a few Si particle spacings, depending, of course, on amplitude of applied loading. Hence, the mechanisms involved in the fatigue damage process zone vary significantly along the crack front, and there is still an insufficient level of the average elevated stresses ahead of the crack to wholly debond or fracture particles; the crack grows by a sequence of successive particle encounters. It is very important to note that the scale of the crack tip plastic zone is typically so small for PSC cracks that it samples individual microstructure elements (Si particles or dendrite cells); hence, there is an insufficient volume of material to achieve the length scale-independent description afforded by homogeneous material ΔK solutions in long crack fracture mechanics. As the crack continues to grow, however, at some point ($\approx$ 500 to 1000 μm), it is large enough to concentrate stress over a sufficient distance ahead of the crack tip so that the mechanisms for crack advance are uniform along the crack front, and the crack is a "macroscopic" stress concentrator in its own right. In this case, the crack front spends most of the time engaged in damaging Si particle/matrix interfaces, in concert with microporosity, fracturing compatible Si particles, and growing principally through and around the eutectic regions. The PSC definition employed here is distinguished from another common definition ascribed to a PSC crack as otherwise mechanically long crack that propagates under the influence of a notch.

- $\mathbf{N_{LC}}$ is number of cycles required for long crack propagation (a > ~10-20 DCS, depending on the amplitude of loading and the corresponding extent of microplasticity ahead of the crack

tip. Ultimately, the crack becomes long enough and the crack tip stress field high enough over great enough distances to dominantly fracture Si particles ahead of the crack tip, leading to overload fracture and relatively rapid crack advance later in fatigue life, as is apparent even in smooth specimens in the later stages of fatigue crack growth across the section. This stage of crack extension is commonly characterized using standard, long fatigue crack growth experiments (da/dN versus ΔK). But from a practical standpoint, this regime of crack growth only encompasses a large fraction of the fatigue life if large defects such as shrinkage pores or large scale oxides are present in the casting.

A hierarchical classification of inclusion severity on fatigue life is employed here. Five inclusion types and the associated range of length scales are listed as follows, according to the order of ascending level of severity:

Type	Inclusion
A	Distributed microporosity and Si particles; no significant pores or oxides
B	High levels of microporosity; no large pores or oxides (length scale of < 60 μm)
C	Large pores (length scale > 60 -90 μm)
D	Large pores near the free surface; no large oxides (length scale > 100 μm)
E	Large folded oxides (length scale greater than 200 μm)

The hierarchical approach to fatigue modeling of cast alloys distinguishes among these length scale classifications of inclusions by bypassing crack growth regimes if the cracks incubate at defects among the higher length scales.

2.3 Crack Incubation

Under HCF loading conditions, crack incubation controls the lifetime in many practical cases, especially for controlled porosity castings. For example, smaller parts made of squeeze cast alloys have limited macroporosity; in this case, microporosity and the heterogeneous microstructure within the interdendritic regions control the processes of fatigue crack formation which may dominate HCF lifetime. On the other hand, castings with large pores or trapped oxides suffer rapid crack propagation after incubation. It is therefore necessary to obtain solutions to boundary value problems which resolve the microstructure heterogeneity. In this manner the issues of applied stress amplitude and microstructure stress concentrations can be jointly taken into account.

2.3.1 Threshold for incubation

Our finite element calculations of digitized cast A356-T6 microstructures (Section 4.2.1.1) have indicated an absence of cyclic plasticity in the microstructure (microplasticity) for a completely reversed uniaxial applied strain amplitude less than 0.05%, which corresponds to a stress amplitude of about 35 MPa. Using the range of values for σ_f' and b for the range of A356-T6 alloys in this study gives a nominal life of about $4x10^{10}$ cycles for this stress amplitude, assuming that this relation holds beyond the data generated in this program. This is comparable to the fatigue limit levels observed for Al-SiC particle reinforced composites by Bathias (1996), who conducted gigacycle fatigue tests 20 kHz. There is no observable *macroscopic* plastic shear

strain for a uniaxial strain amplitude below 0.20% - only microscopic. In fact, the macroscopic yield strength corresponds roughly to an applied macroscopic strain level of 0.23%. For these reasons, the computational micromechanics formulation (Fig. 2.2) for nucleation is a fruitful route to better understand and quantify the role of microstructure on fatigue crack incubation and early growth.

Two criteria for fatigue crack nucleation have been employed in this research. Experimental results and theoretical analyses show that there is an intensification of cyclic plastic strain (slip) between pores and the free surface under cyclic loading (Ting and Lawrence, 1993). A local form of the Coffin-Manson law may be applied to correlate the cycles to nucleation of fatigue cracks in the Al-rich matrix material, i.e.

$$\beta = \frac{\Delta\gamma_{max}^{p^*}}{2} = C\, N_{inc}^{\alpha} \qquad \text{Equation 2.3}$$

where N_{inc} denotes the number of cycles for crack incubation (crack nucleation plus small crack growth within the notch root field), and $\Delta\gamma_{max}^{p^*}$ is the micronotch root maximum shear plastic strain range in the Al-rich matrix. In general, $\Delta\gamma_{max}^{p^*}$ significantly exceeds the macroscopic applied plastic shear strain in the HCF and transition regimes. Constants α and C are material-dependent parameters which have characteristic values for the Al-rich matrix.

With an eye towards treating variable amplitude loading and decohesion/particle fracture effects due to overloads, we may re-state the local approach above to the incremental form

$$\frac{dV}{dN} = C_v \left\langle \beta^{\Omega_v} \right\rangle \qquad \text{Equation 2.4}$$

where $0 \le V \le 1$, and $V(0) = 0$ for undamaged material and $V = 1$ for an incubated crack. This rule, for constant C_v and Ω_v, is equivalent to the Miner's linear damage summation law, i.e. $\sum n_i / (N_{inc})_i = 1$ for i = 1,2,..., N loading levels.

2.3.2 Nonlocal considerations in estimating the micronotch root β-parameter

In order to account for the averaging processes that occur in reality for cyclic plastic deformation over finite volumes of material (plastic deformation does not occur only at distinct mathematical points and therefore cannot exhibit infinite gradients), we must set a limit on the finest length scale of resolution (element size) in our modeling. For example, near the tip of a notch or crack in a wrought polycrystalline alloy, slip within each grain is much more uniform than would be predicted based on the assumption of homogeneity (no grain structure), simply because gradients of plastic deformation are accommodated and spread over finite distances by dislocation glide until barriers such as grain boundaries are encountered. In the case of fatigue crack formation, persistent slip bands form within the interior of surface grains. Upon crack formation, energy is released over a segment of the band ranging from about half a micron to a few microns (Venkataraman et al., 1991a, 1991b). Hence, we must preclude plastic strain gradients and stress gradients from occurring over length scales that are less than some critical dimension which is

associated with scale at which uniform dislocation arrays/structures form in response to applied stress. In other words, any parameter associated with the damage process zone of significant cyclic plastic strain is subject to a nonlocal averaging procedure, i.e.

$$\beta = \frac{1}{V_\beta} \int_{V_\beta} \beta' \, dV \qquad \text{Equation 2.5}$$

where V_β is a process zone volume for crack incubation/nucleation, typically on the order of approximately 0.1 μm^3 to 1 μm^3. This limits the maximum refinement of the linear dimensions of the finite element mesh, for example, to the order of 0.2 μm to 1 μm. Finer elements cannot properly account for the nonlocal nature of the process of damage formation within the microstructure, and instead will always lead to increasingly localized and intensified cyclic plasticity with mesh refinement, a physically untenable result. In reality, slip is transmitted over some finite length scale on the order of interparticle spacing, for example. Selection of a specific value for the minimum element size is important, but so is the application of a consistent definition throughout all calculations. Otherwise, the solutions would display unacceptable mesh sensitivity in terms of fatigue models. In Chapter 4, we adhere to the minimum element sizes listed above in the vicinity of microstructural stress concentrations. For purposes of averaging the notch root cyclic plastic strain, a mesh size of about D/20 is used in the calculations discussed in the next section, where D is the particle or pore diameter. It is found that the results averaged over a constant area are independent of further refinement of mesh size (cf. Gall et al., 2000b).

2.3.3 Microstructure "Notch" Size Effects on Crack Incubation

To account for the effects of size of inclusions (e.g. Si particles, voids, large scale oxides) on crack incubation, we appeal to the notion of a length scale for the fatigue process zone in the vicinity of microstructure stress-raisers or micronotches. Based on our micromechanical calculations (Chapter 4), we may correlate (i) the average local plastic shear strain (averaged over 1% of the particle area) with the applied total strain and (ii) the length scale of micronotch plasticity, $\ell = A/S_A$, with the applied total strain for cracked and debonded Si particles as well as voids. In 2-D calculations, A is the "cyclic plastic zone area", defined as the area over which the cyclic plastic effective strain exceeds 0.01%, and S_A is the perimeter of this area. In the 3-D case, $\ell = V/S_V$, where S_V is the area enclosing the cyclic plastic zone with volume V, which is similarly defined as in the 2-D case. Effectively, ℓ gives a length scale over which local cyclic plastic strain concentration is "substantial" as defined by an *arbitrary* but *consistently applied* definition. Here, we restrict the values of ℓ to lie in the range $0 \le \ell \le D$, such that we regard the case $\ell \to D$ as a limiting case of unconstrained plasticity associated with macroscopic yielding and ultimately extensive plasticity. From 2-D finite element calculations, the relations are captured to first order approximation for debonded Si particles and oxides (most severe local cases) as follows:

$$\frac{\ell}{D} = \frac{\langle \varepsilon_a - 0.0006 \rangle}{0.00567} \quad \text{for} \quad \frac{\ell}{D} \le 0.3$$

Equation 2.6

$$\frac{\ell}{D} = 1 - 0.7\left(\frac{0.0023}{\varepsilon_a}\right)^{\frac{1}{r}} \quad \text{for} \quad 0.3 < \frac{\ell}{D} \le 1$$

where D is the representative inclusion diameter, exponent r ($r < 0.2$) is a constant selected to fit the transition into the domain of unconstrained plasticity (beyond macroscopic yield point), and ε_a is the far field applied strain. Here, the Macauley brackets are defined by $\langle f \rangle = f$ if $f \ge 0$; $\langle f \rangle = 0$ otherwise. The line in Figure 2.2 shows the relation in Equation 2.6 for $\ell / D < 0.3$.

Chapter 4 presents results of 2-D finite element calculations for cyclic plastic strain concentration at voids and debonded inclusions in which the plastic shear strain amplitude is averaged over a notch root region of either 1% of the void or particle cross-sectional area ($0.012D^2$) or 6% of the void or particle cross-sectional area ($0.0625D^2$). The probability of pre-existing matrix-particle debonds following solidification is high, particularly if there is sufficient hydrogen gas level and microporosity in the melt. The results for A356-T6 Alloy with Al-1%Si-0.3%Mg matrix and Si particles are shown in Figs. 2.3-2.4. From the cyclic loading calculations shown in Figs. 2.3-2.4, we select the averaging area of $0.0625D^2$, which corresponds to a length scale of 0.25D over which the plastic strain is averaged at the notch root. Since the cyclic plastic shear strain for debonded inclusions in Fig. 2.3 is nearly linear with the size of the inclusion, for a given area of averaging, we can reduce the calculated results in Fig. 2.4 for an averaging area of $0.01\ D^2$ according to the ratio of 0.1D/0.25D to obtain the average notch root values for R = 0 and R = 0.5 over a notch root length scale on the order of 0.25D for an inhomogeneity diameter of D. In so doing, the results for the R = -1 case agree very well between the two plots. The results are shown in the plotted symbols in Fig. 2.5. We can heuristically assert that formation and earliest growth of small cracks will span this scale, which includes the difficult-to-treat phenomenon of propagation of the small cracks through the notch root field (cf. Smith and Miller, 1977; Dowling, 1979) and eventually out of its dominance. The following R-ratio dependent relation is found between the notch root average maximum plastic shear strain amplitude and applied strain amplitude in Fig. 2.5 **below macroscopic yield (** $\ell / D < 0.3$), for the most severe case of inclusion:

$$\beta = \Delta\gamma^{p*}_{max} / 2 = (0.1666 + 0.0266\,R)\left[\,100\{\varepsilon_a - 0.00025(1-R)\}\right]^{2.45} \qquad \text{Equation 2.7}$$

while for fractured Si particles for the case of intact particle/matrix interfaces, about 1/3 of this level of plastic strain intensification is calculated, i.e.

$$\beta = \Delta\gamma^{p*}_{max} / 2 = 0.32\,(0.1666 + 0.0266\,R)\left[\,100\{\varepsilon_a - 0.00025(1-R)\}\right]^{2.45} \qquad \text{Equation 2.8}$$

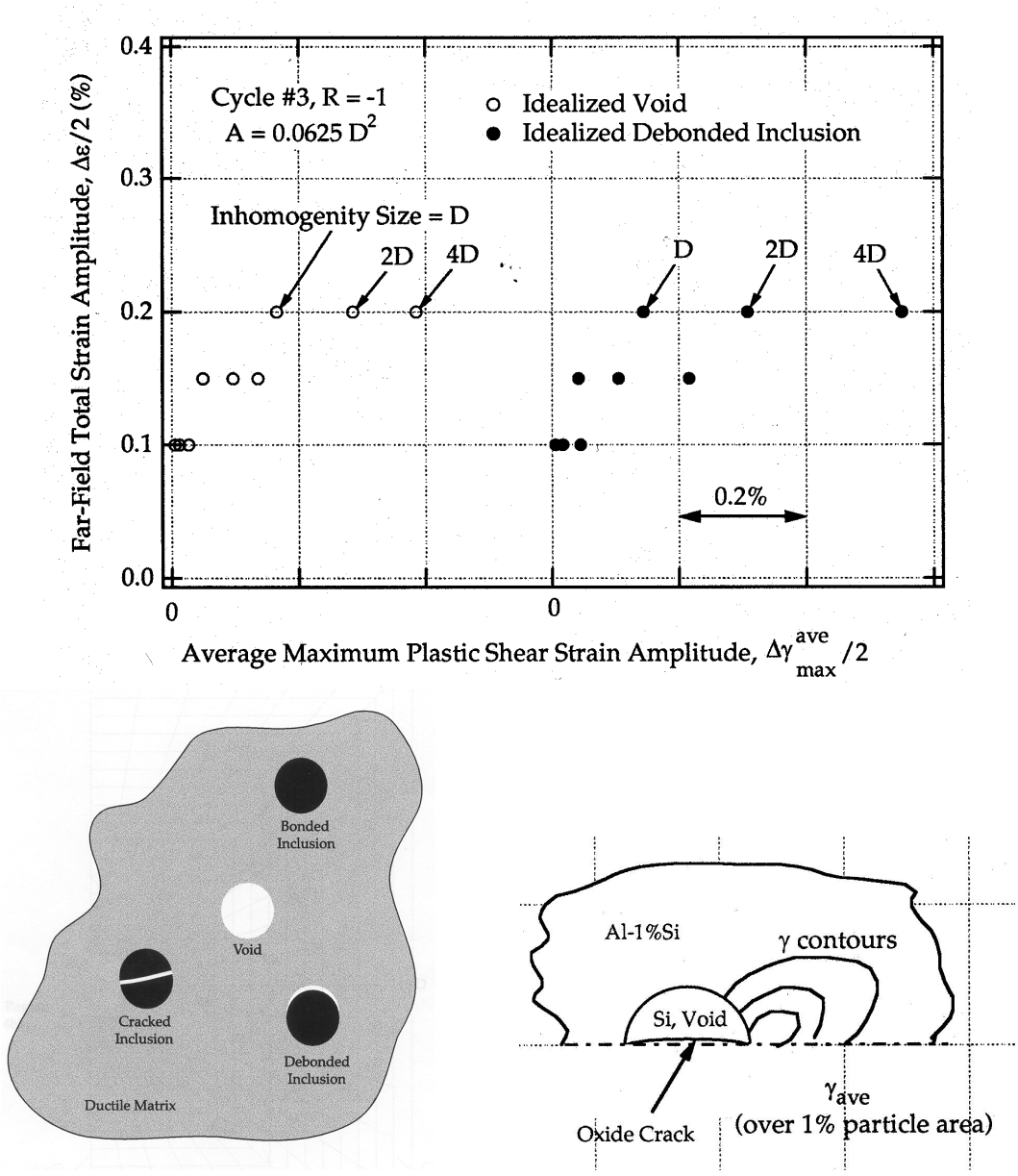

Fig. 2.3 - Effect of inclusion size (multiples of D) on the driving force for fatigue crack formation for the idealized, debonded inclusion and the idealized void, with a notch root area of $0.0625D^2$ for averaging the maximum plastic shear strain amplitude, as a function of the applied far-field total strain amplitude which is below macroscopic yield.

Note that the effect of the R-ratio is included here in the HCF regime via the exponent. From these relations we may derive a relation between β and ℓ/D for constant amplitude loading. Note also that $\varepsilon_a = 0.0023$ is the macroscopic completely reversed cyclic yield strain (percolation limit for heterogeneous microplasticity), so the relations above reveal significant microstructure-scale cyclic plasticity (microplasticity) well below the macroscopic yield. In the vicinity of macroscopic yield the transition to fully developed microplasticity begins to occur. We note that the threshold for β shifts downward with an increase of the R-ratio, evidently in a manner

very similar to that described by the Smith-Watson-Topper parameter - an increase of the applied peak stress due to an overload drops the threshold level for local microplasticity associated with pre-existing debonds.

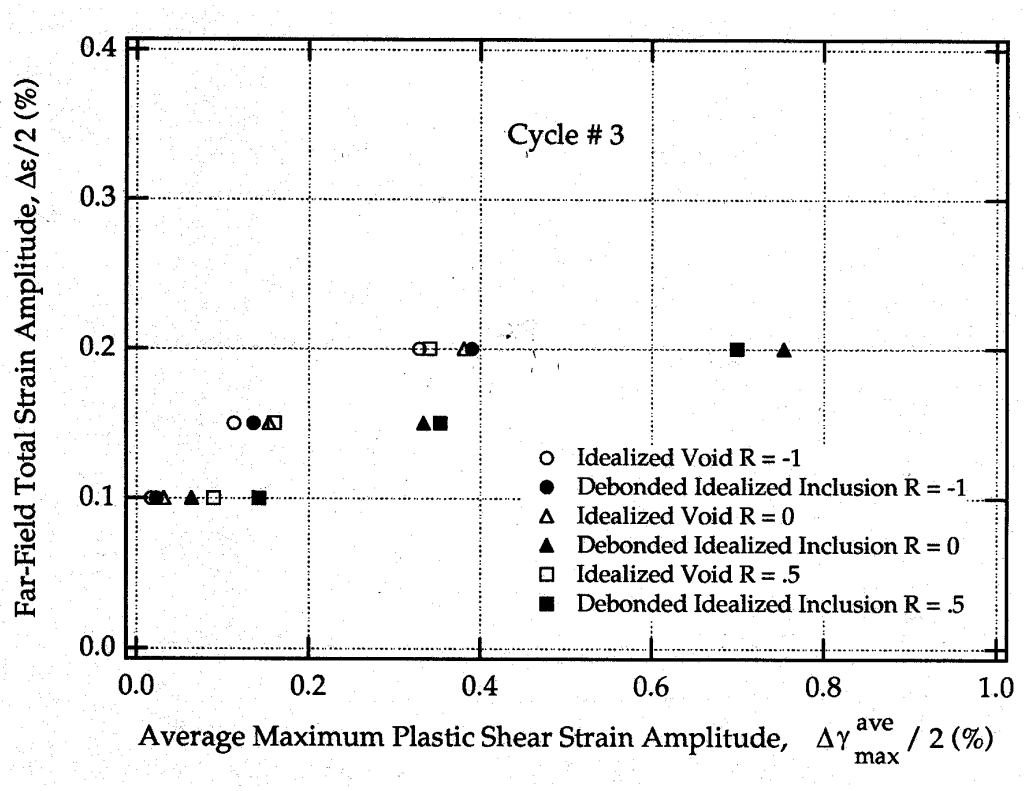

Fig. 2.4 - Notch root average (over an area of $0.012D^2$) maximum plastic shear strain amplitude, $\Delta\gamma_{max}^{ave}/2 = \Delta\gamma_{max}^{p^*}/2$, as a function of the far field total strain amplitude for the third cycle under R = -1, 0 and 0.5 loading conditions below the macroscopic yield point.

We have used debonding to define a worst case local driving force for crack incubation, assuming that it will occur over part of the particle interface due to localized impingement of slip bands on the interface and interface decohesion. Microporosity should effectively exacerbate the decohesion by enhancing plastic strain localization in the vicinity of the interface. From the calculations reported in Figs. 2.3-2.4, it is evident that pores do not display a strong mean stress dependence as is exhibited by debonded particles. However, even for pores/voids, we expect that adjacent Si particles within the zone of cyclic plastic deformation of the void will be subject to the more extreme debonding case; hence, we employ it for all cases of voids or pores for simplicity. These results indicate why the mode of crack incubation may shift from pores to particles as the mean stress is increased in HCF; because of the enhanced intensification of the notch root cyclic plastic shear strain for tensile mean stresses, the particle debonding mechanism for crack formation is expected to dominate void incubation at higher R-ratios. This has been observed experimentally by Bathias (1996, 1998) for hard particle-reinforced ductile matrix alloys.

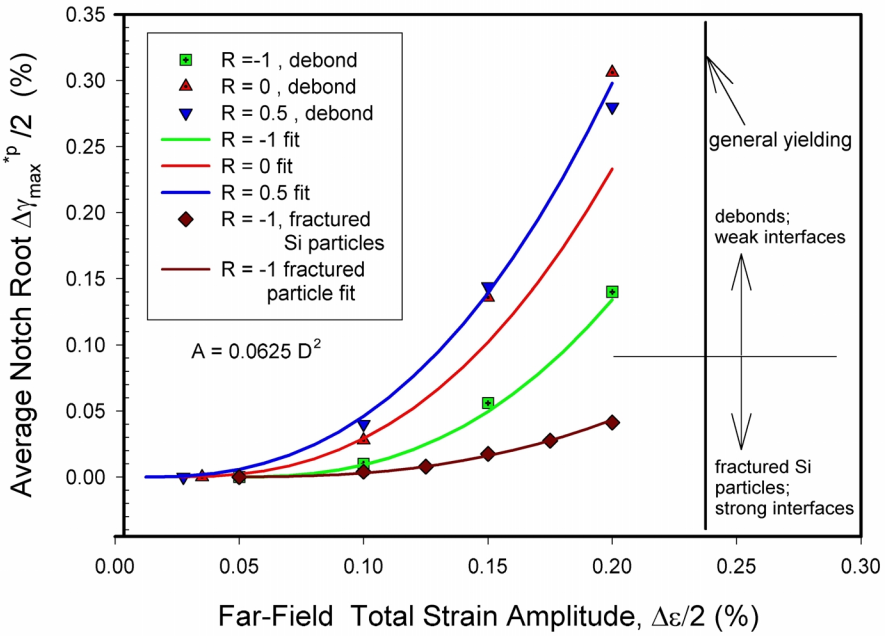

Fig. 2.5 - Correlation of Equations (7)-(8) with the FE computational results of Gall et al. (2000b) for average $\Delta\gamma^{p*}_{max}/2$ (in %) versus far-field total strain amplitude, $\varepsilon_a = \Delta\varepsilon/2$ (in %) for idealized debonded inclusions (Equation 2.7, upper curves) and for cracked Si particles (Equation 2.8, lower curve). An area of A = 0.0625 D^2 was used in averaging the cyclic plastic strain in calculations.

These calculations are conducted for particle sizes typical of those found in A356-T6 Al, but since the calculations are performed for isolated defects subjected to uniform far field loading conditions, the applied ε_a versus notch root average $\Delta\gamma^{p*}_{max}/2$ relation is independent of inclusion length scale and only modestly dependent upon shape of defect (Section 4.2.1.2). To first order, the details of the shape of the debonding defect or pore are not important. Although studies of the effects of aspect ratio indicate some dependence on this variable (although it is not too strong, cf. calculations in Chapter 4 of this report), the random orientation distribution of particles and pores within the microstructure suggest that some inclusions will always be favorably oriented to realize the most severe effect. The calculations of Gall et al. (2000b) demonstrate that the inclusion size relative to the scale over which the plastic strain is averaged has a much stronger effect, with the local notch root average cyclic plastic strain increasing roughly linearly with inclusion diameter for debonded particles and roughly with the $\sqrt{D_v}$ for voids (see Fig. 2.3). This argues in favor of characterizing the most severe inclusion within each inclusion type as the most extreme among the population of sizes. This essentially agrees with the use of the projected maximum area of the inclusion on a plane normal to the maximum

principal stress range, which has been previously used by Murakami and Endo (1994) to define an effective crack size ($\sqrt{area_{max}}$) for use in an equation for the fatigue limit S_f (in MPa), i.e.

$$S_f^n \sqrt{area_{max}} = C = \left[1.43(H_V + 120)\left(\frac{1-R}{2}\right)^{\theta} \right]^n \qquad \text{Equation 2.9}$$

where H_v is the Vicker's hardness (in kg_f/mm^2), $\theta = 0.226 + 10^{-4} H_V$, and $\sqrt{area_{max}}$ has the units of μm. They report a value of $n \approx 6$ for a wide range of materials. This relation is conceptually linked to the fatigue limit for a nonpropagating crack (through a threshold stress intensity factor range in LEFM). The relation in Equation 2.9 has demonstrated agreement to within 15% for a wide range of hardnesses (H_v from 100-740). They consider the valid upper limit on $\sqrt{area_{max}}$ to be 1000 μm.

However, for purposes of determining the average micronotch root cyclic plastic shear strain, the averaging length scale is assumed to be proportional to the defect diameter, D. The local cyclic plastic zone size ℓ scales linearly with the size of the associated defect (e.g. Si particles) for a given applied strain range. Recalling that the process zone volume for slip band formation is on the order of a micron or so, the maximum *local* values of maximum plastic shear strain amplitude at the notch root will increase with an increase of defect diameter; hence, fatigue cracks will form more quickly at large defects, but must still grow away under the influence of the notch root stress-strain field, which is assumed to be on the order of the averaging distance, about 0.25D. The averaging area will therefore be on the order of $0.0625D^2$, as assumed in the calculations in Fig. 2.3. We assume further that:

- The gradient of applied strain range (or strain field at large notches such as machined holes or large scale pores) is weak over distances comparable to Si particle diameter or spacing
- The initial crack size for the MSC propagation relation scales with D, i.e. $a_i = D/2 + \varsigma D/2$, with $\varsigma < 1$.

The Coffin-Manson law in Equation (2.3) for the matrix phase applies to the correlation of crack formation and growth within the finite notch root region over which the maximum plastic shear strain is averaged. For the Al-1%Si matrix, smooth specimen fatigue experiments in the LCF regime (approximately 100-1000 cycles to failure) give the value $\alpha = -0.5$. Therefore, we assume that this relation encompasses not only the formation of cracks (so-called nucleation phase), but also the phase of propagation of tiny cracks within the field of influence of the notch root in which they form. This type of notch root crack growth has been the subject of considerable computational study for large notches, where a decelerative effect on the driving force has been understood for single phase ductile alloys in terms of plasticity-induced closure transients and notch root stress/strain field decay. However, although some have used fracture mechanics approaches for crack incubation and growth for microstructurally small cracks from inclusions in wrought Al alloys (cf. Newman, 1994; DeBartolo and Hillberry, 1998; Laz and Hillberry, 1998;), the MSC growth phase eludes quantitative treatment in terms of the details of

the notch root geometry, dependence of crack tip plastic strain intensification and crack wake plasticity on details of the contact problem with the inclusion, and interface separation relations, not to mention the lingering question of the validity of singularity-based fracture mechanics at these relative scales of crack length to heterogeneity size and plasticity and damage zones at the notch root. For these reasons, we prefer to use the term "crack incubation" for the formation and notch root field growth of cracks in a heterogeneous two phase cast alloy. Of course, in the regime of constrained microplasticity, the value of C in the Coffin-Manson relation must reflect the combined processes of small crack formation and propagation within the micronotch root cyclic plastic field.

The second assumption leads to nonarbitrary assignment of the initial crack length for the propagation analysis, and is justified by the finding (cf. Bazant and Chen, 1997) that energy release for crack extension in real (granular) materials is related to the scale (and configuration) of intensified strain energy density due to heterogeneities. For most practical cases in cast A356-T6 alloy, cracks form in the matrix phase and hence the enclave of local cyclic plastic strain defines the length scale of the initiated crack. The fact that ℓ scales linearly with the size of the associated inclusion (e.g. Si particles) for a given applied strain range results in more intense local driving forces for fatigue associated with large debonded particles compared to small particles due to the relation between β and ℓ implied in Equations 2.6-2.7. This is very commonly observed in systems where particle fracture controls void nucleation. In this case it suggests that only the largest particles/voids among the population control the fatigue crack incubation process, particularly at low applied strain levels. As the cyclic strain amplitude is increased, a broader spectrum of particle sizes in the distribution produce local values of β which are high enough to form a set of more densely distributed, competing fatigue cracks. The same comments apply to pore size distributions for pore-dominated fatigue crack incubation.

The values of notch root average cyclic plastic shear strain for intact particle-matrix interfaces are much lower than those reported in Fig. 2.3. In our view, it seems most appropriate to assume that interfaces will debond, at least for particles with extreme characteristics; furthermore, it is difficult to envision particle fracture without some accompanying degree of local debonding. Plumtree and Schafer (1986) observed particle fracture in low gas porosity A356-T6 at higher strain amplitudes (around 0.5%), while particle/matrix debonding was observed to form cracks in the HCF regime. The effect of hydrogen gas micropores in the neighborhood of particles might be expected to follow the debonding characteristic in terms of intensification of micronotch root cyclic plastic strain.

2.4 Microstructurally and Physically Small Crack (MSC/PSC) Growth Regimes

Since the incubation life includes both crack nucleation and MSC growth within the domain of influence of the micronotch, and in view of the shortcomings of LEFM with regarding to driving forces and threshold concepts for the MSC regime as stated earlier, we employ a cyclic crack tip displacement law of EPFM type to govern the propagation of small cracks in both the MSC and PSC regimes, prior to application of a long crack LEFM growth law. Hence, Equation 2.2 is modified as

$$N_T = N_{inc} + N_{MSC/PSC} + N_{LC} \qquad \text{Equation 2.10}$$

The form of the growth law for the MSC and PSC regimes, including a threshold for crack growth, is given in general terms by

$$\left(\frac{da}{dN}\right)_{MSC/PSC} = G\left(\Delta CTD - \Delta CTD_{th}\right) \qquad \text{Equation 2.11}$$

where G is a constant for a given microstructure, typically less than unity (cf. McClintock, 1999). The threshold value of cyclic crack tip displacement, ΔCTD_{th}, is on the order of the Burger's vector of the Al-rich matrix; this threshold provides a nonpropagating crack limit which is generally applicable at higher stress levels than the intrinsic threshold limit for cyclic microplasticity associated with incubation. Typical fatigue limits reported for cast Al alloys are at stress amplitudes that would be typical of microstructurally small, nonpropagating cracks. They form and grow to a limited extent away from the nucleation sites, but eventually arrest when they lose sufficient cyclic crack driving force according to Equation 2.11. It is noted that the ΔCTD in Equation 2.11 is the local value for the MSC/PSC crack, and is much lower than the value calculated based on homogeneous LEFM, $\Delta CTD_{LEFM} \approx \Delta K^2/(\pi E S_y)$ because of the tortuous, three-dimensional crack path of the microstructurally small crack, with a distribution of pinning points along the front (McClintock, 1999). The threshold is much lower then the long crack LEFM threshold $\left(\Delta CTD_{LEFM}\right)_{th}$ as well, and in principle represents the effect of lattice friction. We assert that when the local value of ΔCTD is used, the irreversibility factor G is on the order of that for long cracks, about 0.5 (cf. Kuo and Liu, 1976; McClintock, 1999); it would be much lower (perhaps two orders of magnitude) if the macroscopic ΔCTD_{LEFM} were used.

Of course, the functional form of Equation 2.11 for growth through a cell interior will differ from that for growth through the eutectic regions. If the particles in the eutectic regions offer little capacity to block or pin the crack front and propagation through the matrix is relatively easy (perhaps assisted by distributed microporosity), then there is little or no retardation at the interdendritic boundaries; at this point the transition begins to occur towards applicability of the long crack solutions for crack driving force based on da/dN versus ΔK. The crack propagates through the dendrites and eutectic region without arresting. If the particles pin the crack front and thereby provide toughening, or if there is substantial distributed microporosity in the cells at or near the interdendritic regions to guide propagation along these regions, then propagation may proceed rapidly within the first few cells but at a decreasing rate as the 3D crack front begins to sample enough interdendritic boundary to effectively pin it, i.e. out to a scale on the order of 1-2 DCS. Under HCF conditions, the number density of cracks should be lower, so that multiple dendrite cells (perhaps a very large number at very low stress amplitudes) can separate adjacent microcracks in the distribution. Triple points of dendrite cells offer particularly potent sites for crack front pinning (cf. Plumtree and Schafer, 1986). The A356-T6 alloy appears to conform to the crack front pinning mechanism – the rate-limiting step is provided by bypass of Si particles in the eutectic regions.

Cyclic elastic-plastic calculations for the A356-T6 alloy presented in Section 4.3.1.2.2 examine the ΔCTD 1-2 μm behind the crack tip for microstructurally small cracks of different initial

lengths (some on the order of the dendrite cell diameter, some on the order of Si particle spacing) as they grow around debonded Si particles. In these calculations, the ΔCTD is on the order of 2 to 60 nm. These calculations are conducted for three cycles at each crack position and include particle/matrix contact. An example is shown in Fig. 2.6.

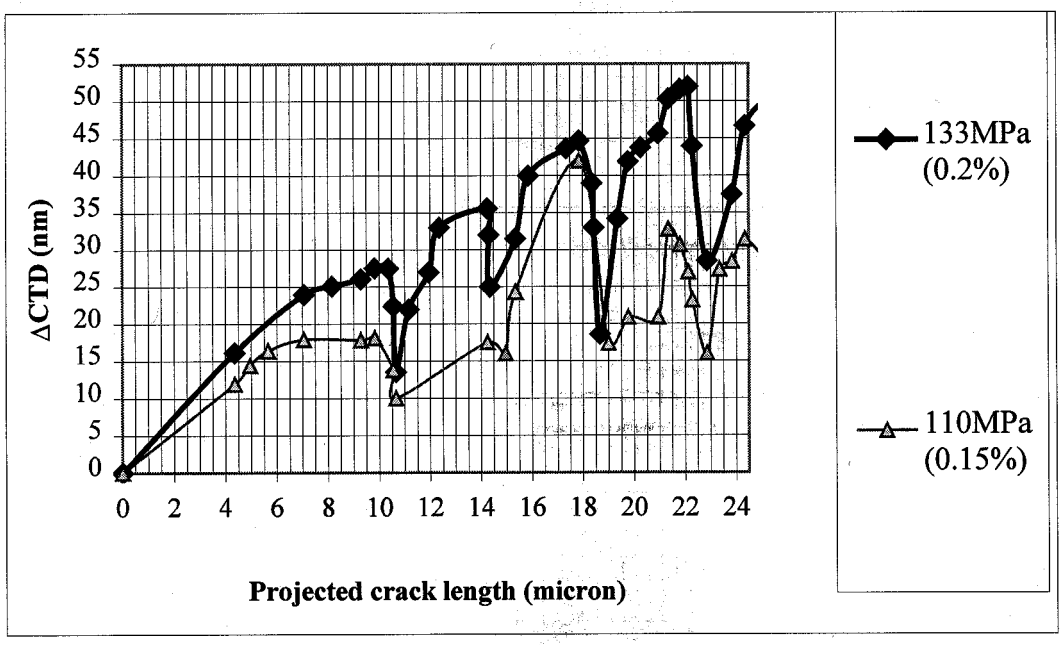

Fig. 2.6 – Effect of the applied stress amplitude on the cyclic crack tip displacement ΔCTD as a function of projected crack length for growth around the first two particles in an in-plane Si particle cluster.

Principal findings/implications are as follows:

- The ΔCTD for crack tips in the middle of dendrite cells are much higher (factor of 2-3) than those for crack tips engaged in Si particle bypass events for similar projected crack lengths.
- Although the ΔCTD is much higher for 50-60 μm initial crack lengths than for 10-20 μm initial crack lengths, once both cracks have engaged 2-3 Si particles in the eutectic regions, they have very similar ΔCTD levels; this implies that cracks can sweep rapidly through the first dendrite cell interior, but become entangled with particle interactions fairly rapidly, a sort of interaction saturation limit. Since cracks are three-dimensional in reality, the crack may expand to the order of the DCS relatively quickly, but then exhibit a growth rate similar to a crack with length on the order of Si particle spacing. Furthermore, the average local ΔCTD values during particle bypass events are considerably lower than would be calculated based on the assumption of homogeneous FCC Al, even for these idealized calculations. Much greater reductions would be expected for more realistic conditions of a 3-D crack front interacting with a set of microstructural obstacles (cf. McClintock, 1999).

- The ΔCTD scales more or less linearly with the crack length a after several Si particle encounters, i.e.

$$\Delta CTD \propto \Delta\sigma^n a \qquad \text{Equation 2.12}$$

certainly not as a^2 or a^3 as might be expected from LEFM concepts, in conformity to the experimental measurements by Shiozawa et al. (1997) on squeeze cast Al-Si alloys for microstructurally small fatigue cracks (see also Equation 2.1).

- There are very significant dips in the ΔCTD as cracks come in contact with particles and propagation around them, followed by a restoration of higher ΔCTD as the cracks re-engage matrix material on the other side of the debonded particle. These dips are on the order of half the magnitude of the peak ΔCTD for crack growth in the matrix after each bypass event. This is on the order of the dip in growth rate observed for A356-T6 for a crack blocked by a dendrite cell triple point by Plumtree and Schafer (1986) at an applied strain amplitude of 0.18%. Shiozawa et al. (1997) measured even larger dips relative to the maximum growth rate in da/dN for squeeze cast Al-Si alloys during particle encounters. Both studies report minimum measured *surface* crack growth rates on the order of 0.1-0.3 nm/cycle, which is likely a lower bound for the actual minimum crack growth rate. This growth rate is on the order of the interatomic spacing in the Al-rich eutectic matrix phase. The average growth rate for crack extension across the scale of a dendrite cell is therefore higher than the minimum and lower than the maximum growth rates at various points within the cell.
- An exponent on stress amplitude (as in Equations 2.1 o r 2.12) of $n \approx 4$ is determined from the FE calculations for the average ΔCTD over the encounter with the third Si particle in the HCF regime, based on strain amplitudes of 0.15% and 0.2%, whereas $n \approx 2$ applies to early propagation in the matrix phase prior to particle encounters (ΔCTD still linear in a in this case). Yet higher values of exponent n are plausible for further particle encounters – they have not yet been computationally studied due to the intensive CPU time involved. If Equation 2.11 applies, the value of n = 2 in this case, as well as a linear dependence on crack length, is expected for the dominantly elastic crack tip field (small scale yielding in homogeneous material) of the elastic J-integral or ΔCTD-controlled growth in the HCF regime away from particles since the matrix yields only locally in the vicinity of particles. Higher values of exponent n observed experimentally therefore derive from crack-particle interactions involving cyclic plasticity and particle contact.
- Similar FE calculations involving higher R-ratios for the remote applied stress indicate that after several particle encounters, to first order the combined effects of plasticity and roughness induced crack closure are that the crack is open over the part of the cycle for which the remote applied stress is tensile. Plumtree and Schafer (1986) observed HCF propagation through the Al-rich matrix in the interdendritic regions (not through the dendrite cell interiors), but along meandering paths away from Si particle/matrix interfaces. Direct encounters with the crack running into Si particles were observed only at triple points. Similar observations were reported by Shiozawa et al. (1997) for squeeze cast Al-Si alloys. This is also consistent with the observation of striations within dendrite cells for MSC cracks. Hence, in-between the interactions with Si particles the crack is likely able to develop limited plasticity-

induced closure which may result in somewhat positive crack opening stress levels with increasing R-ratios, which is classical for purely plasticity-induced closure models. However, Couper et al. (1990) found for an alloy similar to A356-T6 that the effects of mean stress for fatigue lifetime of cracks incubated at interdendritic pores was fairly well described (neglecting any incubation lifetime component and using LEFM) by introducing the assumption that the crack is open over only the tensile part of the cycle for the R = -1 loading case, i.e. U = 0.5 in the relation $\Delta K_{eff} = U \Delta K_{applied}$; they asserted that $U \approx 1/(1-R)$ for $R < 0$, $U \approx 1$ for $R \geq 0$, which is reasonably representative of our computational results. It appears that for cast Al alloys, the influence of roughness-induced closure (contact with Si particles) and constraint of Si particles on plasticity in the wake of the crack leads to a quasi-brittle, normal stress-dominated growth behavior.

- Prior to Si particle encounters, the ΔCTD scales nearly linearly with the size of the initial crack length; this implies that there will be a systematic effect of the dendrite cell size on the fatigue crack growth rate, more or less linear in nature. Higher dendrite cell sizes lead to higher ΔCTD and therefore we may expect a commensurate increase in da/dN based on Equation 2.11.

The last point is expected to apply in particular for eutectic propagation in the HCF regime, since it is more likely that the majority of Si particles will remain intact with the matrix in this case and therefore will provide reinforcement and affect crack deflection around them. At high applied strain amplitudes, particle/matrix decohesion and even particle cracking is extensive enough over a larger fraction of the population of Si particles such that the cracks will likely be 'attracted' to these damaged particles and will prefer to grow by a debond coalescence mechanism, which is an entirely different mode of propagation from the HCF case. At high levels of microplasticity, the field of slip forms an interconnected network through the microstructure, facilitating bypass of the particles in eutectic regions; the particles are much less effective in pinning the crack and therefore the crack growth rate is much higher, on the order of that for elastic-plastic propagation in the aluminum rich eutectic α-phase absent particle interactions. Therefore, we must introduce both modes of propagation into the da/dN versus ΔCTD relation in Equation 2.12, by incorporating the change of mechanism through an applied strain amplitude (or ℓ / D) dependence.

The role of microporosity (e.g. gas porosity) on fatigue resistance has been cited as a complicating effect (cf. Major, 1994), since it is coupled closely with the dendrite cell size by virtue of kinetics of microstructure coarsening during solidification. Of course the level of microporosity is also highly dependent upon the hydrogen gas content in the melt. It seems logical to assert that the role of microporosity is principally to affect cyclic plastic strain localization in the Al-rich matrix within the eutectic regions ahead of the crack tip and in the vicinity of debonds ahead of the crack thereby contributing to an increase in the ΔCTD, which governs the small crack propagation rate. It is observed in recent data from fatigue tests performed on vertically cast specimens obtained from F. Major of Alcan, Inc. (August 1999) that even for very low hydrogen content, the fatigue resistance is enhanced substantially relative to alloys of comparable DCS with higher hydrogen content, even though cracks are observed to form at relatively large shrinkage pores. These results strongly indicate that the eutectic fatigue ductility is effectively compromised by the introduction of microporosity above a certain

threshold level. This is quite independent of the relation between the dendrite cell size and the ΔCTD found in computational simulations in the HCF regime below the microplasticity percolation limit. From the kinetics of growth during solidification, it is necessary to have hydrogen content below about 0.07 ml/100 g alloy (cf. Major, 1994) in order to achieve microporosity levels below 0.1% during solidification times typical of thin section castings. Lower levels yet would be required for thick castings, e.g. < 0.05 ml/100 g alloy. Fatigue experiments conducted on A356-T6 specimens with nearly zero hydrogen content over a systematic range of the DCS from about 20 to 60 μm reveal that the fatigue life for a given strain amplitude in the HCF regime is roughly tripled for the near-zero hydrogen content relative to horizontally cast plate behavior for the *same dendrite cell size* (20-35 μm), while the fatigue life is not much different from horizontally cast plate for a dendrite cell size of 60 μm with equivalent porosity. For the vertically cast specimens with 0.16 ml/100 g alloy content and 20 μm DCS , the fatigue life is roughly doubled relative to the horizontally cast plate, while the fatigue life is increased by only about 20-30% for DCS = 35 μm ; Again, the DCS = 60 μm data are not much different than the horizontally cast plate data. For a 20-30 μm dendrite cell size and 0.16 ml/100 g alloy hydrogen content, the corresponding microporosity level is about 0.1% for a solidification time on the order of 15 sec from Major's plot (1994) for an unmodified alloy. Hence, a combination of 0.1% porosity with a dendrite cell size less than approximately 30 μm (representative of fairly rapid solidification rates in thin sections) is an effective threshold level above which the onset of microplastic strain localization affects propagation by decreasing the eutectic matrix fatigue ductility. If the microporosity is maintained below the 0.1% threshold, then larger dendrite cell sizes can be admitted (longer solidification times) while still maintaining good fatigue ductility of the eutectic matrix. Above this threshold, differences between fatigue life as a function of the dendrite cell size are due to effects of the dendrite cell size on the constraint of the ΔCTD in the MSC/PSC propagation law. One possible explanation for the compounding influence of the dendrite cell size for the case of very low hydrogen content is that for highly refined microstructures it is unlikely that even low levels of microporosity can grow during solidification, whereas for higher gas content the microporosity levels may always exceed the threshold. Indeed for the near zero hydrogen content specimens cited above, post-mortem metallographic examination at Sandia National Laboratories (Yang, 1999) revealed crack incubation at near surface pores on the order of 150 μm in diameter for the 60 μm dendrite cell size, whereas the 20 and 35 μm cell sizes had negligible porosity and small cracks were observed to incubate at small "pre-crack" features or oxides. Only one of the DCS = 35 μm specimens was found to have a 40 μm pore that is 20 μm from the surface that incubated the failure crack, and this was by far the most damaging case. From an engineering standpoint, the tentative conclusion is therefore that when porosity levels exceed approximately 0.1% within some critically stressed volume, the matrix fatigue ductility degrades.

Based on the correlations of Shiozawa et al. (1997) in the MSC/PSC regimes, we choose to express the ΔCTD parameter in the HCF regime as

$$\Delta CTD = f\left(\bar{\phi}\right) C_{II} \left(\frac{DCS}{DCS_o} \right) \left[\frac{U \Delta\hat{\sigma}}{S_u} \right]^n a \qquad \text{Equation 2.13}$$

where $\Delta\hat{\sigma} = 2\theta\bar{\sigma}_a + (1-\theta)\Delta\sigma_1$ is the range of the uniaxial equivalent stress, which is a linear combination of the von Mises uniaxial effective stress amplitude $\bar{\sigma}_a$ (= $\sqrt{3/2\left(\Delta\sigma'_{ij}/2\right)\left(\Delta\sigma'_{ij}/2\right)}$) and the range of the maximum principal stress, $\Delta\sigma_1$; θ is a constant factor ($0 \le \theta \le 1$) introduced by Hayhurst et al. (1985) to model combined stress state effects. Here, C_{II} is a coefficient intended to apply to both the MSC and PSC regimes for crack lengths ranging from a few microns to hundreds of microns, even up to the millimeter range (cf. Shiozawa et al., 1997; Gungor and Edwards, 1993), as long as the crack tip cyclic plastic zone is substantially less than the DCS. The factor U (consistent with FE calculations and Couper et al. (1990)) addresses mean stress effects on propagation which are influenced strongly by interdendritic particle interactions in the ahead of and in the wake of the crack; U = 1/(1-R) for R < 0, U = 1 for R ≥ 0, where R is based on the maximum principal stress. The exponent n ≈ 4.8 in the work of Shiozawa et al. (1997) is much greater than the usual LEFM value due to the local cyclic plasticity associated with interactions with heterogeneities. Furthermore, da/dN is linear in crack length and does not follow LEFM either. The MSC/PSC growth rate is linear in DCS as motivated by our FE calculations. Although this is associated with the decreasing constraint on slip with increasing DCS, other influential factors such as Fe-rich intermetallic particle sizes (Wang et al., 1998; Gall et al., 2000a) and microporosity also may be linked to increases of the DCS.

The fatigue limit which corresponds to the threshold condition in Equation 2.11, $\Delta CTD = \Delta CTD_{th}$, is almost identical to that proposed by Murakami and Endo (1994) in Equation 2.9 for R = -1; it differs slightly for other R-ratios, but Equation 2.13 is consistent with experimental observations of small crack growth (Couper et al., 1990) and our calculations for the R-ratio dependence of da/dN. In the limit plasticity regime, Equation 2.13 must be modified to include the dominant effect of essentially plastic strain driven, linear damage evolution; da/dN is essentially independent of the crack length in this regime. We will discuss this later when the model is completely described.

In accordance with the previous discussion regarding the role of microporosity in decreasing matrix ductility, we assign a dependence of the eutectic matrix fatigue ductility in the HCF regime on the level of microporosity, using the average porosity $\bar{\varphi}$ as a measure, i.e.

$$f(\bar{\varphi}) = 1 + \omega\left\{1 - \exp\left(-\frac{\bar{\varphi}}{2\varphi_{th}}\right)\right\} \quad , \quad \varphi_{th} \approx 10^{-4} \qquad \text{Equation 2.14}$$

where ω is a constant on the order of 2-10. The factor of 2-3 reduction in fatigue life observed for higher microporosity cast specimens relative to low microporosity specimens suggests a value of $\omega \approx 2$, based on ratio of incubation life to total life of about 1/3 for stress amplitudes in the range of HCF-transition regime, as suggested by the data of Shiozawa et al. (1997). For two different low porosity squeeze cast alloys in the HCF regime, Shiozawa et al. (1997) measured the combined coefficient GC_{II} = 3.11x10^{-4} m/cycle for units of crack length in m and for a reference dendrite cell size of DCS_o = 30 μm, assuming that in this case the microporosity is very low, i.e. $f(\bar{\varphi}) \approx 1$.

Hence, in this model both macroporosity (large pores) and microporosity (interdendritic gas pores) play a role in reducing the fatigue strength, the latter through reduction of eutectic matrix fatigue ductility and the former through reduced incubation lifetimes and larger initial crack sizes for the propagation analysis.

The type of small crack growth law of the form given in Equations 2.11 and 2.13 has been shown to be consistent with experimental results for cast Al-Si alloys for cracks exceeding well over 1 mm by Shiozawa et al. (1997) for stress amplitudes ranging from the vicinity of the fatigue limit to 70% of the ultimate strength (well into the transition regime), so it appears that there is no limitation in using Equation 2.13 as a good approximation for the growth law of small cracks in small, smooth, uniformly stressed laboratory specimens over the entire life. Furthermore, it is consistent with the empirical form given in Equation 2.9 which has demonstrated extensive fatigue limit correlations by Murakami and Endo (1994).

2.5 Long Crack (LC) Growth Regime

In this regime, the influence of the crack extends over a sufficient distance relative to D_p and DCS and the cyclic plastic zone and damage process zone at the crack tip is small compared to crack length (less than approximately 1/10) such that the homogeneous material da/dN versus ΔK_{eff} relations may be applied based on constants fit from long crack experiments. It is observed that Si particle fracture ahead of the growing crack is the dominant mode of fatigue process zone degradation, as a high fraction of fractured Si particles appear on the fracture surface for a > kDCS (cf. Fig. 3.17). Note that the effects of R-ratio and plasticity/roughness-induced closure are manifested through $\Delta K_{eff} = K_{max} - K_{open.} = U\Delta K$. A crack which is incubated at large oxides or shrinkage pores may effectively be treated with the LC growth relation, as evidenced in the literature (cf. Ting and Lawrence, 1993). For practical purposes, we may write, for cracks greater than about 10-20DCS (almost always valid for crack lengths exceeding 1 mm) the growth law as

$$\left(\frac{da}{dN}\right)_{LC} = A_p\left(\left(\Delta K_{eff}\right)^M - \left(\Delta K_{eff,th}\right)^M\right) \qquad \text{Equation 2.15}$$

where M is the Paris growth law exponent and A_p is the growth coefficient. Data for A356-T6 (horizontally cast plate) in this program indicate that $M \approx 4.2$ and $A_p \approx 1.5\text{x}10^{-11}$ m-$\left(\text{MPa}\sqrt{\text{m}}\right)^{-4.2}$/cycle. Here we are using the effective or intrinsic (closure free) threshold value of $\Delta K_{eff,th} \approx 1.3\,\text{MPa}\sqrt{\text{m}}$ for A356-T6 (only slightly less than the value of 1.4 found by Couper and Griffiths, 1990). The apparent long crack threshold depends both upon the R-ratio of applied loading in the regime, and is given by

$$\begin{aligned}
&\Delta K_{th} = \left(1.0 + K_{op}\right)\left(1 - R\right) \quad \text{for } \Delta K_{th} \geq 1.0 = \Delta K_{eff,th} \\
&\Delta K_{th} = \Delta K_{eff,th} \quad \text{for } R > \approx 0.8 \\
&\Delta K_{th} \approx 4.4 \quad \text{for } R < 0
\end{aligned} \qquad \text{Equation 2.16}$$

The opening stress intensity factor level is given by (Couper and Griffiths, 1990)

$$K_{op} = 3.4 + 3.8R^2 \text{ for } R > 0,$$
$$K_{op} = 3.4(1+R) \text{ for } 0 \geq R \geq -1, \text{ and} \qquad \text{Equation 2.17}$$
$$K_{op} = 0 \text{ for } R < -1$$

Finally, ΔK_{eff} is defined by $\Delta K_{eff} = K_{max} - K_{op}$ if $K_{min} < K_{op}$, $\Delta K_{eff} = K_{max} - K_{min}$ if $K_{min} \geq K_{op}$. The fit to long crack data from the USCAR program for A356-T6, horizontally cast plate, is shown in Fig. 2.7. It appears that the opening K levels from Couper and Griffiths are reasonably similar to this alloy.

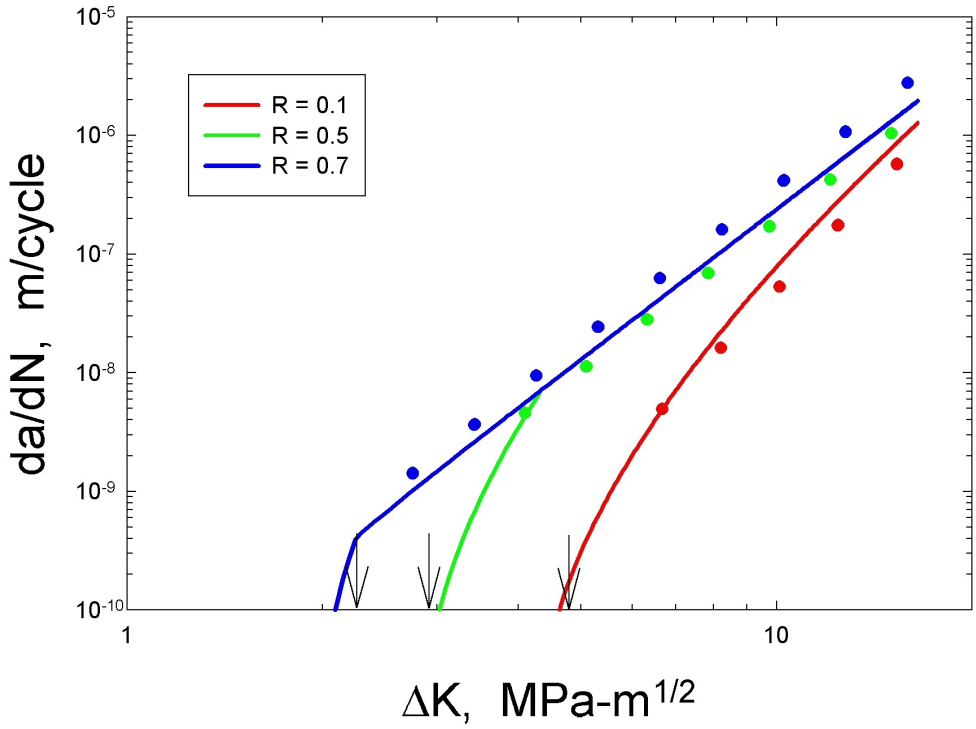

Fig. 2.7 – Fit of Equations 2.15 and 2.17 with data from the horizontally cast plate of the USCAR program for the long crack growth rate versus applied ΔK. Arrows denote the experimentally measured apparent threshold, ΔK_{th}, for each R-ratio.

2.6 Outline of Model

In this section we outline the equations for the comprehensive fatigue model for A356-T6 alloy, in ascending order according to inclusion severity type.

2.6.1 Type A: Distributed Microporosity and Si Particles; No Significantly Large Pores

2.6.1.1 Incubation

$$\frac{\ell}{D} = \frac{\left\langle \bar{\varepsilon}_a - 0.0006 \right\rangle}{0.00567} \quad \text{for} \quad \frac{\ell}{D} \le 0.3$$

$$\frac{\ell}{D} = 1 - 0.7\left(\frac{0.0023}{\bar{\varepsilon}_a} \right)^{\frac{1}{r}} \quad \text{for} \quad 0.3 < \frac{\ell}{D} \le 1$$

where $\langle f \rangle = f$ if $f \ge 0$; $\langle f \rangle = 0$ otherwise. In these equations, D is the maximum Si particle diameter in the distribution, $D = \hat{D}_{part}$. Also, 'r' is a shape constant for the transition to limit plasticity, which we have taken r = 0.1 to provide a rapid transition into the limit plasticity regime as observed in finite element calculations; ℓ / D is approximately 0.951 at a strain amplitude of 0.003. Hence, incubation rapidly becomes insignificant above the percolation limit for microplasticity as extensive shear localization dominates the eutectic regions. The uniaxial von Mises equivalent strain amplitude is defined by $\bar{\varepsilon}_a$. The micronotch Coffin-Manson law for incubation life (nucleation plus growth in the notch root field) is written in terms of the notch root averaged cyclic plastic shear strain amplitude as:

$$\beta = \frac{\Delta\gamma^{p^*}_{max}}{2} = C_{inc}\, N^{\alpha}_{inc}$$

$$C_{inc} = C_n + \frac{1}{0.7}\left\langle \frac{\ell}{D} - 0.3 \right\rangle \left(C_m - C_n \right) = C_n + z\left(C_m - C_n \right)$$

$$C_n = 0.24\left(1 - \langle R \rangle \right)$$

where C_n is the coefficient for nucleation and small crack growth at inclusions in the HCF regime (constrained microplasticity), and C_m is the Coffin-Manson coefficient for incubation (cycles to formation of a dominant EPFM crack) in the limit plasticity regime (LCF), obtained from the dendrite cell Al-1%Si alloy. The localization multiplier $z = {}^{1}\!/_{0.7}\langle \ell / D - 0.3 \rangle$ is nonzero only above the microplasticity percolation limit, and rapidly transitions to unity as the interdendritic plastic shear strain localization sets in just above the microplasticity percolation limit. Beyond this point, the incubation process is negligible (only a few cycles) due to the severe levels of

strain localization around particles or pores. The matrix fatigue ductility coefficient is estimated as C_m = 0.03, based on LCF experiments on Al-1%Si specimens at lives below $5x10^3$ cycles. Note the additional positive mean stress dependence embedded in C_n, which reflects an effective decrease in matrix fatigue ductility at higher positive load ratios due to plastic strain localization associated with significant local monotonic plastic shear strain computed on the first half cycle (order of a few % even for applied strain amplitudes of 0.15%); this localized plastic strain level increases with R-ratio (Gall et al., 2000b). Furthermore, ratchetting or progressive plastic deformation of the notch root plastic shear strain is also evident in the calculations of Gall et al. (2000b) and is known to degrade fatigue ductility. The exponent α also pertains to the eutectic Al-rich matrix, and is estimated from LCF tests on Al-1%Si as α = -0.5. Based on the fit to computational micromechanics solutions below macroscopic yield ($\ell / D < 0.3$), we write:

$$\beta = \Delta\gamma^{p*}_{max} / 2 = Y\left[\, 100\left\{\bar{\varepsilon}_a - 0.00025(1-R)\right\}\right]^{2.45}$$

For debonded particles or pores (default assumption):

$$Y = (0.1666 + 0.0266\,R)$$

For fractured Si particles in case of intact particle/matrix interfaces

$$Y = 0.32\,(0.1666 + 0.0266\,R)$$

For $\ell / D > 0.3$, finite element simulations (Horstemeyer et al., 1999) show that β rapidly saturates to a level well above its value at the percolation limit (on the order of 2% plastic strain in the interdendritic regions), i.e.

$$\beta = Y\left[\, 100\left\{0.0023 - 0.00025(1-R)\right\}\right]^{2.45}(1 + z\,\zeta)$$

For debonded particles, the value of ζ = 9 is estimated based on finite element results as $\ell / D \to 1$, for the R = -1 case. Here, ζ is a multiplier on β to represent eutectic strain intensification in the LCF regime.

It is intended that the R-ratio in these incubation relations is based on the maximum principal stress.

2.6.1.2 Propagation

Initial crack length: assuming spherical inclusions as a reasonable approximation,

$$a_i = \frac{\hat{D}_{part}}{2} + \frac{\tilde{\ell}}{4} = 0.5625\,\hat{D}_{part} \quad \text{where } \tilde{\ell} \approx \frac{\hat{D}_{part}}{4}$$

and $\hat{D}_{part}$ in this case is the largest Si particle diameter from among the population within the highly stressed volume. The length scale $\tilde{\ell}$ corresponds to about ¼ the particle diameter, according to our averaging scheme discussed earlier (0.0625 D^2 at the notch root); this also corresponds closely to the scale of microplasticity at the percolation limit for microplasticity ($\ell / D = 0.3$). The value $\tilde{\ell}/4$ is used for the scale of the initial crack size because it is about 0.125 times the notch root radius, corresponding to the Smith and Miller (1977) estimate of the transition crack length, beyond which the crack growth may be assumed to be outside the primary influence of the notch stress field and therefore subject to the MSC/PSC propagation relation. This is why we have emphasized that the incubation life consists of both crack nucleation and propagation out to the length $\tilde{\ell}/4$.

The growth law is given by

$$\left(\frac{da}{dN}\right)_{MSC/PSC} = G\left(\Delta CTD - \Delta CTD_{th}\right)$$

where we assign the threshold value $\Delta CTD_{th} = 2.86 \times 10^{-10}$ m = b, where b is the Burger's vector for pure FCC Al. This value is just slightly above the minimum cyclic crack growth rates measured for squeeze cast Al-Si alloys (Plumtree and Schafer, 1986; Shiozawa et al., 1997). Plumtree and Schafer (1986) reported the minimum crack growth rate for cracks blocked at dendrite cell triple points. It should not be surprising that the average measured minimum crack growth rates can even be slightly lower, since near threshold the crack front has mobile segments and immobile segments which result in a lower average crack growth rate. We assume that G ≈ 0.3 to 0.5 (cyclic crack advance above threshold is about $1/3$ to $1/2$ of ΔCTD, cf. Kuo and Liu, 1976).

The cyclic crack tip displacement assigned to follow the form

$$\Delta CTD = f\left(\overline{\varphi}\right) C_{II} \left(\frac{DCS}{DCS_o}\right) \left[\frac{U \Delta \hat{\sigma}}{S_u}\right]^n a + C_I \left(\frac{DCS}{DCS_o}\right) \left(\Delta \gamma^p_{max} / 2\Big|_{macro}\right)^2 \qquad \text{Equation 2.18}$$

$$f(\phi) = 1 + \omega \left\{1 - \exp\left(-\frac{\overline{\varphi}}{2\varphi_{th}}\right)\right\} \quad , \quad \varphi_{th} \approx 10^{-4}$$

For horizontally cast A356-T6 plate, we assume that G = 0.32 and the other nondimensional constants that result from data correlation give $C_I = 0.31$, $C_{II} = 1.88 \times 10^{-3}$, n = 4.8, and ω = 2. The reference DCS value is assumed as $DCS_o = 30$ μm , corresponding to the horizontally cast plate. The constraint offered by particles on plasticity-induced closure and effects of particle contact upon unloading are reflected by the assignment U = 1/(1-R) for R < 0, U = 1 for R ≥ 0, where R is based on the maximum principal stress, σ_1; U = 0 if the peak principal stress in the cycle is compressive. For horizontally cast plate, S_u is taken as 310 MPa. The exponent n = 4.8 is used in correspondence to that found for two different squeeze cast Al-Si alloys by Shiozawa

et al. (1997). It is also reasonably close to the stress amplitude dependence of da/dN of the A356-T6 alloy for a given crack length in the long crack regime, and is supported by limited finite element calculations of the ΔCTD versus applied stress for cycling in the HCF regime as discussed earlier.

The ΔCTD expression above has two components, the first addressing propagation in the HCF and transition regimes, and the second addressing crack length independent propagation in the limit plasticity regime. As previously discussed, the linearity with crack length is experimentally well-verified for MSC/PSC cracks in cast Al alloys, as well as in wrought structural alloys (cf. McDowell and Bennett, 1997). Figure 2.8 below shows that close inspection of the data of Gungor and Edwards (1997) for an Al-Mg-Si alloy similar to A356-T6 shows that many of the "strands" of data which each correspond to a constant stress amplitude follow very closely to proportionality of da/dN with crack length a; since $\Delta K \propto \sqrt{a}$, the lines of slope 2 superimposed on this Figure show that da/dN $\propto \left(\sqrt{a}\right)^2$. Some of the data at lower ΔK levels appear to have a somewhat higher slope, but the crack lengths for these lower values are only on the order of a few microns. There is no compelling evidence of departure from linearity with crack length. These authors, and a number of authors, however, have interpreted such data extensively using LEFM concepts. One consequence of such interpretation is that crossovers may occur in predicted growth rates which are somewhat aphysical. For example, the da/dN values for higher stress amplitudes in Fig. 2.8 actually lie below those for lower stress amplitudes in some cases, which would not occur on a plot of da/dN versus crack length.

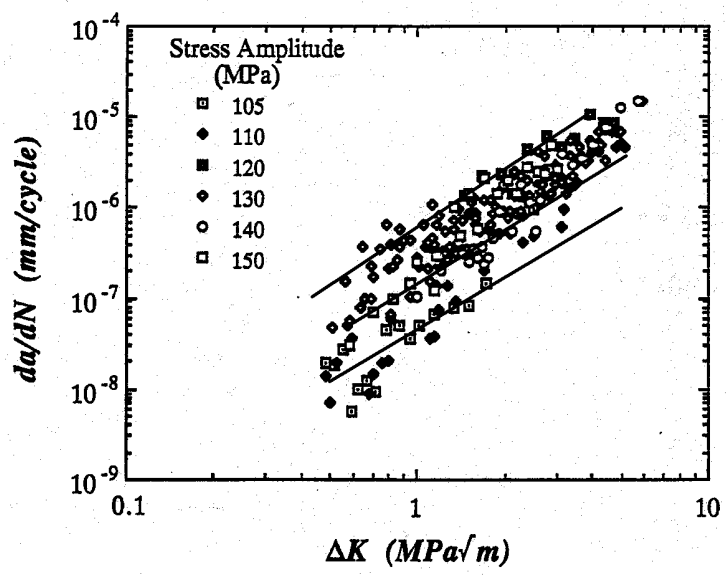

Fig. 2.8 – Data of Gungor and Edwards (1993) for an Al-Mg-Si alloy, with lines that signify proportionality of da/dN with crack length added for reference. It is noteworthy that most of the data well above threshold, when separated by applied stress amplitude, follow these lines.

For the second term in the ΔCTD relation, we determine the macroscopic cyclic plastic maximum shear strain amplitude. In the uniaxial case, for example, we use the experimentally determined cyclic stress-strain curve to write

$$\Delta\gamma^{p}_{max}/2\Big|_{macro} = \frac{3}{2}\left(\frac{\Delta\sigma}{2K'}\right)^{\frac{1}{n'}} = \frac{3}{2}\frac{\Delta\varepsilon^{p}}{2}$$

Finally, the long crack LEFM growth relation is given by

$$\left(\frac{da}{dN}\right)_{LC} = A_p\left(\left(\Delta K_{eff}\right)^{M} - \left(\Delta K_{eff,th}\right)^{M}\right)$$

where for A356-T6 (horizontally cast plate), $M \approx 4.2$ and $A_p \approx 1.5\text{x}10^{-11}$ m-$\left(\text{MPa}\sqrt{\text{m}}\right)^{-4.2}$/cycle. The intrinsic threshold $\Delta K_{eff,th} \approx 1.3\,\text{MPa}\sqrt{\text{m}}$ for A356-T6 (cf. Couper and Griffiths, 1990). The opening stress intensity factor level is given by (Couper and Griffiths, 1990) . ΔK_{eff} is defined by $\Delta K_{eff} = K_{max} - K_{op}$ if $K_{min} < K_{op}$, $\Delta K_{eff} = K_{max} - K_{min}$ if $K_{min} \geq K_{op}$, where

$K_{op} = 3.4 + 3.8R^2$ for $R > 0$, $K_{op} = 3.4\,(1+R)$ for $0 \geq R \geq -1$, and $K_{op} = 0$ for $R < -1$

We select between the MSC/PSC and LC growth laws as the crack extends by selecting the maximum of either of the two rates, i.e.

$$\frac{da}{dN} = \max\left[\left(\frac{da}{dN}\right)_{MSC/PSC}, \left(\frac{da}{dN}\right)_{LC}\right]$$

subject to a constraint that the requirements for validity of the *homogeneous* LEFM approach to model fatigue in the heterogeneous microstructure, as can be approximately expressed by

$$a > 30\,DCS\left(\frac{S_y}{\Delta\sigma_{eff}}\right)^2$$

where $\Delta\sigma_{eff} = \sigma_{max} - \sigma_{op}$. This criterion corresponds to a cyclic plastic zone enclave at the crack tip on the order of the dendrite cell size. The validity limits of LEFM are otherwise less stringent (e.g., the ratio of the cyclic plastic zone to the crack length is small) in the HCF regime, although for many reasons elaborated in this report we advocate using EPFM type relations for growth of cracks up to the range of 0.5 to 1 mm. For stress amplitudes on the order of the cyclic yield strength, this crack length is on the order of 1 mm for typical dendrite cell size, and increases for lower stress amplitudes.

Finally, we sum the various components as follows:

$$N_T = N_{inc} + N_{MSC/PSC} + N_{LC}$$

2.6.2 Type B: Shrinkage or Gas Pores with Maximum Diameter $\hat{D}_p$ < 3DCS but Greater than the Maximum Si Particle Diameter, $\hat{D}_{part}$

2.6.2.1 Incubation

In this case, the relevant definition of maximum inclusion diameter D is the maximum pore diameter, D = $\hat{D}_p$. The incubation analysis is the same as for type A inclusions except that $Y = (0.1666 + 0.0266\,R)$ always for these pores (both below and above $\ell / D = \ell / \hat{D}_p$ = 0.3), since pores do not offer the constraint of bonded particles.

2.6.2.2 Propagation

Same as type A inclusions with the exception that

$$a_i = \frac{\hat{D}_p}{2} + \frac{\tilde{\ell}}{4} = 0.5625\,\hat{D}_p$$

2.6.3 Type C: Large Shrinkage or Gas Pores with Diameter $\hat{D}_p$ > 3DCS

2.6.3.1 Incubation

Same as type A or B inclusions except that for $\ell / D < 0.3$,

$$\beta = \Delta\gamma^{p*}_{max} / 2 = Y\left[\,100\left\{\bar{\varepsilon}_a - 0.00025(1-R)\right\}\right]^{2.45}\left(\frac{\hat{D}_p}{3DCS}\right)$$

and $Y = (0.1666 + 0.0266\,R)$ always for these pores (both below and above $\ell / \hat{D}_p$ = 0.3).

For $\ell / D >$ 0.3, we assume that β is the maximum of either the percolation limit value of $\Delta\gamma^{p*}_{max} / 2$ (at ℓ / D = 0.3) or the macroscopic maximum plastic shear strain amplitude, i.e.

$$\beta = \max\left(\Delta\gamma^{p}_{max} / 2\Big|_{macro},\ Y\left[\,100\left\{0.0023 - 0.00025(1-R)\right\}\right]^{2.45}\left(\frac{\hat{D}_p}{3DCS}\right)(1 + z\,\zeta)\right)$$

These particles are large enough such that there cyclic plastic notch root strain fields may engulf multiple particles; hence, the R-ratio dependent threshold is still used for microplasticity, taking into account effects of particle contact of debonds upon unloading and associated plastic strain intensification. The modification involving the ratio of the pore diameter to three times the dendrite cell size is introduced to reflect the linear dependence of the crack opening displacement on the cell size for small cracks (even those under the influence of a large notch root field) growing away from the large pores as implied by the computational micromechanics studies.

2.6.3.2 Propagation

Same as type A inclusions with the exception that the initial crack size is given by

$$a_i = \frac{\hat{D}_p}{2} + \frac{1}{2}\left(\frac{DCS}{2}\right) = \frac{\hat{D}_p}{2} + \frac{DCS}{4}$$

in order to reflect the fact that the scale of averaging does not increase further in linear fashion with the inclusion size, because large shrinkage pores with typically tortuous shape are observed to exhibit radii of curvature on the order of half the dendrite cell size. Therefore, a limit is placed on the extent of growth of small cracks away from pores in the incubation phase, on the order of a fraction of the dendrite cell size.

2.6.4 Type D: Large Pores Near the Free Surface ($\hat{D}_p$ > 3DCS)

2.6.4.1 Incubation

Same as type C inclusions except that the notch root plastic strain intensification is modified to account for proximity to the free surface according to a fit to finite element simulations (cf. Section 4.2.2.2) of pores interacting with the free surface, i.e.

$$\beta = \Delta\gamma^{p*}_{max}/2 = \Delta\gamma^{p*}_{max}/2\Big|_{Type\ C}\left[1 + 10\frac{\ell}{\hat{D}_p}\exp\left(-\frac{5\chi}{\hat{D}_p}\right)\right]$$

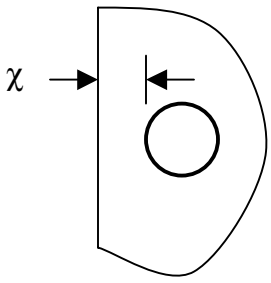

where χ is the nearest distance of the pore to the free surface. Here, $\Delta\gamma^{p*}_{max}/2\Big|_{Type\ C}$ is the value from Type C analysis of pores. The ratio $\chi/\hat{D}_p$ must be below unity for this correction to be significant, following the computational results. Clearly, the intensification is very significant for large pores very near the free surface, rendering a tremendous decrease in the incubation life.

For example, for $\chi / \hat{D}_p$ = 0.2, the incubation life is reduced by a factor of 5 near the percolation limit, whereas it is reduced by a factor of 20 in the LCF regime.

2.6.4.2 Propagation

Same as Type C inclusions with the exception that the initial crack size is given by

$$a_i = \hat{D}_p + \frac{1}{2}\left(\frac{DCS}{2}\right) + \chi = \hat{D}_p + \frac{DCS}{4} + \chi \quad \text{for} \quad \frac{\chi}{\hat{D}_p} < 1$$

in order to reflect the fact that the nucleated crack grows rapidly to the free surface, producing a crack on the order of the particle diameter plus the distance to the free surface. Clearly, this very significantly decreases the crack propagation life relative to the previous cases, as is experimentally observed.

2.6.5 Type E: Large Oxide Films

These inclusions are particularly deleterious if they are contiguous and are on the order of the largest pore size or larger for $\hat{D}_p$ > 3DCS . In the low hydrogen content specimens in the USCAR program 50-100 μm oxide films or plates were found to serve as the initial crack site in many cases when the porosity was insignificant. Of course, oxides and intermetallics are relatively prevalent as "chopped" or small-scale heterogeneities in the Al-rich matrix in the A356-T6 alloy, but this is accounted for implicitly in the crack propagation law coefficients.

2.6.5.1 Incubation

Incubation is negligible as these inclusions act as cracks essentially from the outset. Hence, N_{inc} = 0.

2.6.5.2 Propagation

Same as Type C inclusions with the exception that the initial crack size is given by

$$a_i = \frac{1}{2}\hat{D}_{oxide}$$

where $\hat{D}_{oxide}$ is the maximum length of the oxide, presumably projected normal to the maximum principal stress.

It is noted that for a given constant amplitude loading condition, the crack growth relations can all be integrated explicitly without the need for numerical integration. This greatly facilitates implementation and parameter identification.

2.7 Coalescence and Widespread Fatigue Damage in LCF

Rather remarkably, the scatter in LCF life for a given applied strain amplitude for cast alloys is almost as large as that in the HCF regime. By contrast, the scatter in fatigue life for wrought alloys in the LCF regime is much less significant. This may be understood by virtue of the nature of distribution of crack incubation and propagation in both cases. Under HCF conditions, the fatigue life is controlled by the most severe inclusion and a single, dominant crack normally propagates to failure. Therefore, scatter in HCF is dictated by the extreme statistics of inclusions, namely by the most extreme, life-limiting inclusions within the highly stressed volume. Often, these are present either at or just under the surface for large pores and oxides.

However, as $\ell / D \rightarrow 1$ in LCF, the probability is almost unity for any significant inclusion to form cracks. Hence, the problem of statistical variation shifts entirely to crack propagation from multiple inclusions. Virtually all significant pores can be expected to have a high probability of rapid crack incubation. In addition, the larger, favorably oriented Si particles among the population will fracture (accounting for the roughly 1% fraction of fractured particles under tensile loading at 0.5% strain, cf. Gokhale et al., 1998). Particle fracture begets debonding and formation and propagation of cracks that compete, and indeed may interact, with those formed at large pores or oxides. Coalescence of multiple cracks increases the effective growth rate exponentially. Hence, the statistics of the distribution of the large pores, oxides and larger Si particles becomes critical in considering multi-site fatigue damage and coalescence in LCF.

Some authors have applied continuum damage concepts to fatigue of cast alloys with the notion of multi-site fatigue damage in mind (cf. Weinacht & Socie, 1987). Such approaches consider damage to be continuously distributed. However, we take care to distinguish between the HCF regime in which this sort of approach would not be appropriate and the LCF regime where the approximations involved may become more satisfactory. One treatment of the problem is to apply Monte Carlo numerical simulations for the growth and interaction of cracks from multiple defects in the field involving fairly significant idealizations; this is not particularly difficult (cf. Hoshide and Socie (1988) for wrought alloys), just time-consuming and demanding of quite detailed characterization of inclusion distributions in the case of cast alloys. Instead, we take a simple approach which is aimed more at establishing a sort of lower bound that could be expected for a give average porosity and mean pore size, along with extremal statistics of the spacing of the larger (fractured) Si particles and larger pores/oxides.

The assumption of a dominant crack that propagates from the most severe inclusion might be expected to produce an upper bound (although not a rigorous bound) on the fatigue life for strain amplitudes in the LCF regime (stress amplitudes exceeding the cyclic yield strength). In the HCF regime, experiments indicate that the life is indeed limited by the formation and propagation of dominant cracks at the most severe inclusions among the population, often near surface pores. Above the percolation limit for microplasticity as $\ell / D \rightarrow 1$, however, plastic shear strain localization in the interdendritic regions is intense and cracks incubate rapidly, as is shown in Fig. 2.11. Cracks incubate profusely at all significant pores and the largest Si particles which undergo increasing probability of fracture with increasing strain level, particularly the largest particles among the population with the highest aspect ratios in the direction of the applied principal stress. Since the lifetime is almost entirely propagation-dominated in the LCF

regime, the basic problem is to track the growth of cracks from various incubation sites in the microstructure. To do this, we make use of spatial statistics related to nearest neighbors or mean spacing of large pores and particles. The complicating feature of competitive growth processes is the need to introduce convolution of crack growth at different rates from different characteristic incubation sites to track the network of crack advance and eventual coalescence. Here we take a rather simple but effective approach by considering cracks associated with:

a. maximum pore or oxide film size
b. average pore size and spacing
c. maximum fractured Si particle size and spacing

For a random distribution of pores, the average porosity, $\bar{\varphi}$, is related to the average nearest neighbor spacing between pores, δ_{pore}, of a given average diameter, $\bar{D}_p$, by the relation (Gokhale, 2000)

$$\delta_{pore} = 0.811 \frac{\bar{D}_p}{\bar{\varphi}^{1/3}} \qquad \text{Equation 2.19}$$

where the units of δ_{pore} and $\bar{D}_p$ are in μm. This relation is rigorous for a random (Poisson) distribution, based on the relation of number density to porosity and average particle size. From the stereological work of Gokhale et al. (1998), the fraction of fractured Si particles is well-approximated in tension beyond the percolation limit by the relation

$$f_{part} = 0.01 + 0.8\left(\bar{\varepsilon}_a - 0.0023\right) \quad \text{for } \bar{\varepsilon}_a > 0.0023 \qquad \text{Equation 2.20}$$

In view of the arrangement of Si particles in the interdendritic regions and the morphology of the secondary dendrite arms, we consider a two-dimensional relation for the average spacing between fractured Si particles, δ_{part}, i.e. $\delta_{part} \propto f_{part}^{-1/2}$. Specifically, calculations performed by Horstemeyer (1999) under monotonic tensile loading are fit well by the expression

$$\delta_{part} = 113 \sqrt{\frac{0.01}{f_{part}}} \qquad \text{Equation 2.21}$$

where the units of δ_{part} are in μm. The spacing starts out at around $120\ \mu m$ but reduces to about $90\ \mu m$ at higher strain amplitudes. For torsion, the relation

$$\delta_{part} = 113 \sqrt{\frac{0.01}{f_{part}}} + 107 \qquad \text{Equation 2.22}$$

appears to match Horstemeyer's simulations reasonably well.

For the evaluation of coalescence, we make several assumptions:

a. uniform stress throughout the critically stressed volume
b. constant amplitude loading is applied
c. incubation occurs immediately at all pores and large Si particles, with an initial crack length of ½ the inclusion diameter
d. the crack growth rate for cracks at from each incubation site is proportional to the length of each crack and is well above threshold
e. interaction between cracks prior to joining (propagating together) is ignored.

2.7.1 Recursion Relation for Propagation from Large Pore through a Field of Si Particles

If a crack forms at a large pore of diameter $\hat{D}_p$ and propagates through a field of fractured Si particles with extremal diameter, $\hat{D}_{part}$, on the order of the largest Si particles in the distribution and spacing given by δ_{part} in the last section, then the crack will grow more rapidly from the large pore than from Si particles, and will successively coalesce with cracks incubating at Si particles. As the crack lengthens, it will take successively fewer cycles to coalesce due to more time for crack extension from the Si particles in the field. Accordingly, the crack may only have to grow 2 or 3 average Si particle spacings before the entire field of cracks coalesce. This motivates the introduction of an effective coalescence crack length for growth from the largest inclusion, which is shorter than the specified crack length for dominant crack growth, in general. This effective length can be estimated as follows. After initial incubation at all inclusions considered, we must first compute the distance the crack must grow between the large pore and the nearest fractured Si particle in the same number of cycles at the point of coalescence. Since the MSC/PSC propagation relation is linear in crack length and the stress amplitude is assumed everywhere uniform, the operative fatigue life multiplier is given by

$$\Lambda = \ln\left(\frac{a_{coalesce}}{a_o}\right) = \int_{a_o}^{a_{coalesce}} \frac{da}{a} \qquad \text{Equation 2.23}$$

where a_o is the initial crack length. Defining as $\xi_1 \delta_{part}$ the distance the crack must grow from the large pore to join with the crack from the first Si particle, and $(1-\xi_1)\delta_{part}$ as the distance that the joining crack grows from the particle, it is found from the relation

$$\Lambda_1 = \ln\left(\frac{\frac{\hat{D}_p}{2} + \xi_1 \delta_{part}}{\frac{\hat{D}_p}{2}}\right) = \ln\left(1 + 2\xi_1 \frac{\delta_{part}}{\hat{D}_p}\right) \qquad \text{Equation 2.24}$$

that

$$\xi_1 = \frac{\hat{D}_p}{\hat{D}_p + \hat{D}_{part}}$$ Equation 2.25

such that $1/2 \le \xi_1 < 1$ always if the pore size exceeds the average maximum fractured particle size. During this process, a crack has grown from the second nearest neighbor fractured Si particle by a distance precisely equal to $(1-\xi_1)\delta_{part}$. For the next segment of propagation, therefore, the crack from the large pore has an initial length that encompasses half the pore diameter plus the spacing to the nearest fractured Si particle plus $(1-\xi_1)\delta_{part}$. It need only grow a distance $\xi_2(1-2(1-\xi_1))\delta_{part}$ to meet with the crack from the next Si particle that extends a distance $(1-\xi_2)(1-2(1-\xi_1))\delta_{part}$, and so on. Growth continues until a specified final crack length is reached by the largest crack or until widespread coalescence occurs; eventually cracks will join between evenly spaced fractured Si particles ahead of the crack, resulting in spontaneous coalescence over the entire highly stressed volume considered (on the order of the final crack length selected). For the second coalescence step on, i = 2, 3,…, n, the recursion relation may be written as

$$\xi_i = \frac{\hat{D}_p^i}{\hat{D}_p^i + \hat{D}_{part}^i}, \qquad \Lambda_i = \ln\left(1 + 2\xi_i \frac{\delta_{part}^i}{\hat{D}_p^i}\right)$$ Equation 2.26

where

$$\delta_{part}^i = (1-2(1-\xi_{i-1}))\delta_{part}^{i-1}$$ Equation 2.27

$$\frac{\hat{D}_{part}^i}{2} = \frac{\hat{D}_{part}^{i-1}}{2} + (1-\xi_{i-1})\delta_{part}^{i-1}$$ Equation 2.28

$$\frac{\hat{D}_p^i}{2} = \frac{\hat{D}_p^{i-1}}{2} + \xi_{i-1}\delta_{part}^{i-1} + 2(1-\xi_{i-1})\delta_{part}^{i-1} + \hat{D}_{part}^{i-1}$$ Equation 2.29

where for i = 1 we start the algorithm with Equations 2.24 and 2.25, using the initial pore and particle diameters. $\hat{D}_{part}^i$ may be viewed as the effective particle diameter for the next segment of crack growth (it includes all prior crack extension from that particle). Similarly, $\hat{D}_p^i$ may be viewed as the effective pore diameter at the beginning of the propagation process for the i^{th} particle coalescence event. As such, the recursion is performed until one of two conditions holds:

$$\frac{\hat{D}_p^n}{2} \ge a_f \quad \text{or} \quad \frac{\hat{D}_{part}^n}{2} \ge \frac{1}{2}\left(\delta_{part} + \hat{D}_{part}\right)$$ Equation 2.30

Mathematically, we may view the effects of coalescence as effectively contributing to a decrease in the final crack length for a dominant crack propagating from the largest inclusion, in this case a pore. Well above threshold (easily satisfied in the LCF regime), the lifetime can be expressed for the largest crack as

$$N_T = \left(\sum_{i=1}^{n} \Lambda_i \right) \frac{G\,\Delta CTD\big|_{a=a_f}}{a_f} \qquad \text{Equation 2.31}$$

We may define the effective final crack length as

$$\ln\left(\frac{\tilde{a}_f}{a_o}\right) = \ln\left(\frac{\tilde{a}_f}{\hat{D}_p/2}\right) = \sum_{i=1}^{n} \Lambda_i \qquad \text{Equation 2.32}$$

or more directly as

$$\tilde{a}_f = a_o \exp\left(\sum_{i=1}^{n} \Lambda_i \right) \qquad \text{Equation 2.33}$$

Since $\sum_{i=1}^{n} \Lambda_i$ will always be less than $\Lambda = \ln\left(\frac{a_f}{a_o}\right)$ in the presence of coalescence, it is clear that $\tilde{a}_f < a_f$, often substantially. This is due to the fact that significant jumps of crack length are realized instantaneously during coalescence events. Close inspection of this recursion relation reveals that if the pore size is relatively close to the particle size, then $\xi_1 \approx 1/2$ and the most dramatic reduction of $\tilde{a}_f$ relative to the specified final crack length, a_f, is realized. In fact, for propagation from a field of monosize particles or pores, the lower bound on $\tilde{a}_f$ is realized as

$$\tilde{a}_f = \frac{\hat{D}_{part}}{2}\left(1 + \frac{\delta_{part}}{\hat{D}_{part}}\right) \qquad \text{Equation 2.34}$$

for a field of fractured Si particles, and

$$\tilde{a}_f = \frac{\bar{D}_p}{2}\left(1 + \frac{\delta_{pore}}{\bar{D}_p}\right) = \frac{\bar{D}_p}{2}\left(1 + \frac{0.811}{\bar{\varphi}^{1/3}}\right) \qquad \text{Equation 2.35}$$

for an average pore diameter of $\bar{D}_p$. For example, for the case of extremal fractured Si particle sizes of 12 μm, the resulting $\tilde{a}_f$ is only about 54 μm. Typical $\tilde{a}_f$ values for large pores might be on the order of several hundred μm. All of these values result in fatigue lives that are considerably less than would be required for the growth of a dominant crack in the absence of coalescence.

Conversely, the recursion relation reveals that pores that are large compared to the Si particle size result in $\xi_1 \approx 1$; therefore, in this case the Si particles do not have much effect on reducing the fatigue life because $\tilde{a}_f$ is not reduced nearly to the extent as for $\xi_1 \to 1/2$.

Finally, it is noted that the recursion relations can be applied to the case of a fatigue crack growing from a large pore through a field of monosize pores that are spaced according to Equation 2.19 simply by considering them to play the precise role that the particles played in this formulation. Similarly, we can apply these relations to propagation through a field of Si particles or pores of some average diameter and spacing of a crack originating at an oxide, simply by replacing $\hat{D}_p$ by $\hat{D}_{oxide}$.

2.7.2 Approximation of Recursion Relation Using Only Initial Microstructure Geometry

By considering the geometrically compounding nature of the recursion relation, it is possible to develop a simple series expansion in odd powers of ξ_1 as defined in Equation 2.25. While approximate, this relation has been found to accurate to within 5-10% percent for $\tilde{a}_f$ over a wide range of ξ_1 values, as demonstrated in Fig. 2.9 for several relevant cases. For the preceding problem of propagation of a crack from a large pore through a field of fractured Si particles, it is written quite simply as

$$\tilde{a}_f \approx \frac{\hat{D}_p}{2} + \frac{(0.685-0.04\xi_1)(\xi_1+1)}{2}\left(\delta_{part} + \frac{\hat{D}_{part}}{2}\right)\left\{\sum_{i=1}^{n}(\xi_1)^{2i-1} + \left(\frac{a_f}{\delta_{part}} - \mathrm{INT}\left[\frac{a_f}{\delta_{part}}\right]\right)(\xi_1)^{2(n+1)-1}\right\}$$

Equation 2.36

where $n = \mathrm{INT}\left(a_f/\delta_{part}\right)$. To apply this relation, it is required that $\delta_{pore} > \delta_{part}$, which is the usual case. As before, $1/2 \le \xi_1 < 1$. It should be noted that the series in this expression is strongly convergent as $\xi_1 \to 1/2$, but weakly convergent for $\xi_1 \to 1$; 5-10 terms may suffice for values of ξ_1 up to 0.6, while as many as 40-50 terms may be required for convergence for values near 0.85 or 0.9, in which the recursion relation in the last section may be more efficient.

Another application is to consider the accelerative effect of fractured Si particles in-between a field of monosize pores. This can be easily treated by identifying the final crack length as half the averaging pore spacing, i.e.

$$\tilde{a}_f \approx \frac{\hat{D}_p}{2} + \frac{(0.685-0.04\xi_1)(\xi_1+1)}{2}\left(\delta_{part} + \frac{\hat{D}_{part}}{2}\right)\left\{\sum_{i=1}^{n}(\xi_1)^{2i-1} + \left(\frac{\delta_{pore}}{2\delta_{part}} - \mathrm{INT}\left[\frac{\delta_{pore}}{2\delta_{part}}\right]\right)(\xi_1)^{2(n+1)-1}\right\}$$

Equation 2.37

where $n = \mathrm{INT}\left(\delta_{pore} / \left(2\delta_{part}\right)\right)$. This is not a substantial effect unless the average pore size and Si particle size are of comparable dimensions, with the pore space considerably greater than the particle spacing. This may be the case for gas porosity, for example.

As with the full recursion relation, the set of assumptions we have adopted here permit use of only mean microstructure distribution statistics readily obtained from stereology to assess coalescence. In applying these relations, the inclusion diameter must be equal to or exceed the average pore diameter, since extremal inclusions dominate failure. In the absence of pores, Equation 2.34 holds. There are no adjustable constants in this formulation beyond these quantitative inputs. Figure 2.9 shows the significance of coalescence for cast microstructures with fractured/debonded Si particles, since $\tilde{a}_f \ll a_f$ as the largest inclusion decreases in size. As the maximum inclusion size increases to large values, $\tilde{a}_f \to a_f$ and the effect is much less significant.

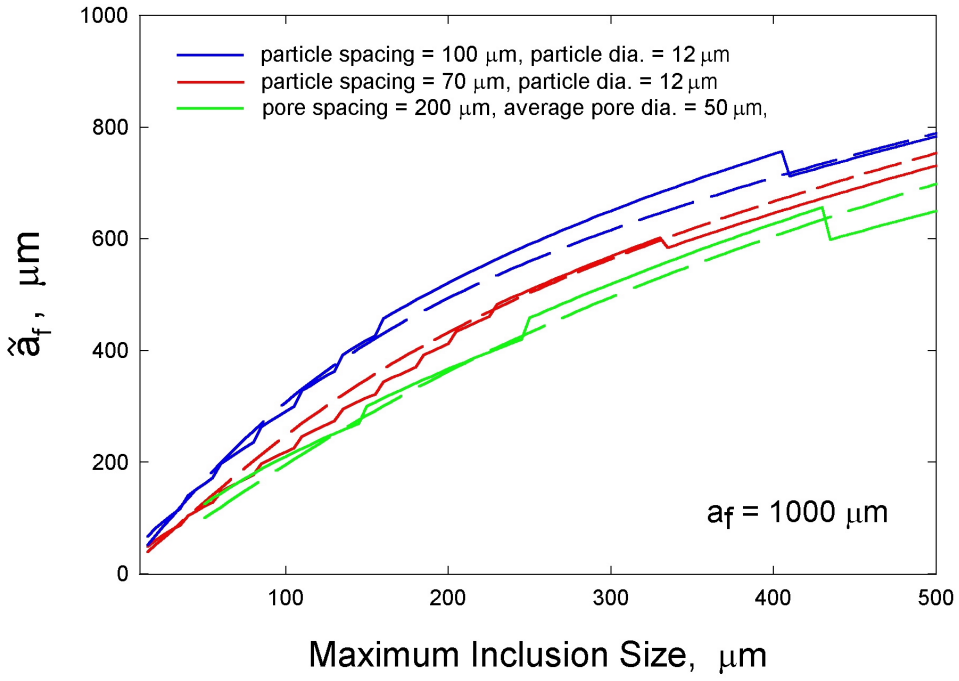

Fig. 2.9 – Effective final crack length versus maximum inclusion (pore) diameter for a specified final crack length of $a_f = 1000\,\mu m$. Solid lines represent results of the recursion relations, while dashed lines represent the approximate series expansion. The top two cases are for a crack growing from pores greater than 12 μm in diameter through a field of fractured Si particles spaced either 70 or 100 μm apart, while the bottom case is for propagation through a field of monosize pores of 50 μm diameter, spaced 200 μm apart.

2.8 Model Correlations and Predictions for USCAR Data, Horizontally Cast Plate

TABLE 2.1 Summary of Parameter/Constant Set for Horizontally Cast Plate A356-T6
(Boxed values indicate experimentally-based)

***Stress-strain behavior**:*

$\boxed{K' = 430\ \text{MPa},\ n' = 0.065,\ E = 71\text{x}10^3\ \text{GPa},\ S_u = 310\ \text{MPa}}$

Average Porosity and Pore Size: $\boxed{\bar{\varphi} = 1.5\text{x}10^{-3}\ ,\ \bar{D}_p = 45-50\ \mu\text{m}}$

Maximum Pore Size: $\boxed{\hat{D}_p = 50-55\ \mu\text{m}}$, Dendrite Cell Size: $\boxed{DCS = 30\ \mu\text{m}}$

Maximum Si Particle Size: $\boxed{\hat{D}_{part} = 12-15\ \mu\text{m}}$ (including effect of aspect ratio)

Incubation:

$\boxed{C_n = 0.24\left(1-\langle R\rangle\right),\ C_m = 0.03,\ \alpha = -0.5}$

for $\ell / D \le 0.3$, $\quad \beta = \Delta\gamma^{p*}_{max}/2 = Y\left[\,100\left\{\bar{\varepsilon}_a - \varepsilon_{th}\right\}\right]^q$

for $\ell / D > 0.3$, $\quad \beta = \Delta\gamma^{p*}_{max}/2 = Y\left[\,100\left\{0.0023 - \varepsilon_{th}\right\}\right]^q (1+z\,\zeta)$, $\qquad z = {}^{1}\!/_{0.7}\langle \ell / D - 0.3\rangle$

$\varepsilon_{th} = 0.00025(1-R)$, $q = 2.45$, $\zeta = 9$

$Y = (0.1666 + 0.0266\,R)$ for debonds

$Y = 0.32\ (0.1666 + 0.0266\,R)$ for bonded particle / matrix

$$\frac{\ell}{D} = \frac{\langle \bar{\varepsilon}_a - 0.0006\rangle}{0.00567} \quad \text{for} \quad \frac{\ell}{D} \le 0.3$$

$$\frac{\ell}{D} = 1 - 0.7\left(\frac{0.0023}{\bar{\varepsilon}_a}\right)^{\frac{1}{r}} \quad \text{for} \quad 0.3 < \frac{\ell}{D} \le 1 \quad , \quad r = 0.1$$

Propagation:

MSC/PSC regime:

G = 0.32, $\boxed{\Delta CTD_{th} = 2.86\text{x}10^{-10}\ \text{m},\ C_I = 0.31\ ,\ C_{II} = 1.88\text{x}10^{-3}\ ,\ n = 4.8}$

$DCS_o = 30\ \mu\text{m}$, $\boxed{DCS = 30\ \mu\text{m}\ ,\ \theta \approx 0.4}$

Microporosity constants: $\boxed{\omega = 2,\ \varphi_{th} = 10^{-4}}$

Long Cracks:

$\boxed{M = 4.2\ ,\ A_p \approx 1.5\text{x}10^{-11}\ \text{m-}\left(\text{MPa}\sqrt{\text{m}}\right)^{-4.2}/\text{cycle},\ \ \Delta K_{eff,th} = 1.3\ \text{MPa}\sqrt{\text{m}}}$

$\boxed{K_{op} = 3.4 + 3.8R^2 \ \text{for}\ R > 0,\ K_{op} = 3.4\,(1+R)\ \text{for}\ 0 \ge R \ge -1,\ \text{and}\ K_{op} = 0\ \text{for}\ R < -1}$

2.8.1 Dominant Cracks

Correlations and predictions of smooth specimen uniaxial fatigue tests for horizontally cast plate A356-T6 are presented in this section, with the constants used in Table 2.1. We assume for purposes of these calculations that the final crack size is 1 mm, which is a reasonable approximation for smooth specimens with failure defined as a 20% increase in compliance. Hence, $N_T = N_{inc} + N_{MSC/PSC}$. The initial crack length corresponds to inclusion type as outlined in the description of the model and in the legends. In these calculations, we assume that a dominant crack forms at the most severe inclusion and propagates to failure, unassisted by any coalesence with other cracks. The influence of coalescence will be examined in the next section, as it is important in the LCF regime at stress amplitudes above the macroscopic yield strength. In the HCF regime, however, dominant cracks are commonly observed since cracks tend to avoid Si (cf. Wang and Zhang, 1994).

Model simulations are shown in Figures 2.10 for strain-life and Fig. 2.11 for stress-life under completely reversed uniaxial loading to a final crack length of a_f = 1 mm for various maximum inclusion sizes for horizontally cast A356-T6 plate. In these plots the case '50 μm pore' is a correlation, while all other cases are predictions.

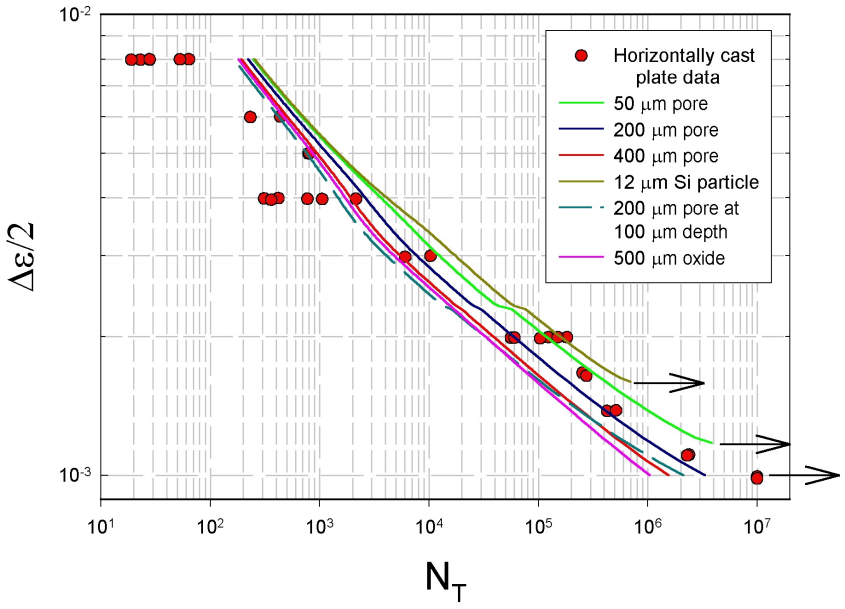

Fig. 2.10 – Model predictions for uniaxial, completely reversed strain-life for incubation at various maximum pore sizes (horizontally cast plate material has a maximum pore size of approximately 50 μm), as well as for the cases of incubation at 12 μm Si particles and

500 μm oxides. Note the drop of fatigue life with maximum pore size, with a strong influence of surface proximity of large pores.

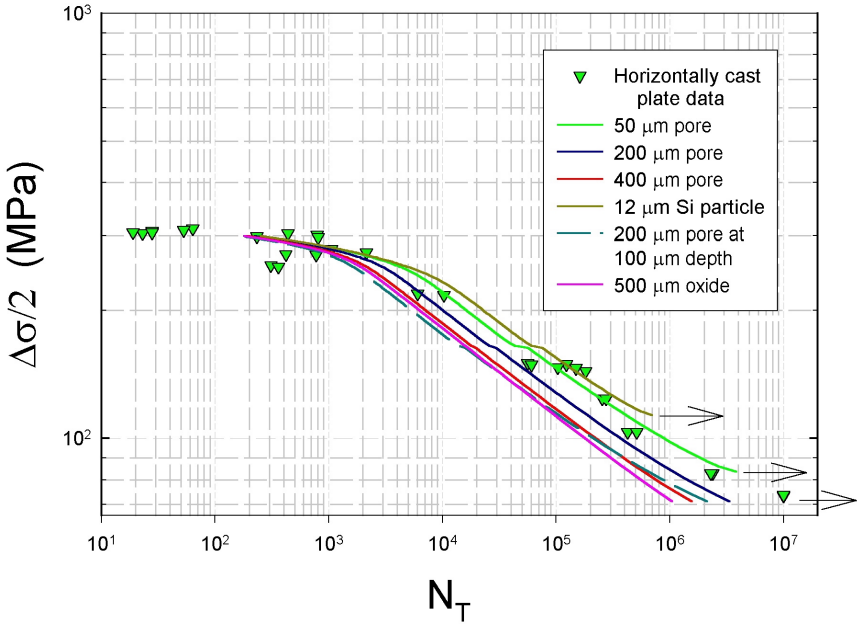

Fig. 2.11 – Model predictions for uniaxial, completely reversed stress-life for incubation at various maximum pore sizes.

It is noted that 200 to 400 μm pores reduce fatigue life in the HCF regime by factors of roughly 2 and 3, respectively, with increasing factors at amplitudes near the fatigue limit. The predicted fatigue limits for each case are shown with arrows pointing to the right, in each case associated with nonpropagating cracks at the end of the incubation phase. Eliminating the 50 μm pores would result in the particle-dominated incubation enhancement in HCF resistance shown in Figs. 2.10 and 2.11. The point where the slope abruptly changes on the strain-life curve corresponds to the percolation limit for microplasticity.

Figure 2.12 compares the correlation of horizontally cast plate with 50 μm pores and predictions for various other inclusion scales/types with the upper and lower bounds of experimental data for the Al-7%Si alloys within the USCAR program. It is noted that the 400 μm pore results are close to the lower bound front cradle tilt-pour material in the HCF regime, which was reported to have maximum pore sizes of approximately 500 μm. Of course, the statistical variation in all the data in the HCF regime, including that of horizontally cast plate, reflects the variations of the incubating pore (inclusion) size from specimen to specimen. It would appear that this variability is predicted reasonably well by the model. The upper bound materials are all characterized by

low porosity levels (in fact, below the threshold $\phi_{th} = 10^{-4}$) which are expected to lead to an increase of the MSC/PSC propagation life by a factor of 2-3 for these materials, commensurate with the upper bound in the HCF regime. It is important to note that the predictions in the LCF regime above a strain amplitude of approximately 0.4% form an upper bound to the observed lives due to the neglect of multisite fatigue damage in the microstructure and associated coalescence phenomena in these particular calculations.

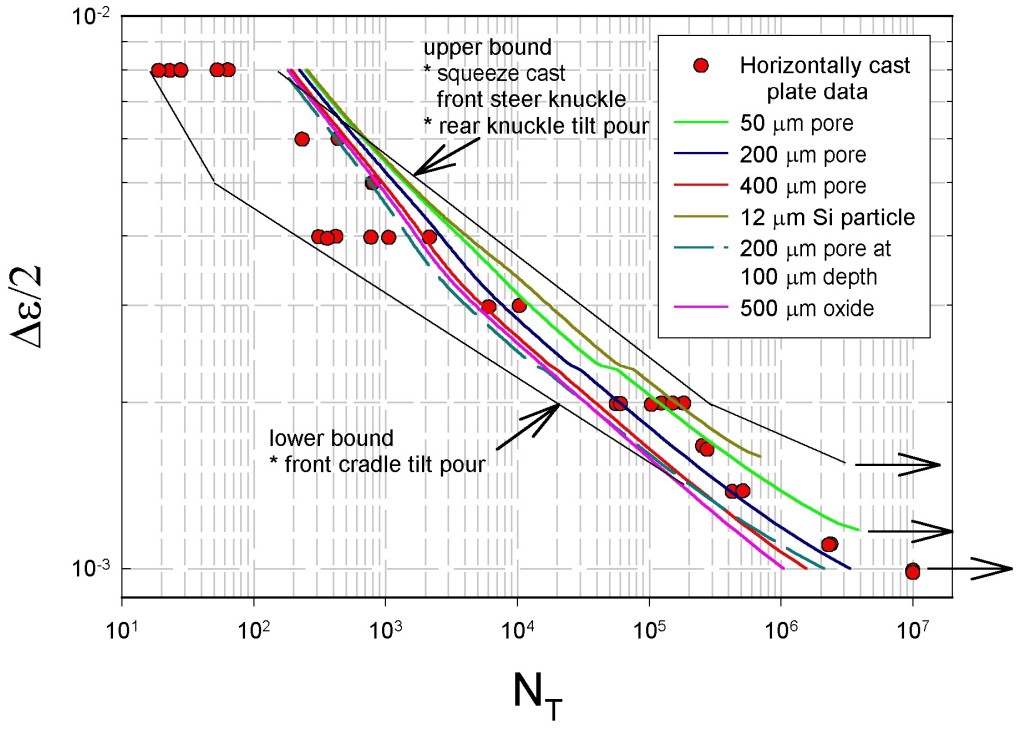

Fig. 2.12 – Strain-life diagram for uniaxial, completely reversed loading for incubation at various inclusion scales/types for horizontally cast plate and comparison with the upper and lower bounds of the strain-life results from the various A356-T6 alloys of the USCAR program.

To illustrate the relative fractions of incubation life and MSC\PSC propagation life, Fig. 2.13 shows the curves for incubation life N_{inc} (dashed lines) for maximum pore sizes of 50 μm and 200 μm. The incubation life is calculated from the relation

$$\beta = \frac{\Delta\gamma_{max}^{p^*}}{2} = C_{inc}\, N_{inc}^{-0.5} \qquad \text{Equation 2.38}$$

Clearly, the incubation life is negligible in the transition and LCF regimes. However, this is not the case in the HCF regime. Since the growth relation is based on a combination of cyclic crack

tip displacement mechanics/calculations and empirical observations, it is conceivable that shielding interactions of small cracks with neighboring Si particles is intrinsic to the model. The incubation life is about 50 to 70% of the total life in the HCF regime for the 50 μm pores, but only about 20 to 30% of the total life for 200 or 400 μm pores in the HCF regime. The data of Plumtree and Schafer (1986) for A356-T6 for a strain amplitude of 0.18% give an incubation to total life ratio of about 65%, while the predictions here are about 50% at that amplitude for a relatively low porosity casting.

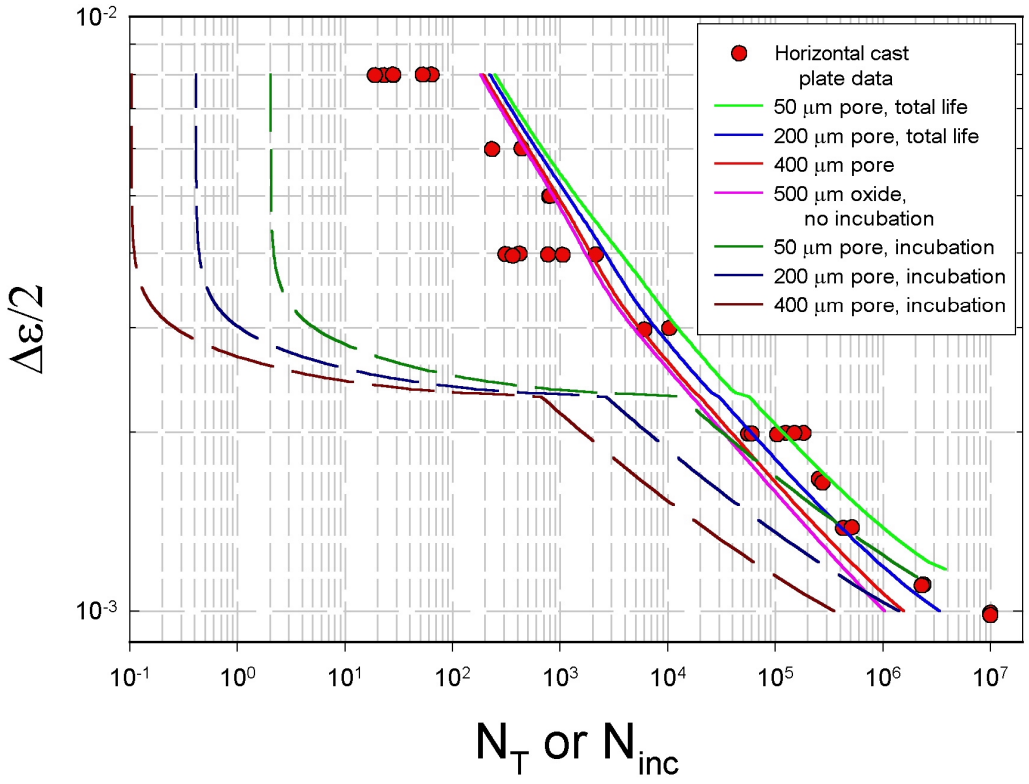

Fig. 2.13 – Strain-life diagram for uniaxial, completely reversed loading for horizontally cast plate with 50 μm and 200 μm pores, including the crack incubation (dashed lines) as well as the total fatigue life (solid lines).

Figure 2.14 shows the effects of tensile mean stress on fatigue life for horizontally cast plate in the HCF regime where these effects are of most practical significance. Note that the fatigue limit is reduced very substantially for tensile mean stresses, as are fatigue lives, relative to the completely reversed case. The R-ratio dependence in the model for C_n was selected to fit the 103.5 MPa mean stress case, and augments the R-ratio dependence of the local cyclic microplastic shear strain range. Note that the predictions for the other mean stress levels appear reasonable, but there is a paucity of data for comparison given the inherent scatter.

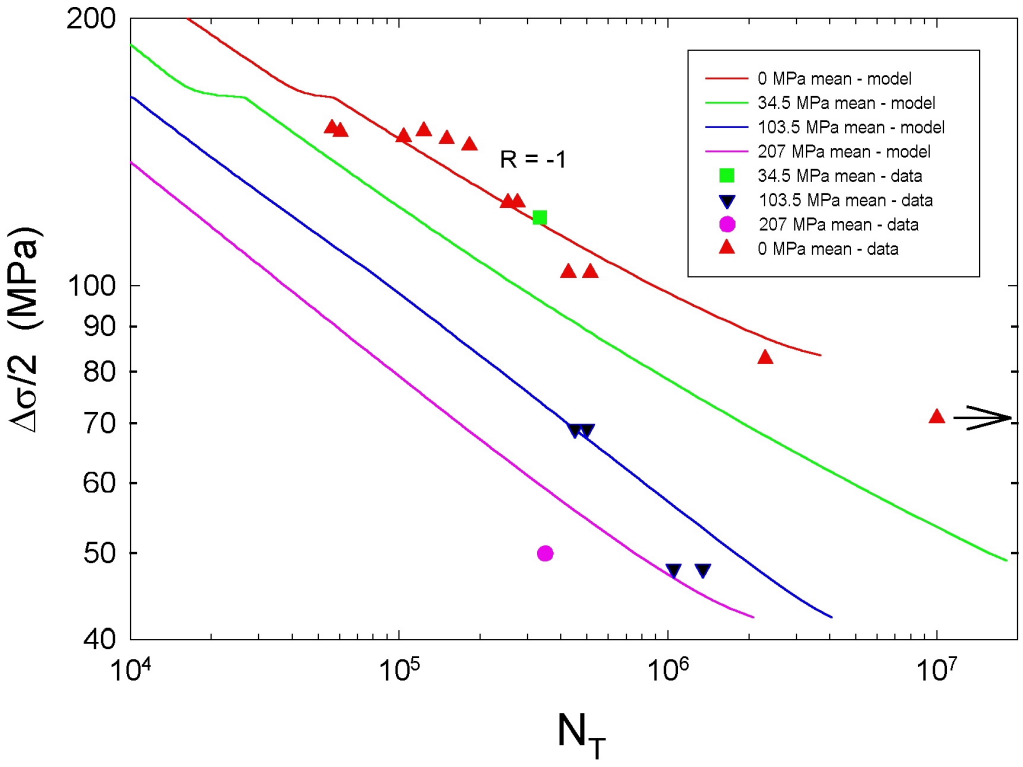

Fig. 2.14 – Mean stress correlations/predictions of model in the HCF regime with horizontally cast plate data for mean stresses ranging from 0 to 207 MPa and uniaxial loading conditions.

A comparison of several different inclusion severity types for three different dendrite cell sizes for A356 alloy with low hydrogen content appears in Fig. 2.15. These vertically cast specimens were obtained from Alcan (F. Major), tested by Westmoreland and then image analyzed by Sandia-Livermore. The 20 and 30 μm dendrite cell size specimens had no large pores and negligible porosity overall ($\overline{\varphi} < \varphi_{th} = 10^{-4}$), containing only 50-100 μm oxides. The larger dendrite cell size (60 μm) specimens had 150 μm pores which served as sites for crack formation and early propagation. It is noted that in this case the fatigue behavior of the small DCS material in the HCF regime is described quite well by Si particle-dominated incubation as an upper bound and 50-100 μm oxide incubation as a lower bound. Of course, $f(\overline{\varphi}) = 1 + \omega = 3$ for the 20 and 30 μm dendrite cell sizes. On the other hand, the case of DCS = 60 μm is well-described by the use of the observed 150 μm pore sizes for incubating cracks; in this case, $f(\overline{\varphi}) = 1$.

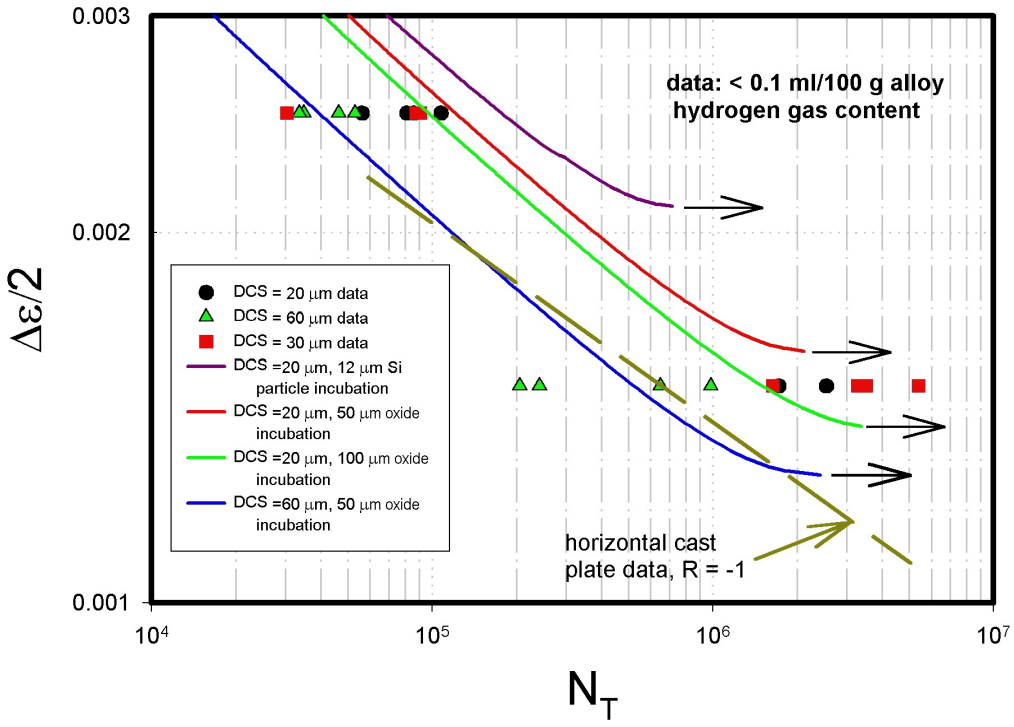

Fig. 2.15 – Comparison of model predictions with data for completely reversed, uniaxial fatigue of specimes with several different inclusion severity types for three different dendrite cell sizes for vertically cast A356-T6 alloy with low hydrogen content (specimens from Alcan, Inc.). The 20 and 30 μm dendrite cell sizes had no large pores and negligible porosity overall, containing only 50-100 μm oxides. The larger dendrite cell size (60 μm) specimens had 150 μm pores.

It is interesting to note that the variation of the fatigue life for a given strain amplitude in A356-T6 over a wide range of maximum pore sizes and dendrite cell sizes is rather well described using nominal stress-strain, incubation and propagation properties for the horizontally cast plate; variability in the HCF regime is reasonably well-predicted using the appropriate maximum inclusion size, as shown in Fig. 2.12. It is likely that the fatigue of this material is strain-controlled, since the incubation phase it is dictated by the micronotches. Furthermore, the small crack propagation behavior is evidently relatively insensitive to details of the alloy (cf. Shiozawa et al., 1997). It is well-known that fatigue of materials with macronotches is a strain-controlled process.

2.8.2 LCF Coalescence

In this section we add the coalescence treatment derived in Section 2.7 to establish lower bounds on LCF life. This is done by assigning the final crack length for propagation of the most severe (largest diameter) inclusion as the effective final crack length, $\tilde{a}_f$, in the LCF regime. Accordingly, we assume that

$$\text{final crack length} = a_f = a_f\big|_{\text{dominant}} + z\left(\tilde{a}_f - a_f\big|_{\text{dominant}}\right) \qquad \text{Equation 2.39}$$

where the dominant final crack length is that which is normally assigned in a propagation analysis which assumes a single crack grows to failure, and $z = \frac{1}{0.7}\langle \ell / D - 0.3 \rangle$ as before. Since z = 0 in the HCF regime, coalescence effects only become significant in the LCF regime, for strain amplitudes above 0.0023.

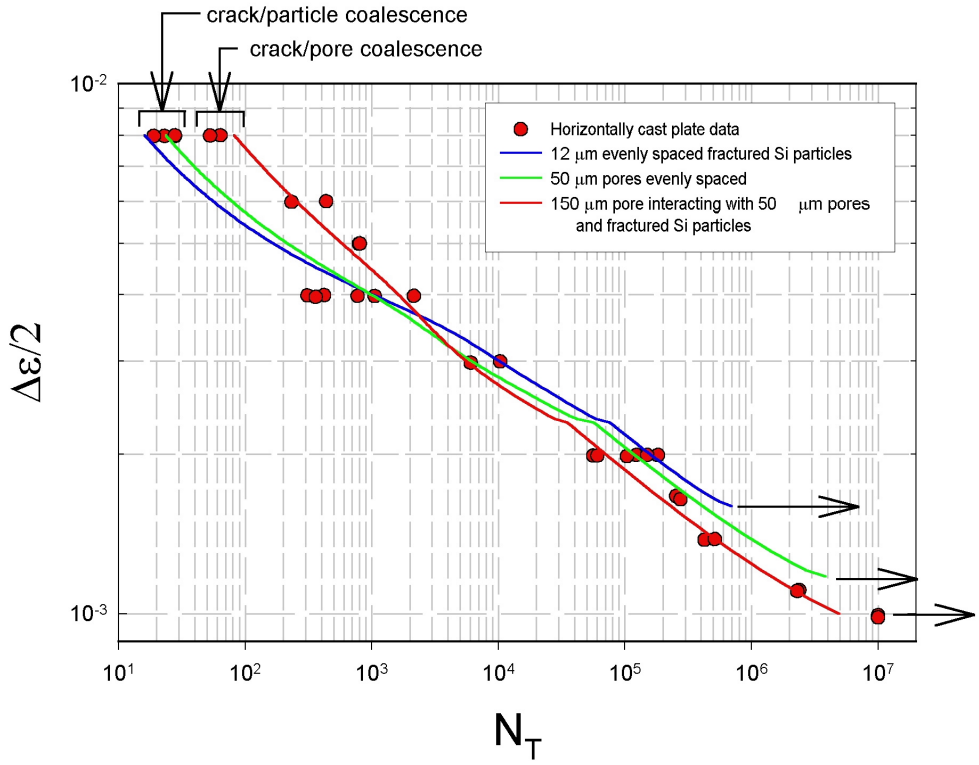

Fig. 2.16 – Variation in completely reversed, uniaxial strain-life behavior as a function of maximum inclusion size for horizontally cast plate, including coalescence effects in the LCF regime. In the coalescence propagation analysis, parameters were assigned as follows based on experimental work: $\bar{\varphi} = 1.5\text{x}10^{-3}$, $\bar{D}_p = 50\,\mu\text{m}$, $\hat{D}_{part} = 12\,\mu\text{m}$, and $DCS = 30\,\mu\text{m}$.

Two observations are noteworthy. First, contrasting Fig. 2.16 with Figs. 2.10 or 2.12, it is evident that coalescence is the most likely explanation for the very significant range of fatigue lives observed experimentally in the LCF regime for this material. Multisite fatigue damage has been frequently observed in experiments conducted at amplitudes near the upper range of the HCF region and above. In fact, it is not uncommon to see crack development at multiple sites in HCF, although only one crack typically becomes dominant. Second, a striking result from Fig. 2.16 is that the case of profuse incubation at the largest Si particles gives the lower bound fatigue life in the LCF regime! This is expected since $\tilde{a}_f$ is minimum in this case (see Fig. 2.9). The fatigue life for the 150 μm pore is much greater, approaching the dominant crack behavior shown in Fig. 2.10. Therefore, we have an important and somewhat counter-intuitive result from the coalescence analysis: highly refined microstructures appear to offer less LCF resistance than coarse microstructures with higher levels of porosity. At first glance, one might assume that the larger pores are responsible for the shortest lives in the LCF regime, but this is not the case according to this analysis. On the other hand, the model predicts that highly refined microstructures (low porosity, small DCS) provide substantial enhancement to HCF resistance relative to coarse microstructures, as observed in the crossover from the LCF regime to the HCF regime for the three cases in Fig. 2.10, for example. This enhanced HCF resistance is experimentally well-documented; near threshold, cracks tend to grow between Si particles in the eutectic regions because most particle-matrix interfaces are intact (cf. Wang and Zhang, 1994). The lack of detailed documentation of variability of fatigue lives in LCF and transition regimes as a function of average and maximum inclusion sites and observed multisite fatigue crack formation and growth likely reflects the rather prevalent bias towards assuming that dominant crack fracture mechanics applies in all cases. In wrought alloys, the variability in LCF response is typically much less than HCF; this analysis suggests that this is because the distribution of initial crack sizes in the former is much tighter than the latter.

Figure 2.16 also labels the cases of fractured Si particle-controlled coalescence as belonging to a characteristically different set than cases of pore-pore crack interactions. The former form the lower bound LCF behavior, while the latter are intermediate to the dominant crack case, which appear to serve as the upper bound for modeling these experiments.

Figure 2.17 shows results of approximate calculations for the behavior of two other A356-T6 castings in the USCAR program, the Control Arm and the Front Cradle, selected as representative of very low and very high porosity, respectively. In these calculations, all properties correspond to those of the horizontally cast plate, except for those pertaining to porosity and inclusion sizes, as well as the DCS. Even though at first glance this may appear crude, in many respects these are the key parameters that control the fatigue behavior of the A356 *system*, irrespective of other properties and fatigue at micronotches is more or less strain-controlled. It is interesting to note that the experimentally observed upper and lower bounds on strain-life behavior (shown as solid black lines in the Figure) are reasonably well-described as between the dominant crack calculations in Fig. 2.10 and the lower bound calculations for Si-particle-controlled crack incubation in LCF. Moreover, the upper and lower bounds in the HCF regime are fairly well predicted using the observed range of maximum inclusion sizes for these materials.

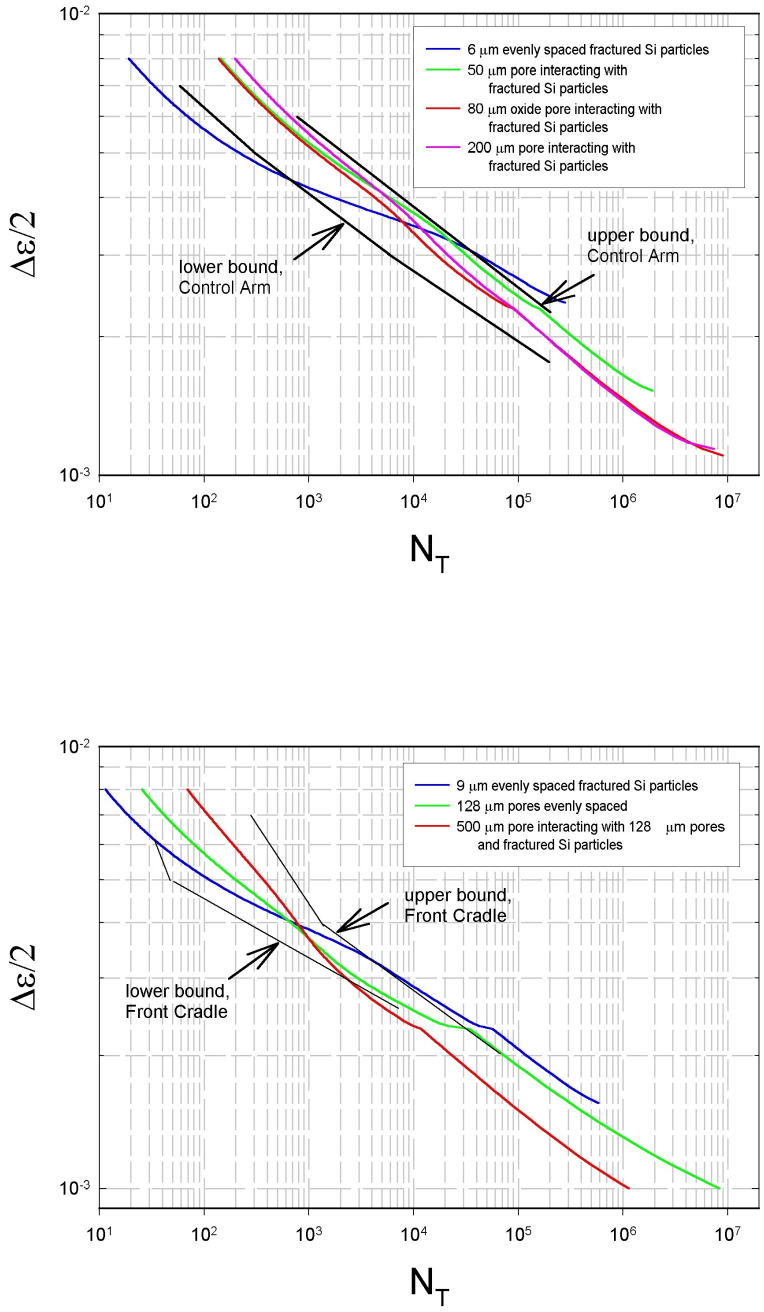

Fig. 2.17 – Estimated variation in completely reversed, uniaxial strain-life behavior as a function of maximum inclusion size for (top) control arm and (bottom) front cradle, including coalescence effects in the LCF regime. In the coalescence propagation analysis, parameters were assigned as follows based on experimental work: control arm ($\overline{\varphi} = 1.0\text{x}10^{-5}$, $\overline{D}_p = 1\,\mu\text{m}$, $\hat{D}_{part} = 6\,\mu\text{m}$, and $\text{DCS} = 25\,\mu\text{m}$); front cradle ($\overline{\varphi} = 1.1\text{x}10^{-2}$, $\overline{D}_p = 128\,\mu\text{m}$, $\hat{D}_{part} = 9\,\mu\text{m}$, and $\text{DCS} = 45\,\mu\text{m}$).

Although the data of any experimental program are necessarily limited and precise statements on upper and lower bounds must be treated with caution, it appears that the following are useful working bounds on fatigue lives for a given constant amplitude loading condition:

HCF (only dominant cracks)
Upper bound – Largest Si particle as crack incubator, porosity < 10^{-4} , fine DCS
Lower bound – Largest possible pore or oxide as crack incubator, occurring just below the free surface

LCF
Lower bound – Largest Si particle as crack incubator, microporosity and larger DCS favored
Upper bound – Dominant, single crack, with largest Si particle as crack incubator producing the longest life

2.9 Load Sequence Effects and Variable Amplitude Loading

The present model decomposes the small crack behavior into incubation and propagation components. It can be integrated in closed form for a given material condition (i.e., given dendrite cell size, flow properties, maximum inclusion and pore sizes, microporosity, etc.) and loading condition (constant strain amplitude and load ratio) to give

$$N_{inc} = \left(\frac{\beta}{C_{inc}} \right)^{-2} \quad , \quad N_{MSC/PSC} = \frac{1}{G\Psi} \ln \left(\frac{\Psi a_f + \Omega - \Delta CTD_{th}}{\Psi a_i + \Omega - \Delta CTD_{th}} \right) \qquad \text{Equation 2.40}$$

and

$$\Psi = f(\bar{\varphi}) C_{II} \left(\frac{DCS}{DCS_o} \right) \left[\frac{U \Delta \hat{\sigma}}{S_u} \right]^n \quad , \quad \Omega = C_I \left(\frac{DCS}{DCS_o} \right) \left(\Delta \gamma^p_{max} / 2 \Big|_{macro} \right)^2 \qquad \text{Equation 2.41}$$

If we neglect long crack propagation, then $N_T = N_{inc} + N_{MSC/PSC}$.

If we regard the rate of incubation damage as an incrementally linear form (see Equation 2.4),

$$\frac{dV}{dN} = C_{inc}^{-2} \beta^2 \qquad \text{Equation 2.42}$$

where $0 \le V \le 1$, and $V(0) = 0$ for undamaged material and $V = 1$ for an incubated crack (at $N = N_{inc}$), leads us to the result that for constant C_{inc}, the incubation damage is subject to the Miner's linear damage summation law, i.e. $\sum n_i / (N_{inc})_i = 1$ for i = 1,2,..., N loading levels/conditions. Here, n_i is the number of cycles applied under the i^{th} amplitude and R-ratio condition. However, if C_{inc} varies from one loading condition to the next, as would be the case for loading above the microplasticity percolation limit (i.e. above macroscopic yield point) or for variable R-ratio even for strain amplitudes below this limit, then C_{inc} depends on amplitude and the linear damage

summation breaks down. The change of C_{inc} for the LCF regimes is due to extensive particle/matrix debonding or particle cracking and commensurate loss of constraint on micronotch cyclic plasticity. In the case of LCF-HCF interaction, Equation 2.42 must be integrated in rate form. It remains to be seen how sequences of loading involving excursions above the macroscopic yield point affect the incubation process for subsequent low amplitude cycles, as the literature does not present many results for this type of history for A356-T6. Of particular interest is whether higher amplitude cycles in the transition or LCF regime result in a lasting increase on the rate of small crack formation and growth within the notch root field; if so, then it might be necessary to write

$$C_{inc} = C_n + \frac{1}{0.7}\left\langle \left(\frac{\ell}{D}\right)_{max} - 0.3 \right\rangle (C_m - C_n) \qquad \text{Equation 2.43}$$

However, the model inherently has sequence effects even without the dependence on $(\ell/D)_{max}$ in Equation 2.43 in the incubation regime, provided that some of the amplitudes within the spectrum exceed the microplasticity percolation limit of $\ell/D = 0.3$. Sequences of high amplitude cycling (above $\ell/D = 0.3$) followed by low amplitude cycling will lead to a model prediction of a cycle summation less than unity, and vice versa for low-high amplitude sequences. As a practical matter, above the percolation limit for microplasticity crack incubation is very rapid and so only a small number of cycles are necessary to reach the incubation life. Therefore, we can regard linear damage summation as valid only for all stress amplitudes within the HCF regime; any overload cycles are expected to result in highly accelerated crack incubation which will invalidate the linear damage summation.

As is the case in classical crack initiation analyses based on rainflow counting a history of applied load or strain and then applying of a damage accumulation procedure to the amplitude histogram, certain approximations may be made, depending on the loading history. For example, for simplicity R-ratio effects in C_{inc} might be neglected by assuming some characteristic value (zero or some positive value) based on engineering judgement. Of course, this is an approximation.

Turning to MSC/PSC crack propagation, almost identical comments apply. As long as (a) Ψ is a constant, independent of strain/stress amplitude and R-ratio, (b) the effect of the Ω term is negligible ($\Psi a \gg \Omega$), (c) coalescence is neglected, and (d) the driving force is sufficiently above threshold ($\Psi a \gg \Delta CTD_{th}$), linear damage summation applies to the MSC/PSC crack growth in the HCF regime as well as up to the limit plasticity regime for given initial and final crack lengths, i.e. $\sum n_i / (N_{MSC/PSC})_i = 1$. Here, n_i is only the number of cycles applied under the condition of MSC/PSC crack growth and <u>does not</u> include cycles involved with crack incubation. The requirement of exceeding threshold is not severe since the driving force depends on a power of 4.8 on the stress range. Similar to incubation, the MSC/PSC growth relation for dominant cracks exhibits amplitude dependence when Ω becomes significant, and therefore linear damage summation breaks down for overload excursions involving limit plasticity. Physically this is sensible in view of the fact that particles and interfaces are damaged at higher amplitudes, increasing the rate of crack propagation in the eutectic regions at higher amplitudes in a manner

disproportionate to the HCF growth relation. Again, load sequence effect studies would shed light on whether periodic LCF excursions are adequately described by the present formulation or whether some permanent memory of overloads should be retained in the crack growth rate relation for lower strain amplitudes. It should be noted that R-ratio effects are introduced in the propagation relation as a modification of the effective stress range and therefore do not contribute to load sequence effects.

It is emphasized that linear cycle fraction-based damage summation never applies over multiple regimes of crack incubation and propagation. It would be inappropriate to argue in favor of linear summation based on the fraction of N_T, for example. Unfortunately, this is common practice when using strain-life or stress-life approaches. The nature of damage accumulation is fundamentally governed by different functions of applied stress and R-ratio in these regimes, and they cannot be combined into one simple summation rule. However, it is fortunately unnecessary to develop ad hoc nonlinear damage summation rules, as the equations of the model may be integrated in rate form to give the actual sequence effects.

Finally, at high strain amplitudes in the LCF regime (limit plasticity), Miner's rule again applies because the coefficients of the damage growth rate saturate to the values corresponding to $\ell / D \to 1$. It is commonly observed that wrought alloys obey Miner's rule for sequences of LCF loading, and the same is predicted for the limit plasticity regime of cast alloys since the influence of particle constraint is lost.

The impact of LCF overloads on the formation of multisite fatigue cracks which may eventually coalesce under lower amplitude HCF loading is an area of uncertainty. Although multiple cracks can form through the microstructure in HCF, only one typically becomes dominant and grows in a manner relatively unaffected by the others. However, periodic excursions in the LCF regime may result in multisite incubation and coalescence of fatigue cracks under even subsequent HCF amplitudes, as discussed in a previous section. The definition of $\tilde{a}_f$ in Section 2.7 would require revision to account for variable amplitude loading.

To summarize, according to the present formulation for variable amplitude loading,

- Miner's rule applies to the incubation component of fatigue life for strain amplitudes in the HCF regime ($\ell / D < 0.3$) and only for a fixed R-ratio.
- Miner's rule applies to the MSC/PSC propagation component of fatigue life for strain amplitudes in the HCF regime ($\ell / D < 0.3$) and into the LCF regime below limit plasticity ($\Psi a \gg \Omega$), but only for driving forces sufficiently higher than the threshold level.
- Miner's rule is invalid if applied on the basis of the total fatigue life, which includes multiple regimes of crack formation and growth.
- Miner's rule does not apply for the incubation component of fatigue life if cycles are applied in the history at amplitudes exceeding the macroscopic yield point ($\ell / D > 0.3$).
- The identification of stronger sequence effects (e.g. permanent) than described in the model due to a single or periodic overloads is a matter for further research, as this study has focused on constant amplitude and R-ratio experiments. However, rather simple modifications are possible to incorporate any such strong sequence effects.

- The equations of the model may be integrated in rate form in any case to give sequence effects or to support other approximations of damage summation for use in spectrum loading.

2.10 Application of Model to Macronotches

It is common industrial practice to use finite element analysis and/or Neuber notch analysis to evaluate the local stresses and strains at component notches or to measure notch root strains directly in instrumented components. The same methodology can be applied with the present model, treating it as an algorithmic equivalent of the strain-life approach, for example. The model requires mechanical parameters (macroscopic stress/strain range history, along with the R-ratio or mean stress) in addition to the various material parameters that may vary from case to case (e.g. maximum pore size, degree of porosity/microporosity, dendrite cell size). The only serious limitation is that for relatively small macronotches the sampling of microstructure within the highly stressed volume near the notch root will be small enough to preclude a statistically representative sample of microstructure. This is not so much of an issue for extremely low porosity, fine dendrite cell castings but more for large dendrite cell, high porosity castings; in this case, even reasonably large notches may behavior differently from smooth specimens with a larger highly stressed volume of material due to the variability of the higher scale inclusions/pores. This will be discussed later in the context of statistical considerations.

The fatigue strength for a given life may be relatively insensitive to small notches (on the order of dendrite cell size, for example) since there may be other defects in the microstructure of comparable dimensions and because the crack growth from such notches is subject to arrest as is the case for wrought alloys (cf. Murakami and Endo, 1994). On the other hand, pre-existing crack-like defects within the microstructure should be treated as initial cracks, especially in the HCF regime, competing with cracks that are incubated at higher scale inclusions. Surface scratches or machining marks are good examples.

The model requires input of stress and strain amplitudes at the root of macronotches. Quite often, linear elastic finite element analyses are employed as part of the design process for cast components. As long as the notch root von Mises uniaxial equivalent effective stress range $\Delta\bar{\sigma} = \sqrt{3/2\,\Delta\sigma'_{ij}\,\Delta\sigma'_{ij}}$ does not exceed twice the macroscopic cyclic yield point (about 300 MPa) for A356-T6, the stresses and strains from elastic analysis are suitable as input to the fatigue model. Of course, large overloads may induce notch root plasticity and residual stresses that can only be addressed using elastic-plastic analysis, whether based on finite elements or Neuber notch analysis. Alternatively, theoretical elastic stress concentration factors, if they have been tabulated, may be used in this case. However, elastic analysis can be used even for higher stresses as long as the component remains elastic everywhere except at the notch root(s) with the highest stress concentration; in this case, standard techniques of Neuber notch analysis can be used to provide input to the model in terms of local, notch root stresses and strains. Other notch root stress analysis algorithms have also been developed in the past 5-10 years as alternatives to the Neuber analysis.

2.11 Multiaxial Stress State Effects

The model is written in a form which is applicable to multiaxial stress states. The incubation driving force is based on the maximum plastic shear strain amplitude at micronotches, while the MSC/PSC driving force is based on the maximum principal stress range. While the former has been reckoned in terms of local cyclic plasticity forming and growing small cracks, the latter is due to the constraint on cyclic crack tip plasticity offered by the Si particles on an otherwise ductile matrix. It is left to future work to identify stress state dependencies based on finite element simulations that include a variation of the applied loading over a broad range of stress states. The current form of the model for combined stress states is therefore subject to modification as these results become available.

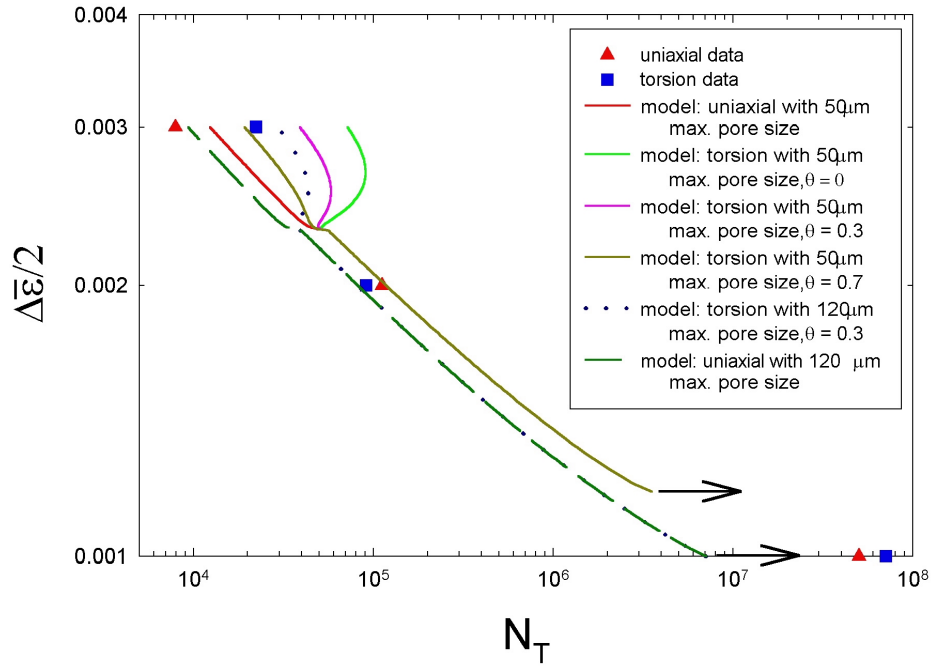

Fig. 2.18 – Comparison of experiments and dominant crack model predictions for completely reversed uniaxial and torsional loading of thin-walled tubular specimens for the horizontally cast plate A356-T6 alloy for several maximum pore sizes and a range of θ values.

Completely reversed torsional fatigue experiments discussed in Section 3.4 at Georgia Tech on thin-walled tubular A356-T6 specimens from the horizontally cast plate show that the fatigue lives for the cases of uniaxial and torsional fatigue are reasonably well-correlated using the Mises equivalent strain for strain amplitudes that are below the percolation limit for microplasticity (for $\ell / D < 0.3$) for final crack lengths of approximately 1 mm, while torsional specimens are longer lived for strain amplitudes exceeding this level (see Fig. 2.18). This suggests that the assumption of uniaxial Mises equivalent strain in the incubation driving force is

appropriate. It is apparent from Fig. 2.18 that a value of $\theta \approx 0.4$ in the uniaxial equivalent stress $\Delta\hat{\sigma} = 2\theta\overline{\sigma}_a + (1-\theta)\Delta\sigma_1$ is necessary to match these results. It is noted that the ΔCTD is in its own right a local mixed mode quantity (cf. McDowell and Bennett, 1999) since it includes the vector magnitude of combined crack tip sliding and opening displacements. The role of the $\Delta\hat{\sigma}$ is to assign a dependence of this mixity on stress state in a phenomenological way, with the relative magnitudes of $2\theta\overline{\sigma}_a$ and $(1-\theta)\Delta\sigma_1$ prescribing the relative effects of crack tip sliding and opening, respectively.

2.12 Transition to Long Crack Fracture Mechanics

The fatigue crack growth rate as predicted by the EPFM-based da/dN versus ΔCTD relation in Equation 2.11 for microstructurally and physically small crack regimes is generally higher than that for mechanically long fatigue cracks. Recalling that the transition from the small crack growth regime to the long crack growth regime described by Equation 2.15 is assumed to occur at the point of crossover of the two rates, i.e.

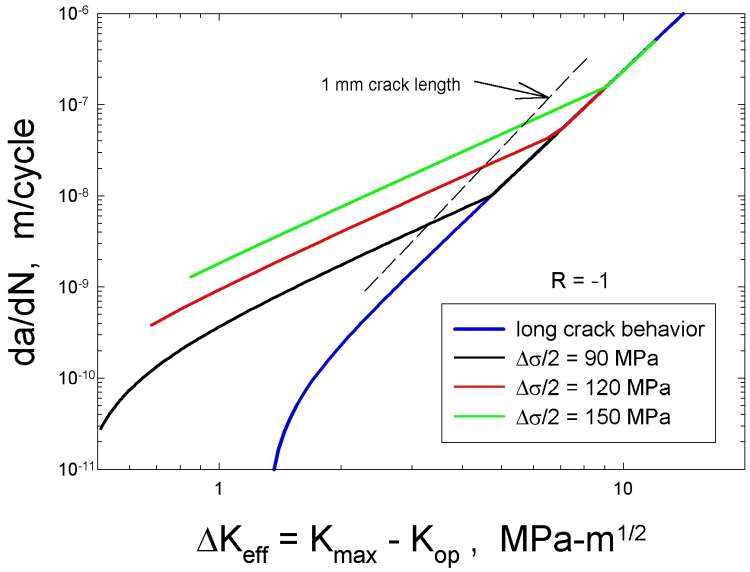

Fig. 2.19 - Plot of predicted da/dN from the model for three constant amplitude, completely reversed stress amplitudes in the HCF regime in terms of the range of the effective stress intensity factor, including transition to long crack behavior where the MSC/PSC and LC growth rates are equal. The dashed line shows the point where a 1 mm crack is reached in the small crack propagation history. The incubation pore size is 50 μm in these calculations.

$$\frac{da}{dN} = \max\left[\left(\frac{da}{dN}\right)_{MSC/PSC}, \left(\frac{da}{dN}\right)_{LC}\right] \qquad \text{Equation 2.44}$$

Note in Fig. 2.19 that the value of the effective stress intensity factor range, ΔK_{eff} ,at the point of transition to long crack behavior is on the order of 6 $MPa\sqrt{m}$ under HCF conditions, for a completely reversed HCF stress amplitudes just above threshold, 90 MPa. This is very close to the value of maximum stress intensity factor determined by Gall et al. (1999) for transition from fatigue crack growth along the interface between Si particles and the Al-1%Si matrix to crack growth through the Si particles, presumably by virtue of particle fracture ahead of the advancing crack.

2.13 Small and Long Crack Thresholds

It is possible to represent the three thresholds graphically, as shown in Fig. 2.20 for horizontally cast A356-T6 alloy with a maximum pore size of 50 μm. The lowest threshold (green line, yellow region) is corresponds to the elastic shakedown limit of cyclic microplasticity within the microstructure absent of cracks. The MSC/PSC crack propagation threshold dominates for cracks up to about 400-500 μm, with the LEFM propagation threshold relevant to longer cracks holding at lower applied stress levels. The dashed line at 84 MPa designates an inadmissible boundary because the maximum pore size is 50 μm in this case.

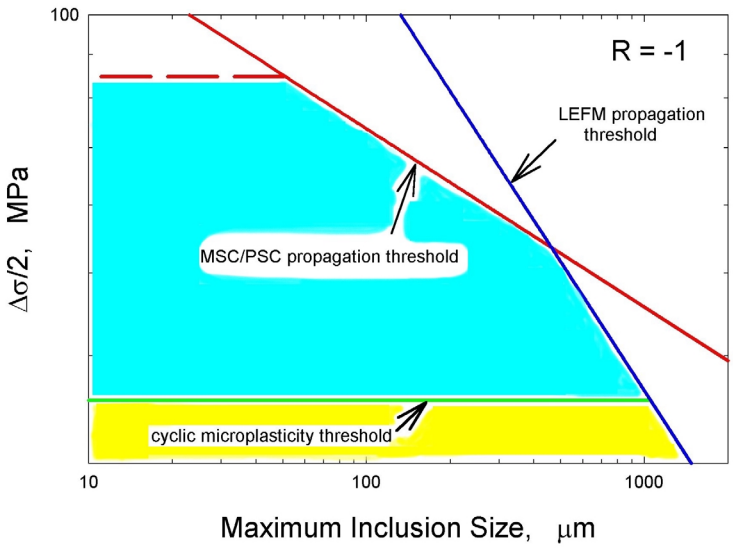

Fig. 2.20 – Kitagawa diagram for completely reversed uniaxial fatigue thresholds constructed from the present model of horizontally cast A356-T6 alloy. In the yellow shaded region, cracks do not incubate. In the blue-shaded region, MSC/PSC cracks arrest. The dashed line represents the stress amplitude corresponding to 50 μm average pore diameter. Note that outside the blue- and yellow-shaded envelopes, MSC/PSC or long cracks can propagate to failure.

2.14 Use of Model for Parametric Studies

The model presented in this Chapter is useful for parametric studies since it explicitly represents the role of various key microstructural descriptors. For example, Fig. 2.21 shows the computed dependence of total fatigue life to a crack length of 1 mm on inclusion size for three stress amplitudes within the HCF and transition regimes for horizontally cast A356-T6 alloy. Such plots can be generated rapidly for a wide range of casting inclusions and stress amplitudes.

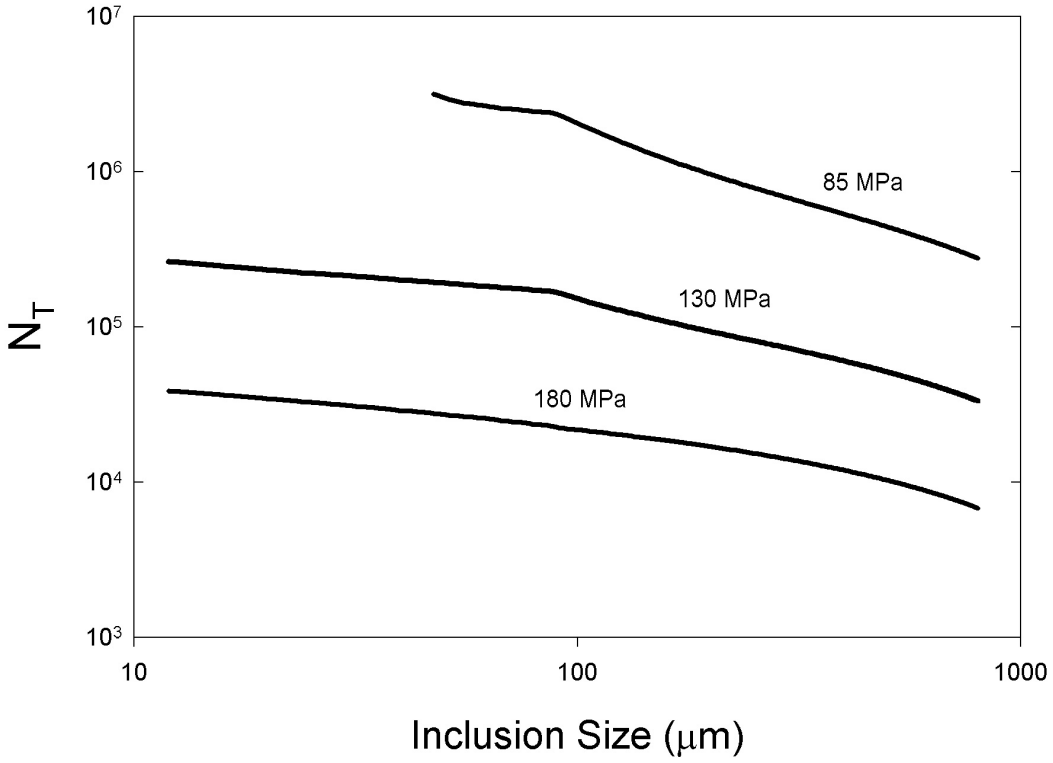

Fig. 2.21 – Example of parametric computational study of total fatigue life (1 mm crack) as a function of completely reversed uniaxial stress amplitude for a wide range of maximum inclusion sizes for horizontally cast A356-T6 alloy.

2.15 Statistical Aspects of Fatigue Life Prediction

This model is deterministic but has been framed to explicitly incorporate microstructure features, thereby allowing for variability of microstructure to enter naturally and directly into the resulting variability in estimated fatigue life. Hence, the model is amenable to prediction of variability to any level of microstructure variability input by the user. Microstructure features include dendrite

cell size, maximum Si particle size, maximum pore size, maximum oxide size, proximity to the free surface (for large pores) and average porosity level.

If the probability distributions of these features are specified based on quantitative metallography, then the probability distributions for the fatigue life can be computed directly from the model, without resorting to ad hoc incorporation of variability in the fatigue constants that is characteristic of probabilistic fracture or damage mechanics. This is a natural feature of a micro-mechanical framework for fatigue.

3. EXPERIMENTAL PROGRAM

A comprehensive experimental program was conducted in order to explore and quantify the small and long crack behaviors for different strain amplitudes, mean stresses, and loading sequences. Scanning electron microscope (SEM) analyses were performed on many of these experimental specimens so that the microstructure/inclusion content could be correlated to the fatigue data. Crack incubation experimental data is difficult to obtain and was not covered here. The crack incubation information was obtained in the micromechanical finite element chapter of this report. The following sections delineate the type of experiments.

1. Smooth specimen, strain-life and stress-life experiments
2. Multiaxial fatigue
3. Small crack experiments
4. Long crack experiments
5. Mean stress experiments
6. Sequence experiments

Westmoreland Mechanical Testing and Research conducted the experiments except for the multiaxial fatigue experiments, which were conducted at Georgia Institute of Technology. The major results of the experimental program are included in this chapter.

3.1. SMOOTH SPECIMEN UNIAXIAL CYCLIC EXPERIMENTS

Smooth specimen uniaxial cyclic experiments were the mainstay of the study although multiaxial and precracked experiments were also performed. The smooth specimen uniaxial experiments are the usual means to obtain strain-life and stress-life fatigue curves. In fact, many designers will not consider other types of data other than evaluation of uniaxial strain-life data. As such, we examine different uniaxial fatigue data in which the specimens had different dendrite cell sizes (DCS) and different initial porosity levels. Furthermore, we examine these data in the context of literature data for this cast A356 aluminum alloy and automotive component data. These experiments were conducted at room temperature and under relatively low frequencies (strain rates) in accordance with ASTM Standard 606-99.

3.1.1. UNIAXIAL STRAIN-LIFE CURVES FROM HORIZONTALLY CAST PLATES

For our study, we considered uniaxial tension/compression experiments and did not consider bending. Bending induces higher stresses/strains at the surface, and we desired to understand the mechanisms internally under uniform stress. As discussed in another section, we determined the surface effects by micromechanical simulations.

Figure 3.1 shows the strain-life and stress-life curves for the horizontally cast A356 aluminum alloy plates used in our study. Numerous smooth cylindrical (dog-bone) shaped fatigue specimens, shown in Figure 3.1c were machined from the cast plate with a gage length of 19 mm and a gage section diameter of 6.35 mm. A voltage (potential) drop was measured across the entire specimen gage length in the dog-bone specimens to determine the number of cycles at failure. Typically, a 50% load drop was used to determine final failure of the specimen, although

most of the specimens experienced catastrophic fracture once the load dropped to approximately 20% of its starting level. The experiments were conducted in strain control with R-ratios of -1 at room temperature. A triangle wave from was applied at a frequency of 0.5 Hz.

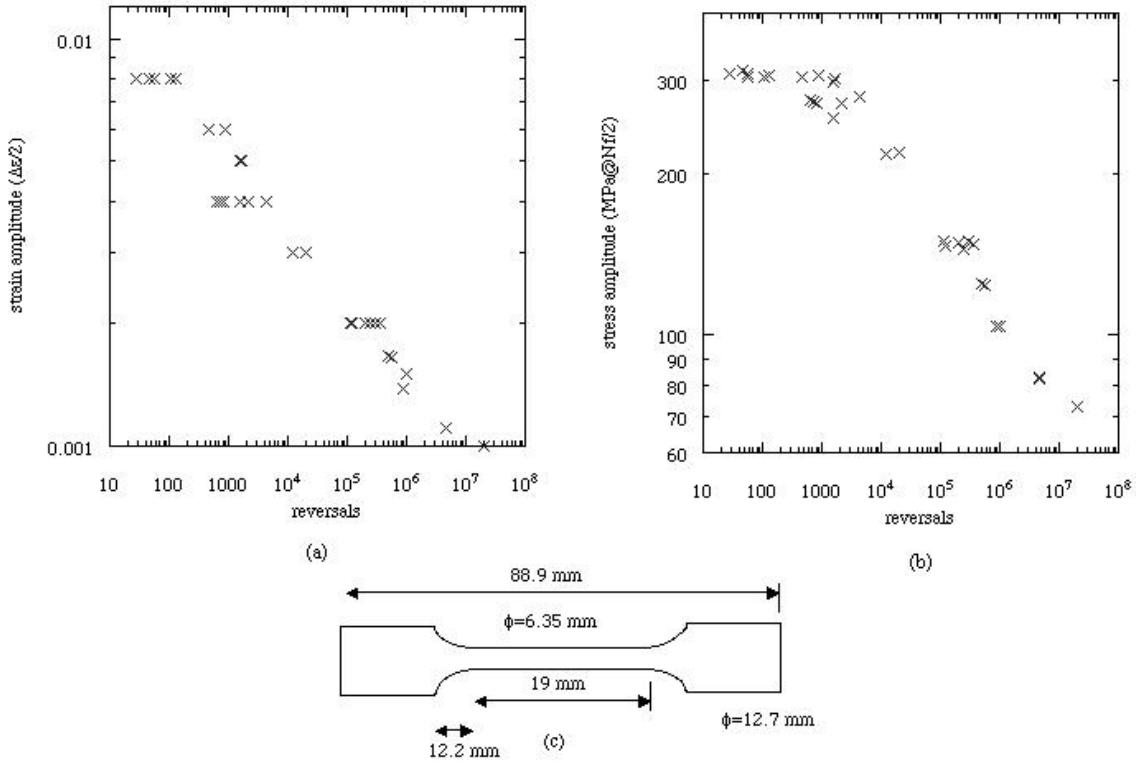

Figure 3.1. (a) Strain-life and (b) stress-life curves from horizontally cast A356 aluminum alloy plate. The smooth cylindrical specimens dimensions are shown in (c).

When comparing the cyclic stress-strain response to the monotonic stress-strain response, one can observe in Figure 3.2 that the material cyclically hardens, that is, an increased work hardening rate under cyclic loading is exhibited when compared to a monotonic loading. We note that this type of cyclic work hardening was observed previously by Stephens *et al.* (1988) for A356-T6.

3.1.2. COMPARISON OF HORIZONTAL CAST PLATE STRAIN-LIFE CURVES TO OTHER DATA

Figure 3.3 shows the strain-life curves from several different types of A356 aluminum castings from uniaxial cyclic fatigue experiments. Horizontal plates were cast in which specimens were machined for round, smooth cyclic fatigue experiments with an average DCS of 30 μm, and an initial average porosity of 0.0015 was determined. The horizontal plates were the main source for specimens in the later sections of this chapter, so characterizing them with actual component data and literature data is worthwhile. From Figure 3.3, one can see that the strain-life curves from the horizontal cast plates fall in the broad scatterband of automotive component data or data from Stephens *et al.* (1988).

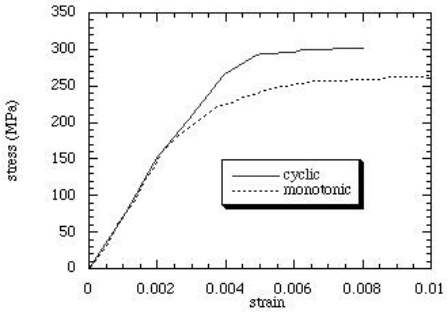

Figure 3.2. Stress-strain responses from monotonic and cyclic loading conditions for the cast A356 aluminum alloy.

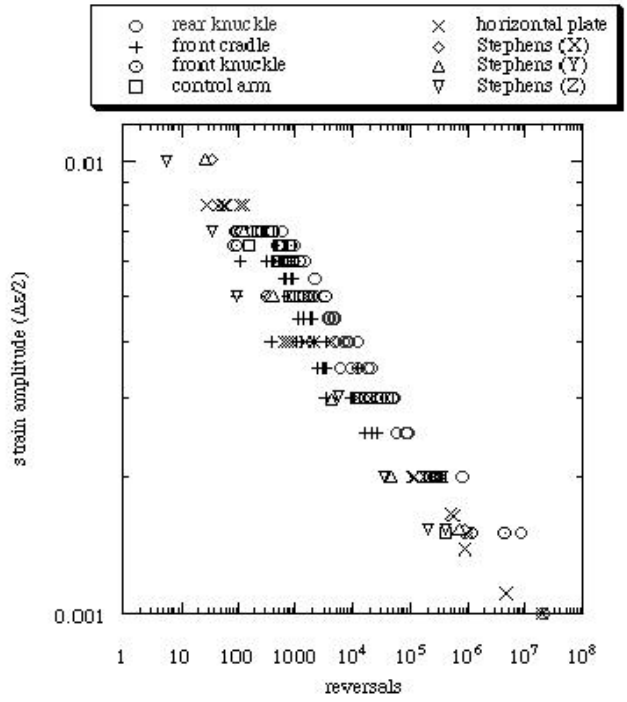

Figure 3.3. Strain-life curves from horizontal plates, automotive components, and literature data (Stephens, 1988).

The strain-life behavior is typically characterized by the following equation which includes an elastic portion (Basquin, 1910) and a plastic portion (Coffin,1954; Manson, 1953),

$$\frac{\Delta\varepsilon}{2} = \frac{\sigma_f'}{E}\left(2N_f\right)^b + \varepsilon_f'\left(2N_f\right)^c \qquad \text{Equation 3.1}$$

where σ_f' is the fatigue strength coefficient, b is the fatigue strength exponent, E is the elastic modulus, $2N_f$ are the number of reversals to failure, ε_f' is the fatigue ductility coefficient, and c is the fatigue ductility exponent.

Tables 3.1 and 3.2 summarize the fatigue property and microstructure/inclusion parameter values for the materials shown in Figure 3.3. Some observations can be made regarding the data. The first observation is that the cyclic yield strength is greater than the monotonic yield strength for all the material data collected indicating that it is a cyclic hardening material. Here, a 0.2% offset was assumed to determine the yield point.

A second observation from Table 3.1 is that in wrought materials, the fatigue strength coefficient, σ_f', is often related to the true fracture strength, and the fatigue ductility coefficient, ε_f', is similarly related to the true fracture ductility. We see that the fatigue strength coefficient is almost twice that of the ultimate strength for each of the materials from the components, horizontal plate, and Stephens *et al.* (1998) data. For the fatigue ductility coefficient, the results are on the same order of magnitude as the elongation at failure. The conclusion is that the fatigue strength coefficient and fatigue ductility coefficients do not directly relate to the elongation at failure and the ultimate tensile strength. A third observation from Table 3.1 is that differences in the fracture toughness, K_{IC}, (17-25 MPa-m^0.5), and the elongation to failure (2-12%) are observed for A356-T6. These differences under monotonic conditions arise from a combination of the microstructure and inclusion content. In particular, they can be delineated as the following:

(1) initial volume fraction of casting porosity,
(2) initial pore sizes and distribution,
(3) nearest neighbor distance of large pores,
(4) volume fraction of particles,
(5) particle size and distribution,
(6) particle nearest neighbor distance, and
(7) dendrite cell size.

The volume fraction of particles was essentially the same at 7%. After viewing Figure 3.3, one might tend to assume equivalence of the data when considering statistical significance, excusing differences to scatter. However, upon closer examination of the microstructures and sites for crack formation at different strain amplitudes, there arises a much more deterministic evaluation. This is also evident by observing that the data in Figure 3.3 are layered or ordered according to the specific component/casting. The seven microstructural aspects mentioned above have a synergistic effect on the outcome, not only on the elongation at failure, but the final number of fatigue cycles as well. One should not just independently assign the final number of cycles to one parameter, for example, the dendrite cell size, unless of course all of the other parameters are

statistically equivalent. Although one might examine just the dendrite cell size, the other parameters/inclusions could play a much larger role in the outcome of the fatigue life. As such, all of these microstructure/inclusions must be considered when evaluating the fatigue life of a material. This is illustrated by the next set of experiments.

3.2. Small Crack Incubation Cyclic Experiments

We cast plates after the method of Major (1997) in order to quantify the different initial porosity levels and DCSs. These plates were cast in a vertical environment to give a gradation in porosity level as the material solidified. The specimen and experiment conditions were identical to those for strain-life experiments on the horizontally cast plates. Figure 3.4 shows the strain-life curves comparing the horizontally cast plate with the vertically cast plate. Note that as the DCS increases, the number of cycles (reversals) to failure decreases. Again, one must not attribute the differences just to DCS though as the initial inclusion size is different for these data.

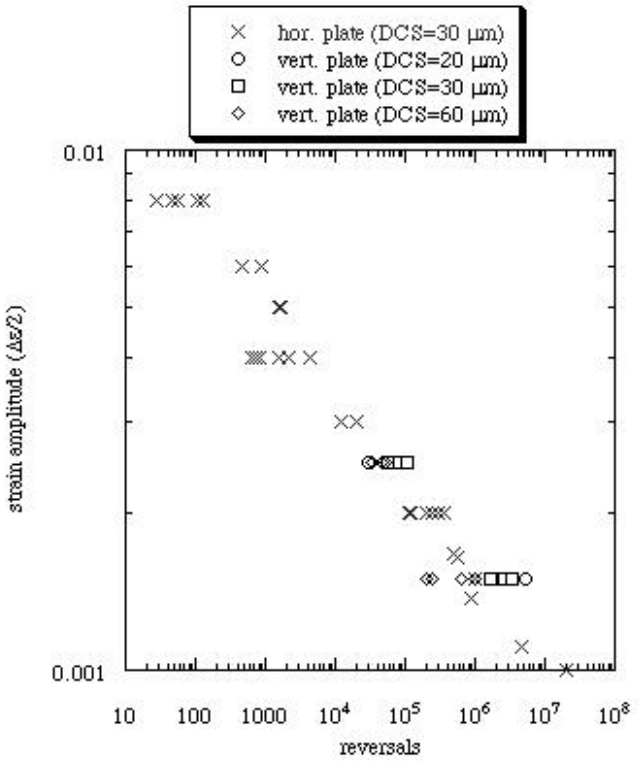

Figure 3.4. Strain-life curves from horizontally and vertically cast plates.

Table 3.1. Fatigue property parameters comparing plate, literature, and automotive components.

Property	Rear Knuckle	Front Cradle	Front Knuckle	Control Arm	Horiz. Plate	Stephens x	Stephens y	Stephens z
Cyclic yield strength (S_y -MPa)	312	272	281	291	290	260	245	230
Cyclic strain hardening exp (n')	0.049	0.082	0.099	0.053	0.065	0.045	0.061	0.057
Cyclic Strength coefficient (K' - MPa)	436	473	528	408	430	384	408	384
Fatigue strength coefficient (σ_f' - MPa)	813	609	543	644	490	594	502	495
Fatigue ductility coefficient (ε_f')	0.061	0.070	0.144	0.149	0.087	0.0269	0.0166	0.0117
b	-.0132	-0.120	-0.101	-.0123	-0.105	-0.124	-0.119	-0.117
c	-.0572	-1.164	-0.687	-0.694	-0.479	-0.530	-0.544	-0.458
Fracture toughness (MPa-m^0.5)	25.7	N/A	22.2	17.1	17.1	18.0	16.7	17.3
K thresh (R=0.5) MPa-m^0.5	2.58	N/A	2.60	2.86	2.85	4.2	3.6	4.0
K thresh (R=0.1) MPa-m^0.5	3.75	N/A	3.66	3.73	4.53	6.0	6.2	6.2
Failure strain	12.3%	7.0%	9.5%	8.5%	8.2%	3.5%	1.8%	1.7%
Elastic Mod (GPa)	72.3	70.7	67.9	74.0	71.0	71.0	70	70
Yield (MPa)	249	222	217	279	249	229	224	217
Ult. Stress (MPa)	327	287	285	336	335	283	266	252

Table 3.2. Summary of microstructure/inclusion parameters comparing plate, literature, and automotive component data.

Property	Rear Knuckle	Front Cradle	Front Knuckle	Control Arm	Horiz. Plate	Stephens x	Stephens y	Stephens z
DCS (μm)	41	45	106	25	30	33	61	66
Ave particle size (μm)	3.3	3.2	2.8	2.8	5	N/A	N/A	N/A
Largest particle size (μm)	25	30	20	25	40	N/A	N/A	N/A
Particle aspect ratio	1.6	1.8	1.6	1.6	2.5	N/A	N/A	N/A
Porosity Volume fraction	1.3e-4	1.1e-2	1e-5	1e-5	1.5e-3	4e-3	5e-3	5e-3
Ave pore size (μm)	28	128	1	1	45	380	380	380
Largest pore size (μm)	50	500	2	2	55	500	500	500
Nearest neighbor distance (μm)	470	210	N/A	N/A	900	N/A	N/A	N/A
Pore type	Isolated shrink	Gas pores	Small pores	Small pores	Isolated shrink	N/A	N/A	N/A
oxides	no	yes	yes	yes	no	N/A	N/A	N/A

Many specimens were analyzed under SEM and Energy Dispersive xray Spectoscopy (EDS) to quantify the size of the initiation site and to determine if the initiation site arose from a pore, oxide, silicon particle, or intermetallic. In some castings with no pores or oxides visible, nucleation sites were determined to be less than a micron in size. Alternatively, when many pores were present, fatigue cracks nucleated at the large pores and coalesced in a ductile manner. Figure 3.5 shows a plot of the number of cycles versus inclusion size for different DCSs in order to show the interactive effects. Here, the trend is not obvious regarding the DCS but the size of the inclusion is clear until a certain volume fraction of porosity is reached. Figure 3.6 shows the number of cycles versus porosity volume fraction for the case when the strain amplitude of 0.0015. Clearly, the volume fraction of pores along with the pore size can be used as a metric to model the phenomenological behavior. As the inclusion size and porosity volume fraction decreased, the number of cycles to failure is increased. In one case one large pore dominated the failure and in another case many small pores initiated fatigue cracks to grow and coalesce. As an

example of the size effects, three specimens with a different number of cycles to failure are shown for illustrative examples in Figures 3.7-3.9. Figure 3.7 shows a specimen that had over $3.28x10^6$ cycles in which an oxide was found on the order of 5 μm. Figure 3.8 shows a fairly large pore (150 μm) near the edge of the specimen in which the fatigue life was approximately $2.05x10^5$ cycles. In this specimen, the volume fraction of pores was fairly low. Figure 3.9 shows a specimen that had over $5.1x10^4$ cycles in which large pores (~200 μm) were found with a fairly large volume fraction of pores.

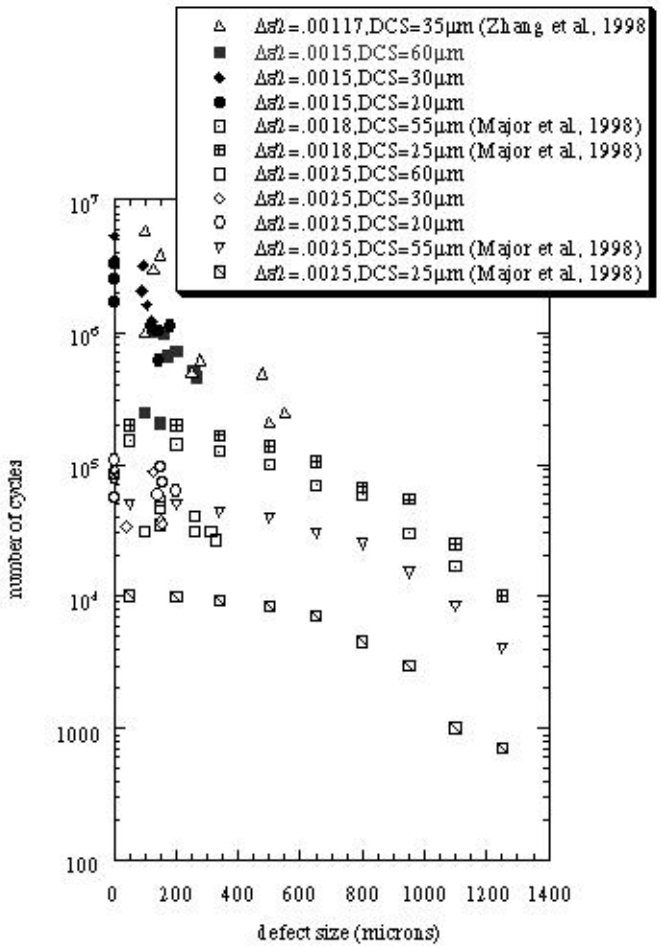

Figure 3.5. Number of cycles versus defect size at different dendrite cell sizes for the vertically cast plate and literature data.

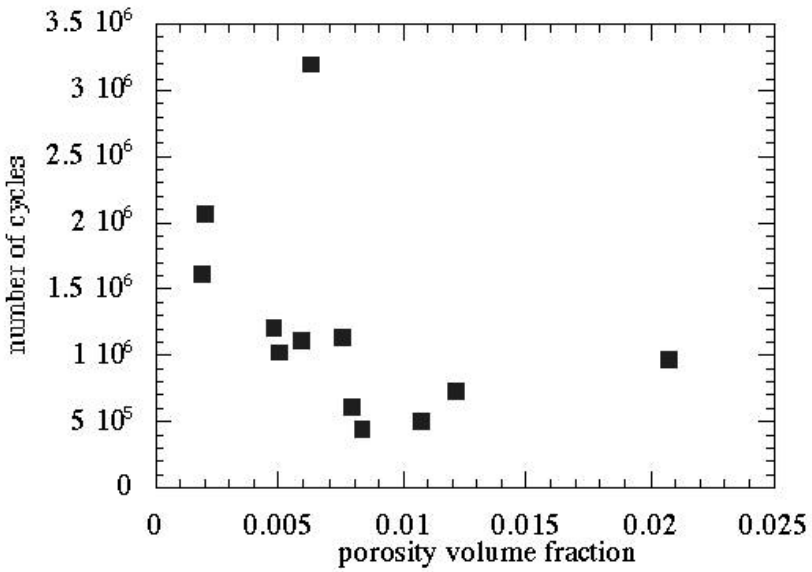

Figure 3.6. Number of cycles versus porosity volume fraction at different dendrite cell sizes for the vertically cast plate at a strain amplitude of $\Delta E/2$=.0015.

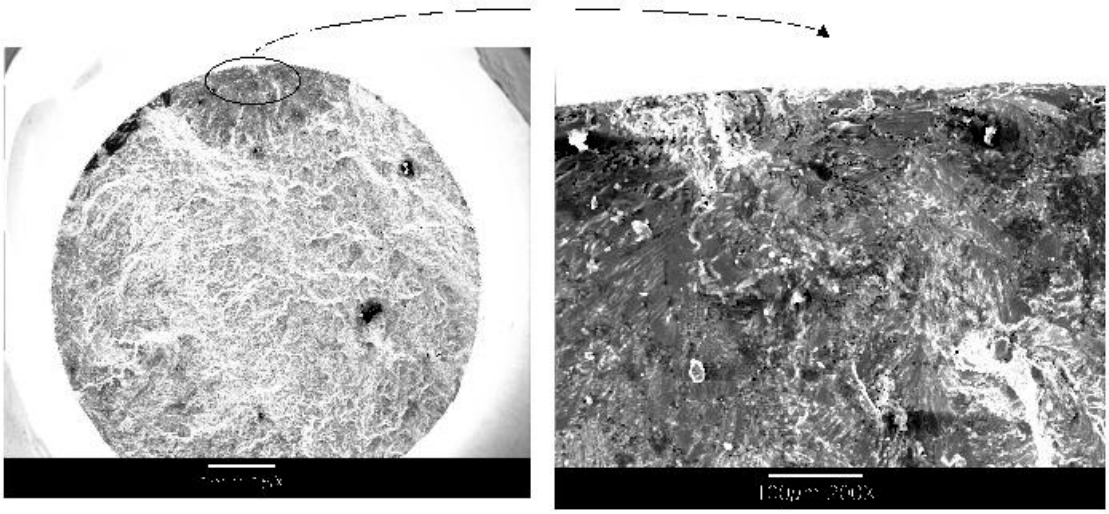

(a) (b)

Figure 3.7. SEM pictures at (a) 15 x and (b) 200 x of specimen tested under uniaxial fatigue at a strain amplitude of 0.0015 with an R-ratio of -1. This specimen ran for 1.7×10^6 cycles illustrating the longevity of life when nothing larger than a micron was observed at the nucleation site.

Figures 3.7-3.9 illustrate the different microstructural features affect the fatigue life. Fatigue striations were observed locally near the inclusions in Figures 3.7-3.9, but after a certain distance, differences arose in the samples with different inclusion types. For example, the specimens in Figures 3.7-3.8 experienced fatigue striations to a fairly large distance in comparison to the specimen in Figure 3.9, which had a larger volume fraction of porosity. On the fracture surface of the specimen in Figure 3.9, we observed that fatigue cracks grew from the pores, and then they coalesced in a ductile fashion. Figure 3.10 shows a close-up of Figure 3.9. The pores designated by "a" and "b" in the pictures signify the same pores. In Figure 3.10, two regions are marked to show the change in mechanisms. Figure 3.10b is a secondary electron image (SEI) at higher magnification to illustrate the fatigue striations near the pore. Figure 3.10b shows a region between two pores illustrating the ductile region where voids and broken silicon particles are observed.

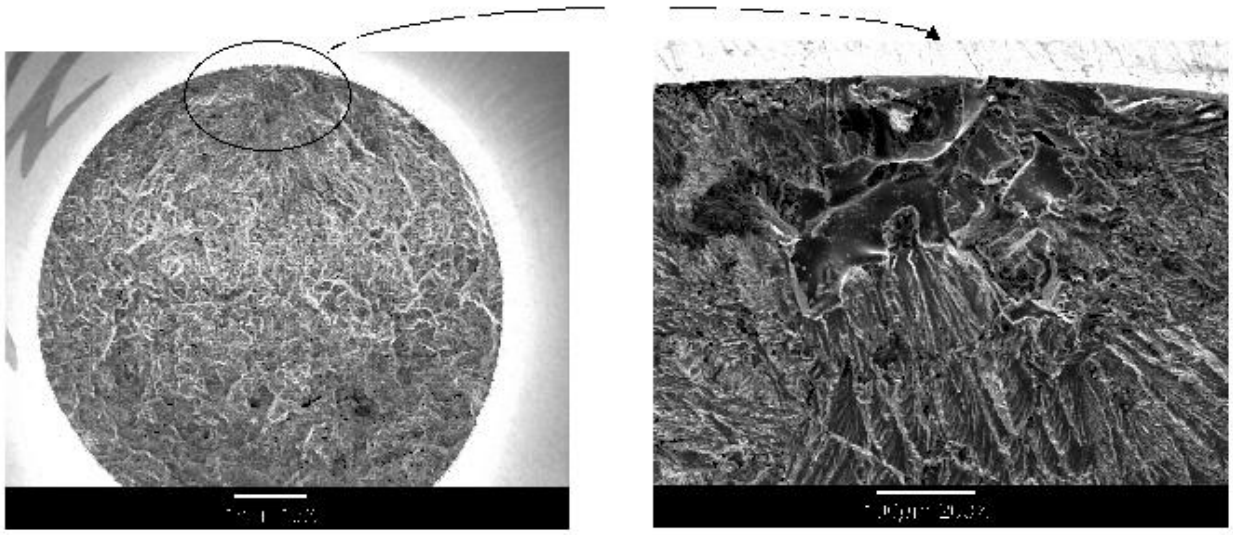

Figure 3.8. SEM pictures at (a) 15 x and (b) 200 x of specimen tested under uniaxial fatigue at a strain amplitude of 0.0015 with an R-ratio of -1. This specimen ran for 2.05x10^4 cycles illustrating the degrading effect of the 150 micron size casting pore.

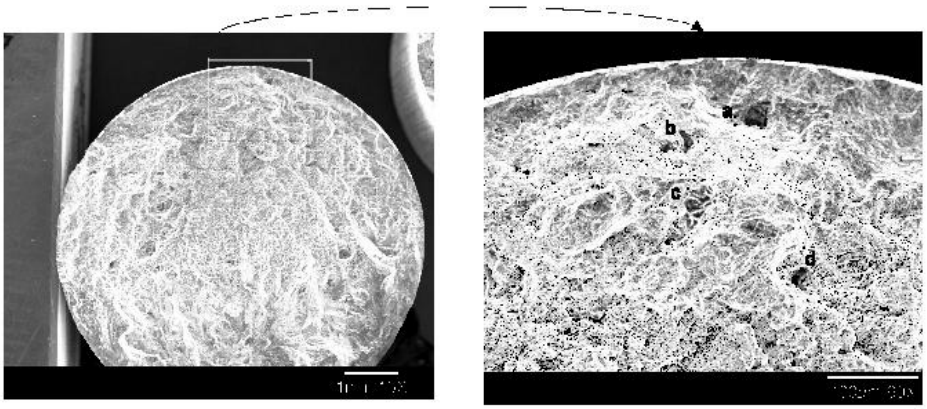

Figure 3.9. SEM pictures at (a) 15 x and (b) 200 x of specimen tested under uniaxial fatigue at a strain amplitude of 0.0015 with an R-ratio of -1. This specimen ran for 51,000 cycles illustrating the degrading effect of the 100 micron size casting pore.

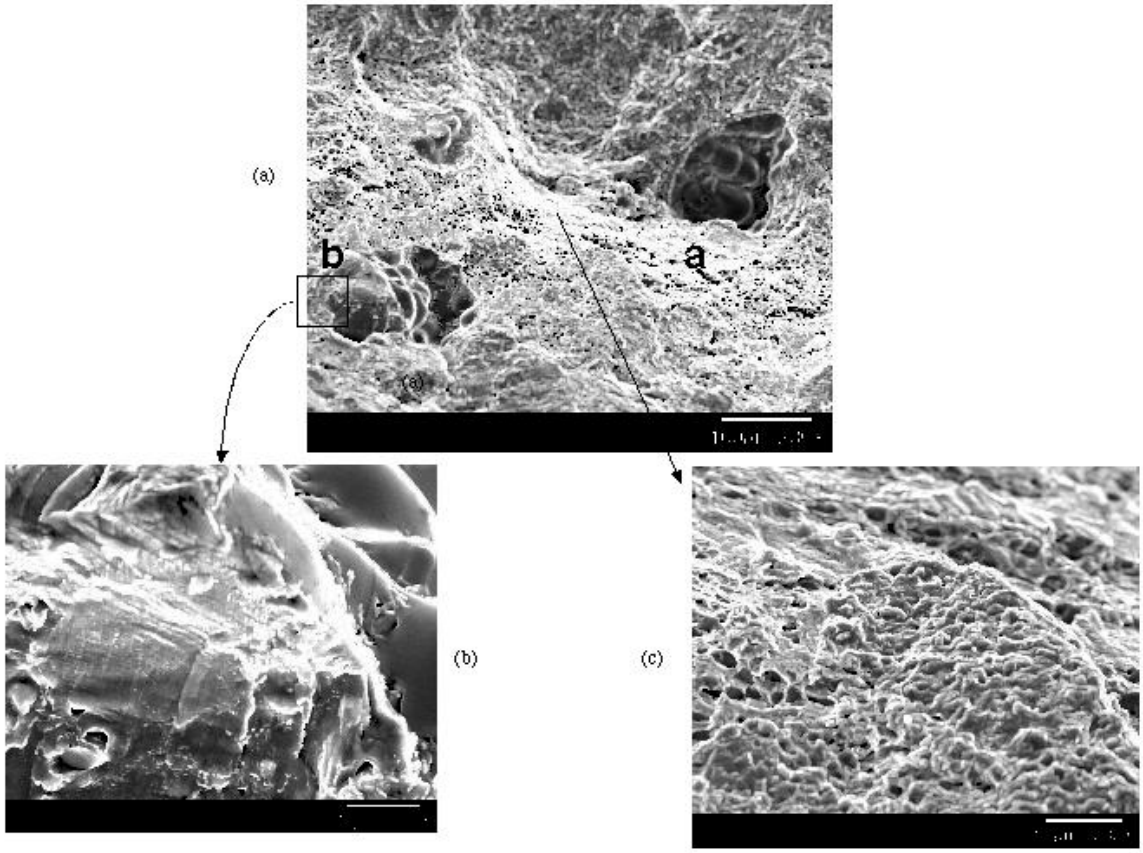

Figure 3.10. SEM pictures at (a) 200x, (b) 2000x, and (c) 1000x of a specimen tested under uniaxial fatigue at a strain amplitude of 0.0015 with an R-ratio o f -1. These images are zoomed in from Figure 3.9.

Table 3.3 summarizes the results from the uniaxial fatigue experiments in which each fracture surface was analyzed with SEM in order to quantify the initiation sites for damage. Parameters of interest were the inclusion type, inclusion size, distance of inclusion to free edge, volume fraction of porosity, and nearest neighbor distance. The number density of pores, volume fraction, and nearest neighbor distances were determined from regions within the bulk specimen from a metallographically polished cross section that were not directly related to the fracture surface. However, the other data in the table were indeed determined from the fracture surfaces. The nearest neighbor distance was calculated from the area of the cross section divided by the number of pores. When more than one pore was present, an average was taken to determine the pore (inclusion) size. An interesting observation can be made from these data. Major *et al.* (1994) have used the DCS as a metric to evaluate the fatigue life of this cast A356-T6 aluminum alloy. Interestingly, the porosity volume fraction maps directly with the DCS. It certainly may be true that the DCS is a length scale related to fatigue life, but it is clouded a bit by the direct link to the porosity volume fraction which is related to the number density of pores and nearest neighbor distances.

3.3. Long Crack Growth Experiments

Long crack growth experiments were performed at different R-ratios on the horizontally cast plates to determine the long crack behavior. The specimen dimensions were 7.62 cm x 1.27 cm with a notch length of 2.5 cm. Experiments were conducted at room temperature, with constant load amplitude in accordance with ASTM 647-95. The frequency was set at 10 Hz, and R-ratios ranged from 0.1, 0.5, 0.7. Pregrowth cracking and testing satisfied the requirements of ASTM E647-83.

The long crack region can be assumed to reflect the Paris Law (1963) relation and is given above threshold by

$$\frac{da}{dN} = C(\Delta K)^m \qquad \text{Equation 3.2}$$

in which a is the crack length, N is the number of cycles, ΔK is the stress intensity range, and C and m are material constants determined from long crack growth experiments. Because this generates a sigmoidal type of response, several regions exist. In the context of this cast A356 aluminum alloy, we examine Region I, where threshold effects are important, and Region 2, where stable long crack growth occurs according to Equation 3.2. Figure 3.11 schematically summarizes the regimes of the crack growth rate curves.

Table 3.3. SEM results from specimens that had experienced a constant strain fatigue amplitude (R=-1) from the vertically cast A356 plate.

DCS (μm)	Cycles	Strain (%)	Inclusion Type	Dist. to edge (μm)	Inclusion Size (μm)	Porosity vol. fraction	Nearest neighbor distance
60	33,603	0.25	2 pores	0	100	-	-
60	34,959	0.25	2 Pores	0	150	-	-
60	46,450	0.25	2 pores	0	150	-	-
60	53,166	0.25	3 pores	0	150	-	-
60	81,409	0.25	1 pore	0	100	-	-
60	30,400	0.25	14 pores	0	145	-	-
60	39,900	0.25	15 pores	0	260	-	-
60	38,000	0.25	15 pores	0	260	-	-
60	26,400	0.25	16 pores	0	325	-	-
35	30,368	0.25	1 Pore	20	40	-	-
35	87,747	0.25	1 pore, 1 oxide	0	175	-	-
35	89,285	0.25	1 oxide, 1 pore	0	150	-	-
35	90,700	0.25	1 thin oxide	0	20	-	-
35	59,600	0.25	35 pores	0	140	-	-
35	63,500	0.25	11 pores	0	200	-	-
35	73,700	0.25	16 pores	0	155	-	-
35	95,900	0.25	33 pores	0	150	-	-
20	56,329	0.25	1 oxide	100	90	-	-
20	86,245	0.25	1 oxide	300	75	-	-
20	107,712	0.25	1 oxide	0	80	-	-
20	38,400	0.25	14 pores	0	165	-	-
20	87,800	0.25	19 pores	0	125	-	-
20	42,000	0.25	15 pores	0	155	-	
60	241,401	0.15	1 pore	0	100	-	-
60	651,460	0.15	1 pore	0	170	-	-
60	983,387	0.15	3 pores	0	130	-	-
60	451,000	0.15	13 pores	0	265	0.0083	488
60	512,000	0.15	11 pores	0	255	0.0107	577
60	724,000	0.15	10 pores	0	250	0.0121	635
60	961,000	0.15	9 pores	0	240	0.0248	705
35	1,636,185	0.15	1 oxide	200	100	-	-
35	3,281,904	0.15	1 thin oxide	0	5	-	-
35	5,405,563	0.15	1 thin oxide	0	100	-	-
35	1,030,000	0.15	13 pores	0	140	0.005	488
35	1,120,000	0.15	17 pores	0	117	0.0059	373
35	1,140,000	0.15	12 pores	0	175	0.0075	529
35	6,140,000	0.15	17 pores	0	147	0.0075	373
20	205,032	0.15	1 pore	0	150	-	-
20	1,722,050	0.15	1 thin oxide	0	0	-	-
20	2,543,075	0.15	oxide	0	150	-	-
20	1,620,000	0.15	15 pores	0	108	0.0019	423
20	2,070,000	0.15	8 pores	0	90	0.0020	794
20	1,210,000	0.15	14 pores	0	124	0.0048	453
20	3,210,000	0.15	15 pores	0	96	0.0063	423

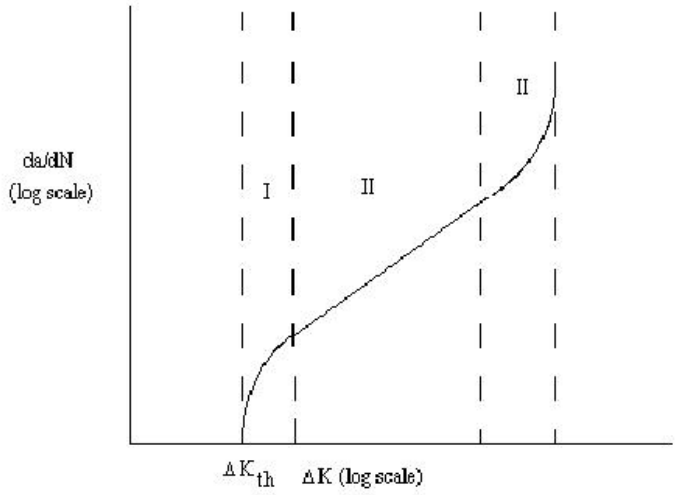

Figure 3.11. Schematic showing three regions of crack growth curve.

Table 3.4. Summary of the Paris Law parameters for the different R-ratios.

R-ratio	ΔK_{th}	C (m/cyc-MPa-$m^{0.5}$)$^{-m}$	m
A356 aluminum alloy			
0.1	-	3.2×10^{-12}	5.3
0.5	-	98.1×10^{-12}	4.3
0.7	-	165.5×10^{-12}	5.1
Al 1%Si alloy in dendritic region			
0.1	3.23	6.8×10^{-12}	4.9
0.5	3.06	45.1×10^{-12}	4.7

Figure 3.12 shows the long crack growth results for the horizontally cast A356 aluminum alloy and Al1%Si dendritic region. Although the coefficient to the Paris Law gradually increases with increasing R-ratio, the exponent essentially remains constant. Several replicates of each test were conducted and the values were averaged. The experimental results were fairly close so averaging was worthwhile. These results contrast those from Wigant and Stephens (1988).

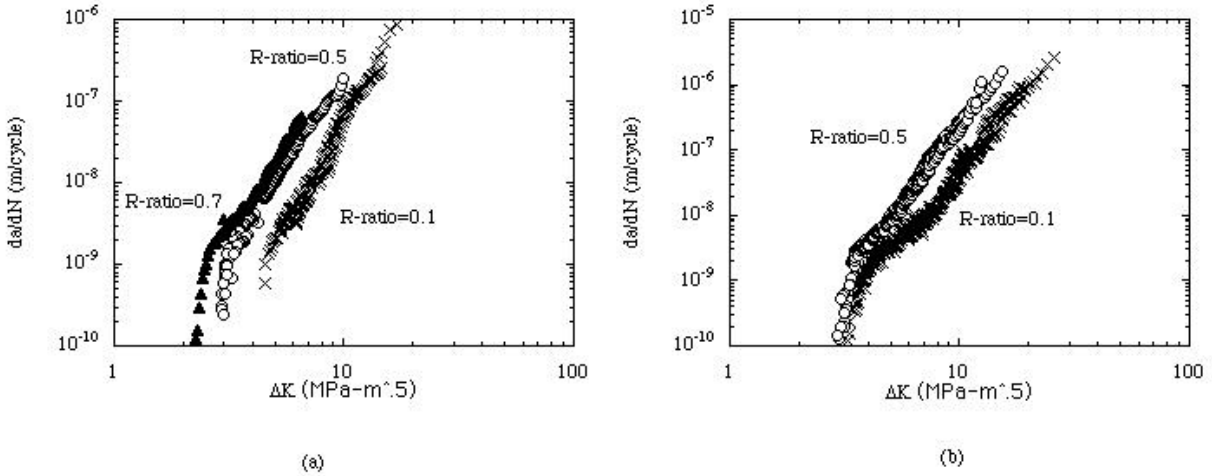

Figure 3.12. Long crack growth versus ΔK for horizontally cast (a) A356 aluminum alloy and (b) Al1%Si dendrites.

The Wigant and Stephens (1988) study only included results for A356-T6 alloy for R-ratios of 0.1 and 0.5. In their R-ratio experiments of 0.1, they noted a wide range of Paris Law coefficients, ranging from 1.5×10^{-20} to 8.6×10^{-17}. Note that these values are much lower than the values observed in this study. They also observed for the R-ratio experiments of 0.1, the Paris Law exponent varied from 8-11, a much broader range than those experienced in this study with a higher value as well. A similar broader range of results owing to microstructure/inclusion variation was observed in the Wigant and Stephens (1988) R-ratio experiments of 0.5 for the coefficient (2.2×10^{-15} to 1.2×10^{-12}) and the exponent (5 to 8.4).

Although Wigant and Stephens (1988) analyzed threshold values for A356-T6, we concerned ourselves only with the threshold values for the Al1%Si because of our modeling framework that examines crack incubation, MSC, and PSC crack regimes. The threshold values for the Al1%Si dendritic material is important for the small crack propagation analysis because the fatigue cracks mainly propagate through the aluminum early on in the fatigue life.

3.4. Multiaxial Cyclic Experiments

The stress states of automobile components are generally three dimensional. In design, however, fatigue data are frequently obtained from uniaxial cyclic experiments. To obtain information regarding the influence of stress state on fatigue life, we carried out fatigue experiments under multi-axial loading. One type of multi-axial fatigue experiment was conducted under completely

reversible cyclic axial-torsional loading of thin-walled tubular specimens, i.e., the maximum and minimum effective strains (Von Mises strain) are opposite in sign and equal in magnitude. These fatigue experiments were conducted under cyclic tension-compression, pure torsion, and under a combination of tension-compression and torsion. In the latter case, the non-proportionality parameter λ is taken as one. Here, λ is defined as $1.732\Delta\varepsilon/\Delta\gamma$ with $\Delta\varepsilon$ and $\Delta\gamma$ indicating the range of tensile-compression strain and shear strain. Figure 3.12 shows the experimental curves of fatigue life versus effective strain amplitude obtained for the three cases of completely reversible cyclic loading.

The results show that when the amplitude of effective applied strain (stress) varies from 0.2% (133 MPa) to 0.3% (188 MPa), the fatigue life varies from 4,000 to 100,000 cycles. For these relatively high stress amplitudes, there are distinct differences between fatigue life obtained for tension-compression, pure torsion, and their combination. However, when the effective strain (stress) amplitude is less than 0.2% (133 MPa), the difference between the three loading conditions is not obvious. This result indicates that using the fatigue data for uniaxial loading is reasonable for design of automobile components in high cycle fatigue under fully reversed cyclic loading conditions. On the other hand, one should be cautious in using uniaxial fatigue for designing components under low cycle fatigue conditions. From Figure 3.13, we see that above the strain amplitude of 0.25% the fatigue life for pure tension is smaller than for the case of a combination of torsion and tension-compression; and it is much smaller than for pure torsion. Therefore, the effects of stress state on the low cycle fatigue life is quite different from that arising under monotonic loading where pure torsion can cause more damage and lower strength than other stress states.

The other type of multi-axial fatigue experiment performed in our work was cyclic symmetric torsion under constant applied tensile stress conditions. This was designed to investigate effects of effective mean stress under multi-axial loading conditions. An increase in the constant tensile stress increased the effective mean stress. Figure 3.14 shows the experimental curve of fatigue life versus applied constant tensile stress for a completely reversible cyclic torsion with effective cyclic strain amplitude of 0.1%. The result indicates that fatigue life drops quickly when the tensile stress amplitude increases, indicating significant effects of the effective mean stress.

3.5 Mean Stress Effects

Various mean stress experiments were performed at different R-ratios on the horizontally cast A356 plates in order to provide more data beyond the fully reversed zero mean stress data. These tests were conducted under uniaxial tension-compression without torsion included. Cordes *et al.* (1988) provided some data for a cast A356 aluminum alloy and showed that the Smith-Watson-Topper (1970) approximates the results fairly well. In the long life regime, the Cordes *et al.* (1988) model gives unconservative estimations of the fatigue life. The data in the study as well as that from Cordes *et al.* (1988) was used for the development of the microstructure-property fatigue model discussed in Chapter 2 of this report.

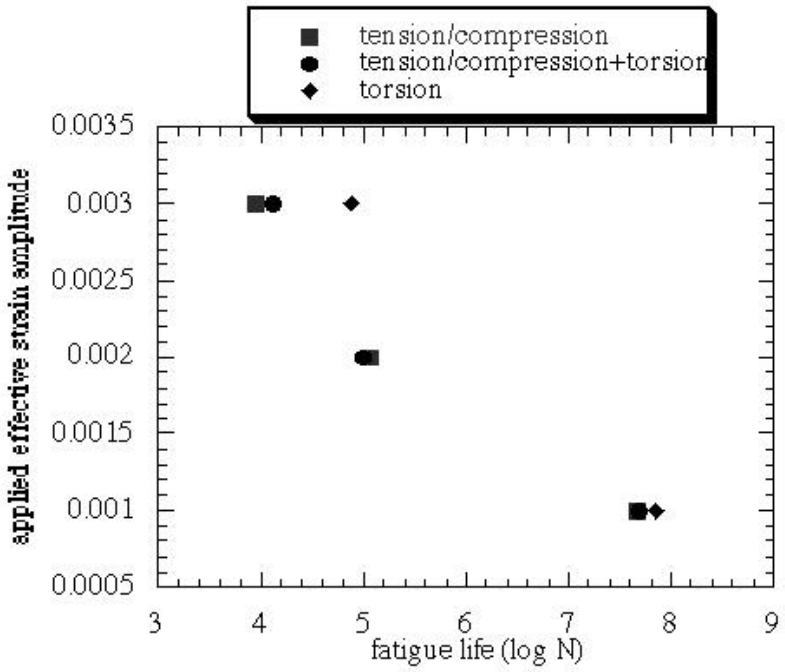

Figure 3.13. Experimental curves of fatigue life versus effective strain amplitude under a completely reversible cyclic loading of pure torsion, tension/compression, and tension/compression+torsion.

Figure 3.15 shows the deleterious effect that increased tensile mean stress has on the fatigue life of cast A356 aluminum. The mean stress levels used in these experiments included 34, 69, 103, and 207 MPa with the stress amplitude ranging from $\pm$ 48 to $\pm$103 MPa. This trend was similar to that observed by Cordes *et al.* (1988). As the tensile mean stress increases, silicon particle fracture and debonding will increase thus weakening the resistance of the material in fatigue. As such, the driving force for crack growth will increase thus reducing the fatigue life when compared to the case when no tensile mean stresses are present.

3.6 Sequence Effects

Besides mean stress effects, we also examined the effect of varying boundary condition sequences on the fatigue life of the horizontally cast A356 aluminum alloy. Different types of sequence effects were examined. In the first set, we examined the effects of overloads. Typically, in wrought materials, the application of overloads was observed to retard crack growth (cf. Schijve, 1960; Hudson and Hardrath, 1961; Hudson and Hardrath, 1963). The crack retardation is related to the plastic zone size that arises when the overload occurs. Some notions to explain the effect of crack retardation have been crack tip blunting, compressive residual stresses at the crack tip, and crack closure effects. Although crack closure somewhat occurs as explained in Chapter 4, the overloads actually degrade the fatigue life in this cast A356 aluminum alloy. Hence, the crack retardation that occurs in wrought metals does not seem to occur with this cast aluminum alloy.

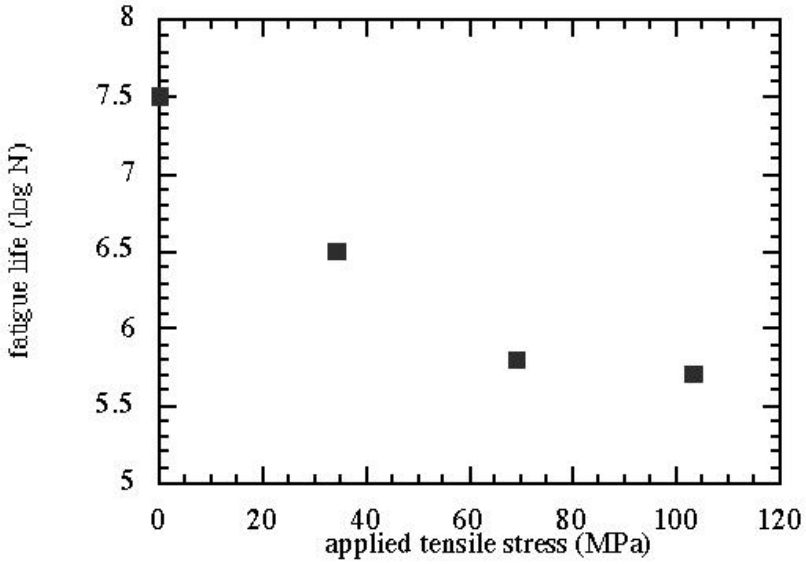

Figure 3.14. Experimental curves of fatigue life versus applied constant tensile stress under a completely reversible cyclic loading of torsion with an effective strain amplitude of 0.001.

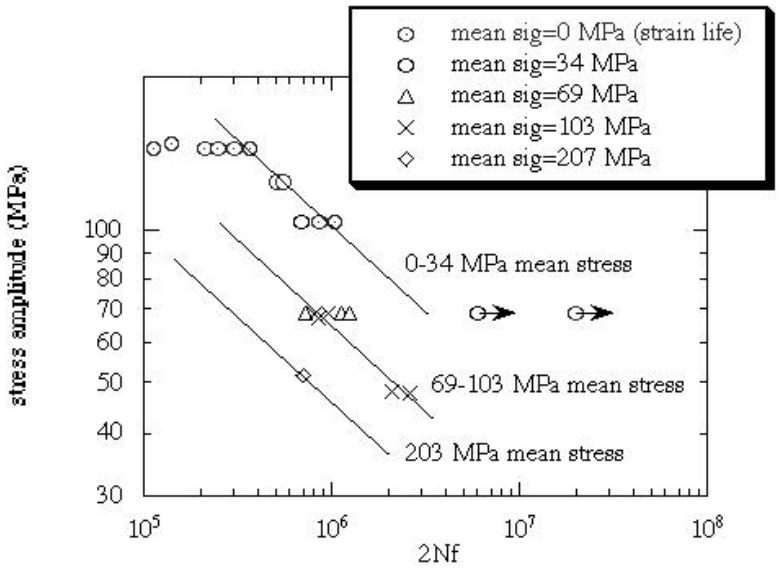

Figure 3.15. Stress amplitude versus reversals illustrating mean stress effects for horizontally cast A356 aluminum alloy

Figure 3.16 shows the stress amplitude versus number of reversals. Data in this figure comes from specimens that were tested at two different overload stress amplitudes (83 and 124 MPa) and applied at three different intervals (every 10, 100, and 1000 cycles) for a stress level of 83 MPa. Several trends can be observed from these data. First, as the frequency of the overload increased, the fatigue life decreased. This occurred for both overload amplitudes. Second, as the overload amplitude increased, the fatigue life decreased. Because both the amplitude and frequency affect the fatigue in an adverse manner, it is worthwhile describing the mechanism.

Every fracture surface of the overload specimens contained multiple fatigue crack nucleation sites that once they reached a certain size coalesced into a larger fatigue crack. Figure 3.17 shows a facture surface images of specimens tested to a stress amplitude of 83 MPa in which one specimen (a) was tested with no overloads and another specimen (b)-(c) which was tested with an overload of 207 MPa every 10 cycles. This figure illustrates that when no overload occurred, one fatigue crack initiation site was observed, but for an overloaded specimen, several fatigue crack initiation sites were observed. For this cast material, fatigue cracks can incubate and initiate at a number of different inclusion sites. However, in the absense of tensile overloads, one dominant fatigue crack may generally arise in the specimen if the porosity is a dilute concentration. When tensile overloads are present, the statistical chances of generating more fatigue cracks is greater because more silicon particles are fractured and debonded in the plastic zone near a crack tip. This fracturing and debonding of silicon weakens the resistance of the material and allows the separate cracks to grow in a distributed manner. This effect is opposite to wrought alloys because the second phase silicon is 7% of the total volume and is distributed everywhere. Other materials with weak second phases would also be expected to experience this same result.

In other sequence experiments, we ran uniaxial (strain-life) cyclic experiments to a certain number of cycles (100, 1000, 10000, and 100,000) and then conducted tensile experiments to examine the effect of fatigue degradation on the strain at failure. The cycling was performed at 0.2% strain amplitude at room temperature in accordance to ASTM E606-92. The tensile loading was performed under ASTM E8-96. Specimens were taken from the horizontally cast A356 plates. Table 3.5 summarizes the results of this study. We mention here that several replicates were used and the average values are included in Table 3.5.

Table 3.5. Summary of failure strain results from different initial pre-cycling.

number of pre-cycles	failure strain (averaged)
0	8.2%
100	7.2%
1000	7.1%
10,000	7.0%
100,000	5.0%

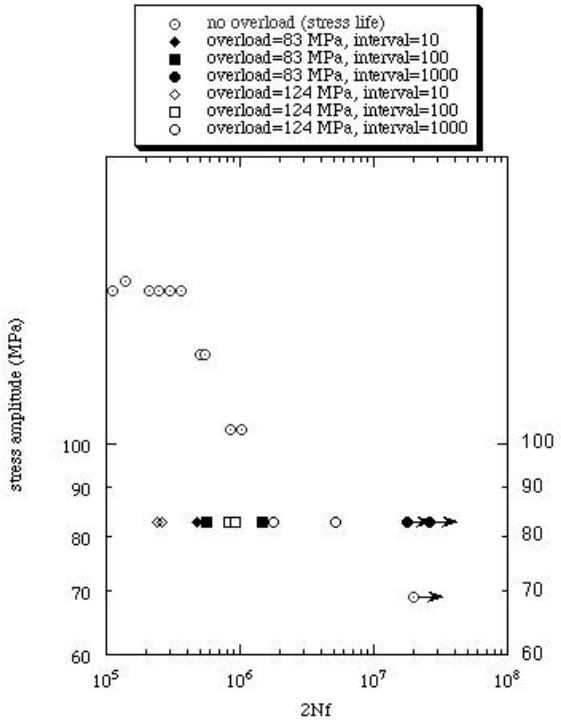

Figure 3.16. Stress amplitude versus number of reversals illustrating effect of tensile overloads.

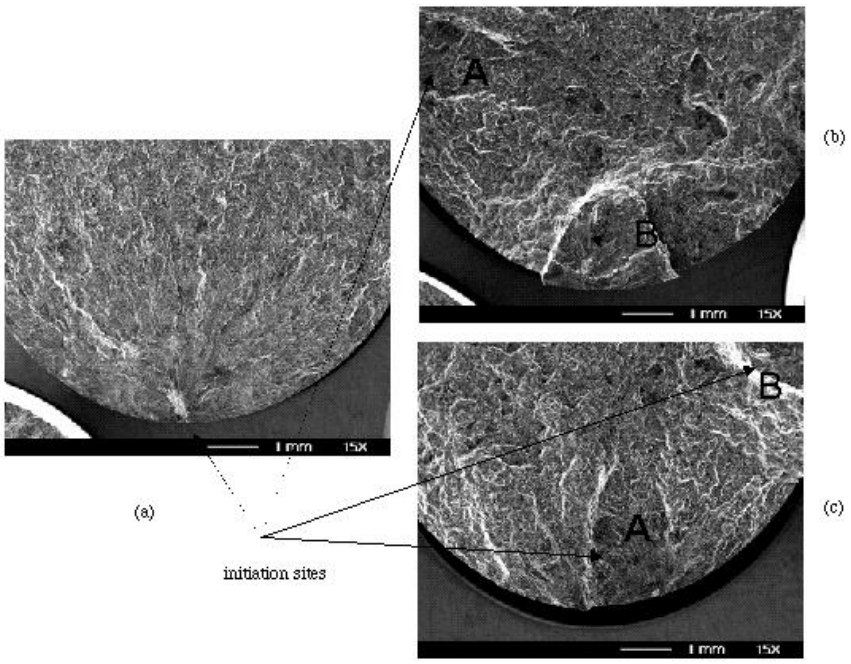

Figure 3.17. SEM images comparing fracture surfaces of specimens (a) with no overloads to those (b), (c) with overloads. Specimen (a) was tested at a constant stress amplitude of 83MPa and ran to almost 2.4e6 cycles. Specimen (b) and (c) are the same images from the same specimen rotated 90 degrees to illustrate the multiple nucleation sites for an overload stress of 207 MPa (amplitude=83 MPa) every 10 cycles. This specimen ran to 131,890 cycles.

For insight into the results summarized in Table 3.5, we should examine other data shown in Figure 3.18. Figure 3.18 shows the (a) number density and (b) area fraction of fractured and debonded particles as a function of number of cycles. As the first half cycle is loaded, some silicon particles are cracked and nucleated. This was also observed and described by Horstemeyer (2000) for monotonic loading. From one cycle up to approximately 30,000 cycles (for a strain amplitude of 0.2%), the number of damaged particles is constant, revealing that the dissipation of energy is not occurring in the breaking and debonding of the silicon, but in the development of fatigue cracks within the aluminum. However, at a certain number of cycles, approximately 30,000, the number of damaged particles increases dramatically. At this point, the driving force of the fatigue cracks is large enough to debond and fracture the silicon particles. This point may signify the transition from incubation to a MSC/PSC crack. At 100,000 cycles, the number of damaged particles was constant again, signifying a saturation of many cracks throughout the specimen. From Figure 3.18 the number of damaged particles that fractured and debonded remained constant from one cycle up to approximately 30,000 cycles and then an exponential growth was exhibited above that number of cycles. Because the tensile failure strain under monotonic loading is a function of void nucleation, growth, and coalescence, the tensile failure strain decreased once the number of cycles reached above 30,000 cycles in the pretests because more void/crack nucleation sites were present.

Another set of experiments included prestrain tension followed by cyclic fatigue. Specimens were strained to different strain amplitudes according to ASTM E8-96 and then fatigued according to ASTM E606-92. The results revealed a consistent trend with the mean stress data and the overload data. The prestrain amplitudes ranged from 1% (265 MPa) to 3% (290 MPa), and the corresponding minimum and maximum number of cycles ranged from 70,000 to 126,000. These quasistatic prestrains seem to have a much more deleterious affect on the fatigue life, as the mean stress experiment and overload experiment specimens reached greater fatigue lives by an order of magnitude more than these quasistatically prestrained experiments even though the peak stresses for the mean stress experiments reached 265 MPa (when adding the mean stress and amplitude) and the overload experiments reached 290 MPa (when adding the overload and amplitude).

3.7 MULTISTAGE FATIGUE MICROSTRUCTURAL ANALYSIS

In order to relate the microstructure/inclusion features to the cyclic fatigue response, we performed several types of post-test analyses on specimens under uniaxial conditions with and without mean stresses. Before we describe the results, we first summarize the methods of evaluation.

Fracture surfaces were examined with a scanning electron microscope (SEM) using either secondary electron imaging (SEI) or backscatter electron imaging (BEI). When information containing the spatial arrangement and area fraction of a particular phase was required, BEI was used. BEI differs from SEI in that the contrast depends on the atomic mass of the constituent elements of a particular phase. Because of this, phases comprised of higher atomic mass elements create more backscatter electrons and thus appear brighter on the SEM image. In the current material, iron has a much higher atomic weight versus aluminum or silicon thus it

appears brighter in BEI. Since aluminum and silicon have comparable atomic weights they appear similar in BEI. Consequently, the chemical compositions on the samples were measured using an energy dispersive x-ray (EDX) analysis. The EDX analysis is a semi-quantitative measurement of the relative composition of the area of interest. The EDX measurements are not used to characterize the exact composition of the alloy, but rather to approximate the relative differences in the area fraction of different phases between fractured samples and undeformed cross sections. In addition, x-ray mapping was used to determine the spatial arrangement of silicon particles on one particular fracture surface.

SEM was used on specimens that underwent various cycles at 0.2% applied strain in uniaxial conditions at room temperature (R= –1) to give us an idea of the progression of number of damaged silicon particles as the number of cycles increased. These damaged particle sites, though not directly identified as fatigue cracks, allow for an assessment of mechanisms and hopefully a definition of when the different stages of fatigue crack growth occur.

The results from Figure 3.18 directly tie in to other fracture surface analyses in which we examined the propagation of MSC/PSC and LCs. A fracture surface of the sample with the smallest fatigue crack nucleating inclusion was examined using the scanning electron microscope for a constant amplitude high cycle fatigue experiments (σ_{max}= 133 MPa, R = 0.1). For low crack tip driving forces (fatigue crack growth rates of da/dN < 1 x 10^{-7} m/cycle), we discovered that a small semi-circular surface fatigue crack propagated primarily through the Al-1%Si dendrite cells. The silicon particles in the eutectic remained intact and served as barriers at low fatigue crack propagation rates. When the semi-circular fatigue crack inevitably crossed the three-dimensional Al-Si eutectic network, it propagated primarily along the interface between the silicon particles and Al-1%Si matrix. Furthermore, nearly all of the silicon particles were progressively debonded by the fatigue cracks propagating at low rates, with exception to elongated particles with a major axis perpendicular to the crack plane, which were fractured. As the fatigue crack grew with a high crack tip driving force (fatigue crack growth rates of da/dN > 1 x 10^{-6} m/cycle), silicon particles ahead of the crack tip were fractured, and the crack subsequently propagated through the weakest distribution of pre-fractured particles in the Al-Si eutectic. Only small rounded silicon particles were observed to debond while the fatigue crack grew at high rates. Using fracture surface markings and fracture mechanics, a macroscopic measure of the maximum critical driving force between particle debonding versus fracture during fatigue crack growth was calculated as approximately $K_{max}^{tr} \approx 6.0\ MPa\sqrt{m}$ for the present cast A356 alloy.

Previous fatigue crack growth studies (Couper *et al.*, 1990; Plumtree and Schafer, 1986: Lee *et al.*, 1995) have qualitatively shown that silicon particles in cast Al-Si alloys have a tendency to debond or fracture depending on the crack tip driving force. However, such investigations have not outlined the microstructural and external conditions that promote particle debonding versus cracking during fatigue crack growth. Furthermore, many previous studies on cast Al-Si alloys have considered fatigue cracks growing from large microstructural inclusions such as casting porosity (Couper *et al.*, 1990: Ting and Lawrence, 1993) or in compact tension specimens with large initial crack sizes (Lee *et al.*, 1995). Such studies do not provide insight into the early stages of fatigue crack propagation when the overall crack size is on the order of several dendrite cells. In the present work, we quantitatively analyzed the transition driving force between crack

growth along the particle-matrix interface versus across a fractured particle. The foundation of the analysis is based on fracture surface observations of the conditions that promote particle fracture versus debonding over a varying range of crack lengths and crack tip driving forces.

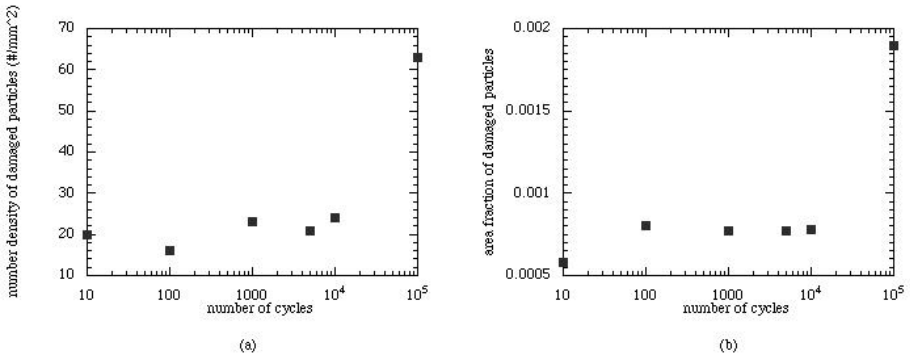

Figure 3.18. The (a) number density and (b) area fraction of fractured and debonded particles as a function of number of cycles Illustrates a trend in the different fatigue crack regimes.

A summary of the fatigue experiments on the cast A356 aluminum specimens is presented in Table 3.6. As shown in Table 3.6, the combined characteristics and overall size (fracture surface area) has a dramatic influence on the number of cycles required to create a crack of significant size (~ 1 mm) in the specimen.

Table 3.6. Crack nucleation site characteristics for constant amplitude fatigue test results (R=0.1) from horizontally cast plate.

ID#	# of Applied Cycles	Crack Nucleation Site Characteristics
5	9,369	Casting pore with major axis (900 μm) along specimen surface
14	49,420	Two near surface casting pores 200 μm apart from each other
8	142,755	Two near surface casting pores 300 μm apart from each other
10	157,569	Distributed casting porosity near specimen surface
11	331,629	Oxides near specimen surface

In general, the larger the inclusion, the smaller the fatigue life of the sample. In order to study the mechanisms of fatigue crack growth over a wide range of crack sizes, the specimen with the

smallest nucleation site (specimen number 11) was selected for further metallographic examination. Figure 3.19 is a SEM image of the overall fracture surface of specimen number 11. The fatigue crack nucleation site is located at the bottom of the fracture surface as indicated in Figure 3.19. The black curve in Figure 3.19 corresponds to the approximate position of the crack front along which the fracture surface demonstrates a noticeable change in the surface roughness. The semi-circular shape of the crack front is consistent with other observations on fatigue cracks growing in a solid circular cylinder (Mackay and Alperin, 1995). In a previous study on cast A356 aluminum (Gall *et al.*, 1999), it has been demonstrated that the increase in the surface roughness corresponds to a change in the fatigue crack growth path at the microstructural level. At low stress intensity ranges, the fatigue cracks grow primarily through the Al-1%Si dendrites, while at high ranges the cracks grow through the Al-Si eutectic regions and iron intermetallics, if present. In the aforementioned study (Gall *et al.*, 1999), this transition point was marked by a drastic increase in the area fraction of damaged iron intermetallics on the fracture surface. The present study will demonstrate that the transition from fatigue crack growth primarily through the Al-1%Si dendrites to growth primarily through the Al-Si eutectic is also accompanied by a change of the debonding and fracture characteristics of the Si particles.

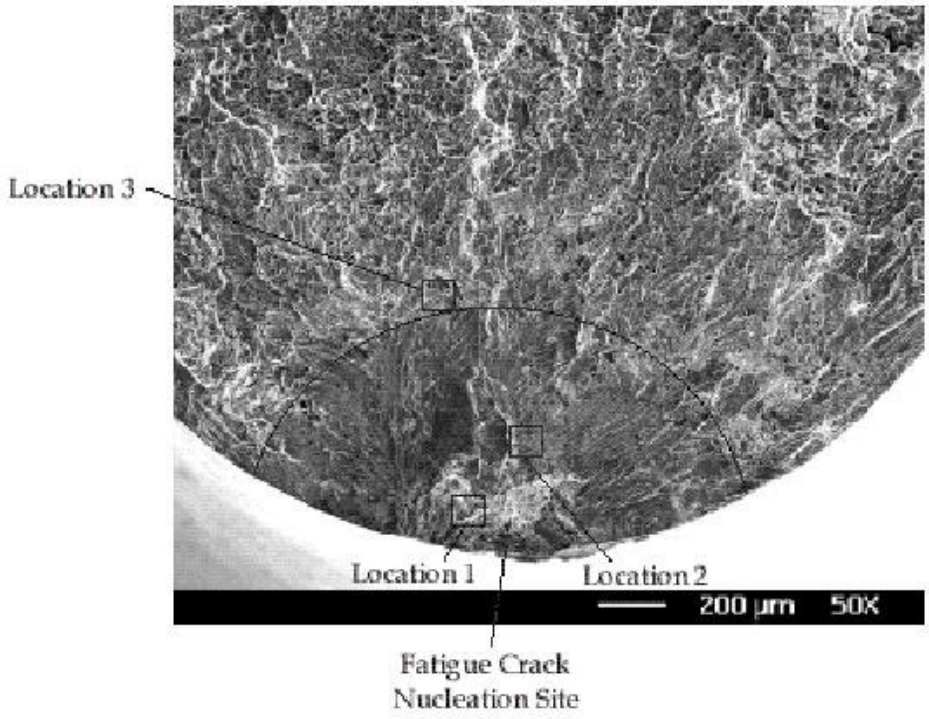

Figure 3.19. SEM image of the overall fatigue fracture surface on sample number 11.

A higher magnification image of the fatigue crack nucleation site is shown in Figure 3.20. A pair of aluminum and magnesium oxides at the specimen surface serves as the fatigue crack nucleation site in specimen number 11. The effective nucleation site is outlined with a black curve on Figure 3.20. As indicated in Figure 3.19, several representative locations were chosen on the fracture surface to elucidate the local fatigue crack growth mechanisms as influenced by

silicon particle fracture and debonding. Images from Locations 1, 2, and 3 are presented in Figures 3.21, 3.22, and 3.23, respectively. Figures 3.21 (a-c) are a series of SEM images of a fatigued region at a distance of 100 μm from the crack nucleation site (Location 1 in Figure 3.19). Although the crack passed primarily through the Al-1%Si dendrite cells very close to the nucleation site, the three dimensional nature of the dendrite cell structure evidently forced the crack to pass through some Al-Si eutectic regions. When the fatigue crack encountered silicon particles within the eutectic, the small crack primarily propagated along the interface between the silicon particles and the Al-1%Si matrix (Figure 3.21a). Crack growth along the interface between the two phases is asserted due to the extremely smooth and rounded surface of the exposed silicon particles at extremely high magnifications (Figure 3.21c). The apparently smooth Al-1%Si matrix material (Figure 3.21b) shows evidence of fatigue crack growth striations at higher magnifications (Figure 3.21c). The striations are extremely fine (less than 0.1 μm), indicating that the fatigue crack growth rate in the vicinity of the debonded particles is very low ($da/dN < 1 \times 10^{-7}$ m/cycle). Low growth rates for a fatigue crack indicate that the crack tip driving force, i.e. the stress intensity range, is also relatively small. It should be noted that the striation spacing was difficult to estimate due to the fine scale of the markings. However, striation spacing is certainly less than 0.1 μm.

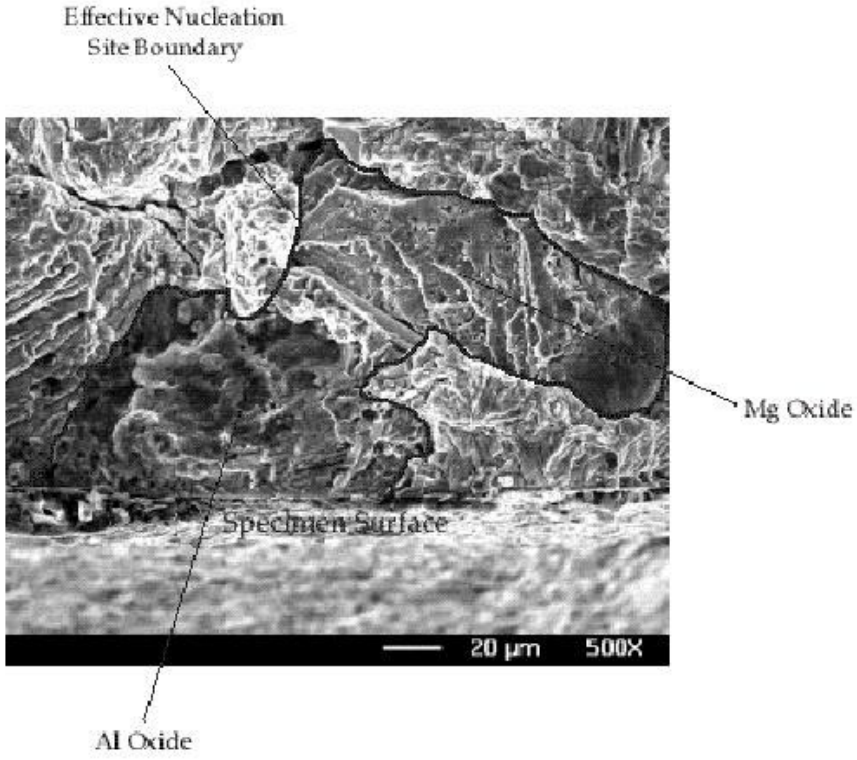

Figure 3.20. SEM image of the fatigue crack nucleation site.

The shapes of the debonded silicon particles on the fracture surface in Figure 3.21 provide insight into the operant fatigue mechanisms. Numerous elongated silicon particles were found on the fracture surface near the fatigue crack nucleation site. The extended (major) axis of the debonded elongated particles was always parallel to the fracture surface plane. Debonded

elongated particles with a major axis protruding out of the fracture surface were not observed. These observations indicate one of two mechanisms: (1) the fatigue crack evaded elongated particles with a major axis perpendicular to the crack plane, or (2) the fatigue crack fractured such particles even at low crack tip driving forces. Since there were a few fractured particles on the fracture surface within 100 μm of the nucleation site, and significant crack tip meandering was not evidenced near the debonded particles, the latter explanation is more plausible.

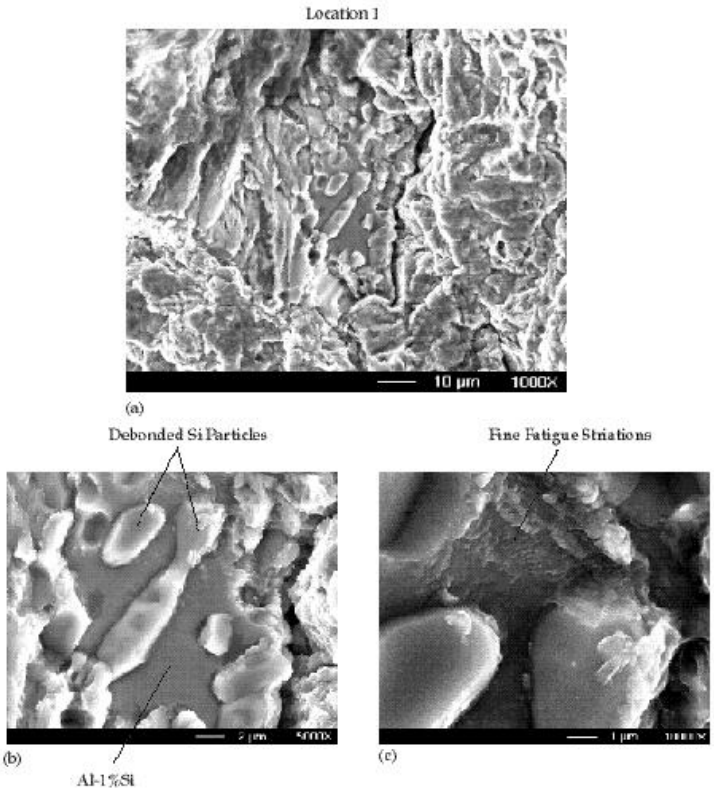

Figure 3.21. SEM image of particle debonding 100 μm from the crack nucleation site (Location 1).

As shown in Figure 3.22a, silicon particle debonding is still the dominant particle failure mechanism 300 μm away from the crack nucleation site (Location 2 in Figure 3.18). Similar to Location 1 near the nucleation site, fine fatigue striations surround the debonded particles (Figure 3.22b). However, the overall tolerance for the fracture of elongated particles with a major axis parallel to the crack plane decreases as the crack size increases (due to the constant amplitude experiment conditions, the maximum crack tip driving force also increases). In other words, the number density of fractured silicon particles on the fracture surface is larger at a greater distance from the nucleation site. For example, in the upper right corner of Figure 3.22a, several silicon particles are fractured rather than debonded. The increase in the number of fractured particles is partially due to a local difference in the crack tip driving force, i.e. the striations in the upper right corner are coarser than the striations near the center of the image. Small differences in the local crack tip driving force and growth rates are inevitable due to the three dimensional nature of the crack fronts and spatial distribution of microstructural features in a heterogeneous material. Nevertheless, when the fatigue crack passed through the eutectic near Location 2, it primarily propagated along the silicon particle and Al-1%Si matrix interface.

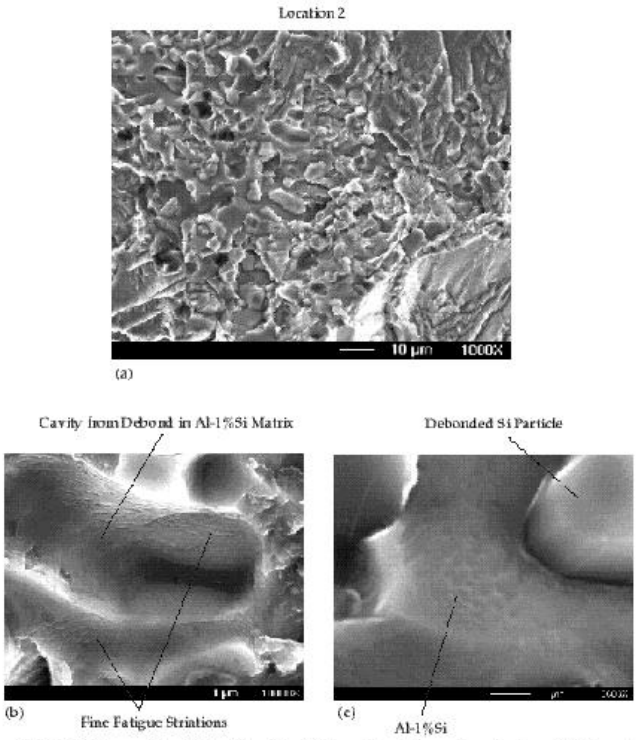

Figure 3.22. SEM image of particle debonding 300 µm from the crack nucleation site (Location 2).

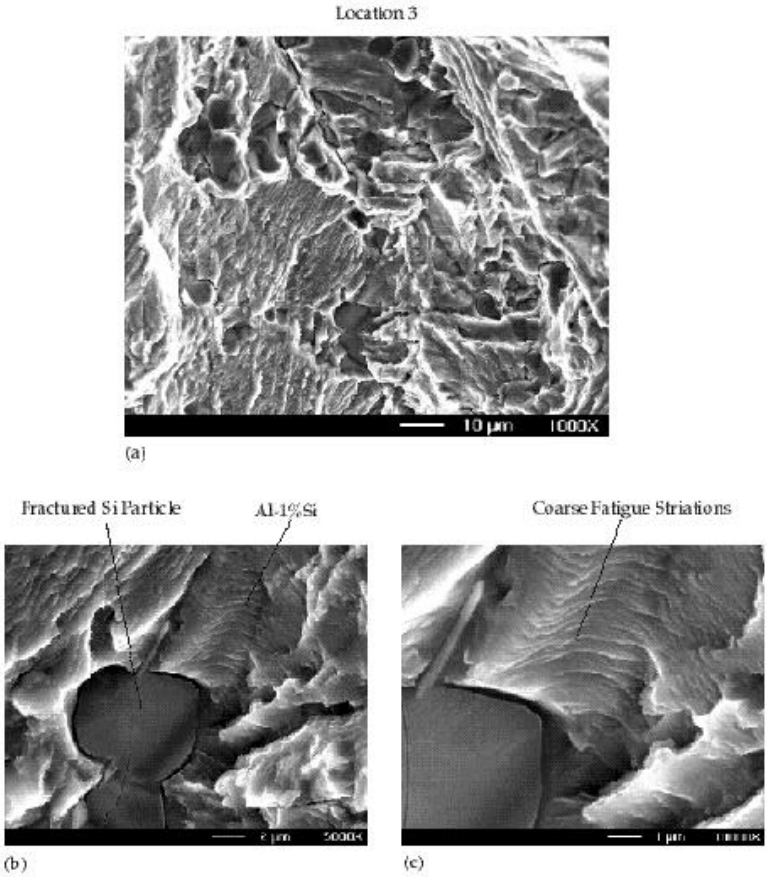

Figure 3.23. SEM image of particle debonding 800 µm from the crack nucleation site (Location 3).

Generally speaking, while the fatigue crack tip was within the black boundary line in Figure 3.19, the crack progressed along the interface between the silicon particles and the Al-1%Si matrix *when eutectic regions were encountered*. However, in an overall sense, the fatigue crack avoided the eutectic regions when it was within the boundary line. The dominant fatigue crack grew primarily straight through the Al-1%Si dendrite cells as evidenced by the large planar sections of Al-1%Si on the fracture surface. Furthermore, within the boundary line, fatigue striations were often observed on the surfaces of cavities that once contained silicon particles (Figure 3.22b). These fatigue striations indicate that debonding occurred gradually as a fatigue crack grew up to and around a silicon particle. Therefore, it can be asserted that the silicon particles retard the growth of the fatigue cracks at low crack tip driving forces since the cracks generally avoid the particles, and must grow around the particles when they are encountered. If the particles were debonding a significant distance away from the crack tip, then the debonded Al-Si eutectic regions would provide a weak material path for the fatigue cracks rather than a deflective one. Subsequently, the fatigue crack would be expected to propagate preferentially through the damaged eutectic region. However, the crack did not grow preferentially through the Al-Si eutectic at low crack tip driving forces within the boundary line.

Observations past the boundary line in Figure 3.19 (Location 3) show a significant change in the fatigue crack growth mechanisms (Figure 3.23). The overall area fraction of Al-Si eutectic (including damaged Si particles) on the fracture surface increases dramatically past this boundary line. On the microscale, the fatigue crack striations are coarser (about 1 μm) and the morphology of damaged silicon particles on the fracture surface changes. Comparing Figures 3.21b, 3.22b, and 3.23b, it is obvious that the striations just past the boundary line are much coarser than within the boundary. The increase in the spacing of the fatigue striations is consistent with an increase in the local crack tip driving force. When the fatigue crack propagates with an increased driving force and growth rate ($da/dN \sim 1 \times 10^{-6}$ m/cycle), nearly all of the silicon particles in the crack path are fractured (Figure 3.23a). Although both round and large irregular shaped particles (in the plane of the fracture surface) are cracked past the transition boundary, the abnormal number of irregular shaped particles indicates that a biased crack path is followed.

The fact that a fatigue crack growing with a large crack tip driving force is biased towards growth through irregular shaped silicon particles is consistent with observations during monotonic material failure (Dighe and Gokhale, 1997). The irregular shaped particles readily fracture since the local stress concentrations are higher than in rounded particles. Furthermore, in order for the crack to consistently locate fractured particles during growth, such particles must experience fracture before the crack tip reaches them. Fractured particles may also act as nucleation sites for microcracks, which increases the local driving force for the coalescence of fractured particle regions and the dominant crack. In other words, the crack will only meander, as evidenced by the rougher fatigue fracture surface, if there is a weak path for the fatigue crack to propagate through. The mechanism of local material weakening through silicon particle fracture at high fatigue crack tip driving forces is in contrast to the shielding mechanism offered by intact silicon particles at low crack tip driving forces.

We assert that the silicon particles have an explicit, discrete influence on the mechanisms of fatigue crack growth when the fatigue crack is small or has a low crack tip driving force. The present observations on cast aluminum alloys are consistent with previous findings on wrought alloy systems. During typical small fatigue crack growth (incubation, MSC, and PSC regimes in our terminology), microstructure plays an explicit role on the fatigue crack growth behavior for many classes of wrought engineering alloys (Pearson, 1975; Lankford, 1982; Lankford, 1985; Tanaka, 1989; Suresh, 1991; McClung et al, 1996). Furthermore, microstructure has an extremely dominant influence on cracks growing in the small crack regime that are very small with respect to pertinent microstructural features (microstructurally small cracks (Pearson, 1975; Lankford, 1982; Lankford, 1985; Tanaka, 1989; Suresh, 1991; McClung et al, 1996)). As the fatigue crack length and corresponding crack tip driving force increases, cracks are characterized as growing in the Long Crack regime. During Long Crack growth, the microstructure still affects fatigue crack growth, but the microstructural effect is accurately represented by overall material properties. The explicit influence of the microstructure at smaller crack lengths and crack tip driving forces is governed by the statistical nature of microstructural features in engineering alloys. The plastic zones of the small cracks simply cannot sample a statistically significant portion of the local microstructural features to represent a continuum. Consequently, average properties do not accurately represent the fatigue crack growth process for such cracks, and information on the influence of microstructural features is necessary to accurately predict fatigue crack growth. With this in mind, the present discussion focuses on mechanisms pertinent to small fatigue crack growth and the transition to Long Crack growth.

The SEM images of the fracture surface on the fatigued samples indicate two distinctly different growth mechanisms through the silicon rich Al-Si eutectic regions. Figure 3.24 schematically illustrates the dominant fatigue crack growth mechanisms that operate depending on the relative intensity of the maximum crack tip driving force. Figure 3.24 summarizes the mechanisms of fatigue crack growth through the Al-Si eutectic regions, not the Al-1%Si dendrites. At low crack tip driving forces, fatigue cracks propagate primarily along the interface between the silicon particles and the Al-1%Si matrix. Only elongated particles with the major axis perpendicular to the primary crack plane are fractured. Furthermore, the particles are gradually debonded as the fatigue cracks grow around the particles. At high crack tip driving forces, silicon particles fracture ahead of the crack tip, and the crack subsequently propagates through the damaged regions (Figure 3.24). Although some smaller particles may debond during this stage of fatigue crack growth, particle fracture is the dominant failure mechanism.

Essentially, we maintain that the transition between particle debonding and particle fracture is controlled by the extent of the crack tip cyclic plastic zone. A small fatigue crack with a low crack tip driving force (small plastic zone) only samples a fraction of a silicon particle, including the particle matrix interface ahead of the crack tip. Among possible particle failure modes, local debonding is the most probable since the small plastic zone at the crack tip cannot produce the elastic strain energy required to fracture the entire silicon particle. Conversely, for particle orientations where the major axis is perpendicular to the crack plane, the resistance to debonding is relatively high since a large area of the interface is parallel to the maximum principal stress field for a fatigue crack growing under Mode I loading conditions (McClung and Sehitoglu, 1989). In addition, numerical simulations show that the resistance to silicon particle fracture decreases as the major axis of a particle is parallel to a principal stress direction (Gall *et al.*,

1999). The counterbalancing effects of shape on fracture and debonding mechanisms promotes the fracture of silicon particles with a major axis perpendicular to the crack plane, even for a small crack tip plastic zone. When the fatigue crack becomes large enough, the crack tip cyclic plastic zone engulfs a representative set of particles and is capable of fracturing particles since the elastic strain energy released by particle fracture is less than the energy supplied by the crack tip. Although the silicon particles may not contain initial precracks *per se*, many of them have discontinuous shapes and local sharp corners. In single crystal silicon deformed at room temperature, such sharp notches lead to failure stresses significantly lower than in a pristine particle as predicted by modified fracture toughness criteria (Gall *et al.*, 1999).

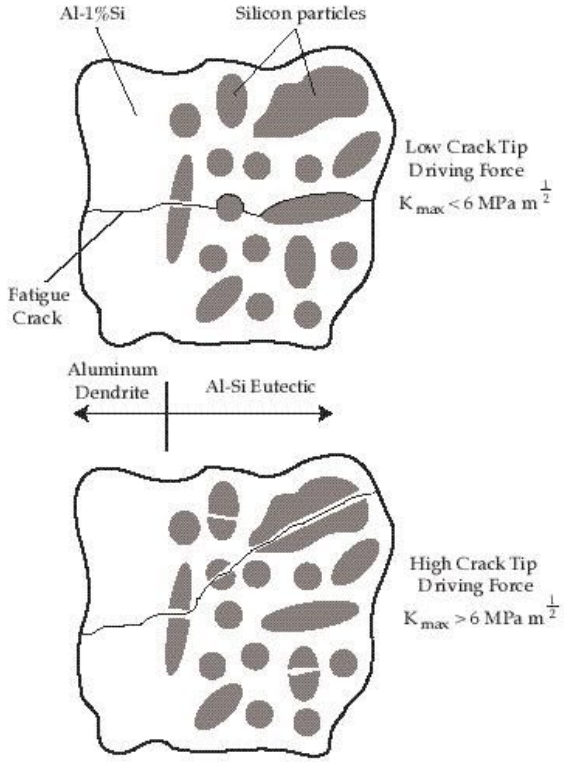

Figure 3.24. Schematic of the fatigue crack process through the silicon particle rich eutectic regions at low and high crack tip driving forces.

Due to the three dimensional nature of fatigue cracks coupled with the heterogeneity of this A356 aluminum alloy, crack growth mechanisms are never uniform along the periphery of a crack front. However, at the macroscale, a relatively abrupt transition between the two different growth mechanisms is observed. This transition point is accompanied by a dramatic increase in the roughness of the fracture surface, as marked by a black line in Figure 3.19. Given the two growth mechanisms outlined in Figure 3.24, an increase in the fracture surface roughness is expected as the fatigue cracks begin to follow paths dictated by the fracture of silicon particles in the Al-Si eutectic. The local crack tip driving force for fatigue is estimated using an effective stress intensity range, ΔK_{eff}. In the present study the maximum stress intensity value, K_{max}, will be calculated and used as the parameter governing the transition between growth patterns in the Al-Si eutectic. The K_{max} and ΔK_{eff} parameters both have potential advantages for analyzing the transition behavior. In general, ΔK_{eff} may better characterize the fatigue crack driving force; however, K_{max} may better characterize the propensity for the silicon particles to crack during

fatigue. Consequently, K_{max} will be used to quantify the transition point between growth through the silicon particles versus around them.

Using computational fracture mechanics, we estimated the value of the maximum applied stress intensity factor at the transition crack size between the two growth mechanisms (the black boundary line in Figure 3.19). Such an analysis provides an average critical value for crack growth through the silicon particles versus crack growth along the interface between the silicon particles and the Al-1%Si matrix. The general solution for the maximum crack tip driving force during fatigue is:

$$K_{max} = f(g)\sigma_{max}\sqrt{\pi a} \qquad \text{Equation 3.3}$$

where f(g) is a function of the specimen geometry and loading configuration, σ_{max} is the maximum applied stress during the fatigue experiment, and a is the crack length. For a round cylinder with a circular edge crack subjected to axial loading, the numerical solution for f(g) is given as (Liu, 1995):

$$f(g) = 0.67 - 1.24\frac{a}{d} + 28.0\left(\frac{a}{d}\right)^2 - 162.4\left(\frac{a}{d}\right)^3 + 472.2\left(\frac{a}{d}\right)^4 - 629.6\left(\frac{a}{d}\right)^5 + 326.1\left(\frac{a}{d}\right)^6 \qquad \text{Equation 3.4}$$

where a is the maximum crack length into the specimen, and d is the diameter of the cylindrical specimen. The values for the crack front marked in Figure 3.19 are: a = 0.75 mm, d = 3 mm, and $\sigma_{\mu\alpha\xi}$ = 133 MPa. From Equation 3.4, the geometry factor is calculated as f(g) = 0.88. Using the above numbers, the maximum stress intensity factor at the transition point is calculated as:

$$K_{max}^{tr} = 5.69 \approx 6.0 \ \text{MPa}\sqrt{\text{m}} \qquad \text{Equation 3.5}$$

The value of $K_{max}^{tr} \approx 6.0 \ \text{MPa}\sqrt{\text{m}}$ is slightly lower than previous calculations, for the same cast material, which gave a transition value of $K_{max}^{tr} \approx 7.0 \ \text{MPa}\sqrt{\text{m}}$ (Gall *et al.*, 1999), which relied on the increase in the area fraction of iron intermetallics on the fracture surface to estimate the transition point between growth through the Al-1%Si dendrite cells versus growth through the Al-Si eutectic regions. The difference between the two values is an indication of the error involved in choosing the crack front position using two different criteria (Figure 3.19).

We conclude that the fatigue cracks propagating with a maximum applied stress intensity lower than $6.0 \ \text{MPa}\sqrt{\text{m}}$ either avoid eutectic regions, weave around the silicon particles, or debond a few particles. Fatigue cracks propagating with maximum applied stress intensity above 6.0 $\text{MPa}\sqrt{\text{m}}$ can travel through eutectic regions and can fracture silicon particles. It should be noted that if the crack length is on the order of the mean silicon particle spacing, then a fatigue crack may debond silicon particles even if it is propagating with a maximum applied stress intensity above $6.0 \ \text{MPa}\sqrt{\text{m}}$. Even with a significantly large crack tip driving force, the extremely small fatigue crack cannot sample a statistically significant number of silicon

particles. Since we do not have definitive data, the transition value determined here cannot be used strictly to quantify the growth behavior of extremely small fatigue cracks. However, the present observations do help to qualitatively understand the growth of microstructurally small fatigue cracks, as will be discussed in closing.

Small fatigue cracks can nucleate from microporosity or damaged silicon particles in the eutectic (Plumtree and Schafer, 1986; Shiozawa *et. al*, 1997). Immediately after nucleation, such cracks are considered microstructurally small. Under typical high cycle fatigue loading conditions, the maximum crack tip driving force for microstructurally small cracks is well below the transition value of 6.0 $\mathrm{MPa}\sqrt{\mathrm{m}}$. Thus, during its propagation life, the microstructurally small cracks are unable to fracture silicon particles, and they are forced to grow along the particle-matrix interface. Consequently, during growth along the particle-matrix interface, the silicon particles should act as barriers to the growth of microstructurally short cracks. Experimental observations have shown that microstructurally small cracks exhibit a severe decrease in growth rates as they approach silicon particles; our micromechanical computations in Chapter 4 provide justification for this statement.

SEM images were used to examine three failed specimens cycled at strain amplitudes of 0.2%, 0.4%, and 0.8% to help determine the progression of fatigue cracks. Of the samples fatigued at different strain amplitudes, the fracture surface on the specimen cycled at 0.2% strain demonstrated the most obvious demarcation between a region that failed by progressive fatigue crack propagation and one that failed by local tensile overload. Figures 3.25a and 3.25b are low magnification images of the overall fracture surface on the samples cycled at 0.2% strain. Figure 3.25a was imaged using SEI while Figure 3.25b was imaged using BEI to reveal the area fraction and spatial distribution of the α intermetallics. On Figure 3.25b, the dark gray regions are Al-1%Si and the Al-Si eutectic, the bright particles are α intermetallics ($Al_{15}(Fe,Mn)_3Si_2$) and the black areas are valleys on the fracture surface. We note that Al_5FeSi or so-called α intermetallics are also common in the present alloy system (Samuel and Samuel, 1995).

The crack initiation site was identified as a horseshoe shaped aluminum oxide inclusion (confirmed with EDX) shown in Figure 3.26. Aluminum oxide inclusions trapped during solidification often serve as nucleation sites for shrinkage assisted gas porosity (Campbell, 1991; Tynelius et al, 1993). However, in this particular specimen machined from the casting, a casting pore surrounding the oxide inclusion was not present.

Although it is difficult to partition the growth of the crack into different regimes using Figure 3.25a, the backscatter SEM picture in Figure 3.25b more clearly identifies the transitions between different growth patterns. Black lines on Figure 3.25b are used to indicate the crack positions corresponding to macroscopic transitions in the fracture surface morphology. The curvatures of the crack paths were drawn to match approximate contours of constant area fraction of the α intermetallics. The positions of the crack paths were chosen where the area fraction of α intermetallics was the largest. Notably, the local fatigue mechanisms do not change abruptly at the distinct crack fronts, but rather undergo a gradual transition at a smaller length scale. However, since there are significant changes in the overall fracture surface appearance at low magnifications, the two crack fronts drawn in Figure 3.25b are meaningful from a macroscopic point of view. The different growth stages proposed within these regions are labeled

on Figure 3.25a (FCGR stands for Fatigue Crack Growth Rates). The justification for the labels in Figure 3.25b will now be discussed in detail using SEM and EDX results.

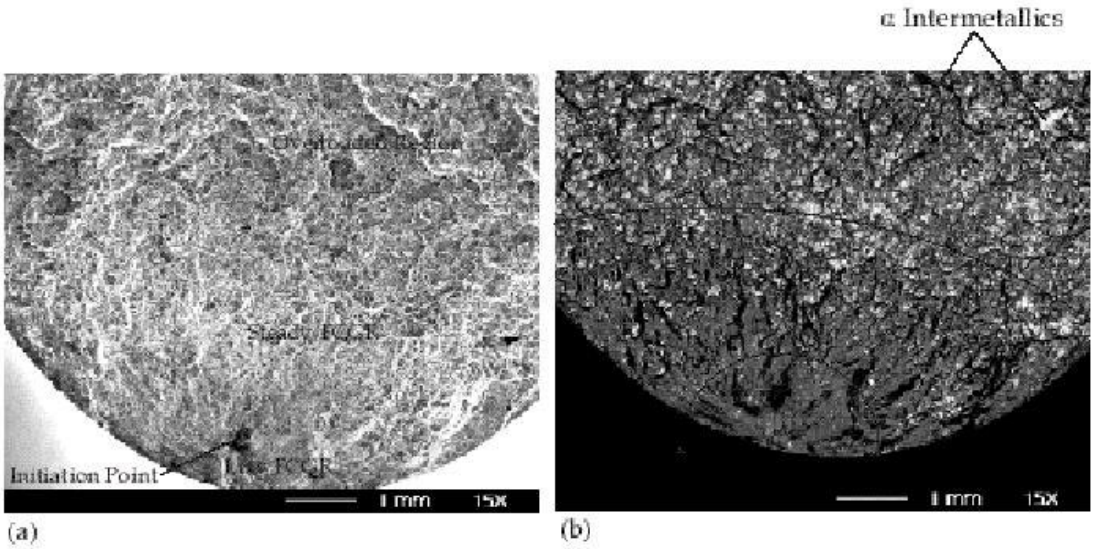

Figure 3.25. Low magnification SEM images of the overall fracture surface on the 0.2% sample taken in (a) secondary electron mode, (b) backscatter electron mode. FCGR stands for fatigue crack growth (specimen life ~ 150,000 cycles).

High magnification images in the low crack growth rate region reveal extended flat areas that are perpendicular to the loading axis (Figure 3.27a). The corresponding backscatter image to Figure 3.27a revealed that the area fraction of α intermetallics in the low crack growth rate region (Figure 3.27b) was only slightly higher than on the undeformed material cross section. At even higher magnifications, we found that the flat surfaces in Figure 3.27 were covered with fine fatigue striations (Figure 3.28a). In these regions, the very low volume fraction of silicon particles on the fracture surface, coupled with the overall planar appearance of the fracture surface, indicates that the fatigue cracks cut straight through the Al-1%Si dendrite cells and likely avoided particles in the eutectic region. Consequently, the cracks did encounter some α intermetallics, which are found randomly within the Al-1%Si dendrite cells (Figure 3.27b). When the crack encountered the α intermetallics, it propagated preferentially along or through them as evident from the slight increase in the area fraction. It should be noted that wherever the area fraction of damaged α intermetallics on the fracture surface was low, the corresponding area fraction of silicon particles was also relatively low. Thus, the α intermetallics served as reliable indicators for the overall silicon particle distribution on the fracture surface. The observations near the crack nucleation site in the 0.2% sample also hold true for the sample cycled at 0.4% strain as demonstrated in Figures 3.29a and 3.29b. The nucleation site in the 0.4% sample was also an oxide inclusion; however, the area of the fracture surface covered by fatigue striations in the Al-1%Si was smaller compared to the 0.2% sample. The sample cycled at 0.8% strain showed very little evidence of fatigue striations on the specimen fracture surface.

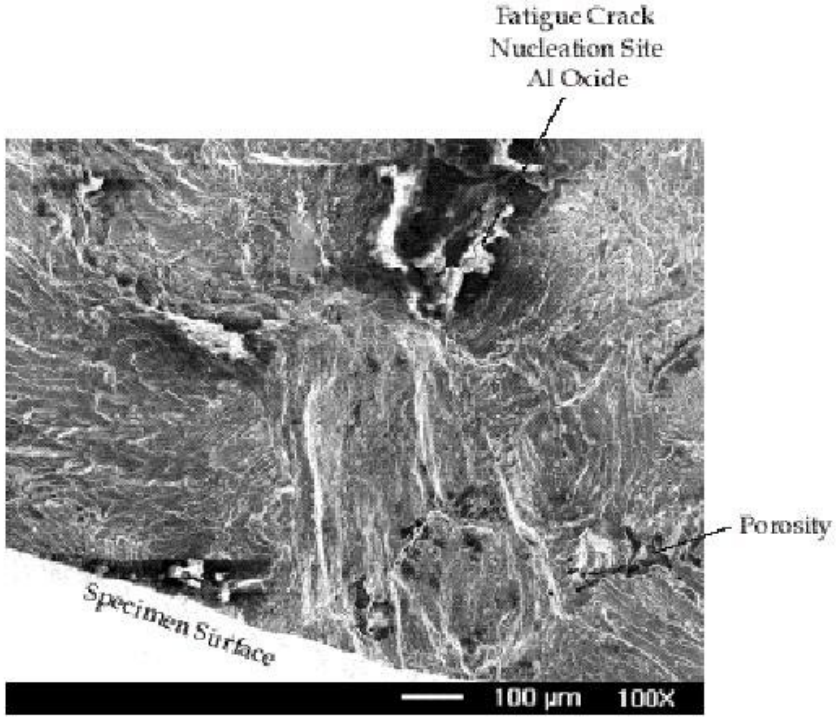

Figure 3.26. SEM image of the fatigue crack initiation point at an aluminum oxide inclusion in the sample cycled at 0.2 % strain.

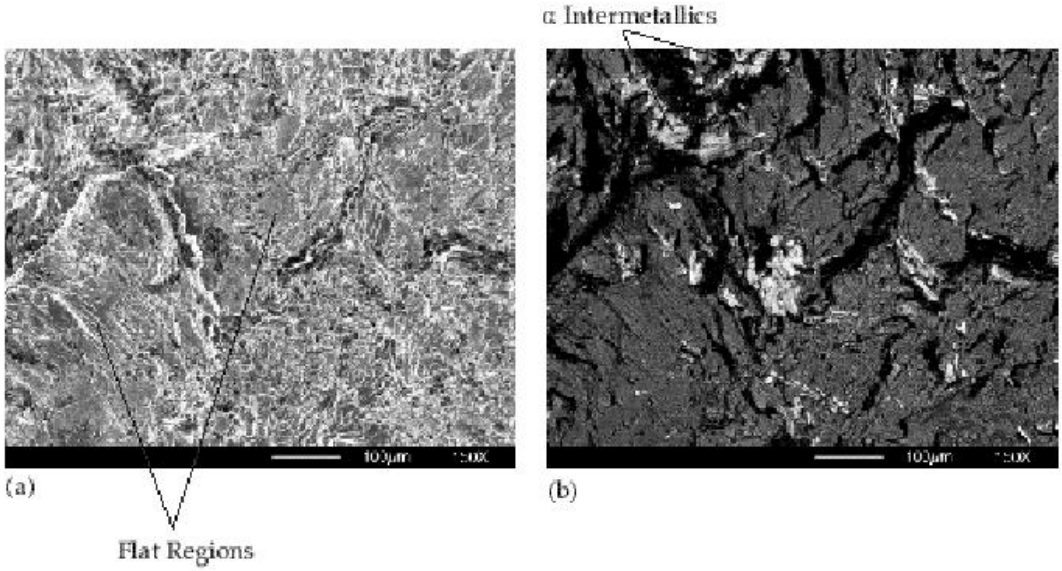

Figure 3.27. Intermediate magnification SEM images of the fracture surface on the 0.2% sample near the fatigue crack nucleation site taken in (a) secondary electron mode, (b) backscatter electron mode.

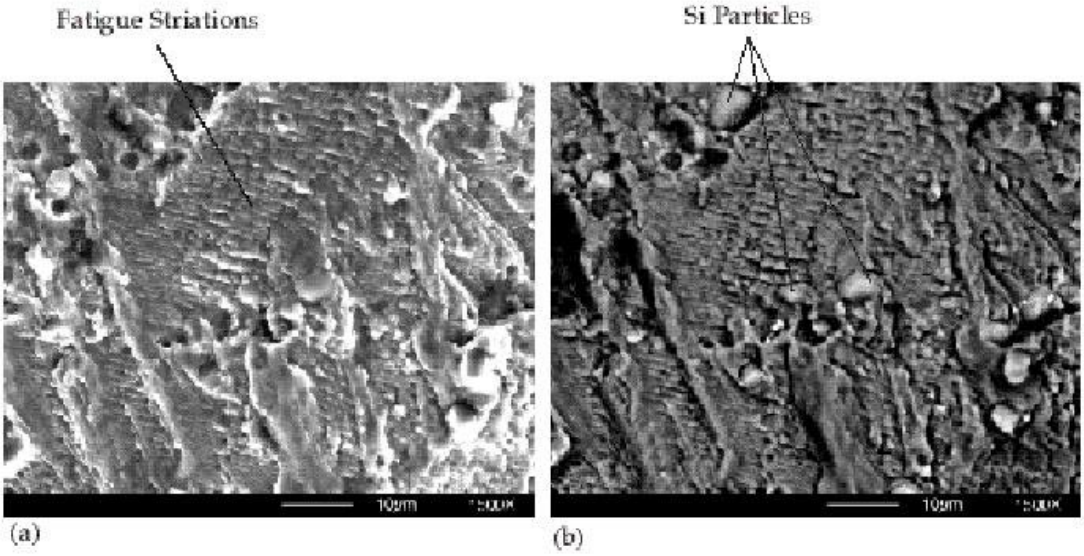

Figure 3.28. High magnification SEM images of the fracture surface on the 0.2% sample near the fatigue crack nucleation site taken in (a) secondary electron mode, (b) backscatter electron mode.

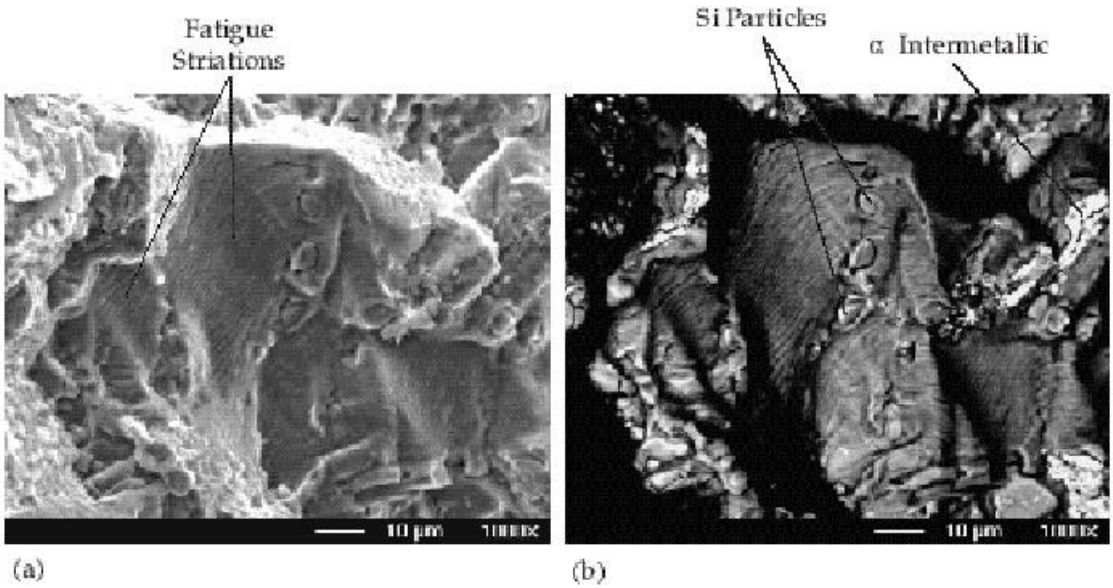

Figure 3.29. High magnification SEM images of the fracture surface on the 0.4% sample near the fatigue crack nucleation site taken in (a) secondary electron mode, (b) backscatter electron mode.

As the crack grows a significant distance from the initiation site, the local crack tip driving force increases since the maximum far field applied strain (stress) amplitude is kept constant. An increase in the local crack tip driving force results in higher fatigue crack growth rates. In the regime of steady crack growth rate, the area fraction of α intermetallics is notably higher compared to regimes where the cracks exhibited a low crack growth rate (Figure 3.25b). Furthermore, the gradual increase in local crack tip driving force is also accompanied by increases in the area fraction of damaged silicon particles during steady crack growth rate. The fatigue cracks exhibit instantaneous extension through the α intermetallics since the particles showed clear evidence of cleavage failure as will be shown in subsequent micrographs. Such a brittle phase is not capable of promoting crack tip blunting and resharpening, a mechanism required for the steady growth of fatigue cracks (Pelloux, 1969; Neumann, 1974). Consequently, the irregular shaped α intermetallics provide little or no resistance to fatigue crack propagation. The silicon particles in the eutectic provide more resistance to fatigue crack growth due to their dispersed and spheroidized nature within the ductile Al-1%Si phase.

When the crack tip driving force becomes large enough, the remainder of the specimen fails by tensile overload. Figures 3.30(a-c) are representative images taken from an overloaded region of the fracture surface on the specimen cycled at 0.8% strain. The fracture surfaces in the overloaded regions on the 0.4% and 0.2% specimens appeared identical to Figure 3.30. The overloaded regions (Figure 3.30a) consist of an even mixture of faceted and dimpled areas. To identify the phases corresponding to the different types of fracture, images of the region in Figure 3.30a were captured using backscattered electrons (Figure 3.30b) and x-ray mapping (Figure 3.31c). Figure 3.31b shows the distribution of α intermetallics (the bright areas) in a typical overloaded region. The area fraction of the α intermetallics on the overloaded fracture surface is significantly larger than in the undeformed material cross section, the low crack growth rate region, or the steady crack growth rate region. By comparing Figures 3.30a and 3.30b, one observes that the faceted regions correspond directly to fractured α intermetallic particles. Figure 3.30c highlights the distribution of silicon particles (the white specks) on the region of the fracture surface that failed through tensile overload. The area fraction of silicon particles on the overloaded fracture surface is also significantly larger than was found on an arbitrarily undeformed material cross section or the low crack growth rate regions. Higher magnification images of the different fractured phases in the overloaded regions are shown in Figures 3.31a and 3.31b. The α intermetallics demonstrate a very flat appearance on the fracture surface, which indicates that they fractured through cleavage. We observed that the α intermetallics demonstrated brittle fracture characteristics in both the fatigued and overloaded regions. The Al-Si eutectic regions are covered with dimples containing fractured silicon particles. Thus the eutectic regions failed primarily through particle cleavage and extensive ductile tearing.

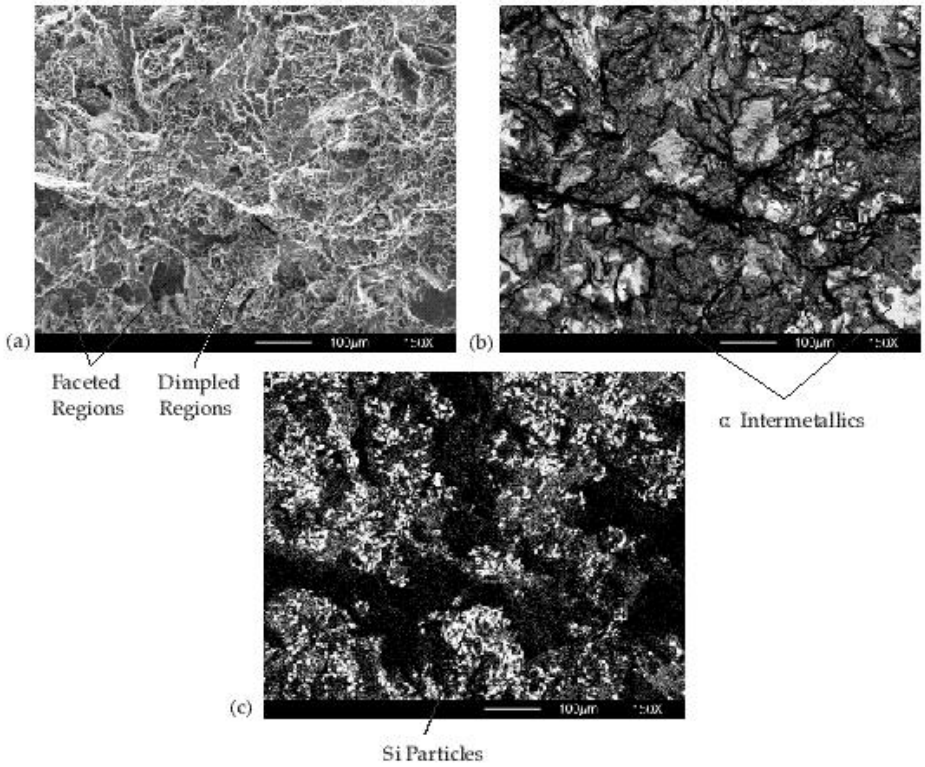

Figure 3.30. SEM images of the fracture surface on the 0.8% sample in a region that experienced tensile overload taken in (a) secondary electron mode, (b) backscatter electron mode, (c) x-ray mapping mode.

To confirm and better quantify the above observations, measurements of element concentrations were made on the fracture surfaces and the arbitrary undeformed material cross section. If a phase area fraction is relatively high on the fracture surface, it can be asserted that the particle provides a weak link for material failure, regardless of the local fracture mechanism. Measurements on the undeformed cross section provide a baseline comparison tool for EDX measurements on the fracture surfaces. Row 1 of Table 3.7 presents the measured elemental concentrations on the arbitrary undeformed material cross section for a sampling area of approximately 4 mm^2.

The measured Fe and Mn concentrations on the surface of the undeformed sample are less than 1.0%. The difference between this result and the nominal composition of the alloy is on the order of the experimental detection limitations (< 1%) of the EDX measurements. The silicon concentration on the undeformed sample surface is twice what is expected, and this is primarily due to the peak overlap between the aluminum and silicon spectra. The peak overlap will affect all semi-quantitative EDX calculations similarly, thus the relative differences in compositions between samples will still have comparative significance. Since all of the iron in the melt will readily form intermetallics (Kearney and Rooy, 1990), the area fraction of α particles, Al, and silicon particles expected on an arbitrary cross section can be calculated from the EDX data. The results of these calculations are shown in the shaded area of row 1 in Table 3.7.

Table 3.7. Average element concentrations on an arbitrary transverse cross section surface and the specimen fracture surfaces. EDX measurements are cumulative values taken at a magnification of 50x, covering large specimen areas. Area fraction calculations assume that the a particles have a $Al_{15}(Fe,Mn)_3Si_2$ composition.

	Measured Elemental Concentrations (at %)				Calculated Approximate Phase Area Fractions (%)		
Sample	Al	Si	Fe	Mn	Al-1%Si	Si Particles	a
Undeformed Arbitrary Cross Section	85.0	14.3	0.2	0.4	84.0	14.2	1.3
0.2 % Low FCGR Region	86.8	11.8	1.0	0.4	81.8	11.1	6.7
0.2 % Overloaded Region	67.8	25.1	4.9	2.2	43.3	21.8	32.7

On the sample cycled at 0.2% strain, EDX measurements were taken over $1mm^2$ areas in the "low FCGR" region and "overloaded region" indicated on Figure 3.21a. The last two rows in Table 3.7 present the results of the EDX measurements on the 0.2% sample's fracture surface. For calculations of the area fraction of different phases on the fracture surfaces, we assumed that all of the Fe forms the α intermetallic. The calculated phase area fractions on the respective fracture surface regions are shown in the shaded regions in Table 3.7. The area fractions found in row 2 of Table 3.7 are consistent with visual SEM observations in regions that failed through progressive fatigue failure on all specimens (0.2%, 0.4%, and 0.8%). The EDX measurements confirm that the fatigue cracks initially propagate straight through the Al-1%Si dendrite cells since the arbitrary material cross section and low FCGR region have comparable phase area fractions. Since the overall area fraction of the silicon phase decreases in the fatigued region, the fatigue cracks growing at low rates are effectively evading the modified silicon particles. Furthermore, the fatigue cracks growing at low rates must be avoiding the eutectic phases altogether since a larger volume fraction of silicon particles on the fracture surface would be observed if they cut through the tortuous network of silicon particles in the Al-Si eutectic. However, fatigue cracks are expected to propagate preferentially along the α intermetallics when the crack tip directly encounters them. This is evident from the slight increase in the area fraction of α in the EDX calculations (Table 3.7) and the fatigued fracture surface images.

The region that failed through tensile overload (Figure 3.25a) demonstrates a greater area fraction of α and silicon on the 0.2% fracture surface compared to the undeformed cross section (Table 3.7). The area fractions found in row 3 of Table 3.7 are consistent with SEM observations in regions that failed through tensile overloaded on all specimens (0.2%, 0.4%, and 0.8%). The increase of silicon on the fracture surface is undoubtedly due to preferential fracture through the Al-Si eutectic. The progression of fracture through the silicon particles in the eutectic under large strain monotonic loading (i.e. an overload) is consistent with previous observations on modified alloys (Murali *et al.*, 1997; Samuel and Samuel, 1995; Voigt and Bye, 1991; Dighe and Gokhale, 1997). However, the progression of fracture through the α intermetallics during a tensile overload has not received considerable attention. It has been previously observed that Fe intermetallics fracture during tensile loading (Voigt and Bye, 1991); however, it was not quantitatively demonstrated that they play such a dominant role as reported here. According to

the results presented in Table 3.7, the α intermetallics cover about one-third of the fracture surface in an overloaded region. Considering the fact that the area fraction of α intermetallics in the undeformed material cross section is about 1% (Table 3.7), this increase is remarkable. The fact that the α intermetallics appear this frequently on the overloaded fracture surface compared to a random cross section decisively identifies them as weak microstructural links for damage progression during an overload. In unmodified cast Al-Si alloys, the large volume fraction of coarse silicon particles in the eutectic controls the ductility of the alloy (Voigt and Bye, 1991). However, in the present alloy, which contains an optimally modified silicon particle microstructure, the α intermetallics limit the macroscopic ductility of the material.

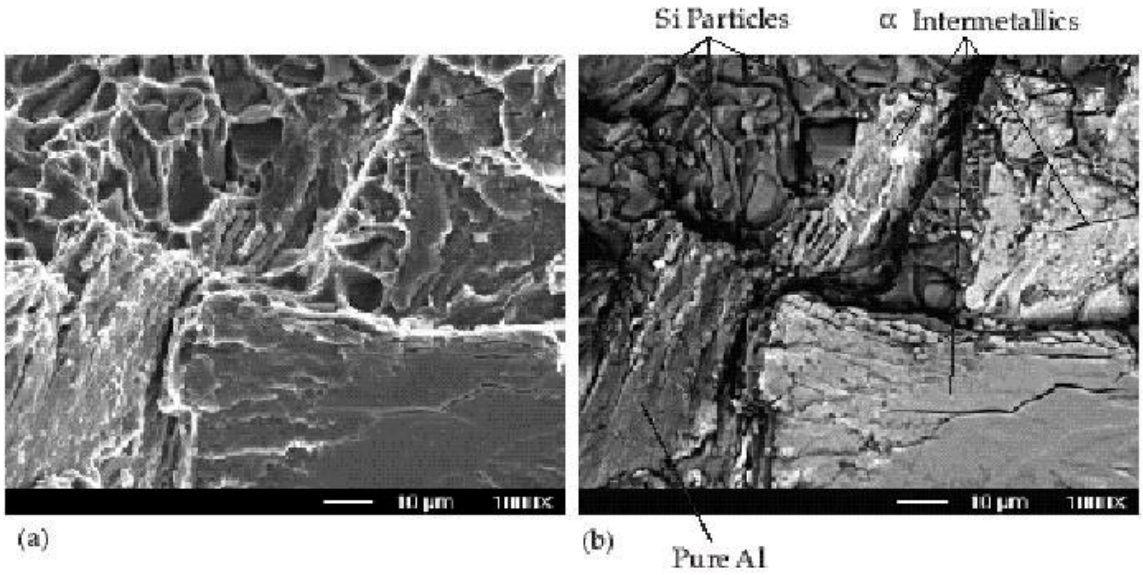

Figure 3.31. High magnification SEM images of the fracture surface on the 0.8% sample in a region that experienced tensile overload taken in (a) secondary electron mode, (b) backscatter electron mode.

Using the SEM and EDX results on the fatigued fracture surfaces as a guide, we can schematically detail the progression of fatigue damage in cast Al-Si alloys is presented in Figure 3.32. As previously reported, the most dominant fatigue crack is envisioned to nucleate from the largest microstructural inclusion such as an oxide inclusion or a casting pore near the specimen surface. The incubation period, as we have defined it, for the formation of such cracks in Al-Si alloys has not received much attention in the literature. A local strain approach for predicting fatigue crack nucleation life from large initial pores (average size of 500 μm) was utilized by Ting and Lawrence (1993) on cast A319 aluminum. For smaller initial inclusions (Si particles and pores ranging from 10 to 190 μm), Shiozawa *et al.* (1997) used a fracture mechanics based approach to predict the nucleation life of fatigue cracks. However, some uncertainty exists concerning inclusions that will control fatigue crack nucleation when the maximum pore size becomes less than approximately 100 μm. In the absence of large pores, it has been argued that

fatigue crack nucleation occurs from the largest silicon particles or clusters (Shiozawa *et al.*, 1997; Plumtree and Schafer, 1986). Gungor and Edwards (1993) observed that fatigue cracks initiate from micropores on the specimen surface on the order of 12 μm despite the fact that silicon particles as large as 15 μm were present. During high cycle fatigue, the time spent forming cracks near inclusions is critical since it will constitute a considerable fraction of the total fatigue life of premium cast Al-Si alloys.

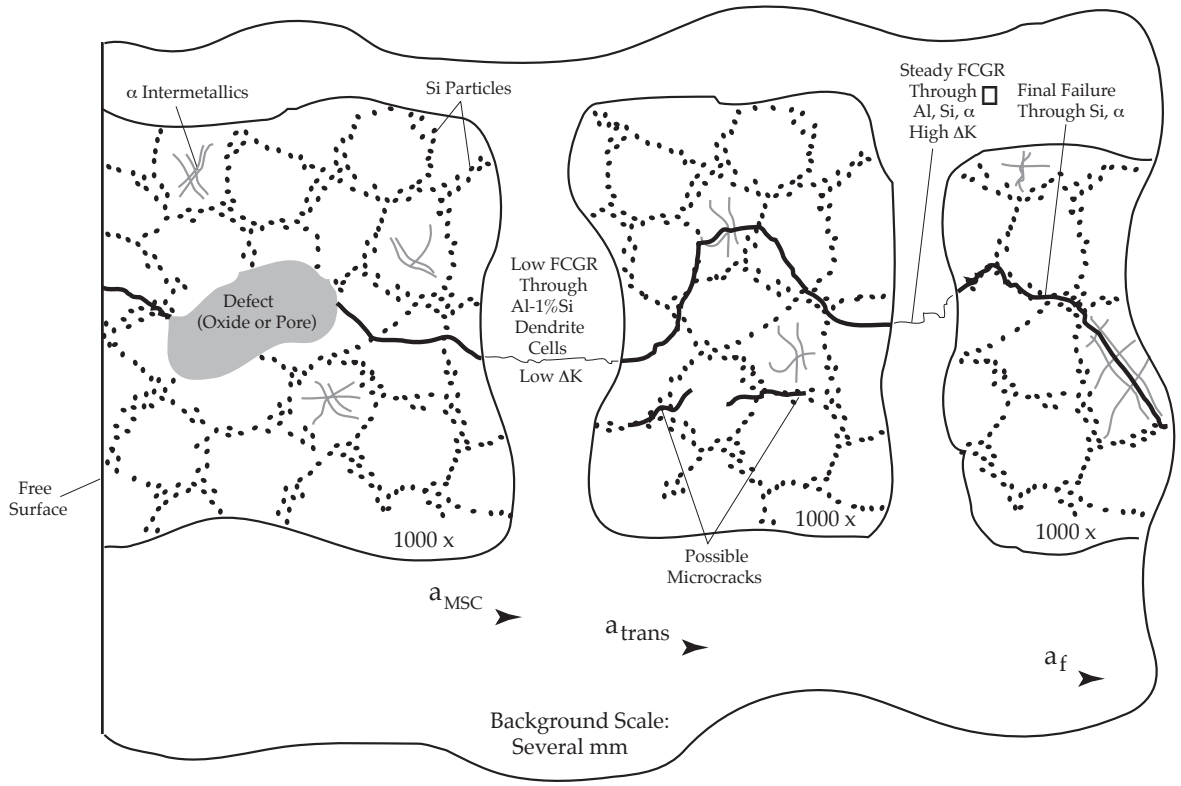

Figure 3.32. Schematic illustration of the crack paths and progression of fatigue damage in cast Al-Si alloys containing defects on the order of several dendrite cells.

After the crack incubation stage, cracks propagate towards the specimen surface and into the bulk material. A crack is considered microstructurally small if the crack length and crack tip plastic zone exist at the same length scale as pertinent microstructural features. The crack tip plastic zone is a region containing highly localized plasticity and relatively high triaxial stress levels. Research on low porosity squeeze cast Al-Si alloys has demonstrated that a crack experiences microstructural small growth rate effects if its length is on the order of several dendrite cell sizes and below (Gungor and Edwards, 1993). Therefore, if the initial inclusion size is larger than several dendrite cell sizes, the crack will, on average, be subjected to less variations of growth rate.

Even after the crack is no longer microstructurally small, it continues to propagate straight through the Al-1%Si dendrite cells (Figure 3.32). During this growth period, the local fracture surface is rather flat and perpendicular to the tensile axis even at the microscale. The advancing fatigue crack avoids silicon particles.

In summary, not all of these experimental details are required for inclusion in the macroscale microstructure-property fatigue model as presented in Chapter 2. For example, the effects of α intermetallics can be captured with the long crack equations in a phenomenological manner without directly incorporating them into the equations. However, other details such as the interactive effects of silicon, porosity, and dendrite cell size are deemed as first order attributes to the include in the model and have been as described in Chapter 2.

This page intentionally blank

4. MICROMECHANICS FATIGUE ANALYSIS

The fatigue life of A356 Al alloy is strongly dependent on casting inclusions and material microstructure, and establishing quantitative relationships of fatigue life with those inclusions and microstructural constituents is the purpose of this computational work. Since local cyclic plastic strain in the microstructure is essential in driving fatigue crack initiation, we concentrate on computational finite element studies at the microscale and present results in this chapter regarding the effects of applied stress amplitude, microstructure, and inclusion structure on the maximum plastic shear, $\Delta\gamma^{p^*}_{max,}$, for crack incubation and the cyclic crack tip opening displacement for MSC/PSC crack propagation. For the MSC/PSC crack propagation regimes, we analyzed the effects of particle shape, particle size, particle nearest neighbor dimension, particle distribution, dendrite cell size, pore size, pore shape, pore nearest neighbor distance, and pore distribution. In this context we examined such characteristics as crack driving force and crack closure behavior during fatigue crack growth in the MSC/PSC regime. These analyses are based on sophisticated constitutive laws with experimentally determined material constants for the Al 1% Si dendritic region and A356 Al alloy under cyclic loading. One final note is worth mentioning. The simulations were not performed in which the cracks had an evolving history but were semi-stationary in nature.

4.1. MICROMECHANICAL FEA PRELIMINARIES

Two very similar internal state variable plasticity material models were used for these micromechanical simulations. They are detailed in the appendix. To determine the material constants for the micromechanical material models, two cyclic stress-strain tests were conducted (experimental results were repeated). One is the cyclic test of A356 Al alloy, and the other is for the Al-1%Si dendritic region, which was used for the aluminum matrix between silicon particles as well. From the experimental stress-strain curves, the material constants and elastic constants are determined and listed in that appendix. Figures 4.1 and 4.2 compare the experimental cyclic stress/strain curves with the models. The material models were embedded into a UMAT, a user-defined subroutine in the ABAQUS finite element code (Hibbitt *et al.*, 1998).

The micromechanical finite element analyses (FEA) were conducted using a plane strain approximation. Figure 4.3 shows the definitions of notations used for particles and pores. All particles and pores are assumed to be ellipses; D_{max} and D_{min} are the maximum and minimum diameters of the ellipse. The size, D, of the particle or pore is defined as the average, i.e., $(D_{max}+ D_{min})/2$. Shape effects are described by the aspect ratio, D_{max}/D_{min}. The radius of curvature is considered by changing the local radius of the major axis of the ellipse in the pore analysis.

Figure 4.4 is a schematic of the geometry and boundary conditions for the finite element analyses related to incubation and MSC/PSC propagation. A completely reversed, uniaxial displacement was prescribed in all of the calculations in this chapter other than the ones that directly describe the mean stress effects. The area in the analysis is divided into two domains: the domain of effective homogeneous medium adjacent to the external boundary and the domain inside this region consisting of particles and the matrix. For the effective medium, macroscopic A356 properties are used. Considering the loading in the y-direction as an example, the bottom boundary is pin supported and can only move along the x-direction. For the left boundary, there are two cases: one is a free boundary, and the other permits motion along the y-direction. The

former case is used for investigating pores near the free surface. The latter case is used for the effects of particle clusters, using the symmetry of the boundary to reduce the number of elements.

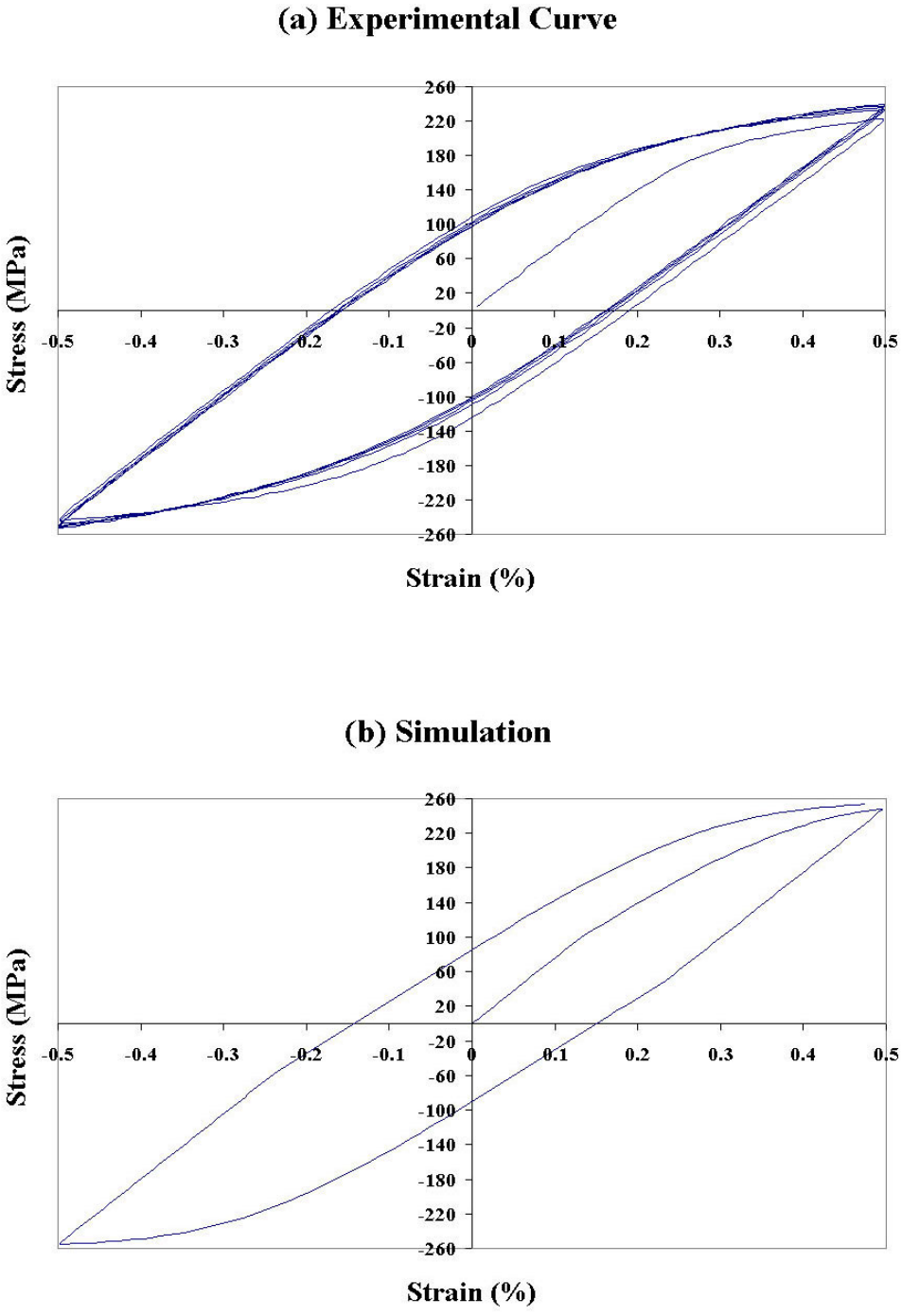

Figure 4.1. A comparison of stress/strain curves for A356 Al alloy showing the cyclic experimental data and the simulation curve using the obtained material constants: (a) experimental curve, (b) simulation.

In most cases, four-node bilinear plane strain quadrilateral elements are used. For a realistic microstructure, three-node linear elements are also used to enhance mesh smoothness. In some cases, mixed meshes are also used; in the effective medium, four-node quadrilateral elements are used, and in the region of detailed analysis, three-node elements are used. Boundary displacements are prescribed. In the y-direction along the top boundary, cyclic displacement is applied while the bottom boundary is held fixed. In general, the boundary region far removed from any microstructure to alleviate extraneous boundary effects in the solutions.

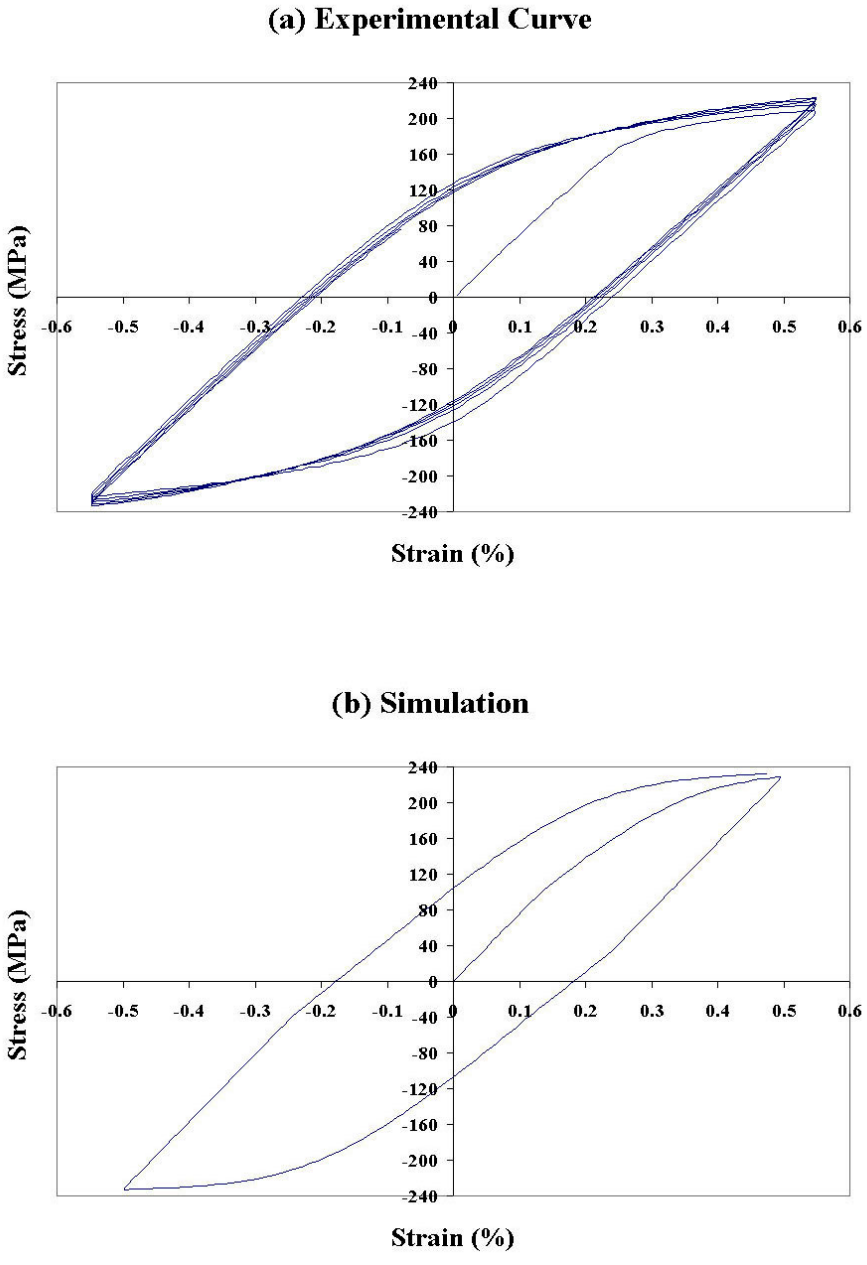

w

Figure 4.2. A comparison of stress/strain curves for Al-1%Si matrix showing the cyclic experimental data and the simulation curve using the obtained material constants: (a) experimental curve, (b) simulation.

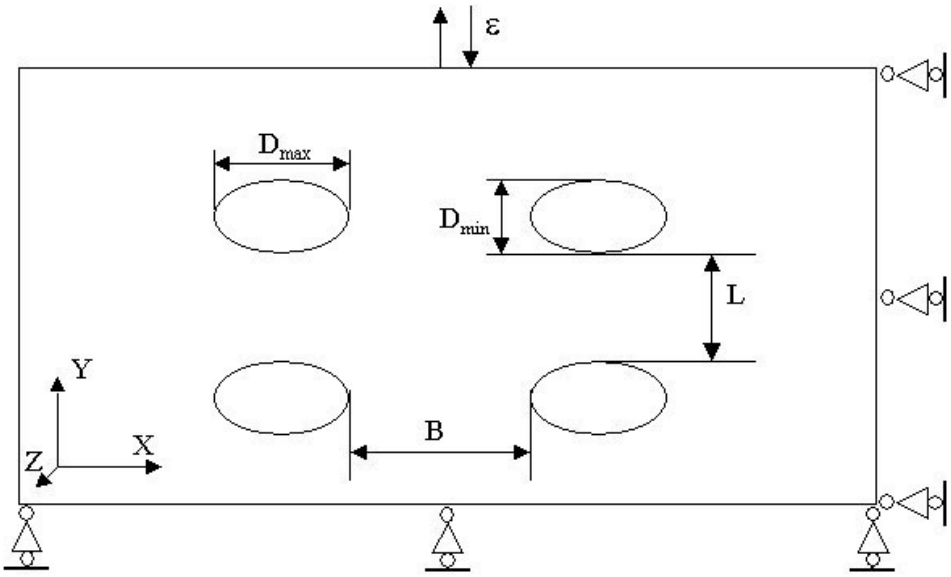

The following notation is introduced for both particles and pores:

aspect ratio: D_{max}/D_{min} size: $D = (D_{max}+D_{min})/2$

remote strain: ε amplitude of remote strain: $\Delta\varepsilon/2$

longitudinal spacing: L transverse spacing: B

strain ratio: $R_\varepsilon = \varepsilon_{min}/\varepsilon_{max}$ effective plastic strain: $\bar{\varepsilon}^P$

maximum principal stress: σ_I

Figure 4.3. Definition of symbols and notations for particle and pore clusters.

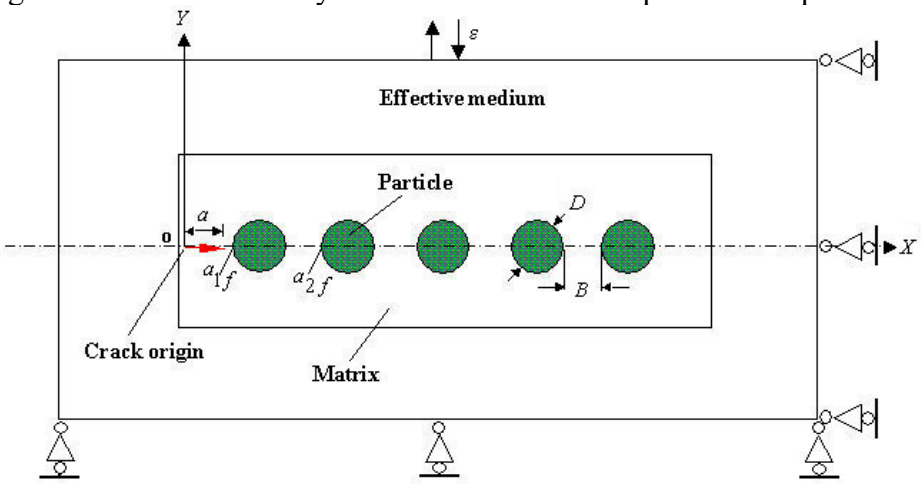

Figure 4.4. An example of domain and boundary design used in finite element analysis for the MSC growth passing through particles under uniformly cyclic displacement at the top boundary. Here, a_{1f} is the crack length from point "o" to the first particle, and a_{2f} is the crack length from point "o" to the second particle. (boundary conditions: uniformly cyclic displacement along the y-direction at the top side, simple support at the right side with u_x=0, simple support at the bottom side with u_y=0, and free at the left side).

4.2 CRACK INCUBATION

Crack incubation may be the most difficult entity to quantify because of the lack of experimental observations. As such, micromechanical calculations are crucial in determining the appropriate effects related to different microstructures and inclusions.

To estimate the number of cycles spent on fatigue crack incubation, fatigue tests of Al-1%Si dendritic material were conducted to determine material constants. The values of C, α, C', and α' are shown in Table 4.1, determined from specimens with homogeneous strain fields. On the other hand, the plastic shear and Fatemi-Socie (1988) parameters are obtained at Gaussian points of small elements with sizes of about 1 μm in highly heterogeneous regions. To use these constants for N_{inc}, average values of the plastic shear should be used in Equation 2.2 and Equation 2.3. The averaging length scale for particle clusters is half of the particle spacing. For pores, the length of averaging is over the smallest length of the plastic zone. The boundary of the plastic zone is determined when the shear plastic reaches 500 $\mu\varepsilon$. For most pores specified in the FEA simulations in this chapter, the length varies from 15 to 25 microns.

Table 4.1. Material parameters of A356 Al alloy for Coffin-Manson Laws.

Parameters	Equation (2.2)	Equation (2.3)
C	0.0211	-
α	0.5001	-
C'	-	0.0622
α'	-	0.5464

4.2.1. SILICON PARTICLES

The issue of fatigue crack incubation at silicon particles arises when no large pores or oxides are present to initiate fatigue cracks. In high quality castings, understanding and quantifying the microstructure-property relationships is mainly based on silicon particle size, spacing, aspect ratio, and cluster density.

4.2.1.1 REALISTIC MICROSTRUCTURE

SEM images were used to obtain a realistic microstructure of A356 Al alloy with minimal porosity. A finite element mesh was developed based on the SEM images (Yang, 1999), and FEA simulations were performed under symmetric cyclic loading of tension and compression. Perfect bonding between the silicon and aluminum was assumed. Perfect bonding means the particles remained intact during the deformation. Figures 4.5 and 4.6 illustrates distributions of effective plastic strain and the largest principal stress in dendrite cells and particle clusters given a remote applied strain of 0.2%. The important results are as follows:

- For intact particle clusters of pore-controlled castings, the maximum plastic strain generally occurred at the following locations: (a) at the middle of intervals between particles which were located along the loading direction, such as point C of Figure 4.5, (b) at the edge of large particles whose maximum axes were perpendicular to the applied loading direction (e.g.

points A and B), (c) near the crack-tip zone of a matrix crack (point D) and an interfacial crack between a particle and the matrix (crack length is assumed).

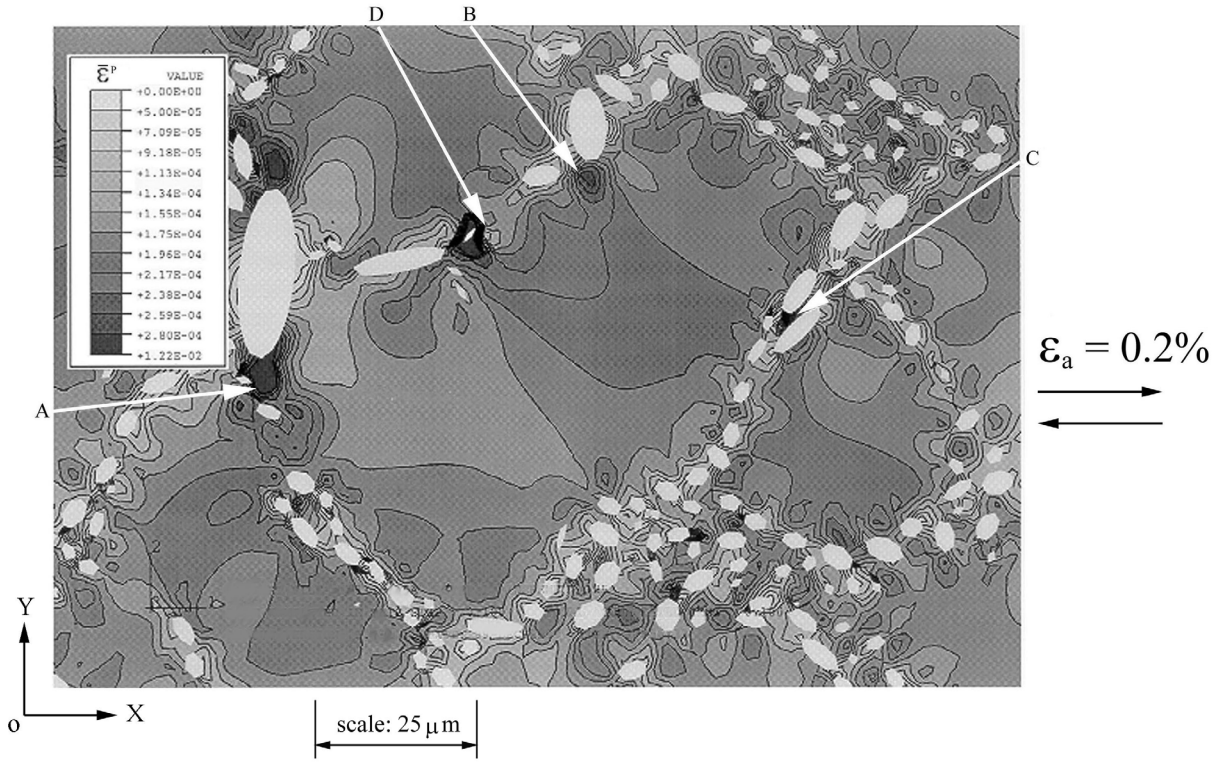

Figure 4.5. Distribution of effective plastic strain, $\bar{\varepsilon}^p$, within a realistic microstructure with ideal, intact particle/matrix interface of A356 Al alloy ($R_\varepsilon = -1$, ε_a=0.2%, boundary conditions: uniformly cyclic displacement along the x-direction at the left side, simple support at the right side with u_x=0, simple support at the bottom side with u_y=0, and free at the top side).

- A quantitative relationship between the maximum effective plastic strain and applied strain amplitude was obtained. The results show that as the applied strain amplitude increased, the percentage of the maximum effective plastic strain over the applied strain amplitude increased. In the limit where the local plastic strain approaches zero, the applied strain amplitude equals about 0.122%. This value gives a calculated proof-fatigue-strength of 90 MPa. Here, the calculated proof-fatigue-strength is defined as the maximum applied stress at which the local plastic strain is zero. The value of 90 MPa is anticipated to be lower, since these calculations assume no possible fracture of silicon particles or debonding of the interface throughout the fatigue cycling.
- The maximum principal stress occurs in large particles whose major axis is along the loading direction as seen in Figure 4.6. They play a large role in transferring the load. For a large particle whose long axis is perpendicular to the loading direction, the stress level is low. The maximum stress at the particle in Figure 4.6 is about 200 MPa. This gives a stress concentration factor of 1.5 at an applied stress amplitude of 133 MPa. This stress concentration may not be sufficient to fracture or debond the particle. From this result, we conjecture that particle fracture or debonding may be caused by overloading associated with

load transfer from existing matrix cracking near the particle, and/or if pre-existing inclusions are present in the silicon.

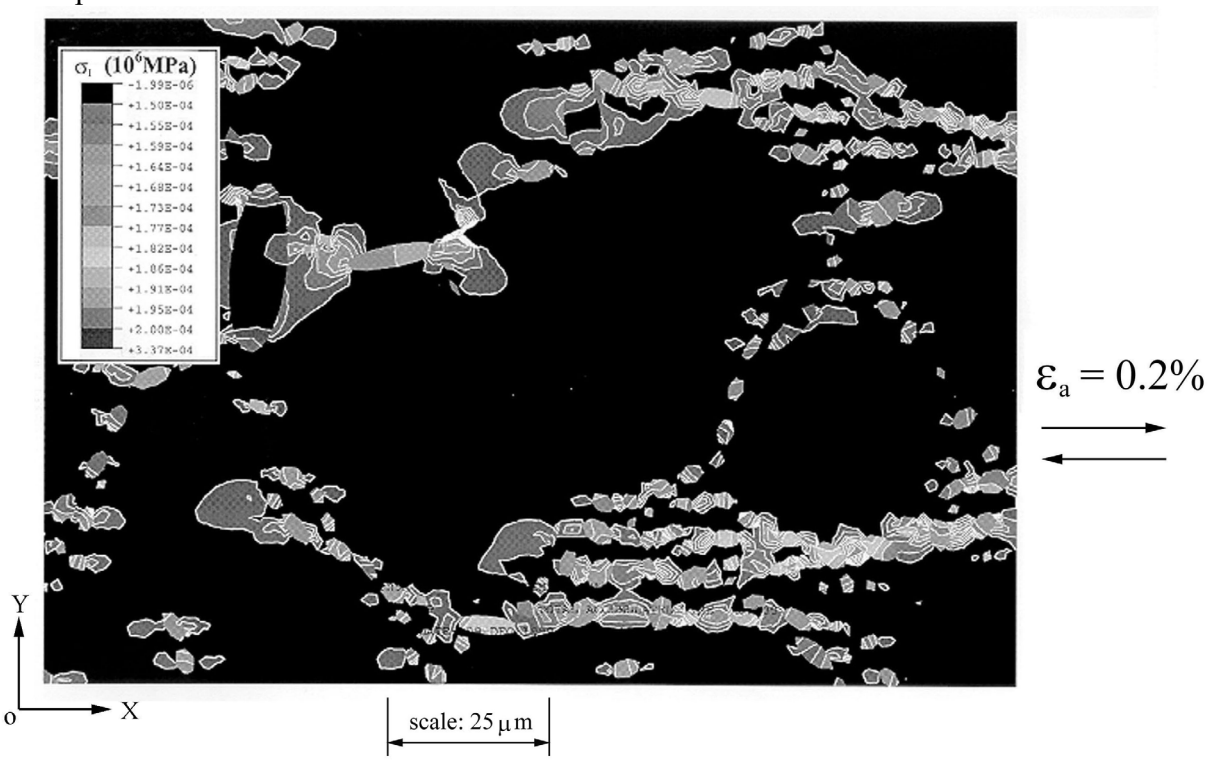

Figure 4.6. Distribution of the maximum principal stress, σ_I , in a realistic microstructure with ideal, intact particle/matrix interface of A356 Al alloy ($R_\varepsilon = -1$, ε_a=0.2%, boundary conditions: uniformly cyclic displacement along the x-direction at the left side, simple support at the right side with u_x=0, simple support at the bottom side with u_y=0, and free at the top side).

Differences in local cyclic plastic strain levels can exist when comparing overloading-produced microcracking, which can spread to a lot of sites, compared to completely reversed loading. These microcracks are more life limiting than isolated cracks (or pores), since they can coalesce and accelerate the crack growth rate. It merits notice that the corresponding microstructure analyzed is not an optimized microstructure, since it includes a largest particle with a size of 17 μm and an aspect ratio of 3.05.

4.2.1.2 IDEALIZED MICROSTRUCTURE: PARAMETRIC STUDIES

Under HCF loading conditions, crack incubation controls the fatigue life, especially for controlled porosity castings, such as squeeze castings. In this case, microporosity and the heterogeneous microstructure within the interdendritic regions control the processes of fatigue crack formation. In this section we examine a myriad of parameters that affect fatigue crack incubation using FEA. Experiments to date are ambiguous with regard to the influence of many of these parameters. For particles and pores we examine the size distribution, shape, spacing, alignment, clustering, and aspect ratio. We also include effects of dendrite cell size and impose different amplitudes of applied strain (stress).

4.2.1.2.1. EFFECTS OF PARTICLE SIZE DISTRIBUTION, SHAPE, SPACING, CONFIGURATION, ALIGNMENT, CLUSTER DENSITY, AND MICROPOROSITY IN RELATION TO EACH OTHER

In this section, finite element simulations are reported concerning the effects of particle cluster morphology on the fracture and debonding of silicon particles embedded in an Al-1%Si matrix subjected to tensile-compressive cyclic loading conditions. Similar to the experiments in which the number of damaged particles was monitored as a function of the number of cycles, these simulations allow us to quantify the effects from silicon particle damage as related to incubation of fatigue cracks. No previous studies have reported the relative influence of each of the pertinent features. A total of seven parameters were varied to create sixteen idealized microstructures: relative particle size, shape, spacing, configuration, alignment, grouping, and matrix microporosity. Clusters of silicon particles (4 to 8 particles) were considered rather than a single isolated particle or an infinite periodic array of particles. The silicon particles were modeled using a linear elastic constitutive relationship and the matrix material was modeled using an internal state variable cyclic plasticity model. A two-level design of experiment methodology was used to screen the relative importance of the seven parameters on the fracture and debonding of the silicon particles. The results of the study demonstrate that particle shape and alignment were undoubtedly the most dominant parameters influencing initial particle fracture and debonding. Particle debonding results in a local intensification of stresses in the Al-1%Si matrix that is significantly larger than that due to particle fracture. The local stresses after particle fracture are primarily concentrated within the broken particle halves. After the fracture of several particles within a cluster, the spacing between adjacent particles enters as a second order effect. When several particles within a cluster debond, the spacing between adjacent particles enters as a dominant effect due to the large local stress intensification in the surrounding Al-1%Si matrix.

Under cyclic loading conditions, the silicon particles in the eutectic have several potential influences on the fatigue response of cast Al-Si alloys. If the maximum internal defect (oxide or pore) size is small ($<<100$ μm), then silicon particles can serve as crack nucleation sites. For example, in squeeze cast Al-Si alloys with silicon concentrations ranging from 7% to 12%, fatigue cracks have been observed to nucleate at silicon particle clusters (Plumtree and Schafer, 1986) or large silicon particles (Shiozawa *et al.*, 1997) and this can affect the crack growth rate of neighboring fatigue cracks. Moreover, cracks growing in the long crack regime have a crack tip driving force strong enough to fracture a statistically significant number of silicon particles near the crack tip (Gall *et al.*, 1999-A, B). The long crack will then subsequently propagate through the damaged silicon particles in the eutectic regions (Gall *et al.*, 1999-A, B). Consequently, the growth rate of long cracks is significantly influenced by the silicon particle morphology through differences in the fracture characteristics of the particles (Hoskin *et al.*, 1988; Lee *et al.*, 1995-A; Lee *et al.*, 1995-B). Finally, the damage associated with silicon particles has also been shown to influence the Bauschinger effect in cast Al-Si alloys subjected to cyclic loading (Horstemeyer, 1998).

Despite the strong influence of the silicon particles on the evolution of damage under monotonic and cyclic loading conditions, the fracture and debonding characteristics of such particles is only

quantified for idealized particle configurations and geometries (Gurland and Plateau, 1963; Needleman, 1987; Yeh and Liu, 1996). It is still necessary to quantify the relative influence of more realistic microstructural parameters on the fracture and debonding of silicon particles embedded in an aluminum matrix. Previous metallurgical investigations (Gurland and Plateau, 1963; Yeh and Liu, 1996) have shown that the fracture of silicon particles embedded in an aluminum matrix is linked to dislocation motion in the Al. The latter study (Yeh and Liu, 1996) further asserted that continuum theory was unable predict the proper dependence of the volume fraction of fractured particles on the applied stress and plastic strain amplitudes. The particle fracture hypothesis was based on the observation that cast materials with drastically different aluminum matrix yield exhibited silicon particle fracture at similar levels of macroscopic plastic deformation. Consequently, Yeh and Liu (1996) concluded that the fracture process was only dictated by the impingement of dislocations on the particles as caused by large scale yielding in the specimens, and that a continuum analysis could not capture such an effect. However, the conclusion by Yeh and Liu (1996) was not based on consideration of the stress and strain distributions for a material containing inclusions that is undergoing plastic flow in the matrix. From a continuum standpoint, the onset of plastic flow in the matrix is also accompanied by sharp increases of the stress in the silicon particles as the elastic inclusion attempts to maintain compatibility with the flowing matrix. In addition, continuum theory predicts trends in particle fracture that are not easily captured with dislocation-based models, as will be further discussed.

A proposed micromechanical model based on dislocation pileups (Yeh and Liu, 1996) captured the overall dependence of the volume fraction of fractured silicon particles on the applied stress and strain. However, despite the fact that particle shape has a strong impact on the fractured silicon particle distribution under monotonic (Gurland and Plateau, 1963; Yeh and Liu, 1996; Dighe and Gokhale, 1997) and cyclic (Gall *et al.*, 1999-B) loading conditions, the model did not capture the geometrical aspects of particle fracture. Localized plastic flow near the particles will lead to dislocation pileups and hardening at the microscale. However, it is insufficient to exclusively consider the local pileup stresses as influenced by the external loading, regardless of the particle geometry. The driving force for particle fracture is also affected by the distribution of mismatch stresses in the particle. If the mismatch stresses did not influence particle fracture, particles would be expected to fracture in a random distribution, irrespective of the particle geometry. However, particles with high aspect ratios consistently show an increased propensity for fracture (Gurland and Plateau, 1963; Yeh and Liu, 1996; Dighe and Gokhale, 1997). In addition, the fracture plane in the silicon is usually perpendicular to the applied loading axis (Gurland and Plateau, 1963; Yeh and Liu, 1996; Dighe and Gokhale, 1997). These two effects are arguably the most dominant ones observed in micrographs, and they are both predicted by continuum analysis of the particles (Gurland and Plateau, 1963). Consequently, the fracture and debonding of silicon particles in a ductile aluminum matrix can be properly modeled by calculating stress values near the particles using a continuum-based approach. An accurate continuum analysis must capture stresses due to mismatches of the elastic and plastic flow properties between the two phases. Other effects such as the relative cleavage plane and slip system orientation will also play a role in the particle fracture (Yeh and Liu, 1996). However, due to the low anisotropy of aluminum coupled with the multiple cleavage plane variants in silicon, it is probable that the geometrical features of particles overshadow these effects.

The current lack of agreement over the relative importance of different mechanisms for local silicon particle fracture is partially due to the complexity of extracting quantitative information from metallurgical studies. Quantifying the relative importance of different microscopic parameters on particle fracture and debonding will contribute to the development of improved monotonic and cyclic micromechanical models, which include more than just the volume fraction of second phase particles as microstructural parameters.

The numerical investigation will consider parameters known to affect particle fracture and debonding based on previous metallurgical studies, such as particle shape, relative particle size, and particle alignment (Gurland and Plateau, 1963; Yeh and Liu, 1996; Dighe and Gokhale, 1997; Gall *et al.,* 1999). In addition, some parameters, which are difficult to obtain from metallurgical observations, will be studied to quantify their relative influence on the fracture and debonding of silicon particles. The latter parameters include particle spacing, particle configuration, grouping of particle clusters, and microporosity. The advantage of using idealized microstructures to study particle fracture and debonding is that the quantitative influence of many parameters can be studied independently. In metallurgical studies, it is difficult to independently quantify the effects of microstructural parameters when complex interactions are inherent. The quantitative predictions of the numerical study are presented in light of metallurgical findings to assure that the numerical results provide insights that are consistent with observations. In addition, the numerical study will compare the effects of particle debonding versus particle fracture. Particle debonding has received considerably less attention than particle fracture even though it is important during the initial stages of fatigue crack growth in Al-Si alloys (Gall *et al.,* 1999-B). Our numerical study does not explicitly consider the mechanics of debonding since this issue has been previously addressed (Needleman, 1987). In addition, particle fracture is assumed to occur instantaneously at a critical stress level due to the brittle nature of silicon particles. We focus on the effect of fully bonded, partially debonded, and fractured silicon particles on the subsequent initiation of debonding and fracture in neighboring particles. A design of experiment (DOE) methodology (Devor *et al.,* 1992) is utilized to help reduce the number of finite element models necessary to systematically determine the effects of all seven parameters in all three damaged states. Ultimately, 48 unique finite element meshes and analyses were required to obtain the desired information. Although the numerical analyses pertain to the behavior of a cast A356 aluminum alloy, the results provide insight into the debonding and fracture characteristics for any alloy system with stiff and strong particles which are surrounded by a work hardenable matrix.

4.2.1.2.1.1. MORPHOLOGICAL PARAMETERS AND MESHES

The seven parameters to be considered in this study are summarized in Figure 4.7. The ranges of the parameters in Figure 4.7 were determined by examining multiple micrographs provided from a previous study on a cast A356 aluminum alloy with modified silicon particles (Dighe and Gokhale, 1997). Unmodified alloys are of little interest from a practical standpoint due to insufficient mechanical properties, such as low tensile ductility. We recognize that more extreme values than indicated in Figure 4.7 could exist in the microstructure for each of the different parameters. However, the high and low values in Figure 4.7 represent a statistically significant deviation from the norm for a given parameter. The proposed ranges are sufficient to screen the

relative influence of the parameters on the debonding and fracture characteristics of the silicon particles. Once these first order effects are understood, the more dominant parameters can be studied over a wider range of values in future studies. With exception of microporosity, all of the parameters in Figure 4.7 may be quantified from micrographs.

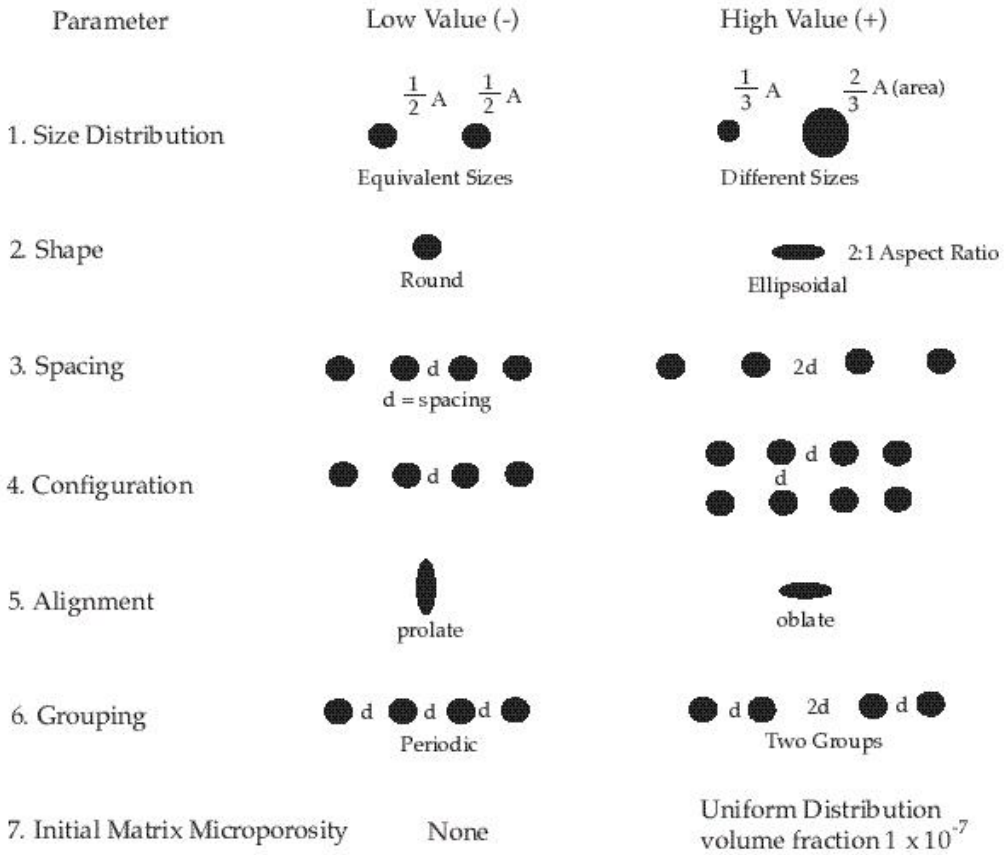

Figure 4.7. Schematic demonstrating the different parameters considered in the present finite element study. The parameter ranges were determined by examining actual micrographs of a modified cast A356 aluminum alloy.

To systematically study the effect of these seven parameters on particle fracture and debonding, a two-level factorial design of experiment methodology (DOE) was incorporated (DeVor *et al.*, 1992). Such a DOE study provides both main effects and interaction effects. A main effect, E, is a quantitative measurement of the average shift in the measured system response due to a change in an input parameter value from the low to high setting. For example, the quantitative main effect of the particle shape parameter on the largest principal stress in the silicon particle, σ_I, is the difference in σ_I for an elliptical versus a round particle. An interaction effect quantifies how the magnitude of the main effect for a given parameter depends on the other parameters in the DOE study. In this study, only main effects are reported since interaction effects were either negligible or obvious from a physical standpoint. For example, a large interaction between particle shape and alignment was determined. An interaction between shape and alignment is consistent with expectations since round particles demonstrate no alignment effects; however, elliptical particles demonstrate significant alignment effects. Table 4.2 demonstrates the computational matrix for studying the effects of silicon particle morphology on particle debonding and fracture in cast Al-Si alloys, for each of the three cases of intact, fractured, and

debonded particles. The high (+) and low (-) levels for the silicon morphological parameters are listed in Figure 4.7. In Table 4.2 the ellipsoidal particles had an aspect ratio of 2:1.

Table 4.2. The design matrix used to create different finite element meshes to study of the effect of morphological parameters on the debonding and fracture of silicon particles embedded in an Al-1%Si matrix. A prolate particle has a major axis parallel to the loading axis, while an oblate particle has a major axis perpendicular to the loading axis.

Mesh #	Size Distribution	Particle Shape	Particle Spacing	Config-uration	Particle Alignment	Grouping Effect	Micro-Porosity
1	Uniform (-)	Round (-)	d (-)	4 (-)	Prolate (-)	No (-)	No (-)
2	Non-Uniform(+)	Round (-)	d (-)	4 (-)	Oblate (+)	Yes (+)	No (-)
3	Uniform (-)	Ellipse (+)	d (-)	4 (-)	Oblate (+)	No (-)	Yes (+)
4	Non-Uniform(+)	Ellipse (+)	d (-)	4 (-)	Prolate (-)	Yes (+)	Yes (+)
5	Uniform (-)	Round (-)	2d (+)	4 (-)	Oblate (+)	Yes (+)	Yes (+)
6	Non-Uniform(+)	Round (-)	2d (+)	4 (-)	Prolate (-)	No (-)	Yes (+)
7	Uniform (-)	Ellipse (+)	2d (+)	4 (-)	Prolate (-)	Yes (+)	No (-)
8	Non-Uniform(+)	Ellipse (+)	2d (+)	4 (-)	Oblate (+)	No (-)	No (-)
9	Uniform (-)	Round (-)	d (-)	8 (+)	Prolate (-)	Yes (+)	Yes (+)
10	Non-Uniform(+)	Round (-)	d (-)	8 (+)	Oblate (+)	No (-)	Yes (+)
11	Uniform (-)	Ellipse (+)	d (-)	8 (+)	Oblate (+)	Yes (+)	No (-)
12	Non-Uniform(+)	Ellipse (+)	d (-)	8 (+)	Prolate (-)	No (-)	No (-)
13	Uniform (-)	Round (-)	2d (+)	8 (+)	Oblate (+)	No (-)	No (-)
14	Non-Uniform(+)	Round (-)	2d (+)	8 (+)	Prolate (-)	Yes (+)	No (-)
15	Uniform (-)	Ellipse (+)	2d (+)	8 (+)	Prolate (-)	No (-)	Yes (+)
16	Non-Uniform(+)	Ellipse (+)	2d (+)	8 (+)	Oblate (+)	Yes (+)	Yes (+)

For each of the sixteen configurations shown in Table 4.2, a representative finite element mesh was constructed. In the interest of space limitations, it is impractical to show all of the finite element meshes; however, a schematic of run number 10 is shown in Figure 4.8a. The silicon particles are enlarged for clarity, and their actual size is indicated in the lower left corner of the Figure 4.8a. In run 10 all of the parameters have the high (+) values (Table 4.2). The finite element analyses were conducted using the code ABAQUS (Hibbitt *et al.*, 1998) which employs a user material subroutine containing the cyclic plasticity model described in the appendix. The finite element models were two-dimensional plane strain analyses with four noded isoparameteric elements. The overall mesh size was 240 x 240 μm to alleviate any boundary edge effects. Because the boundaries remained orthogonal, double periodicity was enforced. The spacing parameter "d" in Figure 4.8 was always 4 μm from edge to edge. In all meshes the total area fraction of silicon particles was also kept arbitrarily constant at 0.174%, regardless of the shape and number of silicon particles. The low value of 0.174% is chosen to alleviate any edge (surface) interactions on silicon particle fracture and debonding. Each mesh contained

approximately 10,000 elements and the fine mesh near the particles contained elements on the order of 0.1 times the particle size. Figure 4.8b is a typical example showing the fine mesh region near the silicon particles for mesh number 10. The applied far-field boundary condition was a completely reversed cyclic tension-compression strain (displacement) with an amplitude of 0.4 % for three cycles. The original sixteen meshes contained silicon particles that were all perfectly bonded to the Al-1%Si matrix. Each mesh was then modified to contain two fractured or two debonded silicon particles within the cluster of silicon particles, resulting in 32 additional finite element meshes. The two damaged particles were always the same as indicated on Figure 4.8 for clusters of silicon particles. The fractured particles were modeled by introducing a crack across the center of the particles perpendicular to the applied loading axis. The debonded particles had a crack introduced along the interface between the silicon particle and the Al-1%Si interface, only on the lower half of the particle. Crack face boundary conditions involved treating the exposed elements as frictionless surface contact elements. The contact conditions prevented the crack faces from interpenetrating during local compressive deformation and the cracked or debonded particles were included from the beginning of the calculations.

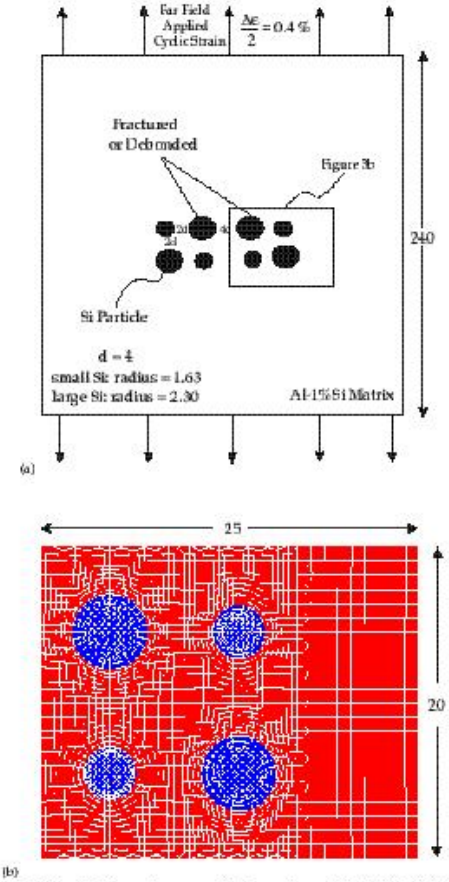

Figure 4.8. (a) Schematic of mesh 10 with the silicon particles enlarged to highlight their distribution. The actual radii are given in mesh units on the lower left corner of the mesh. (b) The finite element fine mesh region near the silicon particles in mesh 10.

Two different stress values were extracted from each of the 48 finite element analyses during the third loading cycle at the point of maximum applied tensile stress: 1. The maximum tensile principal stress in a silicon particle, and 2. the maximum tensile hydrostatic stress at the interface between a silicon particle and the Al-1%Si matrix material. The principal stress in the particle is one measure of the driving force for silicon particle fracture. Likewise, the hydrostatic stress at

the particle-matrix interface is one measure of the driving force for silicon particle debonding (Needleman, 1987). In the meshes where the particles were debonded or cracked *a priori*, the pre-damaged particles were not considered in the determination of stress values. In these cases, the aim was to quantify how the debonding and fracture of adjacent particles affected the stress distribution in neighboring, intact particles.

The computational DOE matrix in Table 4.2 yielded 16 output values chosen from individual finite element analyses (Table 4.3). These output values are denoted as O_i, (i = 1, 2, 3 . . . 16), and may represent the maximum principal stress in the particle or hydrostatic pressure at the particle/matrix interface. In a full factorial design, the main parameter effects (E_1 - E_7) and interaction effects (E_{12}, E_{25}, E_{123}, etc.) can be explicitly calculated from the set of O_i values. However, in this fractional factorial design (DeVor *et al.*, 1992), the values calculated directly from the O_i values represent linear combinations of confounded effects (L_1 - L_{16}). The L_i values are calculated through the following relationship (DeVor *et al.*, 1992):

$$\begin{bmatrix} L_1 \\ L_2 \\ L_3 \\ L_4 \\ L_5 \\ L_6 \\ L_7 \\ L_8 \\ L_9 \\ L_{10} \\ L_{11} \\ L_{12} \\ L_{13} \\ L_{14} \\ L_{15} \\ L_{16} \end{bmatrix} = \frac{1}{8} \begin{bmatrix} +1 & +1 & +1 & +1 & +1 & +1 & +1 & +1 & +1 & +1 & +1 & +1 & +1 & +1 & +1 & +1 \\ -1 & +1 & -1 & +1 & -1 & +1 & -1 & +1 & -1 & +1 & -1 & +1 & -1 & +1 & -1 & +1 \\ -1 & -1 & +1 & +1 & -1 & -1 & +1 & +1 & -1 & -1 & +1 & +1 & -1 & -1 & +1 & +1 \\ -1 & -1 & -1 & -1 & +1 & +1 & +1 & +1 & -1 & -1 & -1 & -1 & +1 & +1 & +1 & +1 \\ -1 & -1 & -1 & -1 & -1 & -1 & -1 & -1 & +1 & +1 & +1 & +1 & +1 & +1 & +1 & +1 \\ +1 & -1 & -1 & +1 & +1 & -1 & -1 & +1 & +1 & -1 & -1 & +1 & +1 & -1 & -1 & +1 \\ +1 & -1 & +1 & -1 & -1 & +1 & -1 & +1 & +1 & -1 & +1 & -1 & -1 & +1 & -1 & +1 \\ +1 & -1 & +1 & -1 & +1 & -1 & +1 & -1 & -1 & +1 & -1 & +1 & -1 & +1 & -1 & +1 \\ +1 & +1 & -1 & -1 & -1 & -1 & +1 & +1 & +1 & +1 & -1 & -1 & -1 & -1 & +1 & +1 \\ +1 & +1 & -1 & -1 & +1 & +1 & -1 & -1 & -1 & -1 & +1 & +1 & -1 & -1 & +1 & +1 \\ +1 & +1 & +1 & +1 & -1 & -1 & -1 & -1 & -1 & -1 & -1 & -1 & +1 & +1 & +1 & +1 \\ -1 & +1 & +1 & -1 & +1 & -1 & -1 & +1 & -1 & +1 & +1 & -1 & +1 & -1 & -1 & +1 \\ -1 & +1 & +1 & -1 & -1 & +1 & +1 & -1 & +1 & -1 & -1 & +1 & +1 & -1 & -1 & +1 \\ -1 & +1 & -1 & +1 & +1 & -1 & +1 & -1 & +1 & -1 & +1 & -1 & -1 & +1 & -1 & +1 \\ -1 & -1 & +1 & +1 & +1 & +1 & -1 & -1 & +1 & +1 & -1 & -1 & -1 & -1 & +1 & +1 \\ +1 & -1 & -1 & +1 & -1 & +1 & +1 & -1 & -1 & +1 & +1 & -1 & +1 & -1 & -1 & +1 \end{bmatrix} \begin{bmatrix} O_1 \\ O_2 \\ O_3 \\ O_4 \\ O_5 \\ O_6 \\ O_7 \\ O_8 \\ O_9 \\ O_{10} \\ O_{11} \\ O_{12} \\ O_{13} \\ O_{14} \\ O_{15} \\ O_{16} \end{bmatrix}$$

The relationships between the L_i values and the main parameter effects (E_1 - E_7) and interaction effects (E_{12}, E_{25}, E_{123}, etc.) are determined through a confounding relationship. For this common design, the confounding relationship is given in (DeVor *et al.*, 1992). It will also be noted that for the present study, three factor interaction effects were ignored which is an accurate assumption for most physically based systems (DeVor *et al.*, 1992). Using the confounding relationship in (DeVor *et al.*, 1992), the following equations were determined which relate L_i values to the E values of interest for the present study:

L_1 = Data-set mean
$L_2 = E_1$

$L_3 = E_2$
$L_4 = E_3$
$L_5 = E_4$
$L_6 = E_{12} + E_{35} + E_{67}$
$L_7 = E_{13} + E_{25} + E_{46}$
$L_8 = E_{14} + E_{36} + E_{57}$
$L_9 = E_{23} + E_{15} + E_{47}$
$L_{10} = E_{24} + E_{37} + E_{56}$
$L_{11} = E_{34} + E_{16} + E_{27}$
$L_{12} = E_5$
L_{13} = Three factor assumption error
$L_{14} = E_6$
$L_{15} = E_7$
$L_{16} = E_{45} + E_{26} + E_{17}$

Hence, given the 16 output values for the meshes in Table 4.2, the present analysis delivers the 7 main parameter effects and the 21 confounded two factor interactions on a chosen output parameter. The main effects (E_1 - E_7) were only considered in this study since the interaction effects were all negligible or obvious from a physical standpoint. For example, a large interaction between particle shape and alignment was uncovered. An interaction between shape and alignment is consistent with expectations since round particles demonstrate no alignment effects; however, elliptical particles demonstrate significant alignment effects.

4.2.1.2.1.2. SCREENING OF DOMINANT PARAMETERS

The data from the finite element analyses are presented in Table 4.3. Completely reversed, uniaxial displacements were prescribed. Each data point represents a maximum stress value (hydrostatic or principal) from an individual finite element analysis. The data in the columns labeled "Bond" were extracted from analyses where the silicon particles were all perfectly bonded within the given mesh. The data in the "Crack" and "Debond" columns were extracted from analyses where two silicon particles in the cluster were cracked or debonded respectively (Figure 4.8). It is difficult to visualize the relative importance of the seven parameters by inspection of the data in Table 4.3. However, by performing the appropriate DOE transformation on the six data columns in Table 4.3, the data reveal the quantitative effects of the seven parameters. The meaning of the DOE data transformation is covered in detail in (DeVor *et al.*, 1992); however, an overview of the required calculations is presented in the Appendix.

From the data in Table 4.3, the main effects of the silicon particle parameters on silicon particle fracture and debonding are presented in Figures 4.9-4.11. In the cases where all of the particles are perfectly bonded, shape and alignment are by far the most dominant effects on particle fracture (Figure 4.9a) and particle debonding (Figure 4.9b). Within the range considered here, the five remaining parameters are shown to have a negligible effect on the initiation of fracture or debonding of silicon particles in an Al-1%Si matrix. Once several of the particles within a group are cracked, the effect of particle spacing enters as a significant effect as demonstrated in Figure 4.10a and 4.10b. When several silicon particles within the groupings are partially

debonded (Figures 4.11a and 4.11b), the effect of particle spacing becomes more dominant than the other parameters studied.

Table 4.3. Results from the 48 finite element analyses on the 16 meshes in Table 4.2. All values were taken from bonded silicon particles during the point of maximum tensile stress in the third loading cycle. Bond, Crack, and Debond differentiate between meshes with all perfectly bonded particles, two cracked particles, and two debonded particles respectively.

	Maximum principal stress within a fully bonded silicon particle σ_I (MPa)			Maximum hydrostatic stress at the Si-Al interface of a bonded Si particle, σ_H (MPa)		
Mesh #	Bond	Crack	Debond	Bond	Crack	Debond
1	267	281	325	153	160	185
2	267	288	339	156	160	185
3	252	288	339	139	160	185
4	308	302	380	175	171	185
5	267	267	284	153	153	160
6	267	274	291	153	153	175
7	302	302	312	175	171	175
8	248	274	289	139	153	175
9	267	281	300	153	164	175
10	267	281	312	153	164	195
11	252	274	298	139	167	190
12	302	302	328	175	175	195
13	267	267	279	153	153	165
14	267	267	279	153	153	165
15	302	302	311	175	171	170
16	248	269	273	139	153	165

Depending on the damaged state of neighboring particles, the finite element results indicate that the following parameters, listed in descending order of importance, have a significant influence on the debonding and fracture of silicon particles in a Al-1%Si matrix:

1. Particle shape
2. Particle alignment
3. Particle spacing
4. Particle configuration

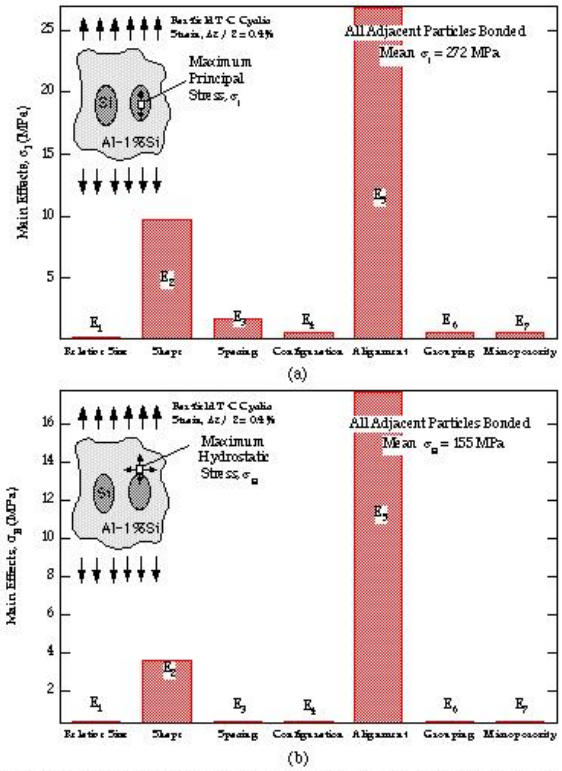

Figure 4.9. The quantitative main parameter effects on (a) particle cracking (b) particle debonding. All of the adjacent particles are bonded.

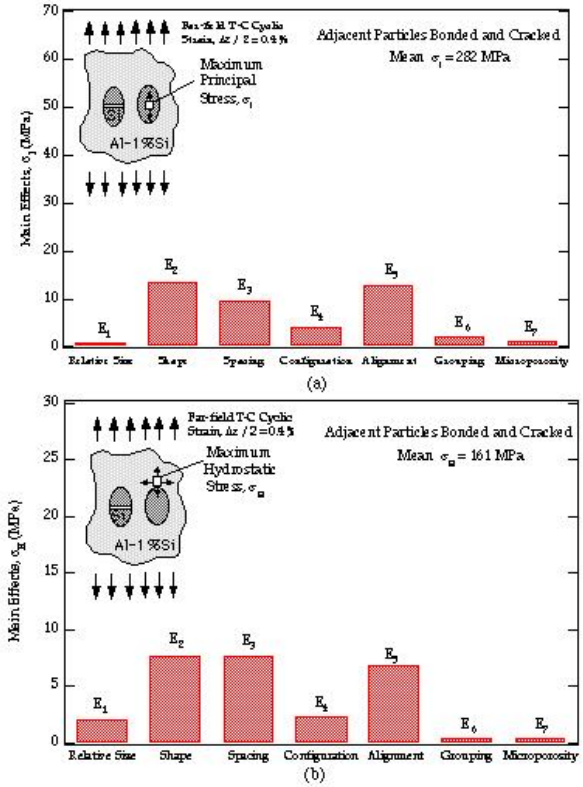

Figure 4.10. The quantitative main parameter effects on (a) particle cracking (b) particle debonding. Some of the adjacent particles are bonded while others are cracked.

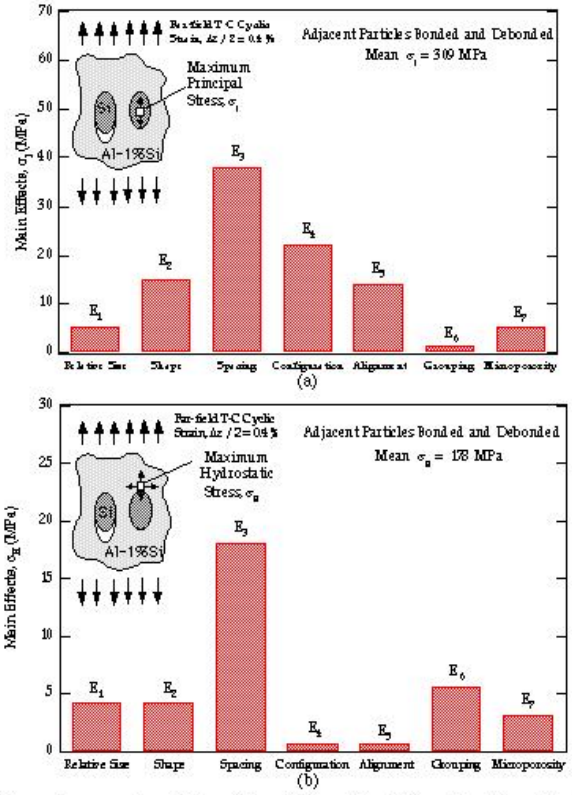

Figure 4.11. The quantitative main parameter effects on (a) particle cracking (b) particle debonding. Some of the adjacent particles are bonded while others are debonded.

To elucidate the influence of the four dominant parameters on fracture and debonding of silicon particles it is necessary to examine the stress distributions in the silicon particles and in the surrounding Al-1%Si matrix. The representative meshes used to study the dominant effects are numbers 10, 11, and 12 (Table 4.2). Figures 4.12-4.14 show contour plots of the maximum principal tensile stresses near the silicon particles. Figures 4.15-4.17 are contour plots of the hydrostatic stresses near the silicon particles (tensile hydrostatic stresses are negative). The contour plots in Figures 4.12-4.17 are symmetric about the left border, such that each analysis contains eight particles. The far-field loading axis is vertical in the plane of the figures. Furthermore, Figures 4.12-4.17 all contain three different damaged particle states: (a) all particles intact, (b) two particles cracked, (c) two particles debonded. In the fractured particles, the center crack runs through the entire silicon particle. The debonded particles have cracks that cover the lower half of the particles along the interface between the silicon and Al-1%Si materials. The contour plots were all created at the maximum applied tensile stress on the third loading cycle. Given this information, we will now discuss the effects of individual parameters on silicon particle fracture and debonding.

The influences of particle shape and alignment on particle fracture for monotonic and cyclic loading are the most heavily documented effects in the materials science literature (Gurland and Plateau, 1963; Yeh and Liu, 1996; Dighe and Gokhale, 1997; Gall *et al.,* 1999-B). The influence of shape and alignment on the debonding of silicon particles has received significantly less attention (Dighe and Gokhale, 1997; Gall *et al.,* 1999-B). Previously, particle shape and alignment effects have been experimentally observed without considering a systematic variation

in other relevant microstructural features. The present study demonstrates the influence of particle shape and alignment relative to other pertinent microstructural parameters such as spacing. The numerical results presented here confirm earlier predictions for isolated intact particles (Gurland and Plateau, 1963), and extend these understandings to the cases where adjacent particles are fractured or debonded. When all of the particles within a cluster are intact, the maximum tensile stress in the particles and the maximum hydrostatic stress at the particle-matrix interface are greatest when the major axis of the particle is parallel to the far-field loading direction (Figure 4.14a and 4.17a). When the particles are rounded (Figures 4.12a and 4.15a), the stress levels inside and surrounding the particles are smaller than the stresses near particles with an elongated axis parallel to the loading direction. Furthermore, when the major axis of a particle is perpendicular to the applied loading axis (Figures 4.13a and 4.16a), the stress levels in and around the particles are even lower than the stresses near the rounded particles.

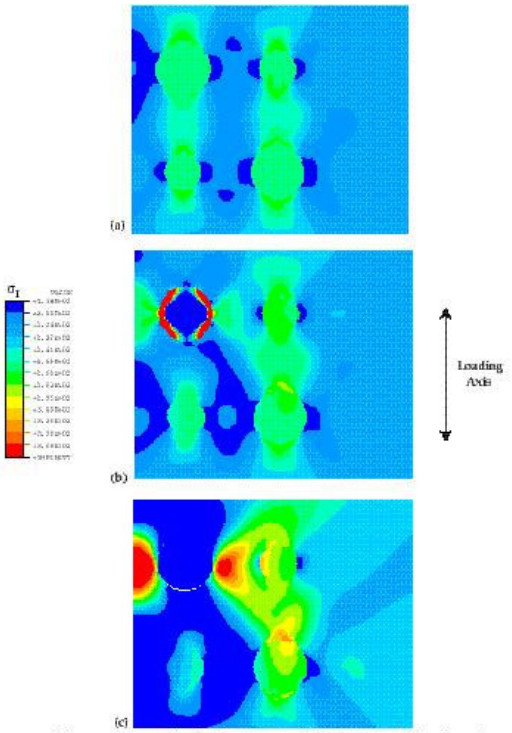

Figure 4.12. Contours of the maximum principal stress, σ_I (MPa), surrounding the silicon particles for mesh 10 at the maximum applied tensile stress in the third loading cycle. The results are symmetric about the left boundary of the plot. The mesh has three different initial configurations, (a) all particle bonded, (b) two particles cracked, (c) two particles debonded.

The principal stresses within the particles are relatively uniform, regardless of the orientation of the elliptical particle. The hydrostatic stress at the particle-matrix interface is always a maximum at the top and bottom of a particle along a line parallel to the uniaxial loading axis and through the center of the particle. As the local particle radius of curvature is decreased at the top or bottom of the particle, the maximum local hydrostatic stress at the particle-matrix interface increases. For example, a particle with a major axis parallel to the loading axis (Figure 4.17a) has an extremely small radius of curvature at the top of a particle compared to a particle with the major axis perpendicular to the loading axis (Figure 4.15a). Consequently, the maximum hydrostatic stress at the particle-matrix interface is much greater in elongated particles aligned parallel to the loading axis (Figure 4.17a) versus round particles (Figure 4.15a) or elongated particles aligned perpendicular to the loading axis.

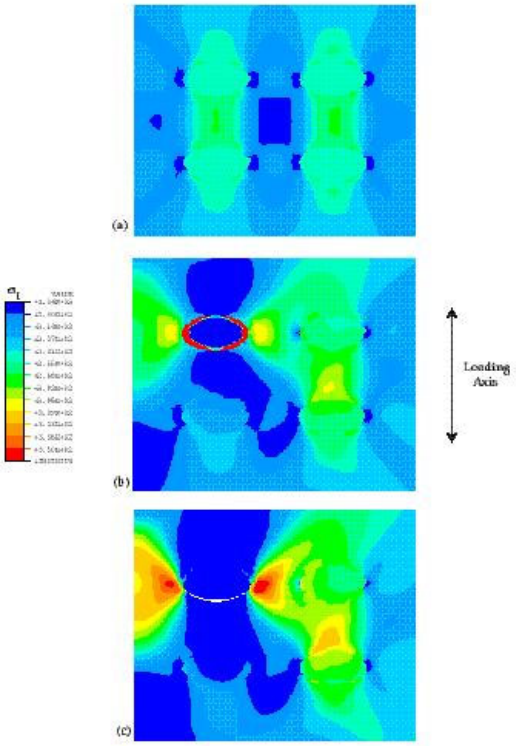

Figure 4.13. Contours of the maximum principal stress, σ_I (MPa), surrounding the silicon particles for mesh 11 at the maximum applied tensile stress in the third loading cycle. The results are symmetric about the left boundary of the plot. The mesh has three different initial configurations, (a) all particle bonded, (b) two particles cracked, (c) two particles debonded.

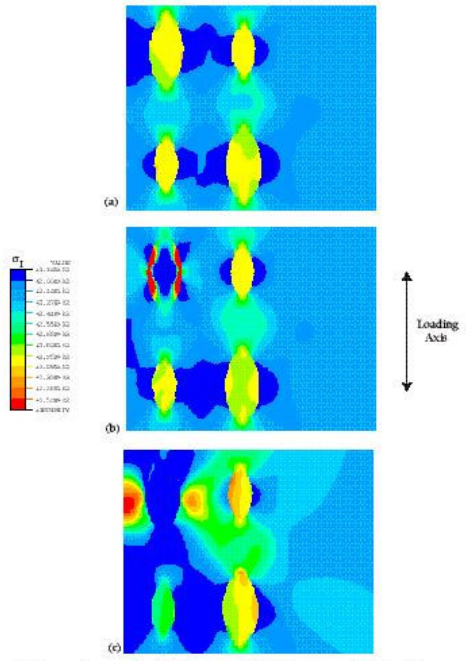

Figure 4.14. Contours of the maximum principal stress, σ_I (MPa), surrounding the silicon particles for mesh 12 at the maximum applied tensile stress in the third loading cycle. The results are symmetric about the left boundary of the plot. The mesh has three different initial configurations, (a) all particle bonded, (b) two particles cracked, (c) two particles debonded.

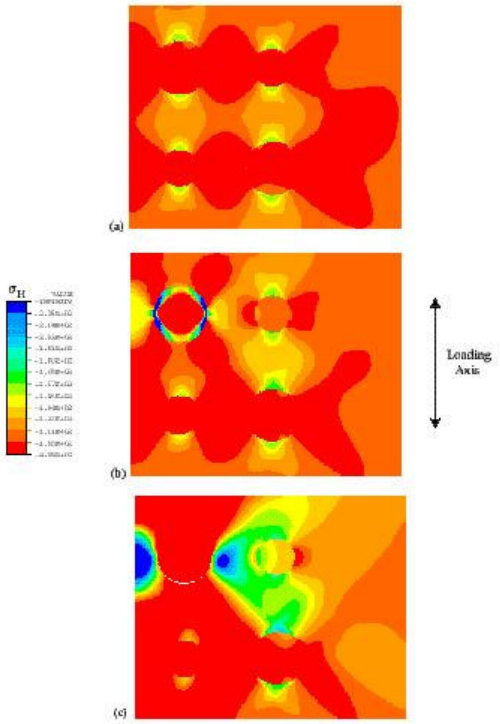

Figure 4.15. Contours of the hydrostatic stress σ_H (MPa, - is tension) surrounding the silicon particles for mesh 10 at the maximum applied tensile stress in the third loading cycle. The results are symmetric about the left boundary of the plot. The mesh has three different initial configurations, (a) all particle bonded, (b) two particles cracked, (c) two particles debonded.

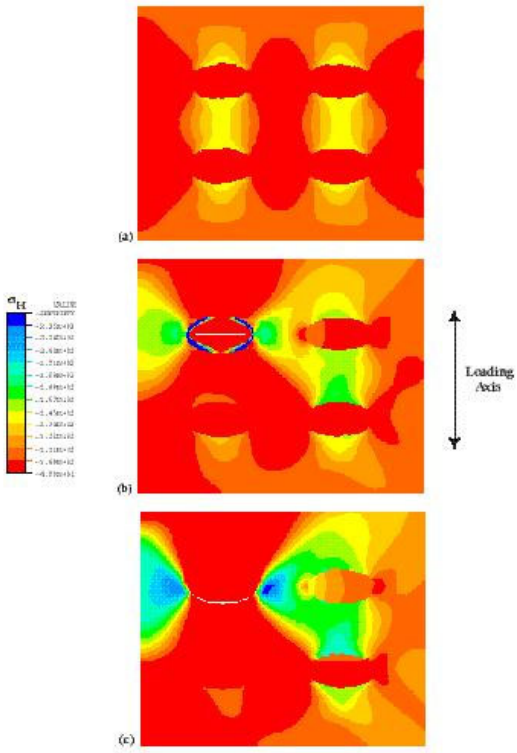

Figure 4.16. Contours of the hydrostatic stress σ_H (MPa, - is tension) surrounding the silicon particles for mesh 11 at the maximum applied tensile stress in the third loading cycle. The results are symmetric about the left boundary of the plot. The mesh has three different initial configurations, (a) all particle bonded, (b) two particles cracked, (c) two particles debonded.

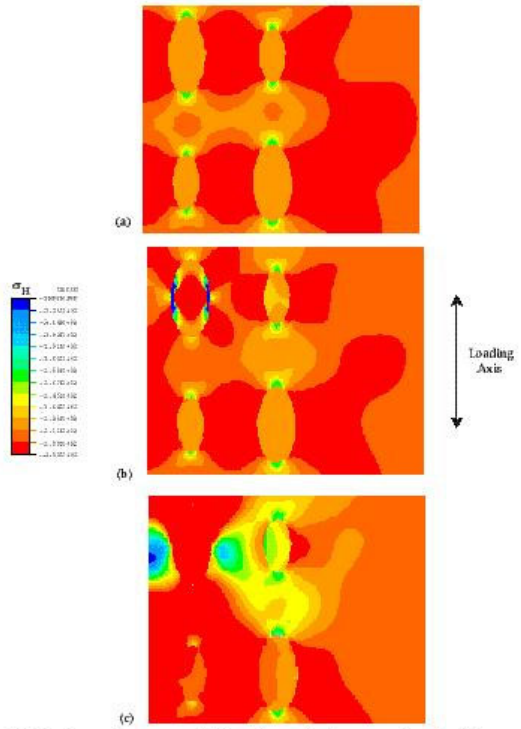

Figure 4.17. Contours of the hydrostatic stress σ_H (MPa, - is tension) surrounding the silicon particles for mesh 12 at the maximum applied tensile stress in the third loading cycle. The results are symmetric about the left boundary of the plot. The mesh has three different initial configurations, (a) all particle bonded, (b) two particles cracked, (c) two particles debonded.

When several particles in a cluster are fractured across their center, the effects of particle shape and alignment are still the dominant influences on particle fracture and debonding of surrounding particles. Irrespective of the shape or alignment of the pre-cracked particle, the intensification of local stresses occurs primarily within the cracked particle (Figures 4.12-4.17 (b)). The Al-1%Si matrix surrounding fractured particles experiences a strain localization over a length scale depending on the shape and alignment of the particle. Although intact particles with a major axis perpendicular to the applied loading axis possess a higher resistance to particle fracture, fractured particles with such orientations facilitate the highest local principal and hydrostatic stresses in the surrounding Al-1%Si matrix. For example, in Figure 4.13b, a zone of magnified local stresses is present in the Al-1%Si matrix near the fractured particle. However, in Figure 4.14b, the zone of intensified stresses near the cracked particle is significantly smaller than that of the cracked particle in Figure 4.14b. The smaller localized zone size in the case of the cracked particle with a major axis parallel to the loading axis is caused by differences in the crack length and constraint of the two particle halves. The cracked particle with a major axis parallel to the loading axis has a much smaller inherent defect size (crack length), and therefore the zone of enhanced plasticity and localized stresses near the crack tip are smaller. Furthermore, the cracked particle with a major axis parallel to the loading axis (Figure 4.14b) experiences local stresses within the fractured particle which are higher and farther reaching compared to the stresses within the particle perpendicular to the loading axis (Figure 4.13b). Consequently, the local stresses immediately outside the fractured particle with the major axis parallel to the loading axis are smaller as expected by energetic arguments. In either orientation, the relatively small localization of stresses surrounding the fractured particles only has a negligible influence on the principal and hydrostatic stresses in neighboring intact particles (compare the stress distributions in the particles surrounding the fractured and intact particles in Figures 4.12-4.17 (b) versus Figure 4.12-4.17 (a)).

When several particles within a cluster debond (Figures 4.12-4.17 (c)), the localization of stresses within the surrounding Al-1%Si matrix is considerably more intense compared to the intact (Figures 4.12-4.17 (a)) or fractured (Figures 4.12-4.17 (b)) particles. In contrast to the high stresses within fractured particles, the stresses within the debonded particles are negligible. The shape and alignment of a debonded particle has a similar influence on the localization of stresses in the Al-1%Si matrix as that of the fractured particles. If the major axis of the debonded particle is parallel to the loading axis (Figures 4.14c, 4.17c), then the intensification of stresses is less than if the major axis of the particle is perpendicular to the loading axis (Figures 4.13c, 4.16c). Debonded circular particles (Figures 4.12c, 4.15c) cause stress intensification bounded by the two orientations of the elliptical particles. In the situations where adjacent particles debond, the stresses in the neighboring particles are influenced by debonded particles of all orientations and shapes. When the major axis of the debonded particle is perpendicular to the loading axis the interaction with surrounding particles is the strongest.

Shape and alignment are the most dominant parameters influencing particle fracture and debonding. It is important to point out that in Figure 4.10 and 4.11 shape and alignment still appear as less dominant effects compared to the other parameters. However, when particles are debonded and fractured, shape and alignment are more dominant than Figures 4.10 and 4.11 portray due to the "average" nature of the DOE effect measures. For example, particles arranged in an array with their major axis parallel to the loading direction have the highest stress fields inside of them. When particles within such an array crack or debond, the crack length is small compared to fractured or debonded particles with a major axis perpendicular to the loading axis (assuming that the cracks form perpendicular to the tensile axis). Consequently, the stress increase in adjacent particles due to neighbors cracking and debonding is smaller for arrays of particles parallel to the tensile axis compared to particles perpendicular to it. In other words, the particles that are most prone for cracking and debonding also inflict the smallest increase in stresses on their neighbors after failure. The counterbalancing effects of internal (self mismatch) and external (neighbor effects) stresses for different shapes and alignments after fracture and debonding yield a low "average" effect of shape and alignment in Figures 4.10 and 4.11.

When all of the silicon particles within a cluster are intact, the local stress fields surrounding the particles are not strong enough to affect the debonding and fracture of neighboring particles. For example, in Figures 4.12-4.17 (a), the stresses inside all of the particles are uniform within the bounds of numerical noise. The uniformity of stresses within an elliptical inclusion is consistent with the classical proof of Eshelby (Eshelby, 1957) for a single isolated inclusion. Consequently, the particles do not feel the influence of the external stress fields from neighboring particles. In Figures 4.12-4.17 (a), the particle spacing is one particle diameter. When the spacing is increased to two particle diameters, the stress distributions within the perfectly bonded particles are nearly identical to the distributions when the particles are one diameter apart.

If several particles within a cluster are fractured, particle spacing becomes a dominant effect in addition to particle shape and alignment. The local stress intensification near a fractured particle (Figures 4.12-4.17 (b)) extends over a distance significant enough to facilitate weak particle-particle interactions. Consequently, when the distance between fractured and intact particles is varied between one particle diameter and two particle diameters, the local stresses near the intact

particles change. However, since the fractured particle contains much of the elastic strain energy after fracture, the spacing of neighboring particles is not as significant of an effect as for the case of debonded particles.

When several particles within a cluster debond, the spacing between particles exerts a strong influence on the stresses in adjacent particles. The significant increase in the stresses in particles adjacent to debonded particles (Figures 4.12-4.17 (c)), is due to the larger extent of the redistributed stress fields in the Al-1%Si matrix surrounding the debonded particles. The principal stress fields within intact particles near a debonded particle show considerable gradients (Figures 4.12-4.14 (c)). In addition, the debonding of adjacent particles increases the hydrostatic stresses at the particle-matrix interface of intact particles (Figures 4.15-4.17 (c)). When the spacing between the particles is increased to two particle diameters, the effect of the debonded particles is weaker since the surrounding particles are not embedded in such intense local stress fields.

Essentially, the effect of particle spacing depends on the length scale of the stress and strain gradients outside the embedded silicon particle. If the particle spacing is on the order of the length scale where strong local stress gradients exist, then spacing will be a dominant effect. In the present study, the particle spacing was varied from one particle diameter to two particle diameters. In the intact and fractured particles, the length scale of the stress gradient was only a fraction of the particle diameter. Consequently, particle spacing does not have a strong influence on the debonding or fracture of adjacent particles when the spacing is more than a particle diameter. On the other hand, strong stress gradients near a debonded particle exist over one or two particle diameters. Therefore, the spacing between intact and debonded particles has a strong influence on the stress distributions near the intact particles when the particle spacing is varied one or two particle diameters.

When all of the silicon particles are intact, the interactions between particles are negligible. Consequently, the spatial location of adjacent particles (at a fixed distance) does not affect the stresses in particles when all particles are intact. However, when adjacent particles are fractured or debonded, particle interactions exist. Furthermore, the spatial location of adjacent particles (at a fixed distance) has a second order effect on the debonding and fracture of silicon particles. Figures 4.13c and 4.16c demonstrate the effect of different particle positions on the principal and hydrostatic stress distributions in intact particles near debonded particles. Aside from a smaller absolute magnitude, configuration effects are similar for fractured particles (Figures 4.13b and 4.16b). For all different particle orientations and shapes, intact particles at a 45 degree angle from a debonded particles experience the greatest principal stresses within the particle (Figure 4.13c) and hydrostatic stress at the particle matrix interface (Figure 4.16c). The strong localization of stresses at a 45 degree angle from the debonded particle is due to “shear bands” aligned with the maximum macroscopic shear strain plane. Intact particles to the right or left (along a line perpendicular the loading axis) of debonded particles also demonstrate significant stress levels. Intact particles below or above (along a line parallel the loading axis) debonded particles demonstrate negligible stress levels.

The results of the present study imply that relative particle size has a negligible effect on the fracture and debonding of silicon particles. However, experimental results indicate that larger

particles consistently show an increased propensity for breakage and debonding (Dighe and Gokhale, 1997). There are two proposed reasons for the biased fracture of larger particles. First, the probability that a particle will contain a flaw that promotes premature fracture and debonding is greater for larger particles (Cox and Low, 1974). The effect of initial defect size within the particles was not considered in the present study, but can be superposed with the predictions made here. Second, after observing numerous micrographs of debonded and fractured silicon particles, we concluded that silicon particles traditionally labeled as "large" are always irregularly shaped. During solidification it is extremely difficult to form a silicon particle which is both large *and* well rounded. Consequently, based on the results of the present numerical study, it is the consistent irregular shape (and aspect ratio) of large silicon particles further lowers their resistance to fracture.

This DOE study provides the relative influence parametric effects on fatigue crack formation. Although generalizations can be made with this study as we have done, remember that we assumed plane strain conditions and we assumed certain limits on our parameters. Certainly the A356-T6 material has three dimensional structure that may skew the results. Although the relative values for the plastic shear strain would change, the trends would probably be similar. This was observed for two dimensional and three dimensional crystal plasticity studies using the DOE methodology (cf, Horstemeyer and McDowell, 1997; Horstemeyer *et al.*, 1999). The limits were chosen based upon observations from micrographs but certainly in some cases they could be changed and thus altering the plastic shear strain response.

4.2.1.2.1.3. IMPLICATIONS ON THE FATIGUE OF CAST Al-Si ALLOYS

The results of the present study have several ramifications on the understanding and modeling of the mechanical response of cast Al-Si alloys subjected to cyclic loading conditions. As a cast Al-Si material is cyclically loaded or exposed to overloads, the first particles crack or debond will be ones with high aspect ratios aligned with a major axis parallel to the loading axis. In addition, owing to a higher probability for internal or interface inclusions, larger particles of such shape and orientation will favorably fracture. Initial particle cracking and debonding is not strongly affected by neighbor interactions. Consequently, it is more important to consider the particle geometry and expected damaged state (debonded versus fractured) of individual particles rather than the local distribution during the very initial stage of fatigue (crack nucleation period).

During continued cycling, fatigue cracks will eventually form in the surrounding material at the cracked or debonded silicon particles. Based on the present results, the small growing fatigue cracks (on the order of the silicon particle size) will interact with neighboring particles and hence be affected by the distribution (configuration and spacing) of such particles. Furthermore, at such small crack sizes and crack tip driving forces, the neighboring silicon particles will act as barriers to fatigue crack propagation (Gall *et al.*, 1999-B). Consequently, isolated damaged particles are expected to produce relatively larger micro fatigue cracks during subsequent cycling. In either case, the local fatigue cracks nucleated at damaged silicon particles can have two effects on the fatigue response of the cast Al-Si alloy. If no inclusions are present at a larger size scale, such as oxides or pores, then the distributed microcracks will grow until coalescence and final failure of the material. In this situation, the growth characteristics and rates of small microcracks within the particle-laden microstructure will have a strong influence on the fatigue life of the material. Modeling efforts of such behavior might include the *effects* of particle alignment, shape, spacing,

and configuration on small fatigue crack growth rates. If large scale oxides and pores are present in the cast material, then a much larger dominant fatigue crack will nucleate and grow from such inclusions. In this situation, the distributed microcracks will weaken the material ahead of the dominant fatigue crack and, on average, lower the resistance to long fatigue crack propagation. Modeling efforts of such an effect can simply incorporate a continuum damage approach, for example, that effectively elevates the Paris law crack growth rate.

In summary, finite element analyses were constructed to independently study the relative effects of silicon particle size, shape, spacing, configuration, alignment, grouping, and microporosity on particle fracture and debonding within an Al-1%Si matrix. The meshes were designed to conform to a two-level design of experiments methodology where the maximum and minimum values for the above seven parameters were determined based on micrographs of a modified cast Al-Si alloy. Particles within some meshes were fractured and debonded *a priori* in order to study the effects of damaged neighboring particles on the stress distributions near intact particles. The maximum principal stress in the silicon particle was used as a measure of the propensity of a silicon particle to fracture. The maximum hydrostatic stress at the interface between the silicon particle and the Al-1%Si matrix was used as a measure of the propensity of a silicon particle to debond.

Regardless of the damaged state of the neighboring silicon particles, the relative size, grouping, and Al-1%Si matrix microporosity were found to have a negligible effect on the fracture and debonding of intact particles. When all of the silicon particles were intact, the particle shape and alignment were the only parameters among those considered which significantly affected the fracture and debonding of silicon particles within the Al-1%Si matrix. Intact elliptical particles demonstrated the most resistance to fracture and debonding when the major axis of the particle was perpendicular to the applied loading direction. When the major axis of an elliptical particle was parallel to the applied loading direction, the elongated particle demonstrated the least resistance to particle fracture and debonding. Circular particles demonstrated a resistance to fracture and debonding bounded by elliptical particles of the two orientations mentioned above.

When a crack was introduced through the center of a silicon particle, the fractured particle carried a significant fraction of the local redistributed stress field. The Al-1%Si matrix near the fractured silicon particle experienced only a small localization of stresses near the crack tip. When the lower half of a silicon particle was debonded, the debonded particle carried a negligible fraction of the local stress field. The Al-1%Si matrix near the debonded silicon particle experienced severe localization of stresses over a significant distance from the particle. The localization of stress near the fractured and debonded particles altered the stresses in the adjacent intact particles and along their interfaces depending on the shape and orientation of the damaged particle. Despite the lower stresses in the intact case, fractured and debonded particles with a major axis perpendicular to the loading axis caused a more severe localization of stresses in the surrounding Al-1%Si matrix and the adjacent particles. Furthermore, intact silicon particles placed at a 45 degree angle, or along a direction perpendicular to the applied loading axis, showed the greatest influence from fractured or debonded particles.

4.2.1.2.2. ABSOLUTE RESULTS OF PARTICLE SIZE, SPACING, ASPECT RATIO, AND CLUSTER DENSITY OF PARTICLES

Now that relative influence of several parameters related to particles have been determined, we now focus our attention more quantitatively determine the effects of particle size, spacing, aspect ratio, and cluster density. An idealized particle cluster with four particles arranged in two rows and two columns, similar to the pattern of Figure 4.3, is used. These simulations assume perfectly intact particles and serve to generate more information for our understanding. Figures 4.18 and 4.19 show the effects of the particle size on the plastic strain amplitude and the number of cycles for crack incubation. These results indicate that the local plastic shear strain amplitude increases and cycles for crack incubation decreases with increased particle size for the size range analyzed. The relative cycles for crack incubation reduction with the same particle size increase is more distinct at the lower stress level of 110 MPa than at a higher stress level of 165 MPa. Figures 4.20 and 4.21 show the effects of cluster density via particle number in a cluster along the loading direction. For the effects of cluster density (particle number in a cluster along the loading direction), results show that the plastic shear strain amplitude increases quickly when the particle number in a cluster increases from 1 to 3, and the increase rate slows down when more than three particles are involved as shown in Figures 4.18-4.19. This causes the cycles for fatigue crack nucleation to decrease due to the increase of particle numbers in a cluster. The effects of particle aspect ratio and normalized longitudinal particle spacing on the plastic strain amplitude and N_{inc} can also be found, respectively, in Fig. 4.22-4.23, and Fig. 4.24-4.25. For a particle aspect ratio ranging from 1-1.65, the N_{inc} is higher when the ratio is close to 1. The relative reduction for a given increase of particle number is more distinct at lower stress levels than that at higher stress levels. Concerning spacing effects between two particles along the loading direction, the results indicate that the maximum plastic shear strain amplitude is higher when the spacing between particles along the loading direction on the order of the particle size.

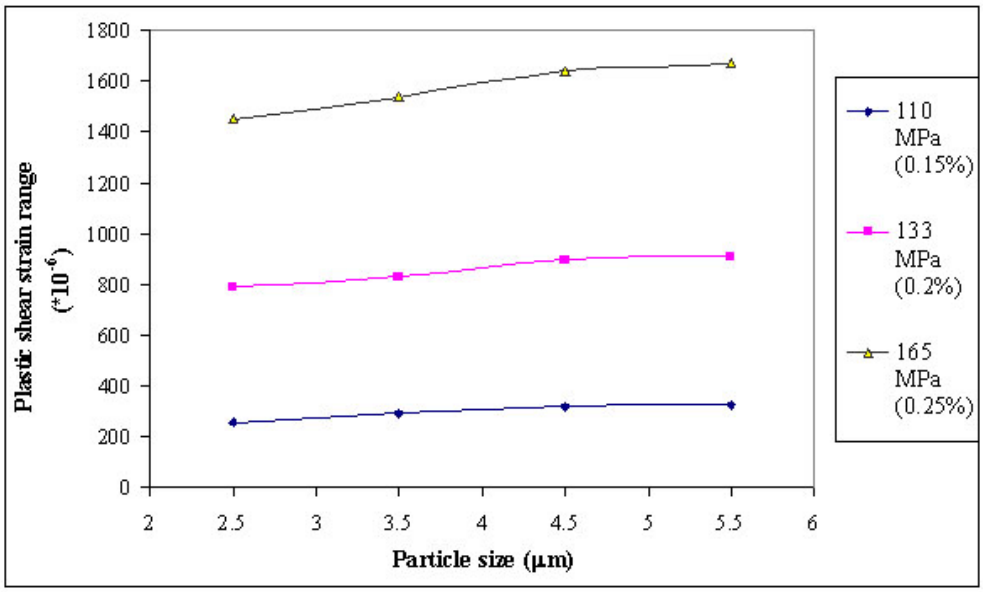

Figure 4.18. Effects of particle size on the average (over a distance of 2μm along loading direction) maximum plastic shear strain range for stress amplitudes of 110, 133 and 165 MPa (R=–1, D_{max}/D_{min}=1.65, L=10 μm, B/L=1, α=0.5, C=0.0211).

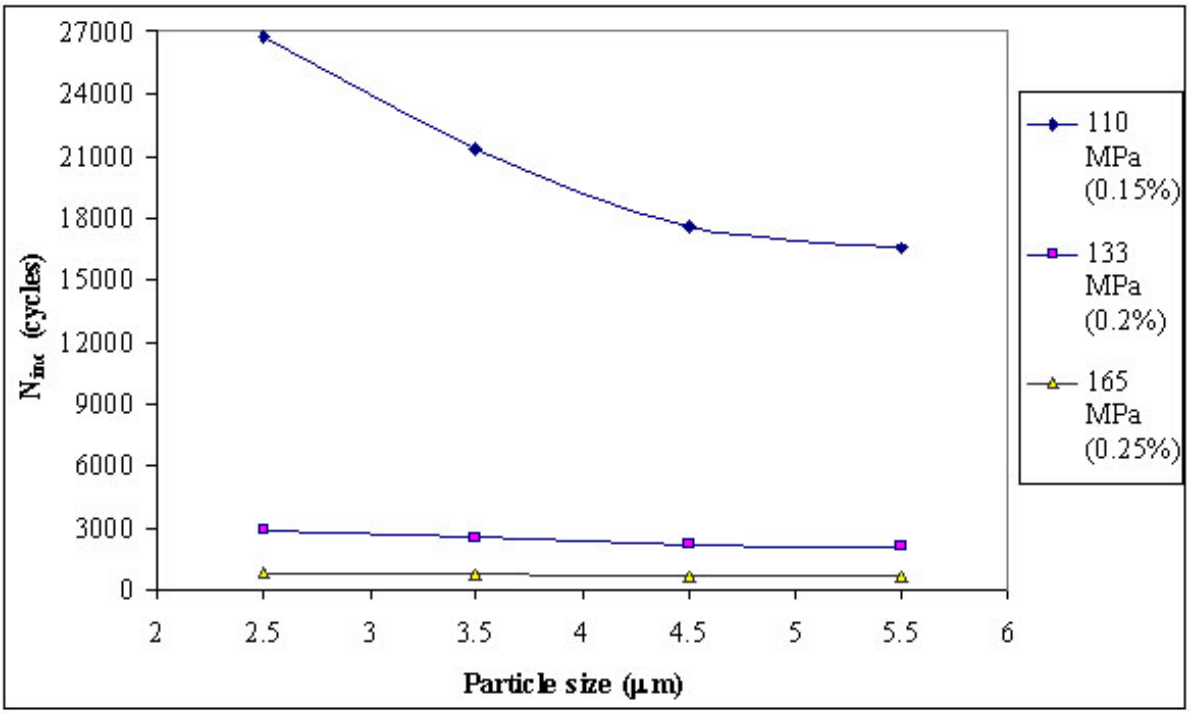

Figure 4.19. Effects of particle size on N_{inc} for stress amplitudes of 110, 133 and 165 MPa (R= –1, D_{max}/D_{min}=1.65, L=10 μm, B/L=1; α=0.5, C=0.0211).

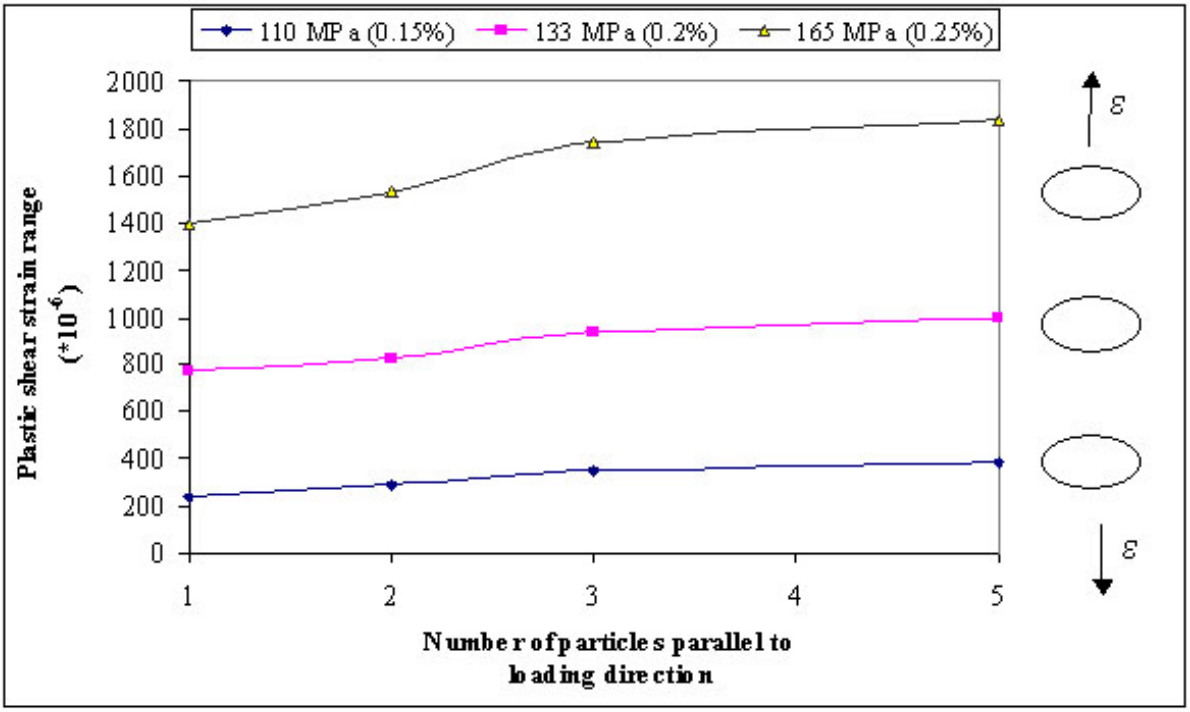

Figure 4.20. Effects of cluster density (number of particles stacked parallel to the loading direction) on the average (over a distance of 2μm along loading direction) maximum plastic shear strain range for stress amplitudes of 110, 133 and 165 MPa (R= –1, D=7 μm, D_{max}/D_{min}=1.65, L/D=0.85, B/L=1.43).

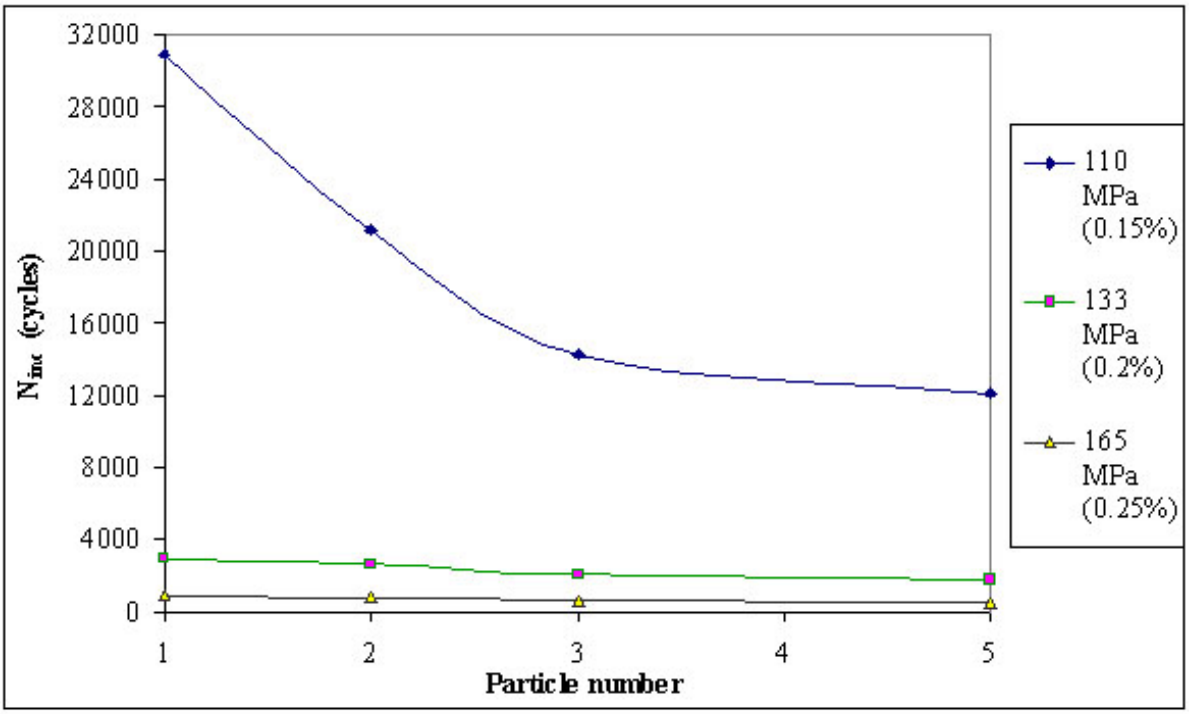

Figure 4.21. Effects of number of particles stacked parallel to the loading direction on N_{inc} for stress amplitudes of 110, 133 and 165 MPa (R= –1, D=7 μm, D_{max}/D_{min}=1.65, L/D=0.85, B/L=1.43, α=0.5, C=0.0211).

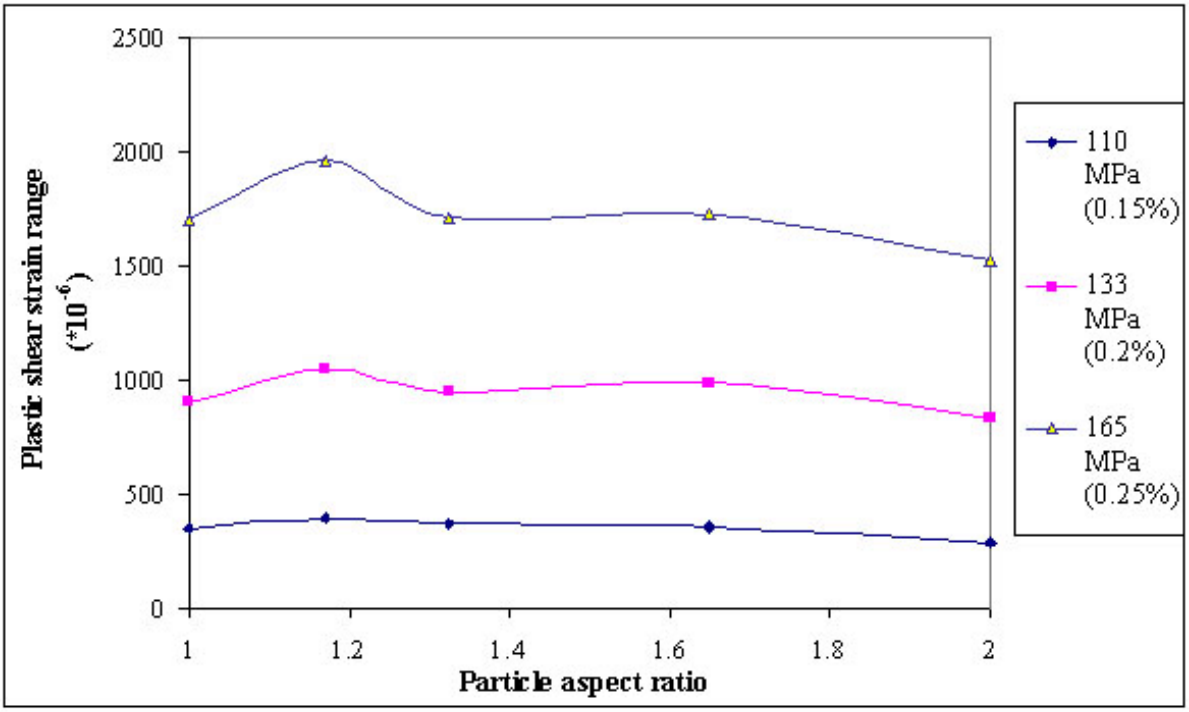

Figure 4.22. Effects of particle aspect ratio on the average (over a distance of 2μm along loading direction) maximum plastic shear strain range for stress amplitudes of 110, 133 and 165 MPa (R= –1, D=7 μm, L/D=1.43, B/D=2.86).

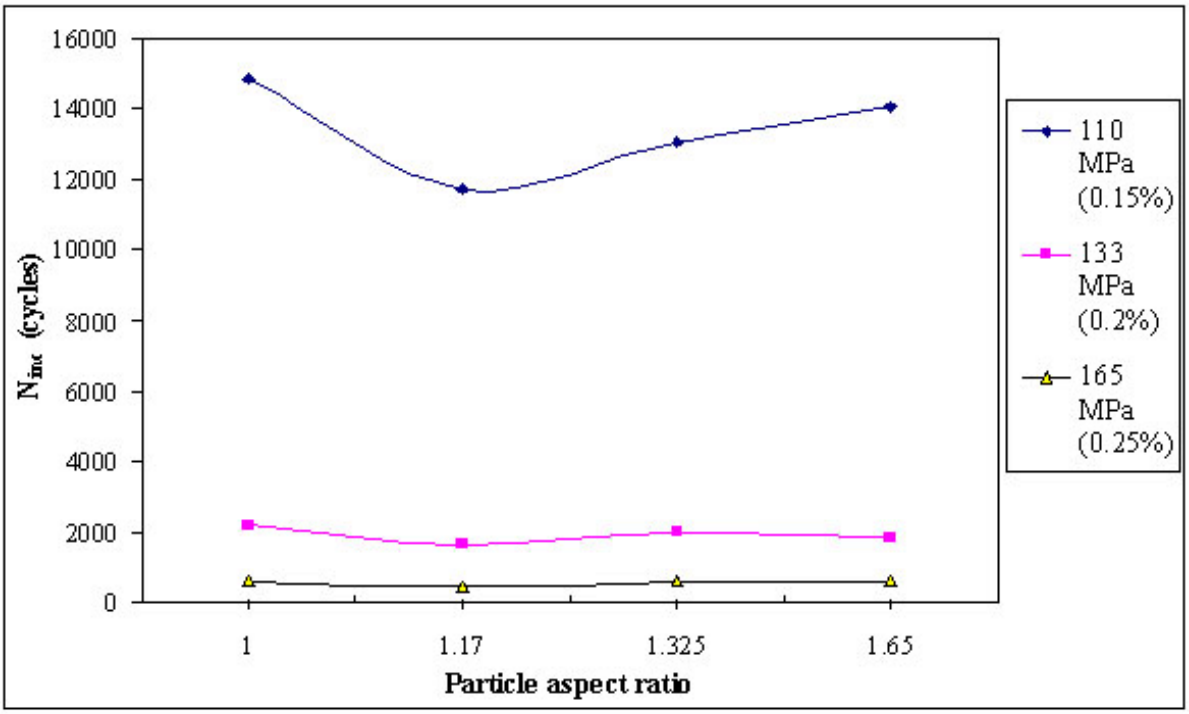

Figure 4.23. Effects of particle aspect ratio on N_{inc} for stress amplitudes of 110, 133 and 165 MPa (R= –1, D=7 μm, L/D=1.43, B/D=2.86, α=0.5, C=0.0211).

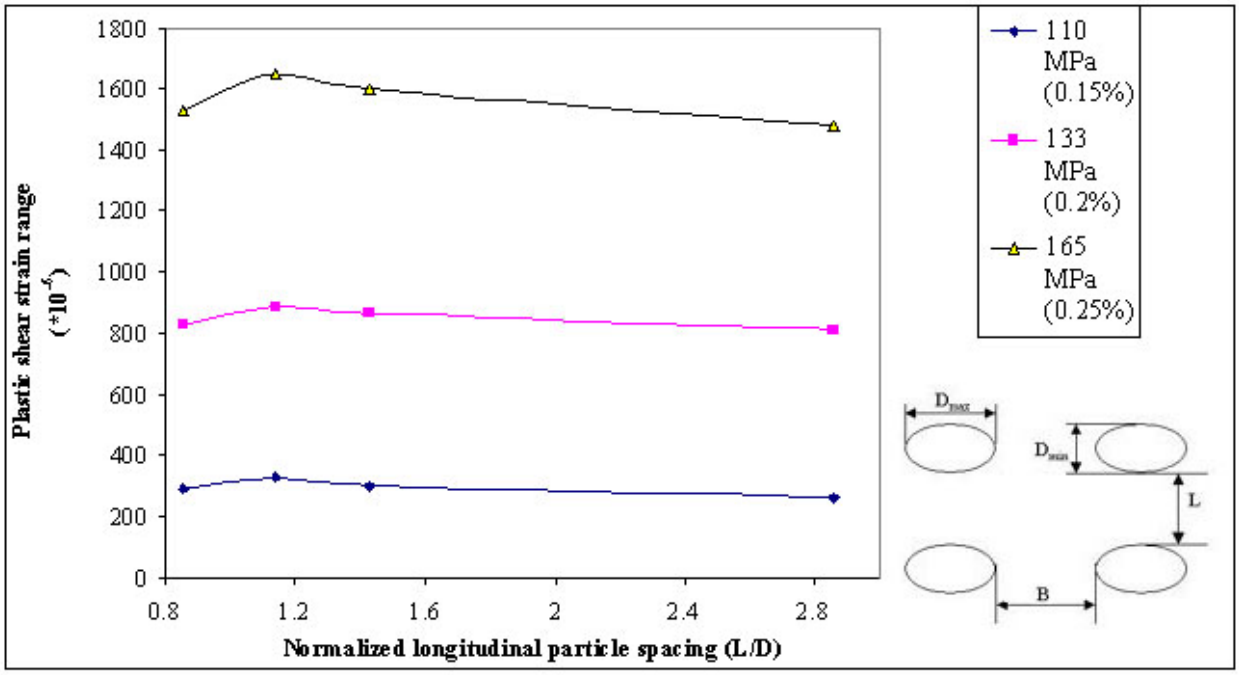

Figure 4.24. Effects of normalized longitudinal particle spacing on the average (over a distance of 2μm along loading direction) maximum plastic shear strain range for stress amplitudes of 110, 133 and 165 MPa (R= –1, D_{max}/D_{min}=1.65, D=7 μm, B/D=2.86).

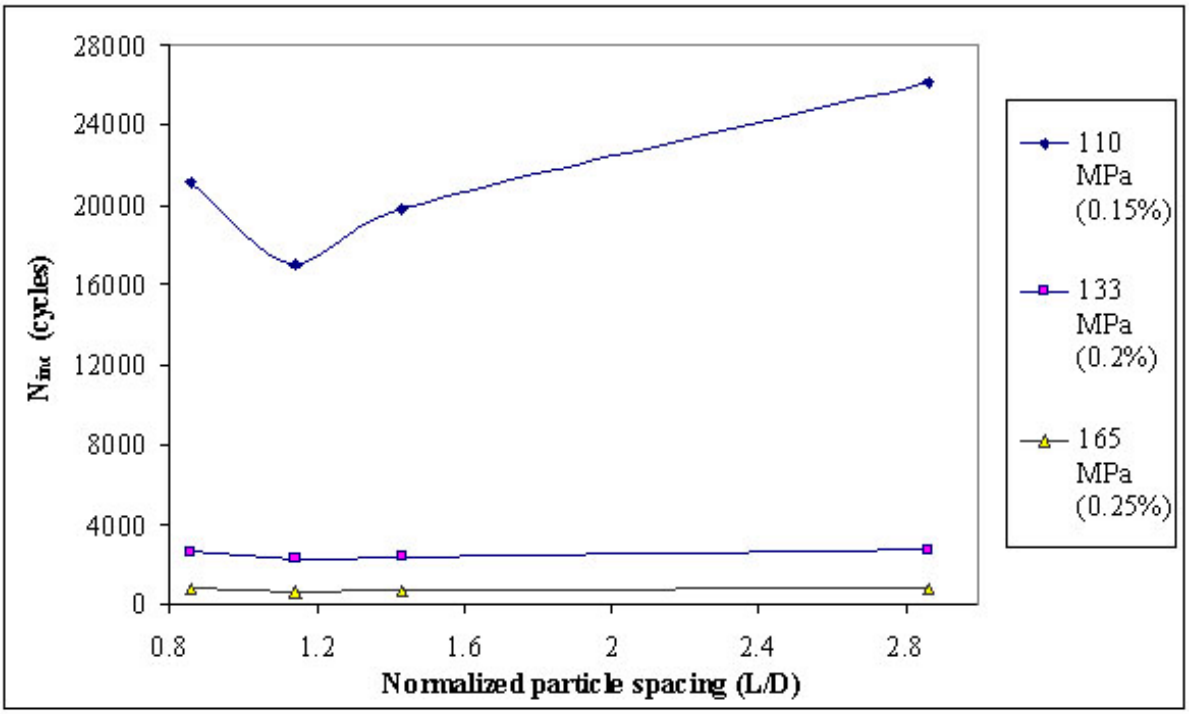

Figure 4.25. Effects of normalized longitudinal particle spacing on N_{inc} for stress amplitudes of 110, 133 and 165 MPa (R= –1, D_{max}/D_{min}=1.65, D=7 μm, B/D=2.86, α=0.5, C=0.0211).

4.2.2. PORES

One of the most deleterious inclusions in cast material is a large pore. In this section, we examine pore effects on crack incubation using both realistic microstructures and idealized geometries for FEA.

4.2.2.1 REALISTIC MICROSTRUCTURE

Figures 4.26 and 4.27 show the distribution of the largest principal stress and effective plastic strain near a realistic pore of A356-T6 Al alloy taken from SEM imaging under symmetric cyclic loading of tension and compression. The maximum and minimum dimensions of the pore in this case are 205 and 131 μm. Over the perimeter of the pore, there are some arcs with small curvature radius. The local curvature radius is about 3.5 μm. The location of the maximum effective plastic strain and principal stress is on the arcs near the major axis that is perpendicular to the loading direction. As the curvature radius decreases, the stress/strain concentration increases. This finding indicates that the local curvature of the pore has an important impact on fatigue crack incubation. The following values from the realistic pore analysis are listed to give a concept of their order. For a pore with effective pore size of 55 μm under strain amplitude of 0.2%, the maximum plastic strain amplitude changed 992 to 1260 με. The stress concentration factor is about two. When the pore size increases to 168 μm, the stress concentration factor increases to about 3.75 and the maximum effective plastic strain is 21,500 μm.

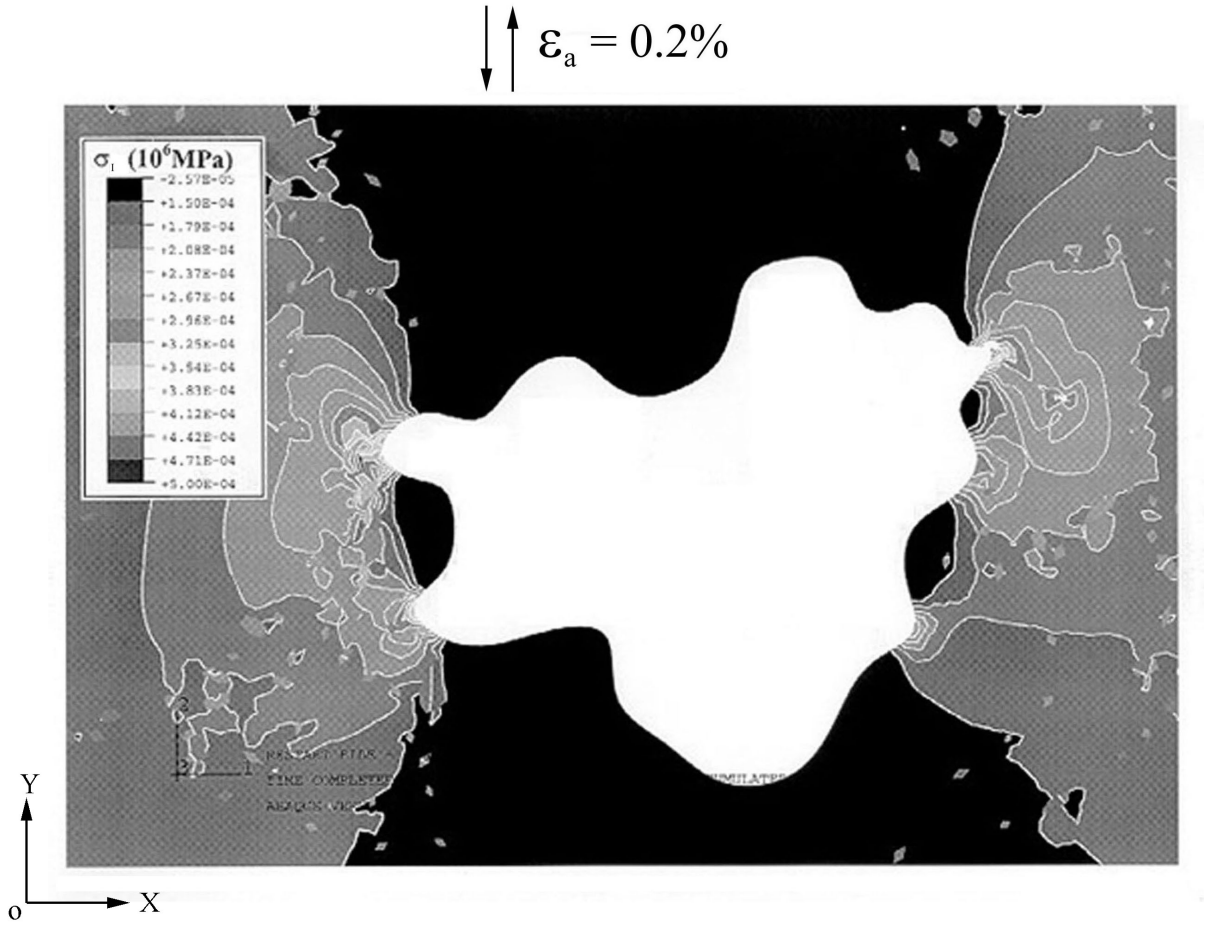

Figure 4.26. Distribution of the maximum principal stress, σ_I, near a realistically shaped pore cross section for A356 Al alloy (R= –1, ε_a=0.2%, pore size = 168 μm, pore ratio=1.6, local radius of curvature=3.5 μm, boundary conditions: uniformly cyclic displacement along the y-direction along the top side, simple support at the right side with u_x=0, simple support at the bottom side with u_y=0, and free at the left side).

4.2.2.2 IDEALIZED MICROSTRUCTURE: PARAMETRIC STUDIES

This section builds on the correlation between the applied strains and the local strains based on FEA from realistic SEM images, focusing on the relative importance of various microstructural features. In particular, we examine pore size, spacing, local curvature, and proximity to the free surface.

To investigate the effects of size, spacing and local curvature of pores on fatigue crack incubation, an idealized pore cluster with pores arranged in the pattern of Figure 4.3 is loaded by remote completely reversed strain amplitudes of 0.15%, 0.2% and 0.25%. Figures 4.28 and 4.29 show distributions of the largest principal stress and the maximum shear plastic strain amplitude in the pore cluster of four pores. The pore size is 500 μm; the pore aspect ratio is two; and local radius of curvature is 35 μm. For an applied strain amplitude of 0.2% (133 MPa), the maximum principal stress is 324 MPa, and the maximum plastic shear strain amplitude is 7960 με. The

stress concentration factor is 2.43, and the ratio of the maximum plastic shear strain amplitude over applied strain amplitude is 3.98. Roughly speaking, the plastic shear strain amplitude of the matrix in pore clusters is about 15-30 times higher than that of the matrix in particle clusters.

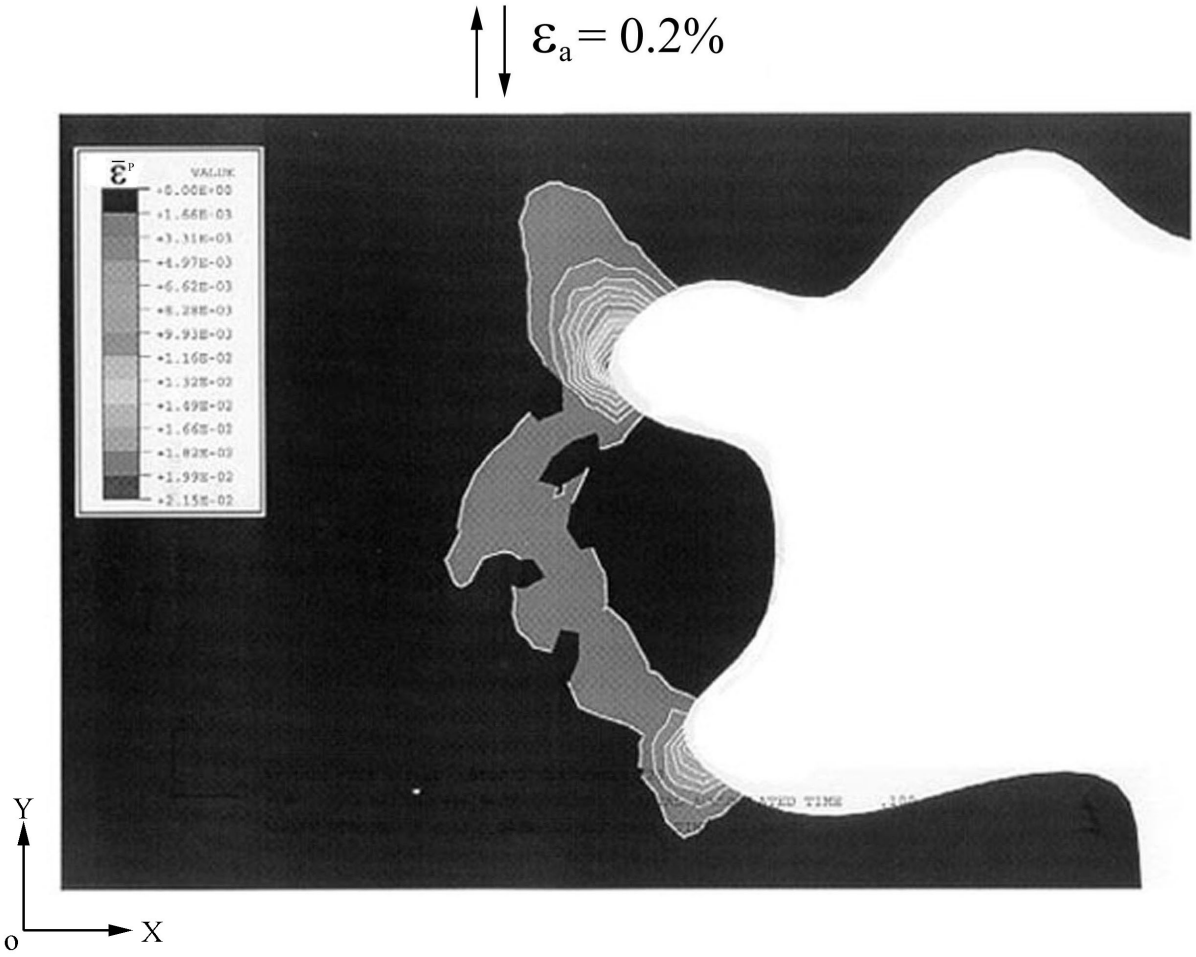

Figure 4.27. Distribution of effective plastic strain, $\bar{\varepsilon}^p$, near a realistically shaped pore cross section for A356 Al alloy (R= –1, ε_a=0.2%, pore size = 168 μm, pore ratio=1.6, local radius of curvature=3.5 μm, boundary conditions: uniformly cyclic displacement along the y-direction along the top side, simple support at the right side with u_x=0, simple support at the bottom side with u_y=0, and free at the left side).

For internal pores, the interaction between neighboring pores is an important parameter for fatigue failure. In these particular analyses, two assumptions need clarification. First, among randomly distributed pore clusters, the fatigue life is mainly controlled by pore clusters with the largest pore sizes. Second, the interaction effects of other pore clusters on the critical pore cluster are only considered through the finite element boundary conditions. Specifically, four pores are taken as a basic set of the largest pore cluster for the analysis. Figures 4.30 and 4.31 show effects of the largest pore size on the maximum plastic shear strain amplitude and the number of cycles

for crack incubation. The effects of pore spacing and the maximum local curvature radius of the pore cluster are shown, respectively, in Figures 4.32-4.33 and 4.34-4.35.

By examining these figures, we conclude several things:
(a) The relative increase of the maximum plastic shear strain amplitude, $\Delta\gamma^{p*}_{max}$, due to the increase of pore size is higher at lower stress amplitudes than at higher stress amplitudes. For example, for a completely reversed, cyclic loading, the computed $\Delta\gamma^{p*}_{max}$ of 8260 με for the 800 μm pore is 2.36 times larger than that for the 100 μm pore under the stress amplitude of 110 MPa; this ratio reduces to 1.9 when the stress amplitude increases to 165 MPa with the $\Delta\gamma^{p*}_{max}$ of 21900 με for the 800 μm pore.
(b) The smaller the pore spacing, the lower the N_{inc}. This arises because smaller pore spacing induces more svere pore interactions, resulting in more plastic shear strain intensification.
(c) When the local curvature radius of the pore reduces from 15 to 7 μm, the local plastic strain range increases quickly. The corresponding N_{inc} is small; 7-100 cycles at the stress amplitudes of 133 and 165 MPa. For a local curvature radius within the range of 15-30 μm, N_{inc} is approximately proportional to the local radius of curvature.

For pores near the free surface, Figure 4.36 shows that there is an intensification of cyclic plastic strain (slip) between the pores and the free surface under cyclic loading. The slip band is nearly $\pm$45 degree to the free surface. The location of the maximum plastic shear strain occurs near the tip of the ellipse that is close to the free surface. This intensification causes crack nucleation near the free surface by persistent slip banding. To simulate this phenomenon, $\Delta\gamma^{p*}_{max}$ and the Fatemi-Socie parameter were calculated for pores with the same geometry and dimension but with different distances between the free surface and the edge of the pore. A quantitative relationship between the maximum plastic shear strain amplitude, the cycles for crack incubation, and the distance between the free surface and the pore extreme under completely reversed tension-compression cyclic loading are shown in Figures 4.37 and 4.38. The results show that $\Delta\gamma^{p*}_{max}$ reduces and N_{inc} increases rapidly from the free surface to the inside of the material. After the distance increases to about the same order of the pore's largest dimension, the decay of $\Delta\gamma^{p*}_{max}$ with distance from the free surface stops, indicating a negligible effect of the free surface on fatigue crack nucleation when the pore is inside of the material. The results show that as the the applied stress amplitude increases, the more severe are the effects of the free surface on the fatigue crack nucleation compared to those at a lower stress amplitude. The tendency of stress amplitude effects differs from that of stress amplitude effects for clusters of interior pores and for particle clusters. In the latter cases, these effects are more pronounced at the lower stress amplitudes.

The $\Delta\gamma^{p*}_{max}$ values obtained for a single pore near a free surface are much higher than those obtained for pore clusters inside of the material. For example, the smallest $\Delta\gamma^{p*}_{max}$ at a stress amplitude of 165 MPa is about 50,000 με for a single pore of 40 μm located 10 μm from the free surface; however, the $\Delta\gamma^{p*}_{max}$ obtained for an interior pore of 100 μm at the same stress amplitude is only about 25,000 με.

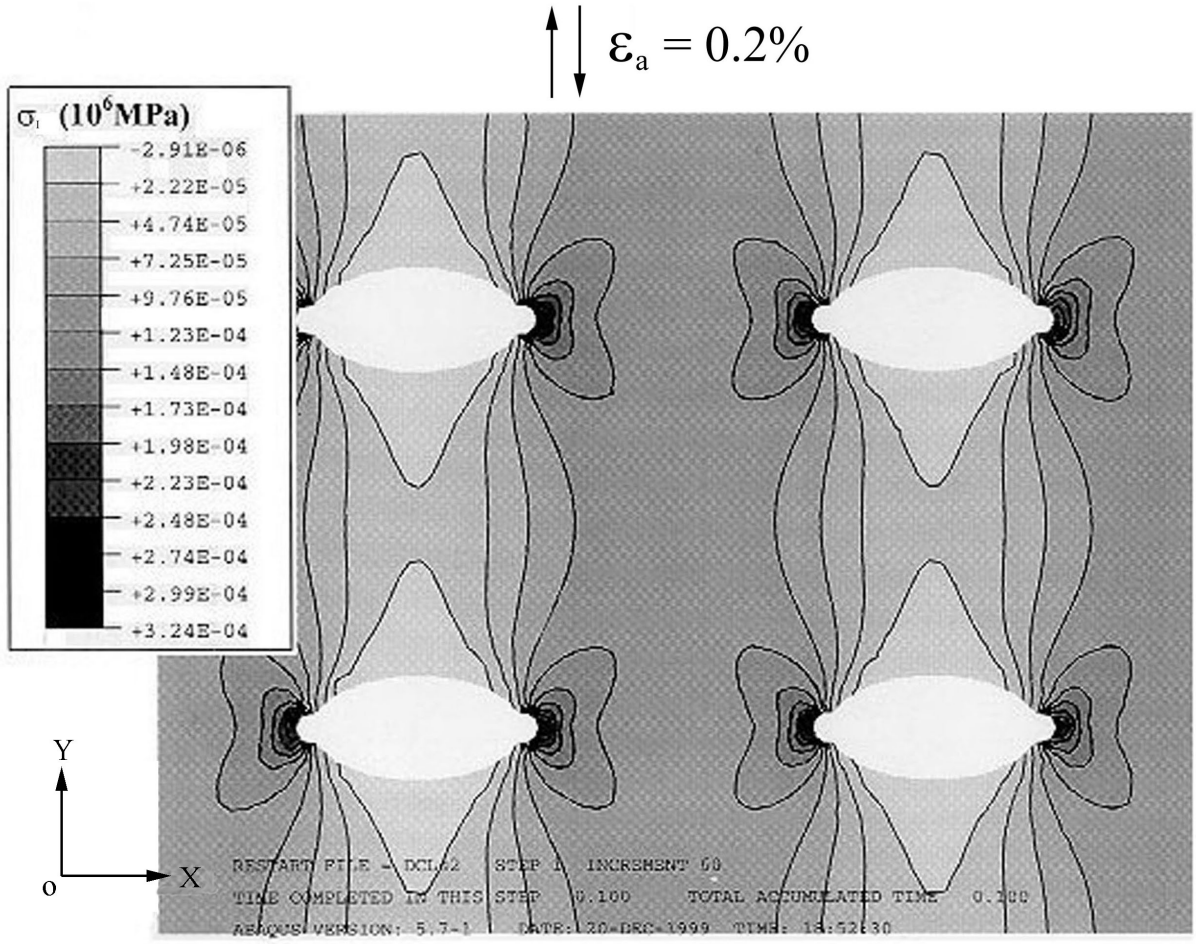

Figure 4.28. Distribution of the maximum principal stress, σ_I, in a contrived cluster of four pores (R=–1, ε_a=0.2%, D=500 μm, D_{max}/D_{min}=2, L=B=720 μm, minimum radius of curvature=35 μm, boundary conditions: periodic conditions along the right and top edges, simple support at the left edge with u_x=0, simple support at the bottom edge with u_y=0).

4.2.3. CRACK INCUBATION: CYCLIC PLASTIC STRAIN INTENSIFICATION

In this section, FEA results are reported that give understanding of the driving force for crack formation. From a continuum standpoint, the primary driving force for fatigue crack formation is assumed to be the local maximum plastic shear strain amplitude, $\Delta\gamma^{p*}_{max}$, with respect to all possible shear strain planes. Three loading amplitudes ($\Delta\varepsilon/2$ = 0.10%, 0.15, 0.20%) and three strain ratios (R = -1, 0, 0.5) were considered in determining the crack opening displacement for cracks near silicon particles and pores. The results show that perfectly bonded particles have $\Delta\gamma^{p*}_{max}$ values two orders of magnitude less than those for voids, cracked, or debonded particles. A cracked particle facilitates extremely large local stresses in the broken particle halves, which will invariably lead to the debonding of a cracked particle. Based on these two observations, debonded particles and voids are asserted to be the critical inhomogeneities for fatigue crack formation. Furthermore, for voids and debonded particles, shape has a negligible effect on fatigue crack formation compared to other significant effects such as inhomogeneity size and reversed loading conditions (R-ratio). Increasing the size of a particle by a factor of four

increases $\Delta\gamma^{p*}_{max}$ by about a factor of two. At low R-ratios (R=–1) equivalent sized voids and debonded particles have comparable $\Delta\gamma^{p*}_{max}$ values. At higher R-ratios (R=0, 0.5) debonded particles lead to $\Delta\gamma^{p*}_{max}$ values twice that of voids.

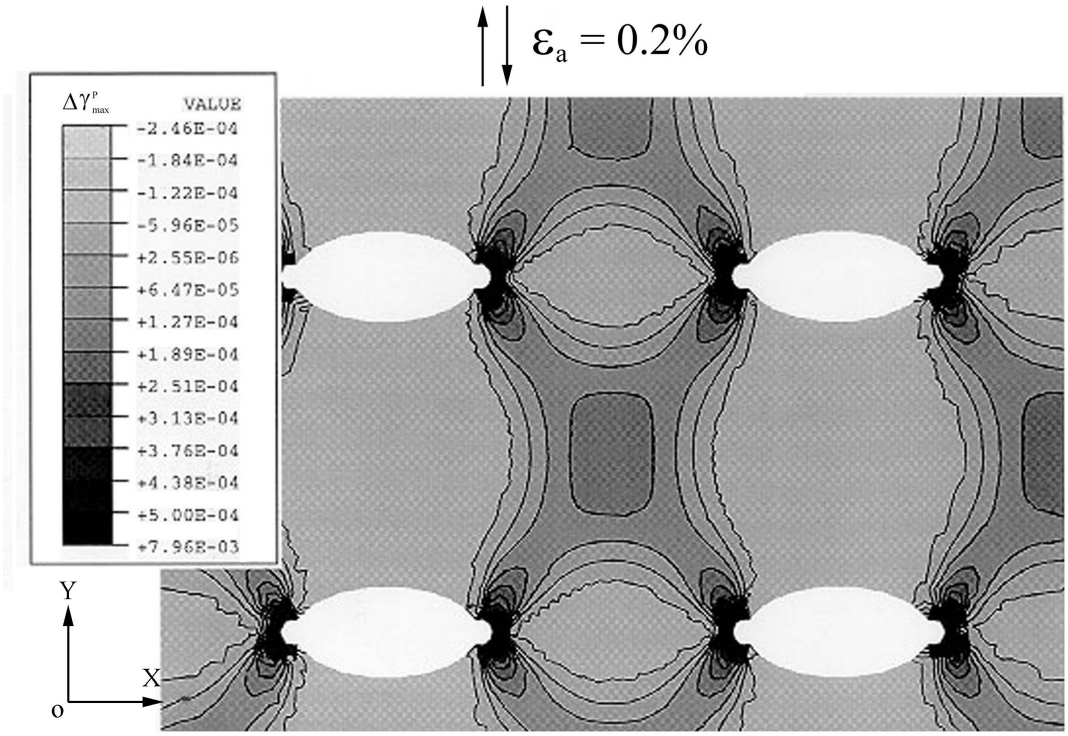

Figure 4.29. Distribution of the maximum plastic shear strain range in a contrived pore cluster of four pores (R=–1, ε_a=0.2%, D= 500 μm, D_{max}/D_{min}=2, L=B=720 μm, minimum radius of curvature=35 μm, boundary conditions: periodic conditions along the right and top edges, simple support at the left edge with u_x=0, simple support at the bottom edge with u_y=0).

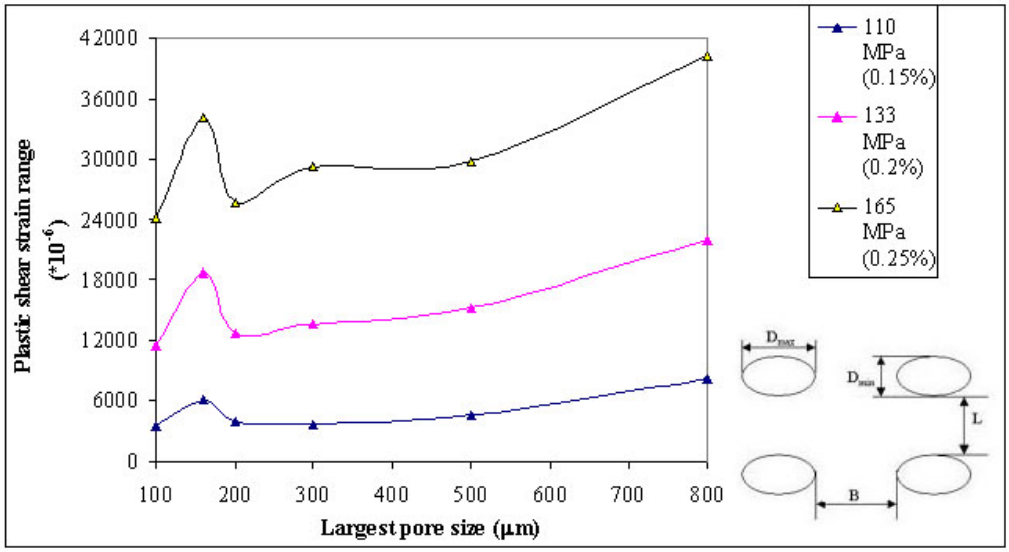

Figure 4.30. Effects of pore size on the average (over a distance of 20μm perpendicular to the loading direction) maximum plastic shear strain range in a contrived cluster of four pores for stress amplitudes of 110, 133 and 165 MPa (R= –1, D_{max}/D_{min}=2, B=L=720 μm).

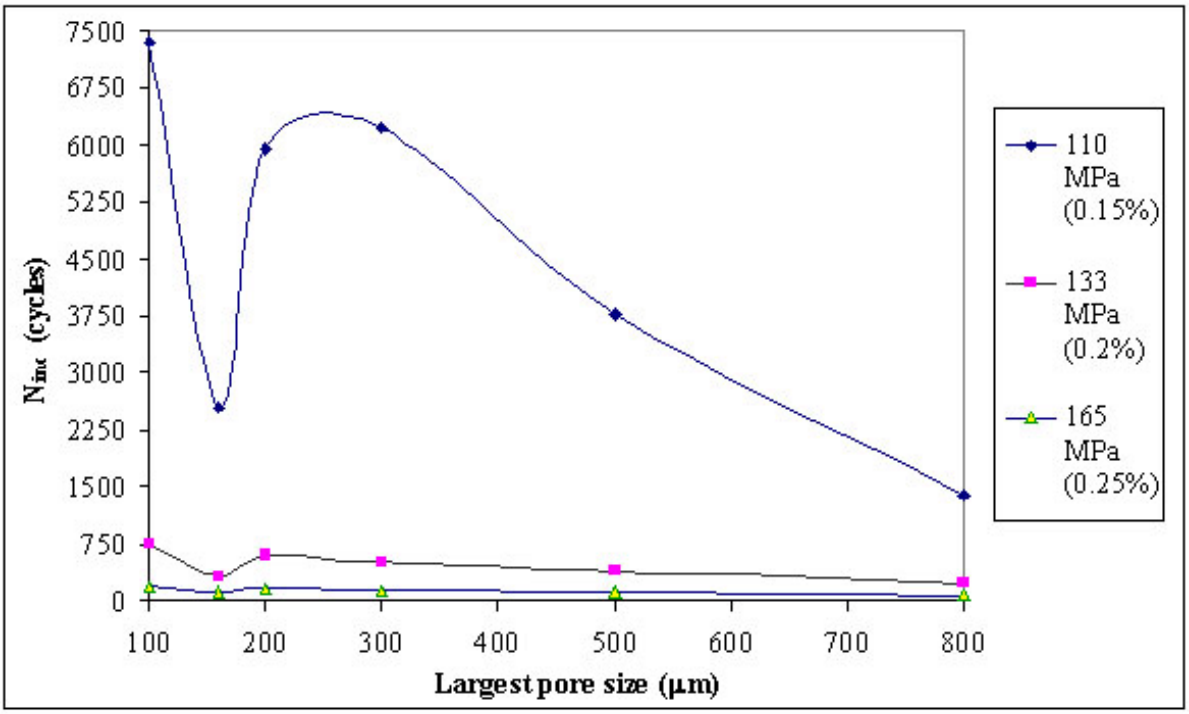

Figure 4.31. Effects of pore size on N_{inc} in a contrived cluster of four pores for stress amplitudes of 110, 133 and 165 MPa (R= –1, D_{max}/D_{min}=2, B=L=720 µm, α' =0.5464, C' =0.0622).

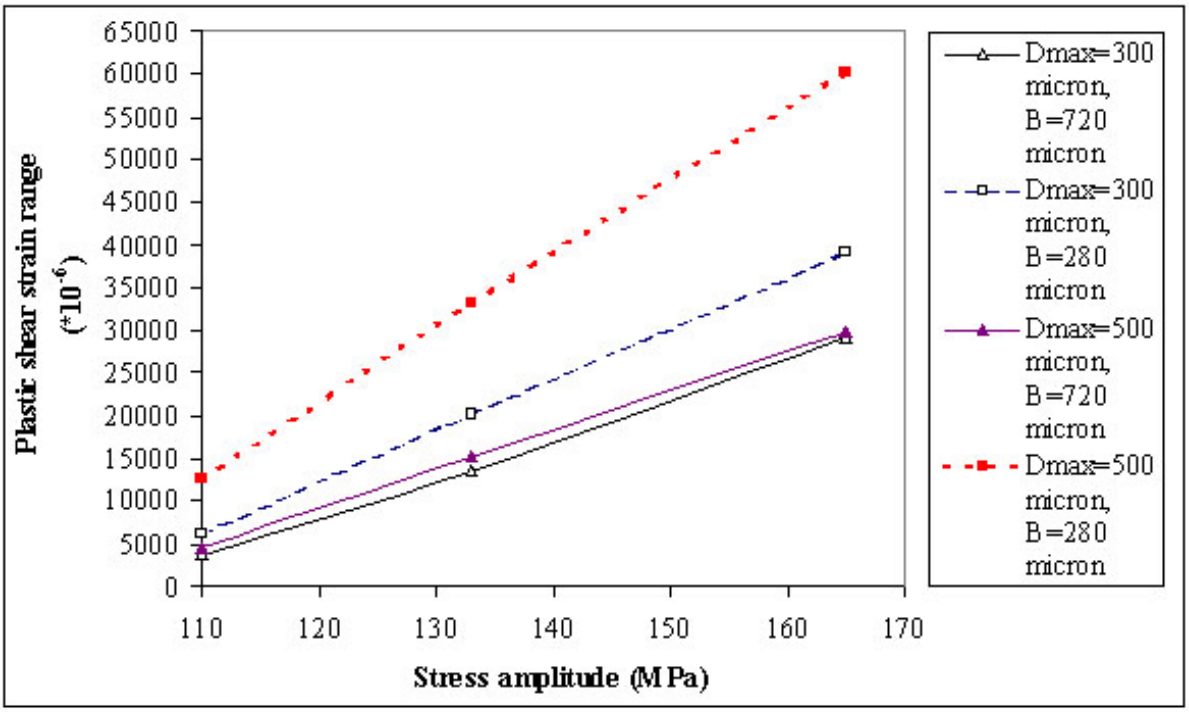

Figure 4.32. Effects of pore spacing in a contrived cluster of four pores on the average (over a distance of 20µm perpendicular to the loading direction) maximum plastic shear strain range for the pore sizes of 300 and 500 µm versus applied stress.

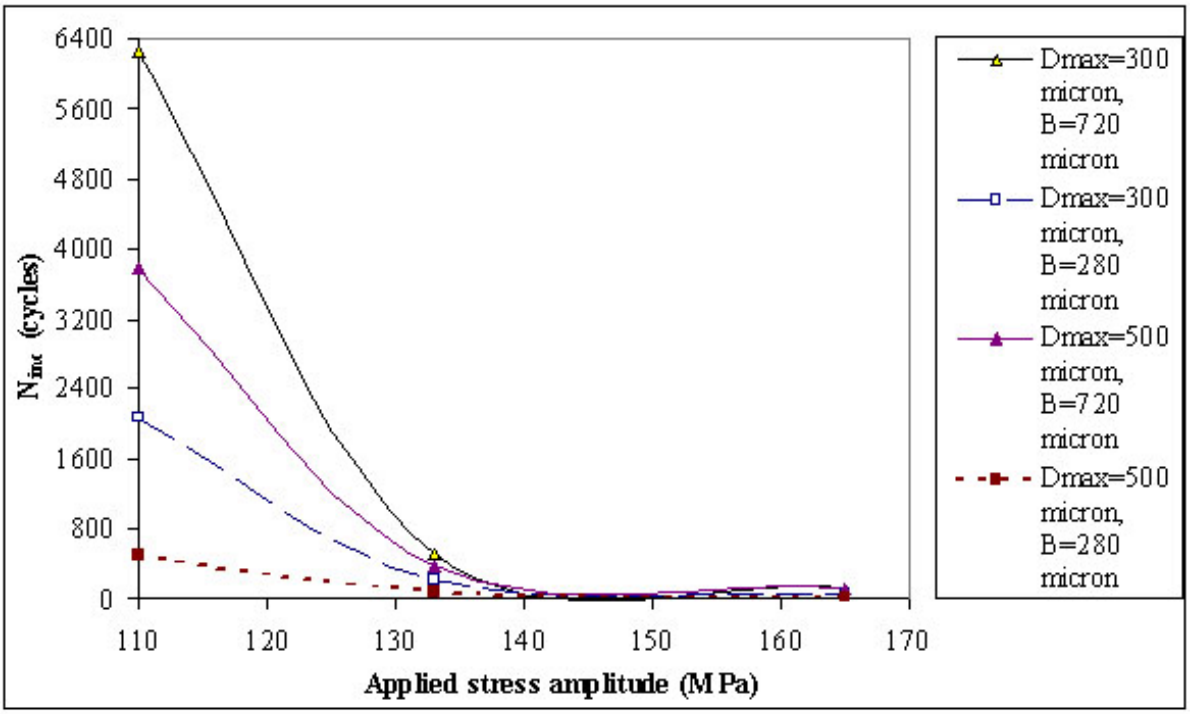

Figure 4.33. Effects of pore spacing in a contrived cluster of four pores on N_{inc} for the pore sizes of 300 and 500 μm versus applied stress (R= –1, D_{max}/D_{min}=2, B/L=1, α' =0.5464, C' =0.0622).

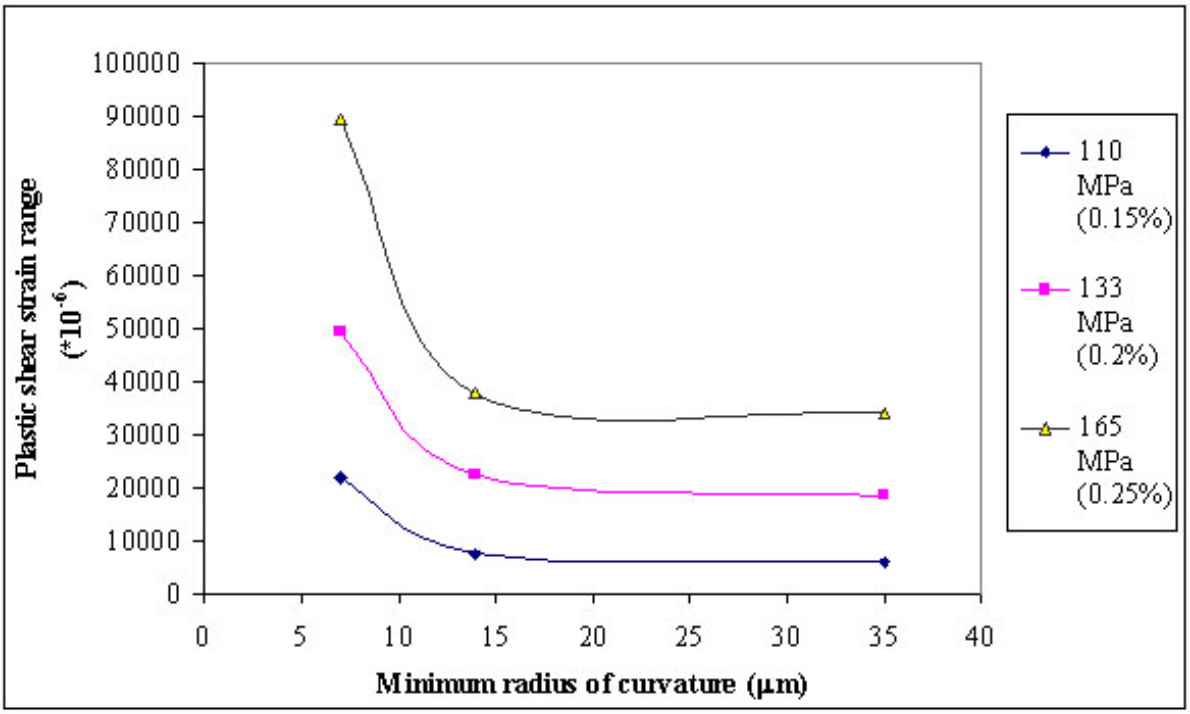

Figure 4.34. Effects of the minimum radius of curvature in a contrived cluster of four pores on the average (over a distance of 20μm perpendicular to the loading direction) maximum plastic shear strain range at applied stress amplitudes of 110, 133 and 165 MPa (D_{max}/D_{min}=2, D_{max}=150 μm, R= –1).

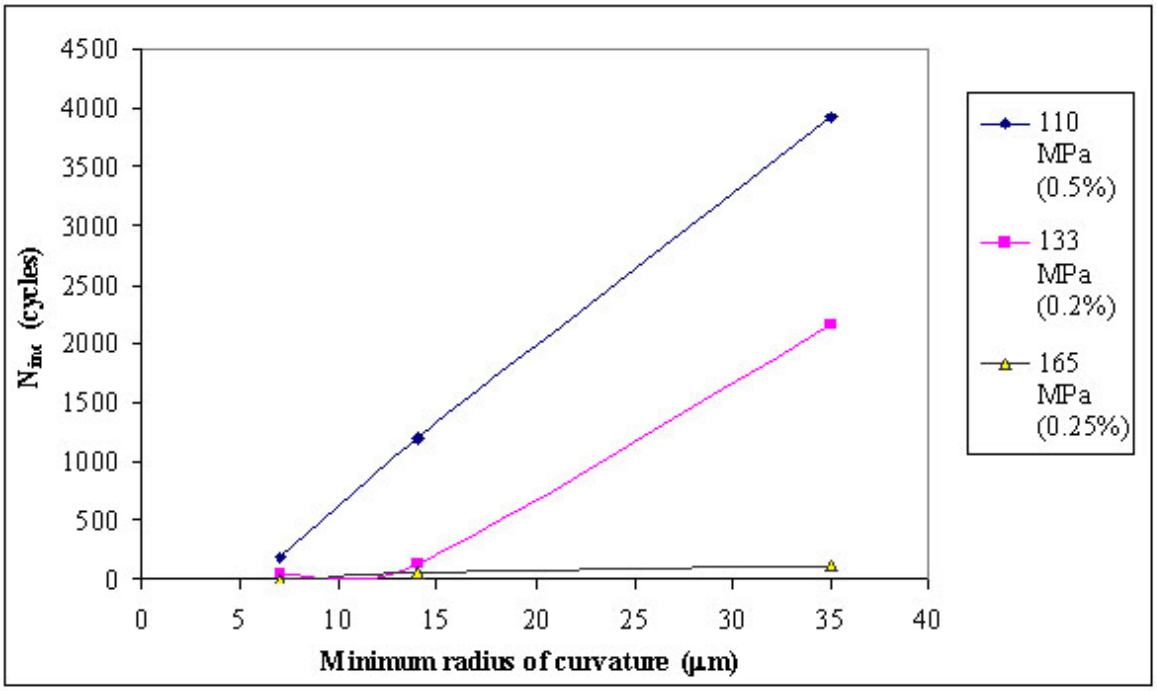

Figure 4.35. Effects of the minimum radius of curvature in a contrived cluster of four pores on N_{inc} at applied stress amplitudes of 110, 133 and 165 MPa (D_{max}/D_{min}=2, D_{max}=150 μm, R= –1, α'=0.5464, C'=0.0622).

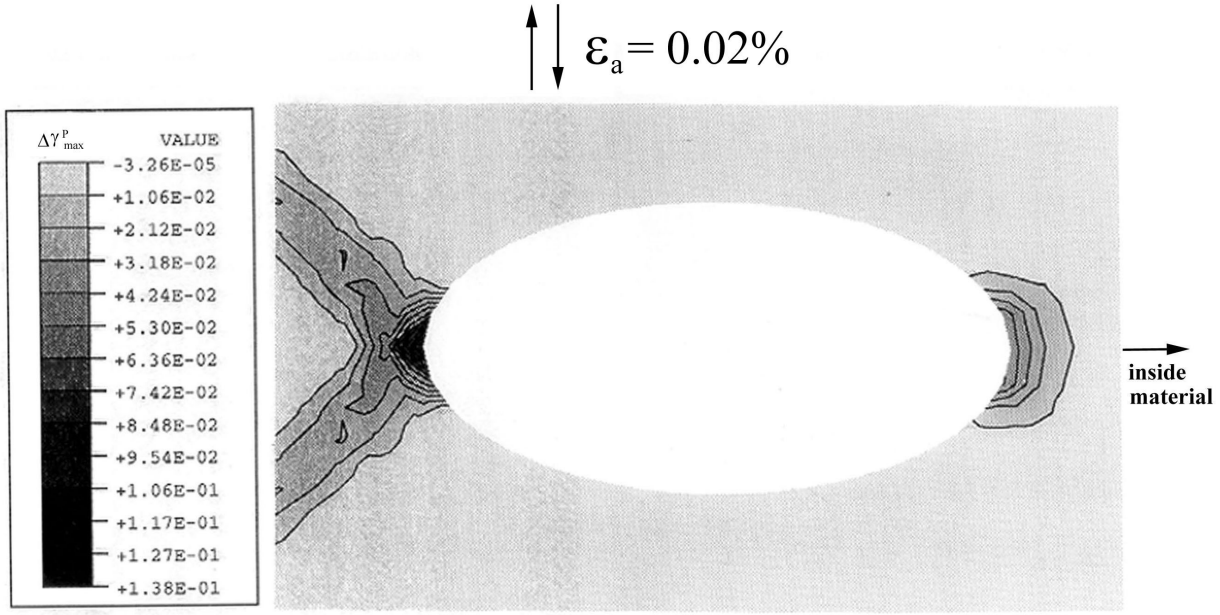

Figure 4.36. Contours of the maximum plastic shear strain range around a pore near a free surface (R=–1, D_{max}/D_{min}=2, D_{max}=40 μm, ε_a=0.2%, boundary conditions: uniformly cyclic displacement along the y-direction at the top side, simple support at the right side with u_x=0, simple support at the bottom side with u_y=0, and free at the left side).

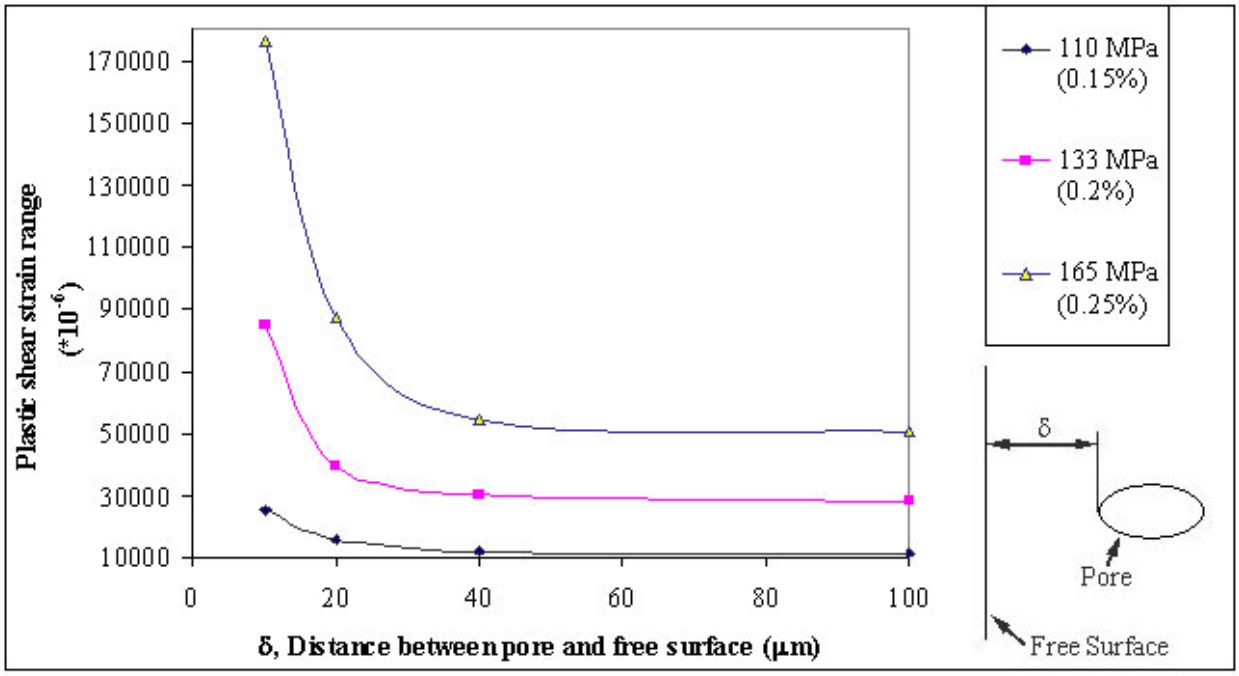

Figure 4.37. Effects of the distance between a pore and a free surface on the average (over a distance of 7.5 μm perpendicular to the loading direction) maximum plastic shear strain range for applied stress amplitudes of 110, 133 and 165 MPa (R= –1, D_{max}/D_{min}=2, D_{max}=40 μm).

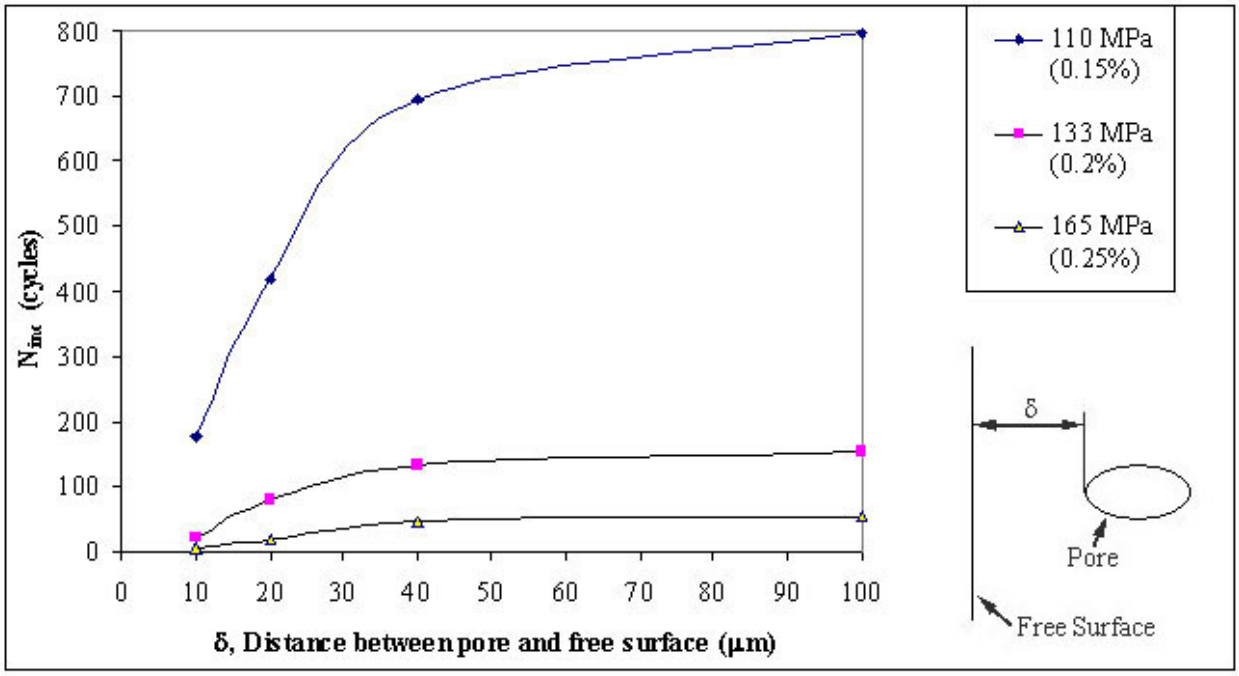

Figure 4.38. Effects of the distance between a pore and a free surface on N_{inc} for applied stress amplitudes of 110, 133 and 165 MPa (D_{max}/D_{min}=2, D_{max}=40 μm, R= –1, α'=0.5464, C'=0.0622).

4.2.3.1. FEA PRELIMINARIES

SEM images from the fracture surface of a cast Al-Si-Mg alloy (A356-T6) subjected to cyclic loading conditions ($\Delta\varepsilon/2 = 0.2\%$, $R = -1$, $N \sim 100{,}000$ cycles) were used to motivate the study for the plastic strain intensification. Figure 4.39 shows the pertinent images related to our study. The image on the left shows a typical casting pore (void) and the image on the right shows an Al-Oxide inclusion. The inhomogeneities in Figure 4.39 are located at the specimen surface and were determined to be the initiation sites for the fatigue crack which ultimately caused final fracture. The inhomogeneities in Figure 4.39 have curved interfaces with the matrix material, as evident from the black outlines marking the inhomogeneity-matrix boundary. The present study will consider both realistic shaped inclusions with local radii of curvature as observed in Figure 4.39, and idealized circular inhomogeneities.

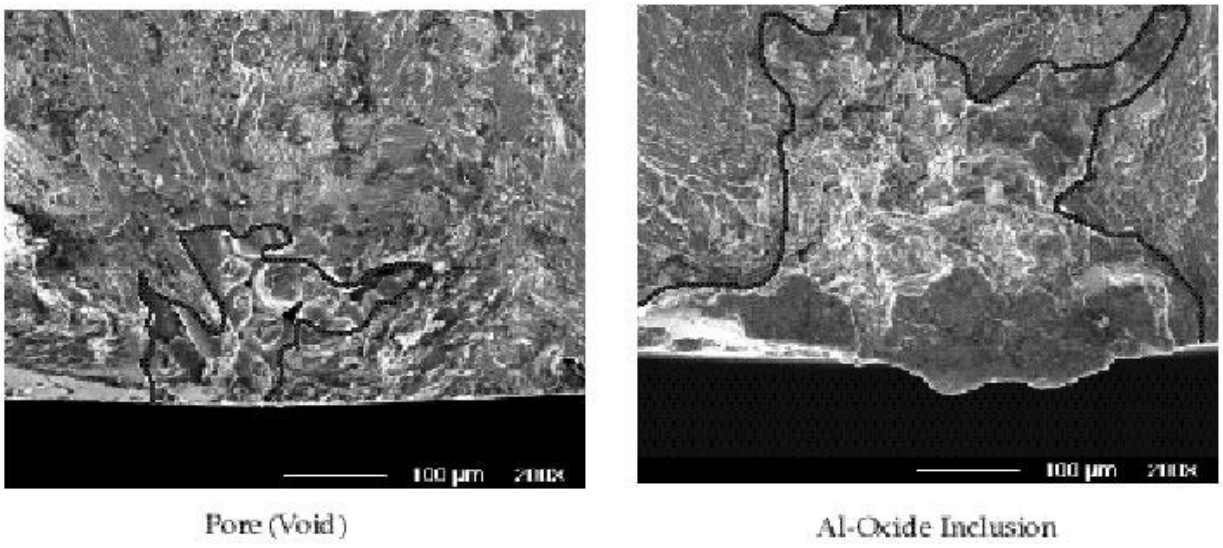

Figure 4.39. Scanning electron microscope (SEM) images from the fracture surface of a cast A356-T6 aluminum alloy showing a pore (void) and an inclusion as fatigue crack nucleation sites.

Figure 4.40 is an idealized schematic of the material inhomogeneities imaged on the fracture surface in Figure 4.39. The pore (void) is considered to be a domain over which the matrix material is absent. The inclusion is a domain over which the matrix material is replaced by a brittle, elastic second phase with no initial misfit stresses. The unique feature of a second phase inclusion, in contrast to a void, is that different local boundary conditions must be considered in the case of the smaller inclusion. The inclusion can be considered to exist in three different states; perfectly bonded, cracked, and debonded. A perfectly bonded and pristine inclusion

contains no crack-like inclusions and is forced to obey radial and tangential displacement compatibility across the interface with the matrix material. A cracked inclusion still maintains displacement compatibility across the particle-matrix interface; however, the inclusion itself contains a traction free crack. A debonded inclusion is assumed to be defect free itself, however, the interface between the matrix and the inclusion contains a crack. The cracked particles will have a defect that spans the entire inclusion, since it is unlikely that such a brittle phase will contain a significant partial crack. Moreover, the debonded inclusion will have an interface crack that covers only a portion of the particle circumference as experimentally observed (Lankford and Kusenberger, 1973; Lankford, 1976).

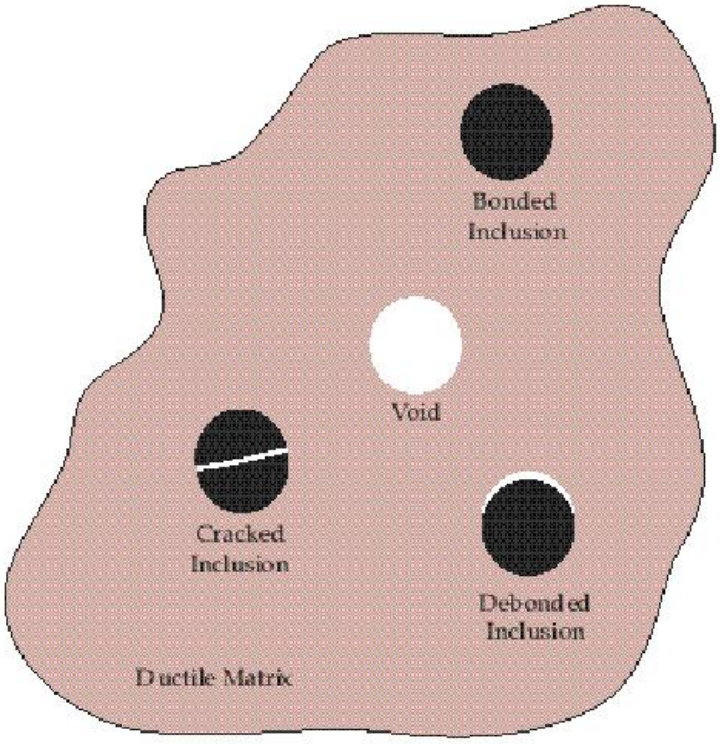

Figure 4.40. Schematic of the different types of inhomogeneities considered in the present finite element study of fatigue crack formation.

Two-dimensional finite element meshes used for the fatigue crack formation study are presented in Figure 4.41. The elements in Figure 4.41 are plane strain isoparametric elements with four nodes each. The entire mesh is shown in Figure 4.41a, while the different fine mesh regions are shown in Figure 4.41b. The mesh in Figure 4.41a has symmetry conditions applied to the left face ($u_x = 0$), the right face is specified as a free surface, and the bottom face is constrained from moving in the y-direction ($u_y = 0$). Far-field displacement boundary conditions were applied to the top face by prescribing the u_y displacements in a linear monotonic or cyclic ramp. The finite element simulations were conducted in the commercial code ABAQUS (1994) with a UMAT material subroutine containing the Bammann *et al.*, (1993) plasticity model. Three different fine mesh regions were considered in the present finite element study; an idealized circular shape and two star-like shapes (Figure 4.41b). The meshed inclusions are set below the respective fine mesh regions when appropriate. The idealized circular shape is used for finite element studies of voids, bonded inclusions, cracked inclusions, and debonded inclusions. Whenever internal surfaces were introduced into the finite element meshes, frictionless contact conditions were

prescribed on the exposed elements. The contact conditions prevented the aphysical overlap of internal surfaces during deformation. The awkward star shaped inhomogeneities are specific to either an inclusion or a void (pore). The shapes of the star inclusion and pore attempt to model the worst case scenario for the respective inhomogeneity. The star inclusion contains sharp corners and fingers extending into the matrix material, consistent with a realistic solidification front for an inclusion. The star pore contains very sharp internal radii of curvature where the advancing solidification fronts inevitably contact during casting. Moreover, in processed powder metallurgy alloys, the sintering of spheroidal particles during compaction will invariably lead to void inclusions with inner radii as modeled in Figure 4.65b. The overall size of the different inclusions is kept constant to appropriately compare the results from inhomogeneities of different shapes.

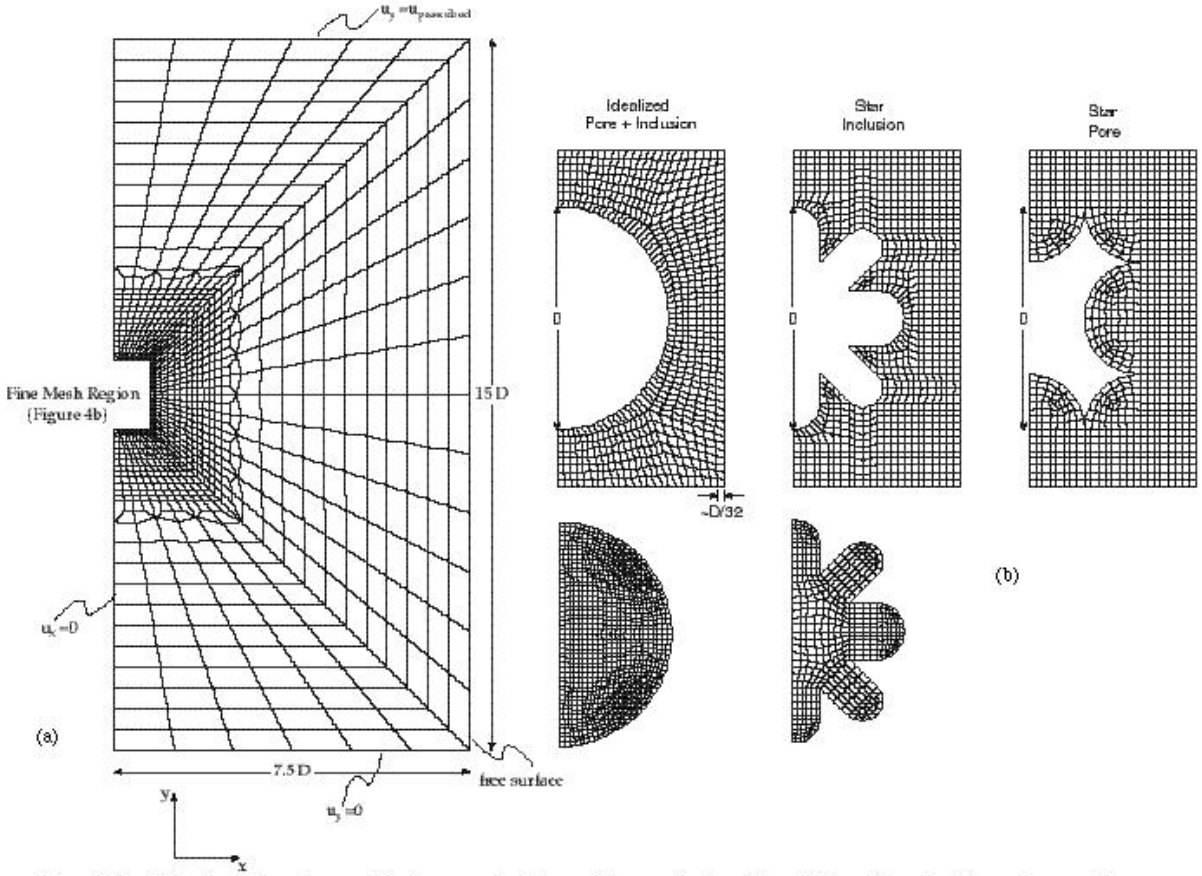

Figure 4.41. Finite element meshes used for the present study on fatigue crack formation. (a) Overall mesh and boundary conditions. (b) Fine mesh regions for different inclusion and void shapes. The meshed inclusions are set below the appropriate fine mesh regions.

In order to extract meaningful results from finite element models it is important to determine the sensitivity of the results to the chosen finite element mesh. To study such dependence, three finite element meshes were constructed with an idealized half-debonded inclusion surrounded by a matrix of Al-1.0%Si-0.3%Mg. The debonded inclusion was chosen as the model situation for the mesh refinement analysis since it causes extremely localized plasticity compared to the other inhomogeneities as will be shown in the Results and Discussion. The different meshes were designed such that the approximate size of the elements in the fine mesh region changed from 1/12 D to 1/20 D to 1/32 D (Figure 4.41b), where D is the diameter of the idealized circular inclusion. The far ends of the meshes were displaced in monotonic tension to a remote nominal strain of 0.25%, which is just above the macroscopic yield strain (0.23%) of the Al-1.0%Si0.3%Mg matrix material. The maximum plastic shear strain, $\Delta\gamma^{p*}_{max}$, was tracked throughout the deformation for all three meshes. We note that the present study considers the maximum plastic shear

strain with respect to the spatial location within the mesh *and* the associated shear strain plane. Two different methods were used to quantify of $\Delta\gamma^{p^*}_{max}$ for the three different mesh sizes:

1. The point-wise maximum (for individual elements) γ_{max} value near the debonded inclusion.

2. An average value of γ_{max}, denoted as $\Delta\gamma^{p^*}_{max}$, defined over an equivalent spatial area, A, near the debonded inclusion.

A schematic demonstrating the determination of $\Delta\gamma^{p^*}_{max}$ for a typical finite element mesh subjected to a total tensile strain of 0.2% is presented in Figure 4.42. Only the fine mesh region is shown in Figure 4.42, since the plasticity is concentrated near the inhomogeneity. The averaging domain, A, for calculating is placed in a region where the γ_{max} contours are a maximum (Figure 4.42). In Figure 4.42, the domain A covers about 12 elements, or approximately $0.012\ D^2$. The finite element predictions will depend on the selected averaging area, and the appropriate choice of A depends on the physical phenomenon of interest. In the finite element study, A was scaled with the particle diameter D since there is not a length scale inherent in the present finite element analysis. In reality, fatigue crack formation mechanisms operate over size scales on the order 0.2 μm, depending on the material of interest (Harvey *et al.*, 1994). Consequently, when extracting the driving force for fatigue crack formation from a continuum based analysis, it is appropriate to average over a size scale no larger than several microns. Furthermore, the averaging size scale should not be smaller than about 0.2 μm since local continuum calculations for the matrix are unable by themselves to describe the materials capacity to resist singularities by virtue of dislocation self-organization processes. In any case, since the present finite element analysis does not contain a length scale, the averaging size is considered relative to the inhomogeneity size. Such an approach limits the extension of the results to situations where the modeled inclusion is extremely large or small since the averaging size may lose physical meaning.

The largest local γ_{max} and $\Delta\gamma^{p^*}_{max}$ values in the mesh are both plotted as a function of the applied far-field strains in Figures 4.43 (a) and 4.43 (b), respectively. When the maximum plastic shear strain is determined using a point-wise measurement of γ_{max}, the finite element results diverge as the mesh is refined (Figure 4.43a). The divergence of the finite element model is an artifact of the extremely strong plastic strain gradients near a debonded particle, which essentially serves as a crack-like singularity. As the mesh is refined, the elements near the tip of the debond crack are capable of extrapolating over a smaller length scale, thus the peak plastic shear strain increases as the element size cuts the local plastic strain distributions closer to the crack tip. Conversely, when the maximum plastic shear strain value is extracted by considering an average value, $\Delta\gamma^{p^*}_{max}$, over $A = 0.12D^2$, the finite element results are invariant to the mesh size to within numerical error for the D/20 and D/32 meshes (Figure 4.43b). The mesh with a fine mesh region size of D/12 appears a bit too coarse to capture the relevant local plastic shear strain gradients for this averaging size. When the mesh is refined there is an increase in γ_{max} over a small spatial area adjacent to the inclusion for finer meshes. However, such an increase over a small area is negligible when averaging over larger spatial length scales, hence the invariance in the average γ_{max}. The remaining finite element analyses use the mesh with a local element size of D/32 (Figure 4.41).

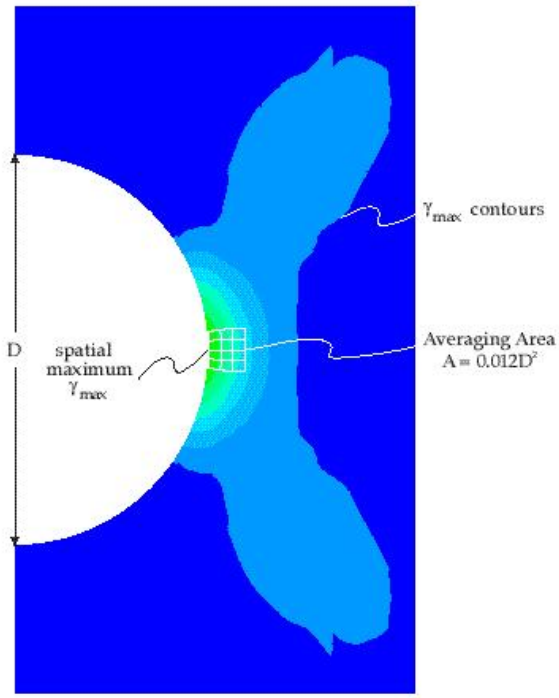

$$\gamma_{max}^{ave} = \frac{1}{A}\int_{A} \gamma_{max}\, dA$$

Figure 4.42. Schematic demonstrating the determination of the local average maximum plastic shear strain, γ_{max}^{ave}, from contours of the maximum plastic shear strain, γ_{max}.

4.2.3.2. FEA SIMULATIONS FOR LOCAL CYCLIC PLASTICITY: DISCUSSION

The monotonic results provide the relative intensification of plastic strains and stresses near the inclusions and pores. Figures 4.44 through 4.47 present contour plots of the maximum plastic shear strain, γ_{max}, where the maximum is with respect to all possible shear strain planes. The contour plots in Figures 4.44 through 4.47 are only small sections of the finite element mesh near the fine mesh region, and the plots are symmetric about their left face. The discretized finite element mesh was left overlaid on the inclusions to clearly identify their domain. Moreover, all of the contour plots in Figures 4.44 through 4.47 were created at an applied far-field strain of 0.20%, which is below the macroscopic yield strain of the matrix material (0.23%). The cracked inclusions (Figure 4.46) have a crack-like defect across the center of the particle, and the debonded inclusions (Figure 4.47) have a crack along the entire bottom half of the interface between the particle and matrix. We note that the monotonic results only consider the maximum plastic shear strain, γ_{max}, which is used for screening the relative intensity of plastic strains near the different inhomogeneities. In reality, the maximum plastic shear strain amplitude, γ_{max}, is an appropriate measure of the driving force for fatigue crack nucleation based on experimental observations under multiaxial loading conditions (Fatemi and Socie, 1988; Fatemi and Kurath, 1988; McDowell, 1996a, b). Consequently, the latter sections of the section will focus on the plastic shear strain amplitude under realistic cyclic loading conditions.

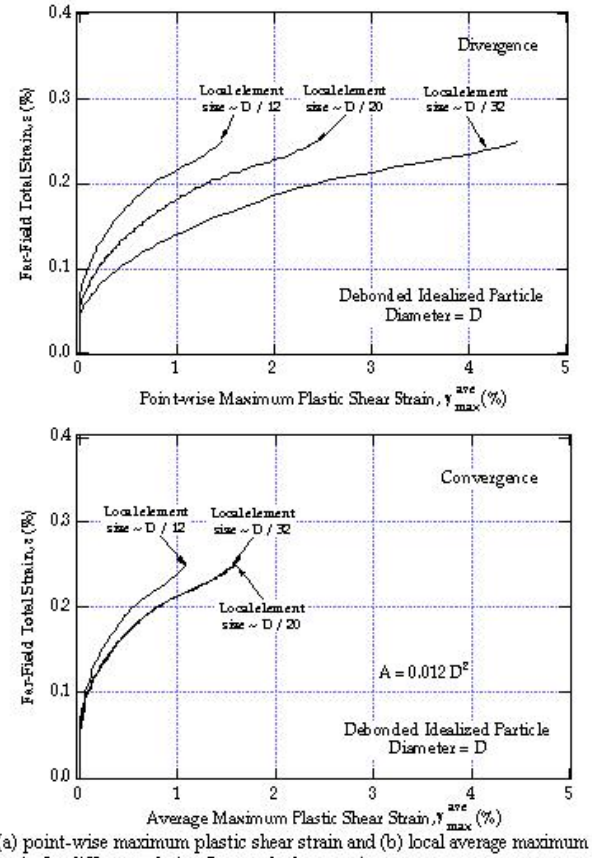

Figure 4.43. Plot of the (a) point-wise maximum plastic shear strain and (b) local average maximum plastic shear strain as a function of the far-field applied strain for different relative fine mesh element sizes.

Aside from the crack-like defect in the matrix (Figure 4.44c), the partially debonded inclusion (Figure 4.47) causes the largest intensification of γ_{max} in the matrix material. The perfectly bonded inclusions (Figure 4.45) cause the smallest intensification of γ_{max} in the matrix. In fact, the γ_{max} values in the case of the bonded particles are so small that they may be considered negligible in light of γ_{max} values near the other inhomogeneities, which are two orders of magnitude higher. The cracked inclusions (Figure 4.46) do not localize plasticity in the matrix as severely as the debonded inclusions. The effect of inclusion and void shape on the local γ_{max} values is negligible, in light of the severe difference in γ_{max} for the different inhomogeneity types. For example, in the cases of a void (Figure 4.44), a cracked inclusion (Figure 4.46), and a debonded inclusion (Figure 4.47), the awkward shaped star inhomogeneity does not generate maximum γ_{max} values significantly different than the round idealized cases. This is not to say that shape will not have an indirect influence on the nucleation of fatigue cracks since inclusions with different shapes will surely possess a different resistance to debonding and fracture (Gall *et al*., 1999-C). However, if the propensity of an inclusion to debond and/or fracture is accounted for, then an idealized round defect shape appears appropriate to model fatigue crack formation from inhomogeneities. Undoubtedly, the relative insensitivity of the γ_{max} values and distributions to the inhomogeneity shape (for an equivalent overall size) is one reason why the projected $\sqrt{\text{area}}$ criterion employed by Murakami and Endo, (1994) has proven useful to characterize the detrimental effect of inclusions and voids on fatigue life.

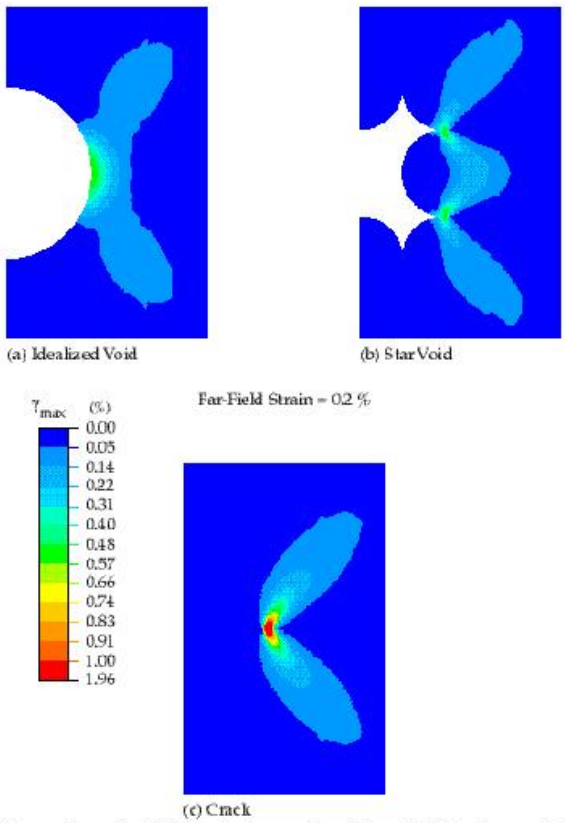

Figure 4.44. Contour plots of the maximum plastic shear strain, γ_{max}, for voids with different geometries. The applied far-field strain is 0.2%.

The aforementioned observations for monotonic loading at 0.20% strain, hold over a wide range of applied strain amplitudes. In Figure 4.48 the local $\Delta\gamma^{p*}_{max}$ values are plotted as a function of the applied far-field strain for the eight different inhomogeneities in Figures 4.44 through 4.71. The local $\Delta\gamma^{p*}_{max}$ values in Figure 4.48 were calculated by averaging γ_{max} over areas of $A = 0.012\ D^2$, where D is the size of the inhomogeneity (Figure 4.42). The hierarchy of the γ_{max} values for different inclusions is basically independent of applied far-field strain amplitude under monotonic loading conditions.

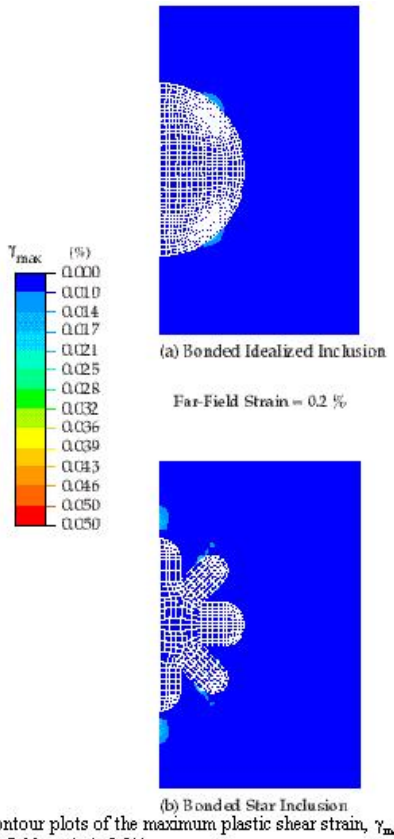

Figure 4.45. Contour plots of the maximum plastic shear strain, γ_{max}, for bonded inclusions with different geometries. The applied far-field strain is 0.2%.

The extremely high γ_{max} values near the debonded inclusions are caused by the crack like defect at the tip of the debond seam coupled with the constraint and contact of the embedded inclusion. For example, in Figure 4.47b, intense γ_{max} values are generated both at the tip of the debond seam (the far right of the inclusion) and at the contact point between the matrix and the debonded lower right finger of star inclusion. This observation circumvents the possible argument that severe localized γ_{max} values only occur near debonded inclusions owing to the artificially arrested interface crack. The cracked inclusions do not lead to local γ_{max} values as high as those of the debonded particles, due to the difference in the crack geometry and the local balance of stresses. Figure 4.49 presents contour plots of the effective stresses near a cracked, debonded, and a partially debonded-cracked inclusion. The cracked inclusion (Figure 4.49a) carries a significant fraction of the local stresses in the broken particle halves after particle fracture, while the debonded inclusion (Figure 4.49b) is virtually stress free. The extremely large stresses in a cracked particle have a propensity to facilitate debonding at the particle matrix interface. Regardless of the strength of the inclusion-matrix interface, it is unlikely that the interface can support such large local stresses. The introduction of a debond in the region of high stresses near the cracked inclusion (Figure 4.49c) drastically lowers the stresses in the inclusion. Hence, we assume that a particle cannot remain just cracked without some local debonding surrounding it. Metallurgical observations support local debonding near cracked particles (Gall *et al.*, 1999b). In addition, the finite element calculation predicts that once a cracked particle begins to debond, the local plastic strains are intensified in the matrix the same order of magnitude as an uncracked but partially debonded inclusion.

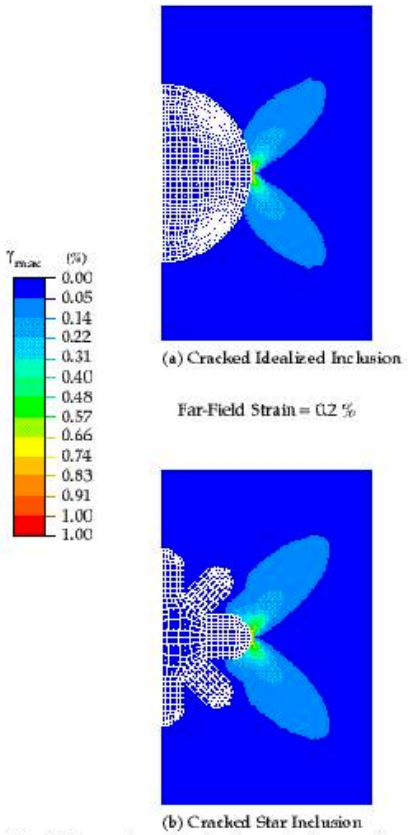

Figure 4.46. Contour plots of the maximum plastic shear strain, γ_{max}, for cracked inclusions with different geometries. The applied far-field strain is 0.2%.

Based on the results under monotonic loading, the debonded inclusion and the void will be the focus of the remainder of this paper. The small γ_{max} values near bonded inclusions, coupled with the low probability that the fatigue-crack-nucleating inclusions will remain completely bonded or perfectly cracked (no local debonding) removes them as critical components. The fact that debonded inclusions and voids are considered critical inhomogeneities is consistent with metallurgical observations on fatigue crack formation (Gosskreutz and Shaw, 1969; Lankford and Kusenberger, 1973; Lankford, 1976; Kung and Fine, 1978; Murakami and Endo, 1994). We further note that only the idealized inclusion and void will be considered. The more realistic star shaped inhomogeneities do cause more severe local γ_{max} fields compared to the idealized inclusions, for an equivalent defect size.

Strictly speaking, the primary driving force for fatigue crack formation is the maximum local plastic shear strain range, $\Delta\gamma^{p*}_{max}$ or amplitude $\Delta\gamma^{p*}_{max}/2$, over all possible shear strain planes (Fatemi and Socie, 1988; Fatemi and Kurath, 1988). In this section we apply various cyclic boundary conditions to the debonded idealized inclusion and the idealized void to determine local values of γ_{max} and $\Delta\gamma^{p*}_{max}$.

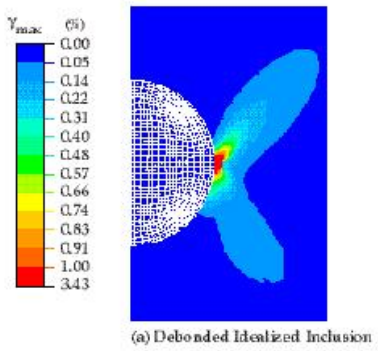

(a) Debonded Idealized Inclusion

Far-Field Strain = 0.2 %

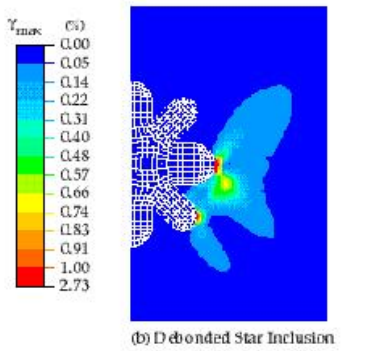

(b) Debonded Star Inclusion

Figure 4.47. Contour plots of the maximum plastic shear strain, γ_{max}, for debonded inclusions with different geometries. The applied far-field strain is 0.2%.

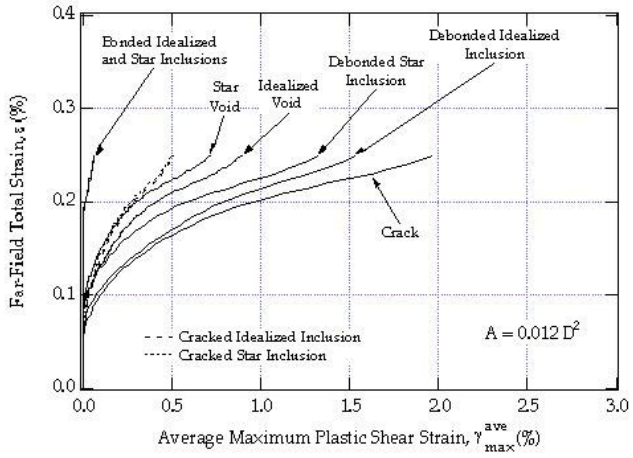

Figure 4.48. Plot of the local average maximum plastic shear strain, , as a function of the far-field applied strain for the different inhomogeneities in Figures 4.44 – 4.47. The area used for averaging is A = 0.012 D ², where D is the inhomogeneity size.

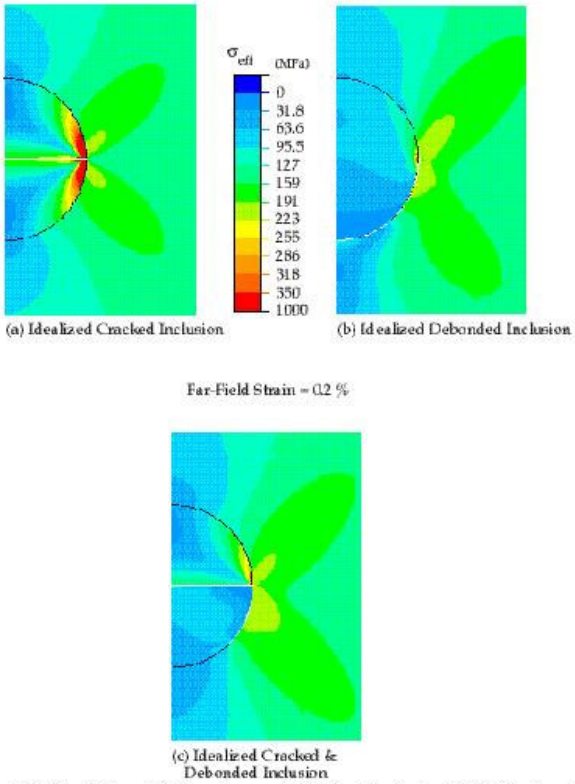

Figure 4.49. Contours of the Von-Mises effective stresses at 0.20% strain for the (a) idealized cracked inclusion, (b) idealized debonded inclusion, and (c) idealized cracked and partially debonded inclusion.

Moreover, we will compare the local plastic shear strain distributions under monotonic and cyclic loading conditions. Such a comparison is useful since many previous analytical models of stress and plastic strain intensifications near inhomogeneities only considered monotonic conditions (Harkegard, 1973; Sundstrom, 1974), or far-field cyclic conditions linearly extended to local cyclic conditions (Tanaka and Mura, 1982). However, reversed plasticity, elastic constraint, and local stress redistribution often make the transitions from far-field cyclic conditions to local cyclic conditions non-trivial, as will be further demonstrated.

The results from the constant amplitude cyclic finite element simulations are presented in Figures 4.50 through 4.54. All cyclic finite element simulations were conducted for either three or six cycles at strain amplitudes of $\Delta\varepsilon/2$ = 0.10, 0.15, and 0.20 and R-ratios ($\varepsilon_{min}/\varepsilon_{max}$) of –1, 0, and 0.5. This preliminary study will not consider the effects of variable amplitude loading sequences or large cycle numbers. Figure 4.50 presents contour plots of g_{max} for the $\Delta\varepsilon$ /2 = 0.20, R = -1 simulation at the maximum (0.20) and minimum (-0.20) applied strain for the debonded idealized inclusion and the idealized void. Under monotonic tensile loading the void experiences lower amplitudes of γ_{max} compared to the debonded inclusion. At the maximum tensile strain, the cyclic results confirm the observations under monotonic loading; however, the effects of reversed cyclic plasticity under elastic constraint have a significant influence on the cyclic γ_{max} distributions at the minimum applied strain. During compressive loading, the plasticity near the void undergoes a change in the shear direction of γ_{max}, while the magnitude of plastic shear strain near the debonded inclusion remains. Even under far field compressive strains of 0.2%, the residual γ_{max} near the debonded inclusion has the same shear direction as under the maximum tensile strain. As such, the reversed plasticity levels near the void are substantial; however, the reversed plasticity near the debonded inclusion is negligible (Figure 4.50).

The representative contour plots in Figure 4.50 demonstrate the overall spatial distributions of γ_{max} under cyclic loading conditions. However, to provide more quantitative insight into the reversed cyclic plasticity near the inhomogeneities, Figures 4.51, 4.52, and 4.53 present plots of the far-field total strain versus $\Delta\gamma^{p^*}_{max}$ for R = –1, 0, and 0.5 loading conditions, respectively. In all figures, the results from constant applied strain amplitudes of $\Delta\varepsilon/2$ =

0.10, 0.15, and 0.20 are plotted on the same graph. Under R = –1 loading $\Delta\gamma^{p^*}_{max}$ for the void and the debonded inclusion demonstrates a hysteresis with respect to the applied strain (Figure 4.51). As the applied far-field strain is increased, the plastic shear strains begin accumulating at a critical strain level. During unloading, the plastic strains do not begin to decrease in magnitude until a reversed critical strain level is reached. Moreover, under R= –1 loading, the shape of the hysteresis loop for the debonded inclusion shows a discontinuity at an applied compressive strain of –0.5% (Figure 4.51a). The discontinuity is caused by contact between the particle and the matrix, which decrease the rate of accumulation of local plastic shear strains as a function of the far-field applied strain. Of course, such a change in the rate of plastic shear straining is not observed in the case of the void (Figure 4.51b).

For R-ratios of 0 and 0.5, the material near the debonded inclusion and the void still show a hysteritic behavior of $\Delta\gamma^{p^*}_{max}$ with respect to the applied strain (Figures 4.52 and 4.53). Contact conditions are not encountered in the case of the debonded inclusion cycled at high R-ratios. Consequently, the overall shape of the hysteresis loop is the same for the void and the debonded inclusion at R-ratios of 0 and 0.5. Due to the imposed mean strain (stress), cyclic ratcheting is observed.

The precise modeling of cyclic ratcheting, with respect to experimental observations, is beyond the scope of the present study. We do note that, consistent with experimental observations, the ratchet strain diminishes with cycling and is expected to reach an equilibrium state (McDowell, 1995). In all cases, six cycles were sufficient to reach a hysteresis loop size with only a few percent change from the previous loop. Arguably, the most important observation in Figures 4.52 and 4.53 is that the width of the hysteresis loop is consistently larger for the debonded inclusion versus the void.

The widths of the hysteresis loops in Figures 4.51-4.53 are equal to the assumed driving force for fatigue crack formation from a particular inhomogeneity, $\Delta\gamma^{p^*}_{max}$. Figure 4.54 summarizes the values of $\Delta\gamma^{p^*}_{max}/2$ at different applied strain amplitudes and R-ratios for the debonded inclusion and the void. The points in Figure 4.54 follow the same overall trends as the monotonic curves (Figure 4.55), but provide some contrast with respect to the different inhomogeneities. Based on tensile monotonic results, the debonded inclusion facilitates local $\Delta\gamma^{p^*}_{max}$ values about twice those near a void, irrespective of the applied strain amplitude (Figure 4.48). On the other hand, the value of $\Delta\gamma^{p^*}_{max}$ for voids compared to the inclusions depends strongly on the R-ratio considered. Under cyclic loading conditions, the intensification of $\Delta\gamma^{p^*}_{max}$ near the debonded inclusion is extremely sensitive to the R-ratio (Figure 4.54). By way of contrast, for voids, the local $\Delta\gamma^{p^*}_{max}$ values are relatively insensitive to the R-ratio (Figure 4.54). At low R-ratios, the debonded inclusion and void have driving forces for fatigue which are nearly equivalent (Figure 4.54). However, as the R-ratio is increased, the driving force for fatigue crack formation is much higher for a debonded inclusion compared to a void (Figure 4.54).

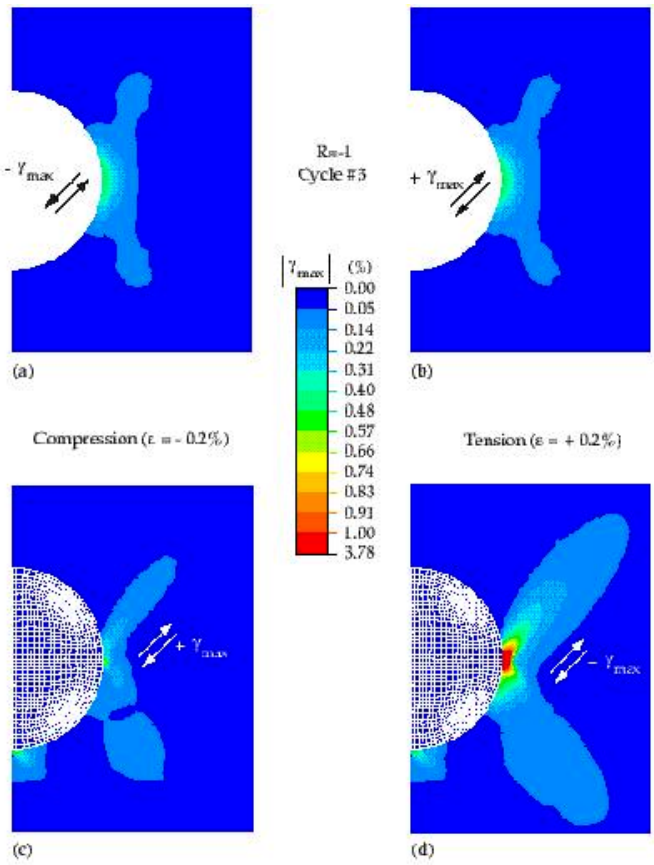

Figure 4.50. Contour plots of the maximum plastic shear strain, γ_{max} under R = –1, Δε/2 = 0.2 cyclic loading conditions.

The different sensitivity of the plastic shear near voids and debonded inclusions to the R-ratio is a result of the different local cyclic plastic strain distributions near the two inhomogeneities. The debonded inclusion facilitates higher plastic strains under monotonic loading conditions, which in turn lead to higher local stress states. Consequently, the reversed yielding occurs more readily near the debonded inclusion, and the hysteresis loop is naturally larger.

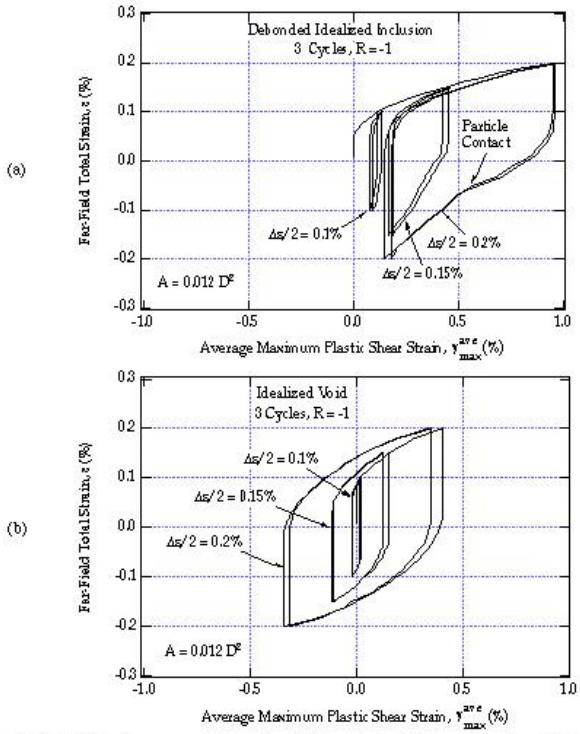

Figure 4.51. Plot of the local average maximum plastic shear strain, γ_{max}^{ave} as a function of the far-field applied strain under R=-1 cyclic loading conditions. The plots are for (a) a debonded idealized inclusion, and (b) a idealized void.

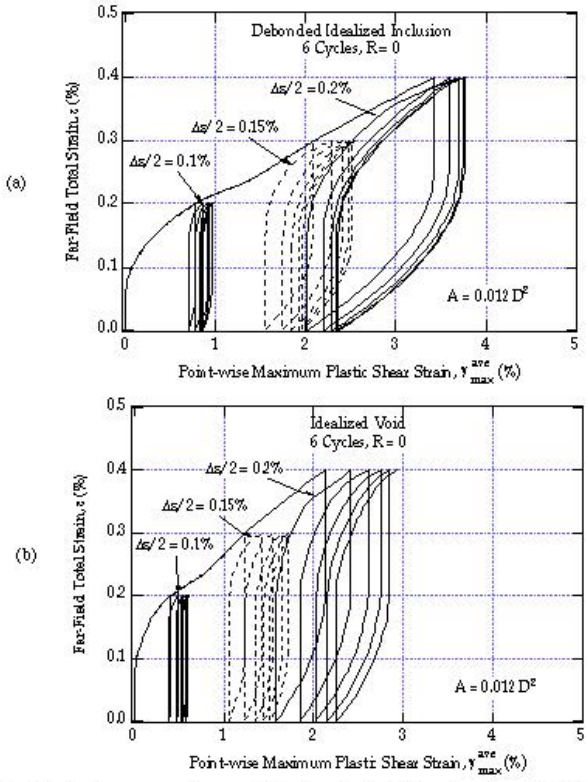

Figure 4.52. Plot of the local average maximum plastic shear strain, γ_{max}^{ave} as a function of the far-field applied strain under R=0 cyclic loading conditions. The plots are for (a) a debonded idealized inclusion, and (b) a idealized void.

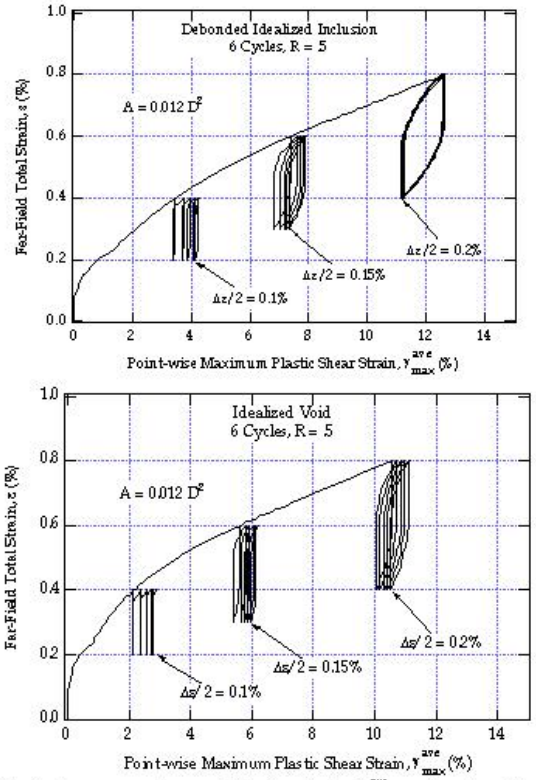

Figure 4.53. Plot of the local average maximum plastic shear strain, γ_{max}^{ave} as a function of the far-field applied strain under R=0.5 cyclic loading conditions. The plots are for (a) a debonded idealized inclusion, and (b) a idealized void.

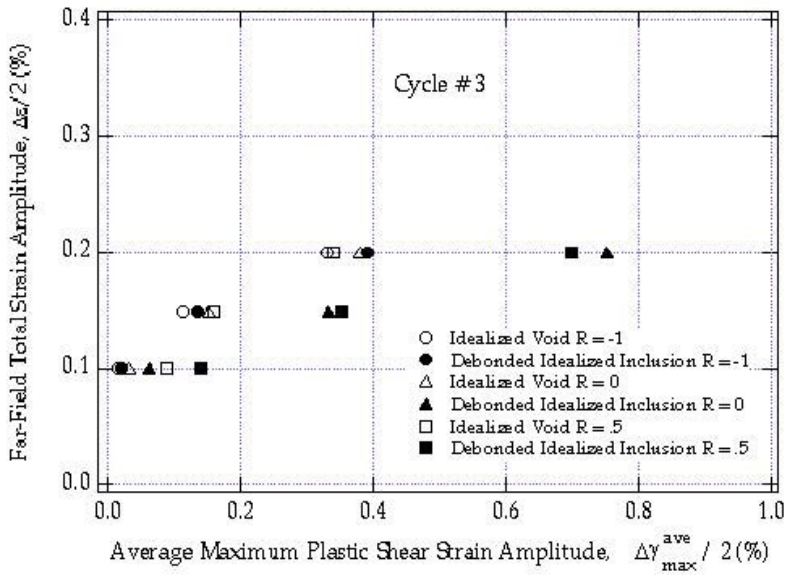

Figure 4.54. Plot of the local average maximum plastic shear strain amplitude, $\Delta\gamma_{max}^{ave}/2$, as a function of the far-field total strain amplitude, $\Delta\varepsilon/2$, for the third cycle under R= –1, 0, and 0.5 loading conditions.

At high R-ratios, the aforementioned mechanism allows for plastic shear strains to be higher near the debonded inclusion versus the void. However, under fully reversed conditions, the contact of the inclusion with the matrix inhibits reversed plasticity near the debonded inclusion in the same location as observed under maximum tensile strain. Such constraint causes an R-ratio effect since very low R-ratios will result in relatively small $\Delta\gamma^{p*}_{max}$ values for the debonded inclusion. The symmetric local plastic deformation near the void under forward and reversed loading circumvents any significant geometrically driven R-ratio effects for the void.

The aforementioned observations on the differences in reversed plasticity levels for the debonded inclusion and the void support the experimental observations of Bathias (1998). Bathias (1998) noted that high R-ratios consistently favor fatigue crack formation from inclusions, while low R-ratios favor fatigue crack formation from similar sized voids. In addition, the present study demonstrates that high R-ratios accentuate γ_{max} values near debonded inclusions compared to voids (Figure 4.54) due to differences in local plastic strain distributions during reversed loading. We also note that the higher maximum applied stress amplitude encountered during cycling at high R-ratios facilitates another contributing mechanism for such behavior. Greater stresses increase the chance that a pristine inclusion will become fractured and debonded, subsequently increasing its propensity for fatigue crack formation.

The present section is devoted to modeling the effects of inhomogeneity size on fatigue crack formation from debonded inclusions and voids. Differences in the relative sizes of voids versus inclusions (voids are often larger) is one reason that experimental observations sometimes indicate the preferential formation of fatigue cracks from voids versus inclusions (Gungor and Edwards, 1993; Murakami and Endo, 1994; Shiozawa *et al*., 1997; Bathias, 1998), aside from R-ratio effects. The formation of a fatigue crack is a mechanical process, which occurs over a finite physical size scale (Harvey *et al.,* 1994). Furthermore, the size scale of fatigue crack formation can be assumed to be a constant dependent on the properties of the matrix material. As such, the size of an inclusion or void will affect the formation of a fatigue crack since inhomogeneities of different characteristic sizes facilitate intense and localized plasticity over a length scale proportional to their own size. For example, if the intense plasticity spans a length scale much smaller than the size required for fatigue crack formation, then it will be difficult for a crack to form near an inclusion. At the other extreme, if the intense plasticity acts over a length scale much greater than the size required for fatigue crack formation, a crack will readily form near an inclusion.

The effect of inclusion size on the driving force for fatigue crack formation in the matrix can be quantified using finite elements by assuming that the physical size scale for fatigue crack formation is a constant, independent of the inclusion size. Figure 4.55 plots the average plastic shear strain amplitude, $\Delta\gamma^{p*}_{max}/2$, as a function of the far-field applied strain for idealized voids and debonded idealized inclusions of sizes D, 2D, and 4D. The plastic shear strain amplitude was calculated at the third loading cycle under R = –1 cyclic loading conditions. The area used for calculation of the $\Delta\gamma^{p*}_{max}$ values in Figure 4.55 was kept constant at $A = 0.0625\ D^2$. Both the debonded inclusion and the void demonstrate a significant size effect. The inhomogeneity size effect is approximately proportional to the square-root of the defect size. If the size of the void or debonded inclusion, D, increases by a factor of four, then the driving force for fatigue crack formation, $\Delta\gamma^{p*}_{max}$, increases by about a factor of two. Such an observation seems to support the semi-empirical $\sqrt{area}$ approach of Murakami and Endo (1994).

In closing, we note that statistical variations of inclusions in the microstructure also favor fatigue crack formation from larger inhomogeneities. The probability that a weak local region of material, for example a grain orientation with a low resistance to cracking, will be subjected to intense plasticity is greater for a larger inclusion. We will not focus on the statistical aspects of fatigue crack formation, although the present approach has the framework to consider such effects through statistical variations in the fatigue resistance of the matrix material.

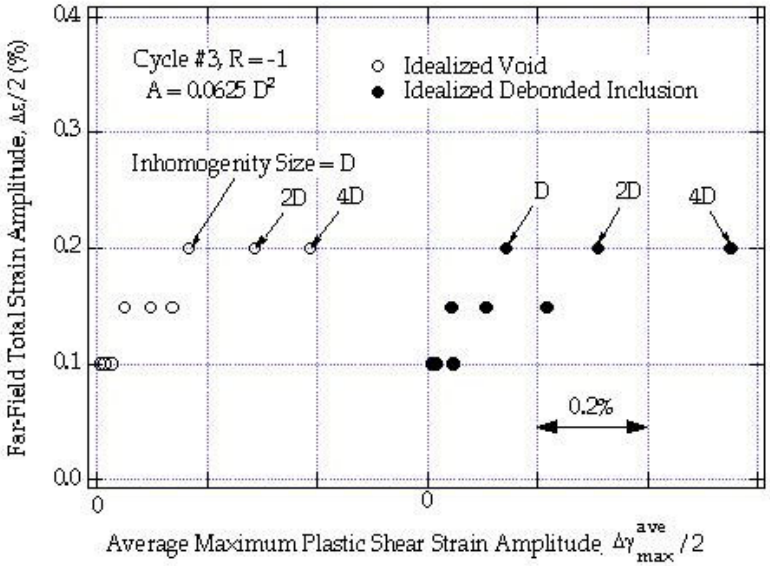

Figure 4.55. Effect of inclusion size on the driving force for fatigue crack formation for the idealized debonded inclusion and the idealized void.

Monotonic and cyclic finite element simulations are conducted on linear-elastic inclusions (cracked, bonded, and debonded) and voids embedded in a matrix material described by cyclic plasticity relationships. The local maximum plastic shear strain, γ_{max}, with respect to all possible shear strain planes is monitored throughout the simulations. A local spatial average range of γ_{max}, denoted as $\Delta\gamma^{p*}_{max}$, is used as a measure of the driving force for fatigue crack formation.

Under tensile monotonic loading conditions, at all applied strain amplitudes below macroscopic yielding of the matrix (0.23%), debonded inclusions, voids, cracked inclusions, and bonded inclusions demonstrate descending local levels of γ_{max}. The γ_{max} levels near bonded inclusions are two orders of magnitude smaller than near the other inhomogeneities, thus they are not considered critical fatigue-crack-initiating inhomogeneities. Owing to the extreme stress levels near the edges of a cracked inclusion, it is improbable that a cracked inclusion will remain completely bonded to the matrix material. Thus, a cracked inclusion is also discarded as a critical inhomogeneity since it is practical to treat it as a debonded inclusion.

Irregular shaped inclusions and voids containing sharp corners and local radii of curvature do not magnify local plastic strains in the matrix significantly more than idealized round inhomogeneities *of equivalent overall size*. As such, the shape of inclusions or voids is proposed to have a *relatively* small effect on the driving force for fatigue crack formation compared to other critical effects such as size, damaged state, and reversed plasticity. The relative indifference to the local driving force for fatigue crack formation to inclusion shape is consistent with the success of the semi-empirical projected $\sqrt{area}$ approach of Murakami and Endo (1994).

Based on the concept of a constant physical size for the process of fatigue crack formation in the matrix material, the size of an inhomogeneity has a significant influence on the driving force for fatigue crack formation. Increasing the size of a debonded inclusion or void from D to 4D, increases $\Delta\gamma^{p*}_{max}$ by about a factor of 2.

Under monotonic tensile loading, the debonded inclusion exhibits $\Delta\gamma^{p*}_{max}$ values about twice as high as those of a void. Conversely, under cyclic loading, the value of $\Delta\gamma^{p*}_{max}$ for the debonded inclusion and the void is strongly dependent on the applied R-ratio. At low R-ratios (R=–1), equivalent sized voids and debonded inclusions have comparable γ_{max} values. At higher R-ratios, (R=0, 0.5) debonded inclusions have γ_{max} values twice that of voids.

4.3. MICROSTRUCTURALLY/PHYSICALLY SMALL CRACK (MSC/PSC) GROWTH REGIME

Once a crack has incubated to its lifetime, a fatigue crack has started. It is this range of the small fatigue cracks that we now focus on in the next set of simulations. Here, the driving force versus resistance of material is intimately related to the details of the microstructural features. Similar to the crack incubation, little experimental observations are published. As such, we performed several calculations examining the pertinent microstructural features in relation to the crack driving force, that is, the crack tip displacement, ΔCTD.

In these calculations, the definition of ΔCTD proposed by Lankford, Davidson and Chan (1984) is adopted; that is, it is defined as the crack face separation of points initially 1 μm behind the crack tip. We consider the magnitude of the entire vector of separation of two points on opposite crack faces. Hence, we use the label ΔCTD after Li (1990). In the discretization of the matrix and particles by finite elements, the crack path is simultaneously discretized by a number of element nodes. The crack propagation process is also discretized by discontinuous growth-stopping processes. During the i^{th} individual process, the loading is cycled for the crack tip at the site x_i for a certain number of cycles N_i. The crack is then advanced a distance, Δx_i, by release of the crack tip node. This distance equals the size of the element ahead of the tip. The "crack length versus time criterion" of ABAQUS is used for release of the crack tip node. Here, the time is not Newtonian, but a parameter proportional to the applied loading. To ensure the accuracy of the calculation of theDCTD, the element size near the crack growth area is taken as 0.5 μm for most meshes, which was decided by a mesh refinement study discussed later; the ΔCTDs were therefore determined based on displacements of nodes which are two elements behind the crack tip. In case of an element size other than 0.5 μm, an extrapolation from the data at the first and second nodes is used to obtain the ΔCTD at a distance of 1 μm.

4.3.1 SILICON

Once a fatigue crack has started, it must move through the forest of silicon particles in the eutectic region. In this section, we study the effect of silicon particles on cracks in the MSC/PSC regime.

4.3.1.1. REALISTIC MICROSTRUCTURE

In this section, realistic morphology is used via SEM images for FEA but perfectly bonded silicon particles are assumed. Figure 4.56 shows the crack tip displacement ΔCTD versus projected crack length for a realistic particle cluster at the stress amplitude of 133 MPa. Figure 4.56 (a) shows that the symmetric top and bottom parts are taken as effective medium; the middle part with microstructure configuration obtained by image analysis is taken for detailed quantitative analysis of crack growth; a part of this region is shown in Figure 4.56 (b). The crack

initiates from point O. The crack path is assumed be along the curves, passing through succeeding points O_1, O_2, A, A_1, A_2, B, C, D, E, F, G, H, I, J K, and L from the right to the left. This assumption is based on the experimental results that the crack in the MSC regime tends to debond the interface between the matrix and the particles (Gall *et al*., 1999). The obtained ΔCTD versus the projected length on the OX axis is shown in Figure 4.56 (c). One observes that when the growing crack meets a particle at point G the ΔCTD reaches a local minimum. Since the growing crack may be temporarily arrested when the crack meets a strong barrier, the realistic average crack growth rate of the A356 Al alloy should be smaller than otherwise estimated.

4.3.1.2. IDEALIZED MICROSTRUCTURE: PARAMETRIC STUDIES

In this section, we used idealized plane strain geometries to help determine the effects of various microstructural features on ΔCTD. The parameters that were varied included an in-plane particle cluster, initial crack length, applied stress (strain), crack branching, particle size, particle aspect ratio, particle spacing, dendrite cell size, and mean stress.

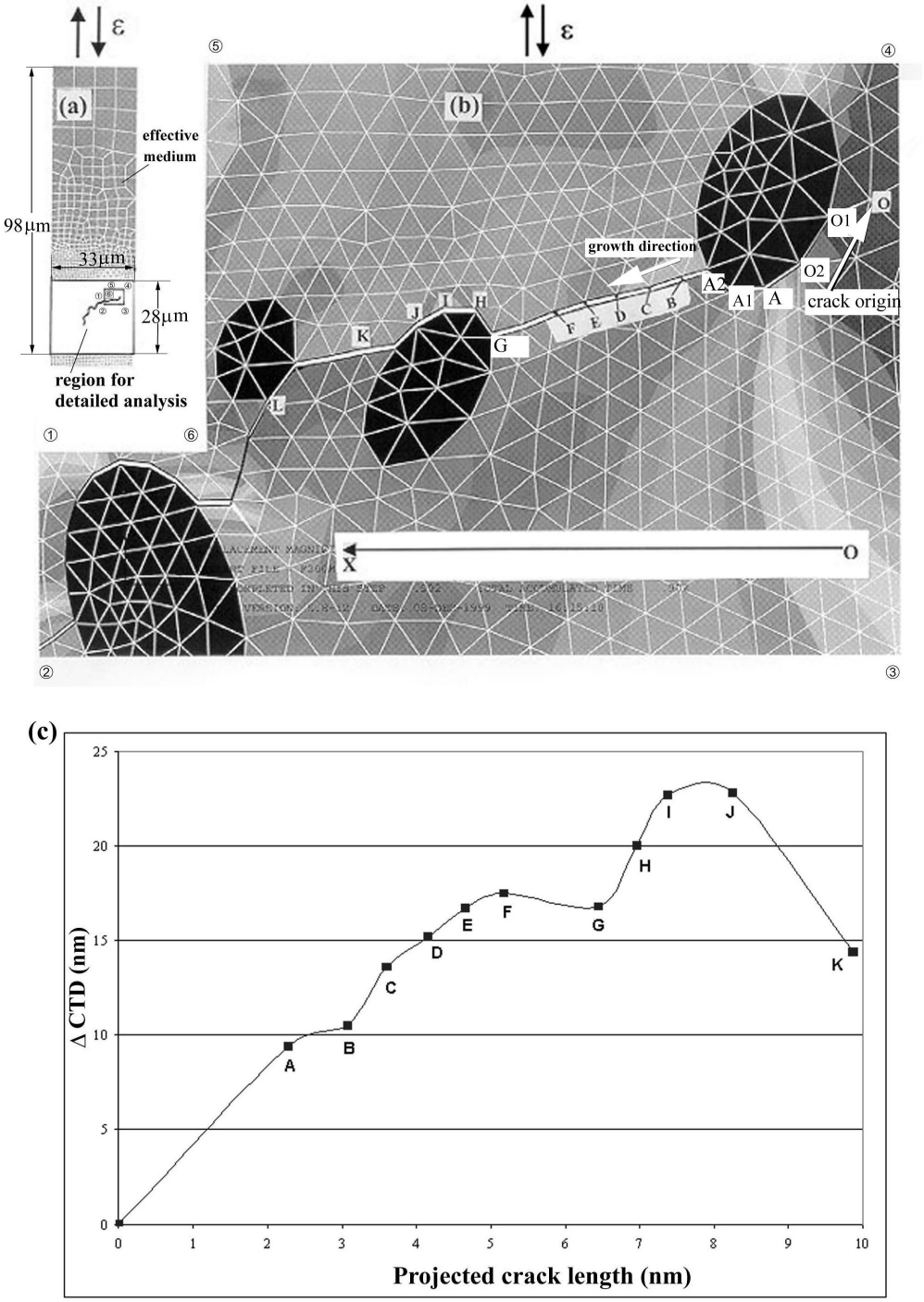

Figure 4.56. Cyclic crack tip displacement ΔCTD versus projected crack length for a realistic particle cluster morphology at the stress amplitude of 133 MPa. The projected crack length is the length of the realistic crack length projected onto the OX axis which is perpendicular to the loading direction (R= –1, ε_a =0.2%, boundary conditions: uniformly cyclic displacement along the y-direction at the top side, simple support at the right side with u_x=0, simple support at the bottom side with u_y=0, and free at the left side).

4.3.1.2.1. CYCLIC CRACK TIP DISPLACEMENT CALCULATIONS FOR A CRACK PASSING THROUGH AN IN-PLANE PARTICLE CLUSTER

The geometry used for the MSC fatigue crack growth FEA is given in Figure 4.4. Five silicon particles are embedded in the matrix in the OXY plane. A crack initiates at site O, grows in the matrix from left to the right, encounters the first particle at a point a_{1f} with projected crack length a_{1f}. After the crack meets the particle, it is assumed that the crack debonds the upper half of the interface between the particle and the matrix. We assume that this crack pattern is based on the experimental observation of the particle debonding in the MSC regime (Gall *et al*., 1999). If the driving force is not sufficient, the crack will stop growing. Otherwise, the crack will continue to grow, passing along the interface and then growing into matrix again along the OX direction until it meets the second particle at point a_{2f} (with projected crack length a_{2f}), and so on.

Figure 4.57 schematically shows the crack path and the calculated ΔCTD versus projected crack length. The results are obtained under completely reversed cyclic tension-compression loading with an applied strain amplitude of 0.2% (133MPa) for D=B= 4 μm, and D_{max}/D_{min}=1. The results show that ΔCTD increases quickly at the onset of growth. ΔCTD reaches a first plateau at point A when the distance between the crack tip and the particle reaches about 0.75D (3 μm). However, when the distance reduces to about 0.25 D (1μm) and below, ΔCTD increases again until an abrupt drop to a minimum value of 13.5 nm. Compared to the maximum value of 31.3 nm at point B before the crack meets the particle, the ΔCTD decreases by about 57%. This abrupt decrease indicates a greatly reduced driving force for crack advance as a crack encounters a particle. As a result, the crack may be arrested until the interface damage accumulates to the critical value so that debonding occurs. After the crack overcomes the particle resistance, the crack growth rate will accelerate again. The acceleration-retardation process is repeated as the crack encounters successive barriers.

4.3.1.2.2. CYCLIC CRACK TIP DISPLACEMENT CALCULATIONS WITH DIFFERENT INITIAL CRACK LENGTHS

Figure 4.58 shows a comparison of ΔCTD between two cracks of length 10.5 and 65 μm prior to encountering the first particle within the same set of particle clusters at the stress amplitude of 133 MPa (R=–1, D=B=4 μm). This comparison of two different initial crack lengths shows that the particle clusters have stronger relative retardation effects on the long crack. No matter how different the ΔCTD for the two cracks, they follow a common retardation pattern, especially after the interaction with the first particle. The long-crack case may be considered as a simulation of the case of a crack first passing through a dendrite cell of 65 μm, and then encountering particle clusters. Figure 4.41 shows that when the DCS is large, the driving force is much higher than that when the DCS is small. This point will be investigated later from the viewpoint of fatigue crack closure.

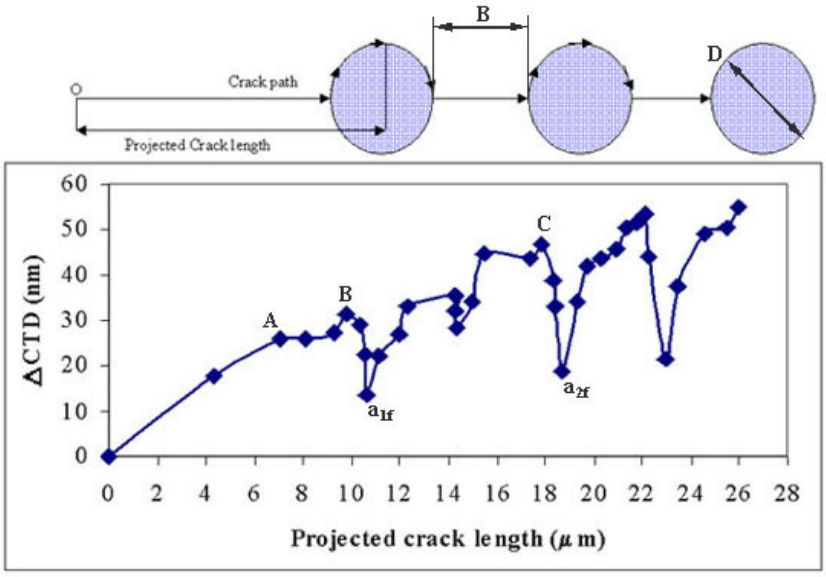

Figure 4.57. Cyclic crack tip displacement ΔCTD versus projected crack length for an idealized in-plane particle cluster for a stress amplitude of 133MPa (R= –1, D =B=4 μm, ε_a =0.2%).

An average of crack tip displacement over a certain distance of microstructure is clearly a measure of average driving force. This is useful in developing a phenomenological fatigue model. Figure 4.59 shows a comparison of the average ΔCTD between two cracks of initial length 10.5 and 65 μm before they each meet the first particle of the same set of particle clusters at the stress amplitude of 133 MPa. The results show that the average ΔCTD of the long crack is about 1.61 times that of the short crack. This indicates that the average driving force is higher for the long crack than for the short crack.

4.3.1.2.3. CYCLIC CRACK TIP DISPLACEMENT CALCULATIONS WITH DIFFERENT APPLIED STRESS AMPLITUDES

Figure 4.60 shows effects of applied stress amplitude on ΔCTD with one curve at the stress amplitude of 110 MPa, and the other at the amplitude of 133 MPa. The results show that the trends of the effects of particle clusters on ΔCTD are similar at different stress amplitudes. The quantitative relationships, however, are quite different at different intervals of the crack path. Roughly speaking, before the crack meets the first particle, the ΔCTD at the stress amplitude of 110 MPa is proportionally less than the ΔCTD at the amplitude of 133 MPa. At the debonding intervals (at the top half of the particles), the reduction of the ΔCTD at the 110 MPa amplitude is much less than the ΔCTD at the amplitude of 133 MPa. In contrast, the corresponding reduction is much smaller at the intervals between particles. This phenomenon may be related to the microstructure effects on the MSC. More specifically, the results indicate that the particle cluster has different effects on ΔCTD at different intervals: it reduces the driving force greatly at the debonding intervals, but it reduces the driving force much less in the intervals between particles.

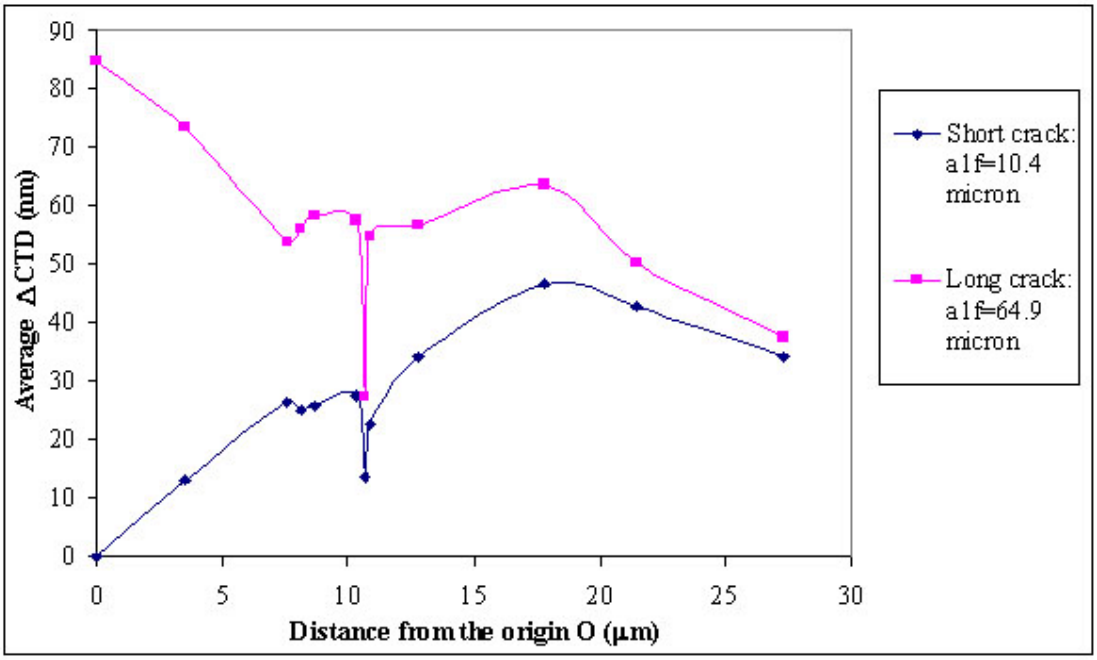

Figure 4.58. Comparison of cyclic crack tip displacement ΔCTD between two cracks of initial lengths of 10.4 and 65 μm prior to encountering the first particle of the same set of particle clusters for the stress amplitude of 133 MPa (R= –1, D =B=4 Δm, ε_a =0.2%).

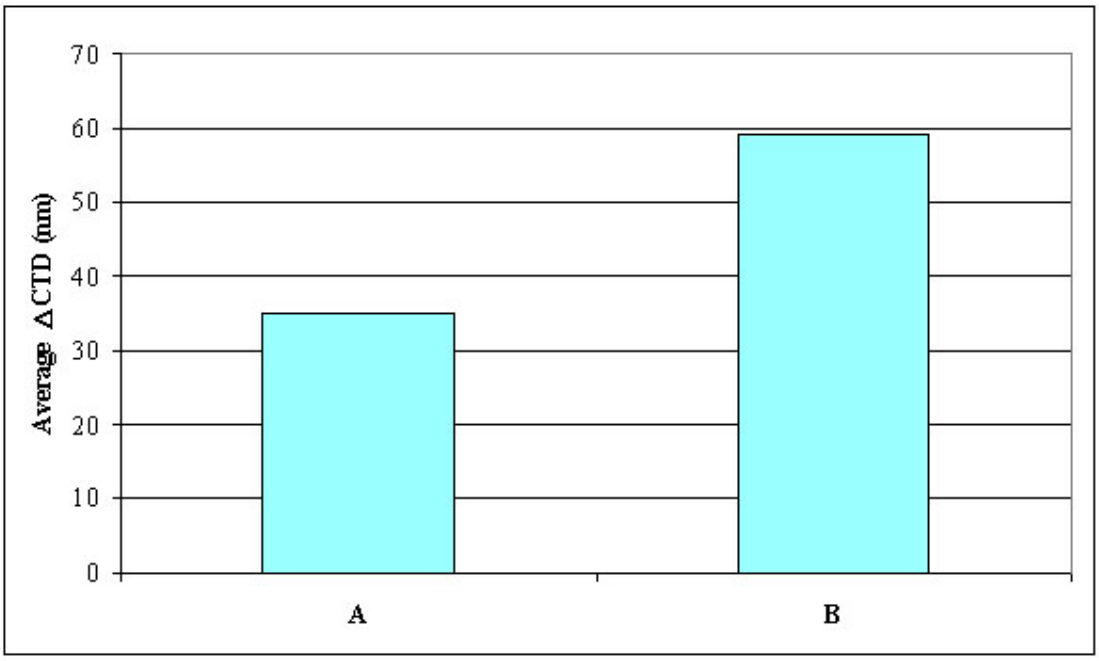

Figure 4.59. Comparison of the average (over the maximum projected crack length) ΔCTD between two cracks of initial lengths 10.4 and 65 μm prior to encountering the first particle of the same set of particle clusters for a stress amplitude of 133 MPa (R= –1, D=B=4 μm, ε_a =0.2%).

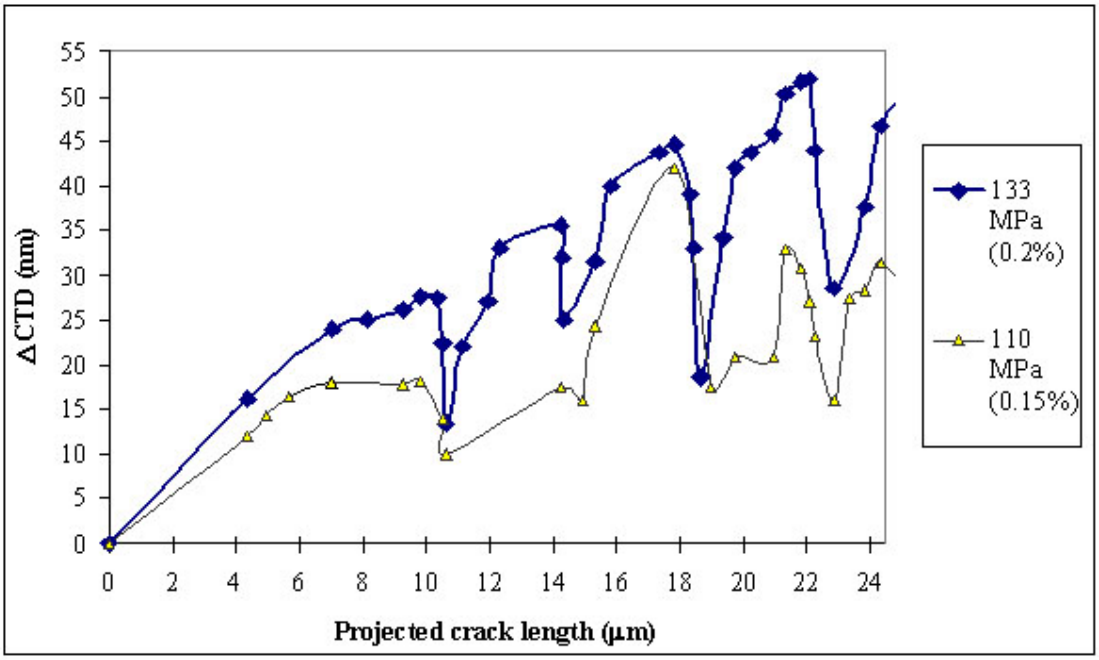

Figure 4.60. Effect of applied stress amplitude on cyclic crack tip displacement ΔCTD versus projected crack length for an idealized in-plane particle cluster for stress amplitude of 110 and 133MPa (R= –1, D =B=4 μm).

4.3.1.2.4. CYCLIC CRACK TIP DISPLACEMENT CALCULATIONS WITH DIFFERENT CRACK BRANCHING ANGLES

Figure 4.61 shows the effects of crack branching angles on ΔCTD at the stress amplitude of 133 MPa. The crack meets a particle of D=4μm and D_{max}/D_{min}=1.67 at its surface when the crack length is 10.5 μm. Then two paths are chosen: case A has an angle of 73^0 between the previous crack growth direction and the new growth direction; the corresponding angle for case B is 145^0. The results show that the driving force for the small angle is much higher than that for the large angle. This is significant in determining the crack growth path.

4.3.1.2.5. CYCLIC CRACK TIP DISPLACEMENT CALCULATIONS WITH DIFFERENT CRACK GROWTH PATHS

To see the effects of the crack growth path on the average driving force, four crack paths were taken for a comparison of the average ΔCTD over a certain degree of projected crack growth under completely reversed tension-compression cyclic loading at the stress amplitude of 133 MPa. Figure 4.62 shows the results of the comparison. Path A with the maximum driving force passes through the Al-1%Si matrix. In this case, there are no particles, so the crack path is a straight line along the OX axis of Figure 4.4. Path B is the crack path which is investigated in detail in Section 4.3.1.2.1 and passes through the in-plane particle cluster. Paths C and D are passing through an hexagonal cell of six particles placed at each corner.

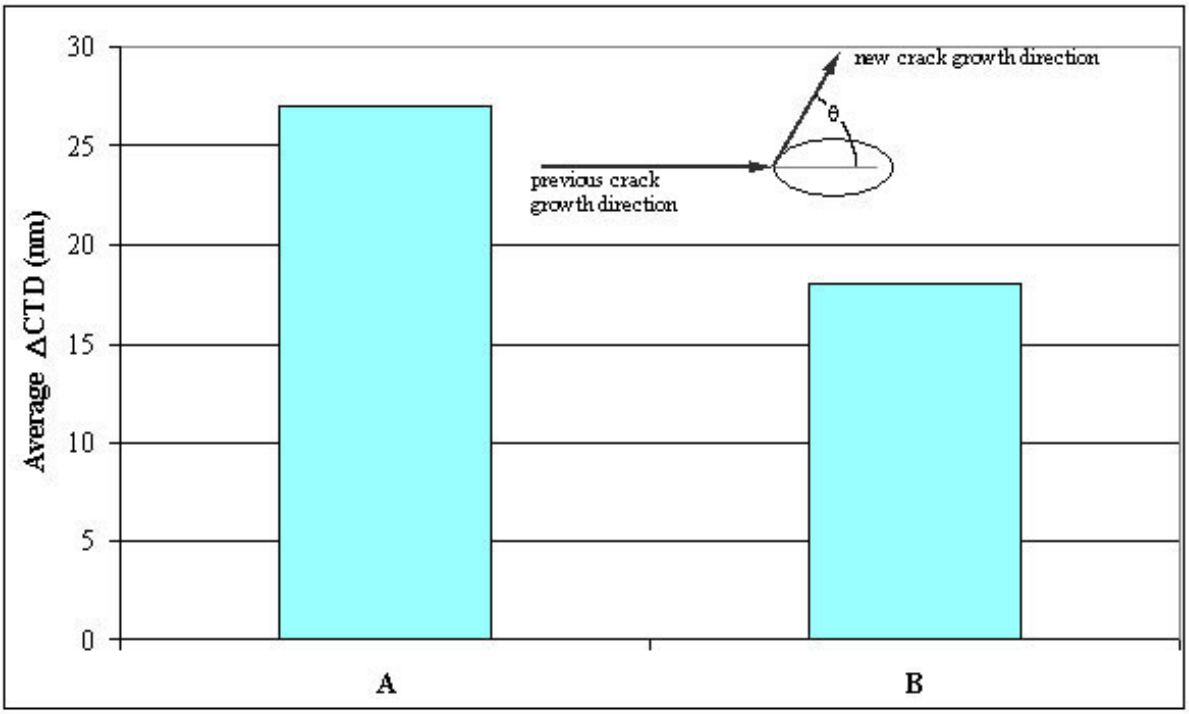

Figure 4.61. Effect of crack branching angles on ΔCTD for a stress amplitude of 133 MPa: (A) $\theta=73^{o}$, (B) $\theta=145^{o}$ (D=4 μm, $D_{max}/D_{min}=1.67$, $\varepsilon_a=0.2\%$).

The difference between paths C and D is that path C passes through the central line of the hexagon, but path D is along the boundary of the same hexagonal cell. The details of the geometry and the paths C and D can be found in the upper-right hand corner of Fig. 4.62. The results show that the average ΔCTD decreases according to the order of A, B, C and D. The ratio of the average ΔCTD according to this order is 1.74, 1.3, 1.08 and 1. The results indicate a very important point in that silicon particle clusters can reduce the fatigue driving force to a large extent and, in turn, can increase the fatigue life for A356 Al alloy. If one compares the results of case B with those of case C, one can see that the ΔCTD calculated for the in-plane particle cluster of Fig. 4.4 is much larger than that for the case of a hexagonal cell, indicating that the shielding effects of the particle cluster are important to reduce the local crack driving force. Finally, since the average ΔCTD for the paths of A, B, C and D are all larger than the average ΔCTD of the realistic structure, which is about 15 nm (see Fig. 4.39C), one should be cautious in directly applying the obtained ΔCTD of the parametric studies for fatigue analysis. On the other hand, these idealized analyses are important to investigate the relative effects of different factors on fatigue life.

4.3.1.2.6. EFFECTS OF SIZE, ASPECT RATIO, AND SPACING OF PARTICLES ON THE CYCLIC CRACK TIP DISPLACEMENT

Figure 4.63 shows the effects of the particle size on the average ΔCTD when a fatigue crack grows along the in-plane particle cluster of Fig. 4.4. The results show that the average crack driving force (or average ΔCTD) reaches a minimum when the particle size D equals the particle spacing B. This is different from the particle size effects on N_{inc} where the smaller the size, the

larger the $N_{inc.}$ Hence, particle size has a different influence on crack incubation versus the MSC regime.

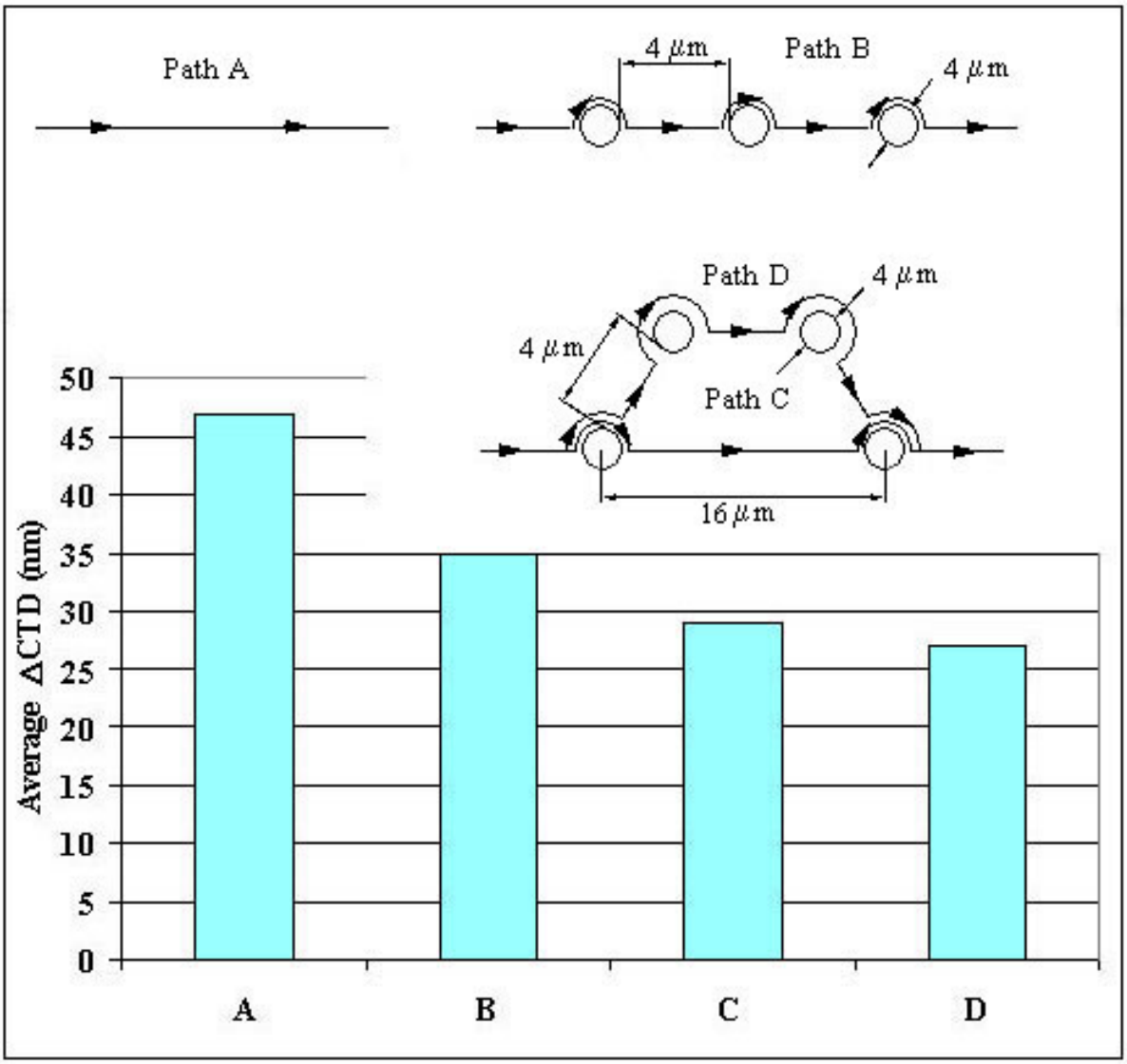

Figure 4.62. A comparison of average (over the maximum projected crack length) ΔCTD for growth paths through (A) Al-rich matrix, (B) in-plane particle cluster, (C) central line of a six-particle cluster arranged as an hexagonal cell, and (D) along the boundary of the same hexagonal cell (R= –1, D =B=4 μm, ε_a =0.2%).

Figure 4.64 shows the effects of the particle aspect ratio on the average ΔCTD when a fatigue crack grows along the in-plane particle cluster of Fig. 4.4. The results show that the average crack driving force (or average ΔCTD) reaches its minimum when the particle aspect ratio reaches unity. This is consistent with the particle size effects on the N_{inc} where the maximum N_{inc} is also at the aspect ratio of unity. It merits notice that when the aspect ratio increases, the driving force (or ΔCTD) increases quickly.

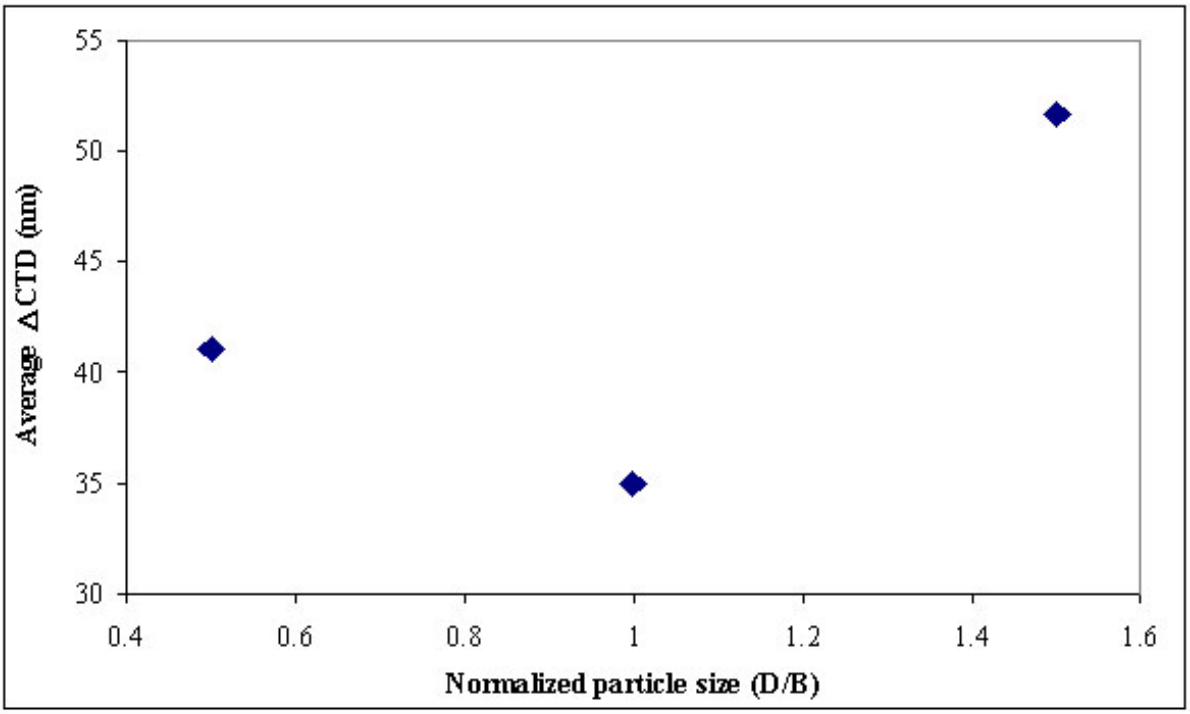

Figure 4.63. Effects of particle size on the average (over the maximum projected crack length) ΔCTD for fatigue crack growth along the in-plane particle cluster for a stress amplitude of 133 MPa (R= –1, B=4 μm, ε_a =0.2%).

As the aspect ratio increases from 1 to 2.5, the average ΔCTD increases from 35 nm to 49.5 nm. This will cause the number of cycles, $N_{MSC/PSC}$ for the MSC and PSC regimes to reduce rapidly. Since a large aspect ratio corresponds to a rod-like particle, this result means that the fatigue life is much lower for particles with rod-like shape. This tendency is consistent with the recent experimental report (Kennerknecht, *et al*., 1997). The report stated that for a plate thickness of 25.4 mm and a heat treatment of four hours, in a smooth A356 Al specimen subjected to a stress amplitude of 151.6 MPa, the fatigue life for a rod-like eutectic structure is approximately 77% of that for globular eutectic structure, under the same loading conditions. The rod-like shaped particle's greater crack driving force may be partially explained by the angle effects mentioned in Section 4.3.1.2.4.

Figure 4.65 shows the effects of the particle spacing on the average ΔCTD during fatigue crack growth along the in-plane particle cluster of Fig. 4.4. The results show that the average crack driving force (or average ΔCTD) reaches its minimum when the particle spacing B equals to the particle size D. This tendency is the same as that of Fig. 4.63. The difference is that in Fig. 4.63, the spacing B is fixed while the size, D, changes; in Fig. 4.65, D is fixed while B changes.

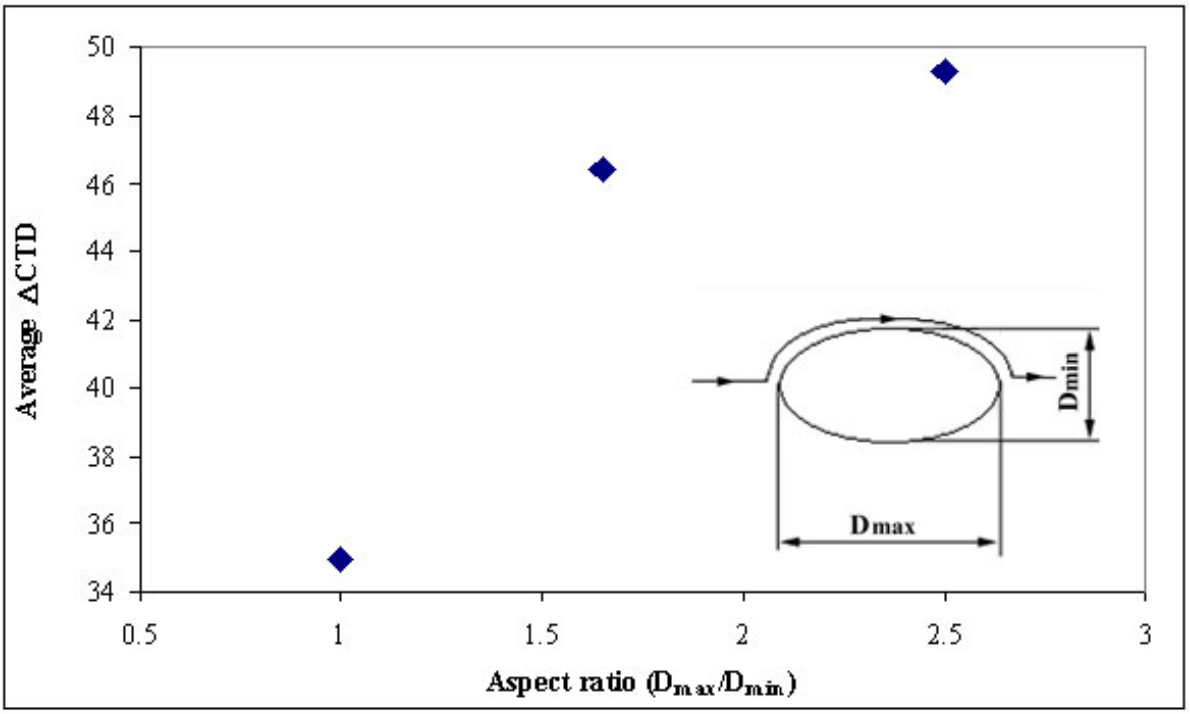

Figure 4.64. Effects of particle aspect ratio on the average (over the maximum projected crack length) ΔCTD for fatigue crack growth along the in-plane particle cluster for a stress amplitude of 133 MPa (D=B=4 μm, R= –1, ε_a= 0.2%).

4.3.1.2.7 EFFECTS OF STRAIN AMPLITUDE ON THE FATIGUE CRACK CLOSURE FOR A CRACK GROWTH PASSING THROUGH AN IN-PLANE PARTICLE CLUSTER

To explore the effects of fatigue crack closure on the fatigue behavior of A356-T6 Al alloy, the time variation of crack opening displacement (COD) at a fixed node were determined. Considering crack propagation along the path of Figure 4.4, for example, node 251 in the path is chosen to investigate the particle effects on crack closure. The distance from that node to the first particle is 6 μm. The variation of COD at that node with time is shown by a line in Figure 4.66. We observed that before the time (ABAQUS measure of "time") 0.54, the node 251 is not fractured and the ΔCTD is zero. After t=0.54, this node opens and reaches its maximum value. The ΔCTD then gradually decreases until the crack is fully closed when the node 251 is on the wake of the crack tip. The crack tip at that node begins to open at point O, which is at t=0.78. In the Figure, another line shows the stress in a remote element adjacent to the top boundary. The stress, σ_P, at point P on the stress curve, which corresponds to point O on the COD curve, approximately equals the applied stress when the crack re-opens. Two parameters R_{cl} and R'_{cl} are introduced to denote the relative period of the crack closure over a quarter of a loading cycle. Their definitions are as follows:

$$R_{cl} = \frac{\sigma_{open}}{(\sigma_{\max} - \sigma_{\min})/2}, \qquad R'_{cl} = \frac{\sigma'_{open}}{(\sigma_{\max} - \sigma_{\min})/2} \qquad \text{Equation 4.7}$$

where $\sigma_{open} = \sigma_P - \sigma_{\min}$ and $\sigma'_{open} = \sigma_{P'} - \sigma_{\min}$. The latter is shown in Fig. 4.66. Based on these definitions, it is seen that the larger the values of these parameters, the larger the crack closure effect (or the smaller ΔCTD) can be found. Figures 4.66-4.68 show results at the strain (stress) amplitude of 0.2% (133MPa), 0.15% (110MPa) and 0.25% (165MPa) under fully reversed cyclic loading conditions (strain control). For the three cases all R'_{cl} are about 100%, indicating crack closure all over the whole compressive loading period. From the results of these figures, R_{cl} can also be determined. They are about 100% for 0.15% (110MPa), 65% for 0.2% (133MPa), and 74% for 0.25% (165MPa).

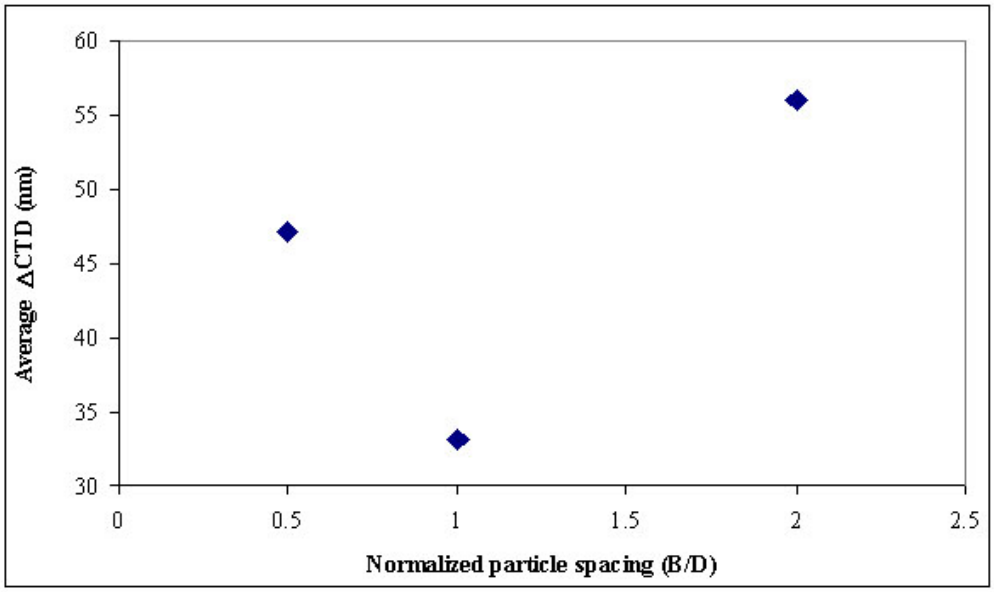

Figure 4.65. Effects of particle spacing on the average (over the maximum projected crack length) ΔCTD for fatigue crack growth along the in-plane particle cluster at a stress amplitude of 133 MPa (D=4 μm, R= –1, ε_a= 0.2%).

4.3.1.2.8 EFFECTS OF REMOTE STRAIN RATIO ON THE FATIGUE CRACK CLOSURE FOR A CRACK GROWTH PASSING THROUGH AN IN-PLANE PARTICLE CLUSTER

Figures 4.66, 4.69-4.70 show the effects of the remote strain ratio, R, on crack opening displacement and crack closure at node 251, 6 μm ahead of particle 1 of the in-plane particle cluster of Figure 4.4. These results were obtained at the same strain amplitude ε_a=0.2%, but with different strain ratio R. In Fig. 4.66, the R ratio is -1. In Figure 4.69 and 4.70, the R ratios are 0 and 0.2. The opening stress are as follows: $\sigma'_{open} = \sigma_{open}$=75 MPa for R_ε=0; $\sigma'_{open} = \sigma_{open}$=0 for R=0.2; σ'_{open}=133MPa and σ_{open}=86MPa for R=–1. From these figures, $(\sigma_{\max} - \sigma_{\min})/2$ can also be determined. It turns out that $R_{cl}=R'_{cl}$=0 for R_ε=0.2 and $R_{cl}=R'_{cl}$=56% for R=0. They are smaller than the corresponding values for R=–1, indicating that the higher the mean stress, the lower the crack closure period (or higher ΔCTD).

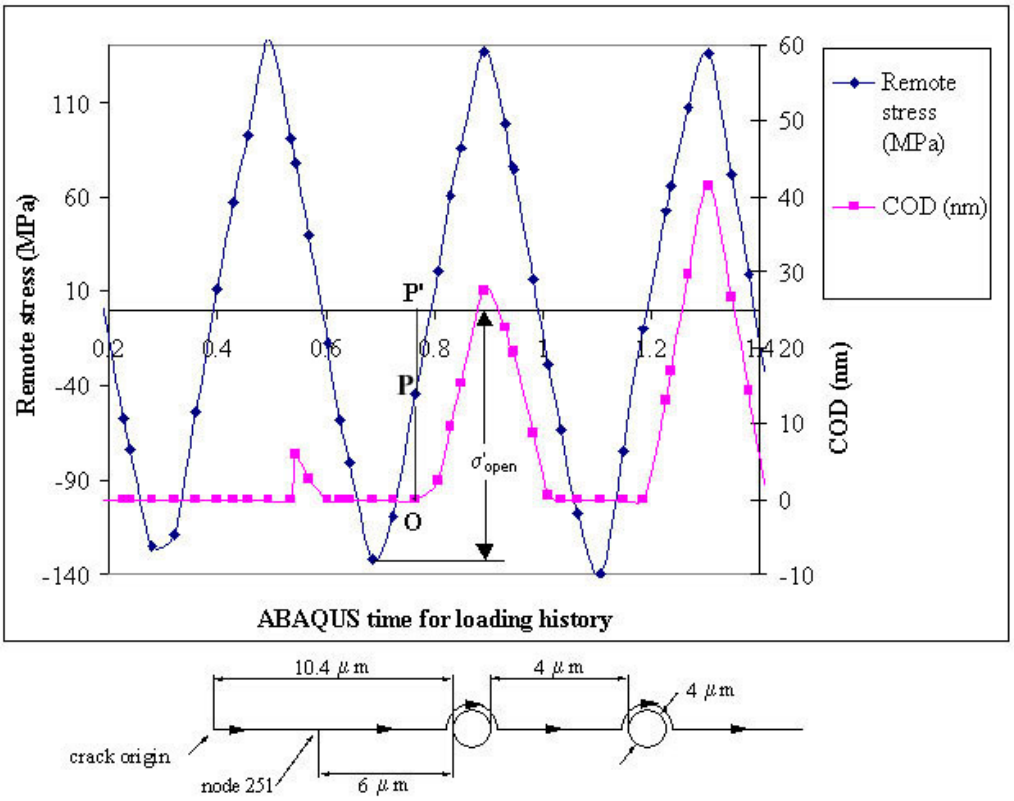

Figure 4.66. Crack opening displacement with crack closure effects at node 251 for a stress amplitude of 133 MPa (R= –1, D=B=4 μm, ε_a=0.2%).

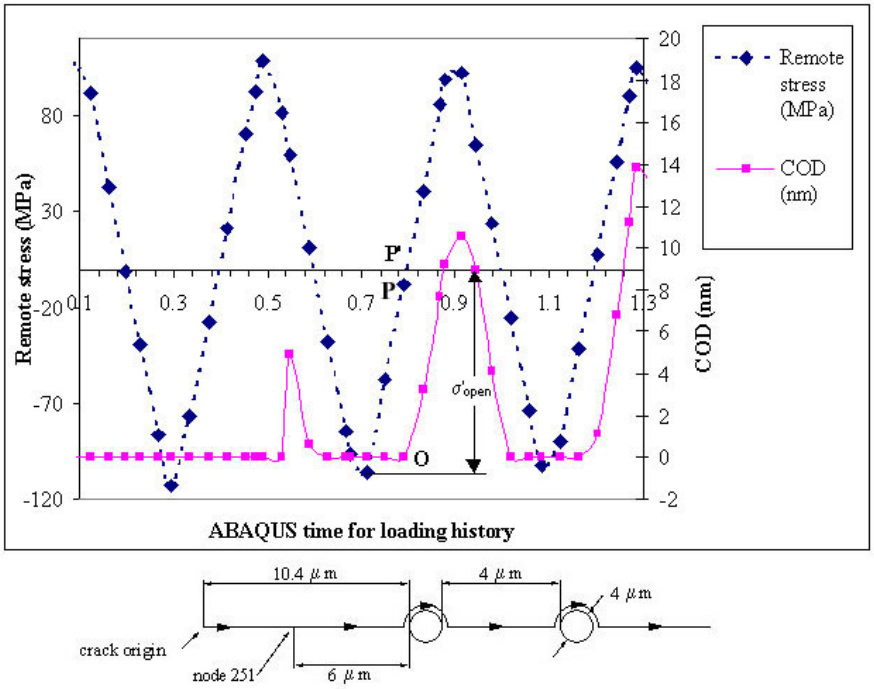

- Figure 4.67. Crack opening displacement with crack closure effects at node 251 for a stress amplitude of 110 MPa (R= –1, D=B=4 μm, ε_a=0.15%).

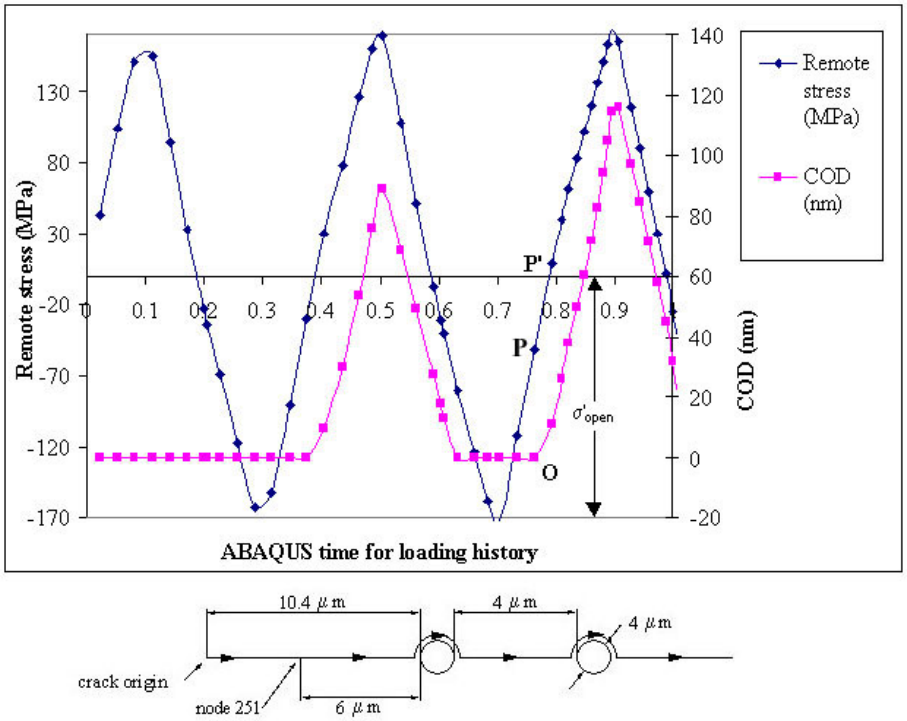

Figure 4.68. Crack opening displacement with crack closure effects at node 251 for a stress amplitude of 165 MPa (R=–1,D=B=4 μm, ε_a =0.25%).

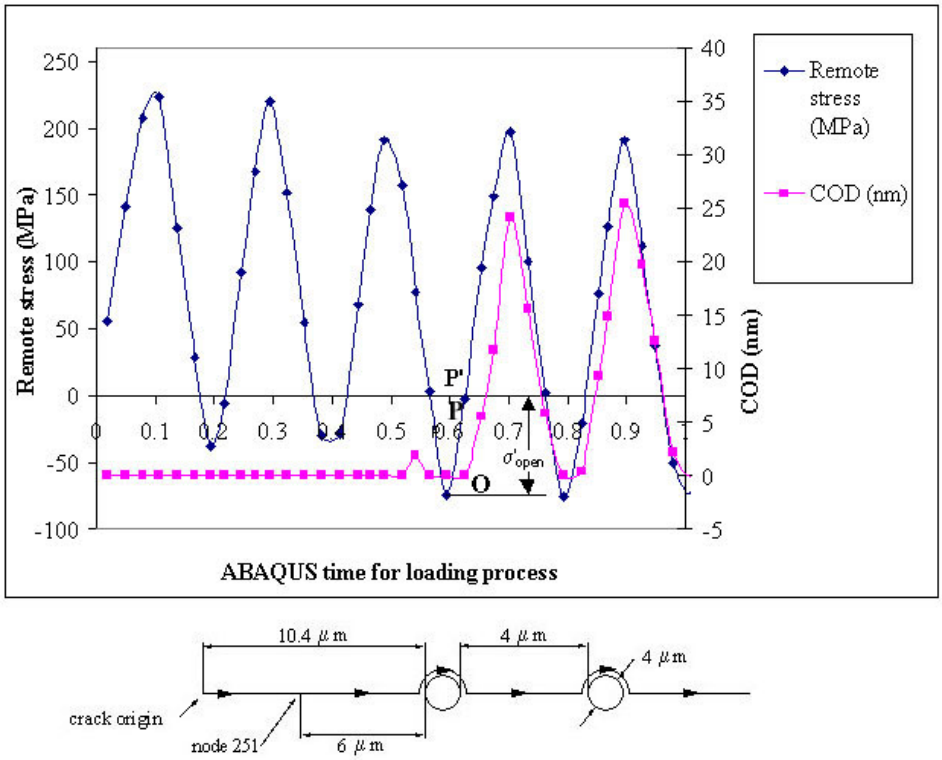

Figure 4.69. Crack opening displacement with crack closure effects at node 251 for a stress amplitude of 133 MPa (R=0, D=B=4 μm, ε_a =0.2%).

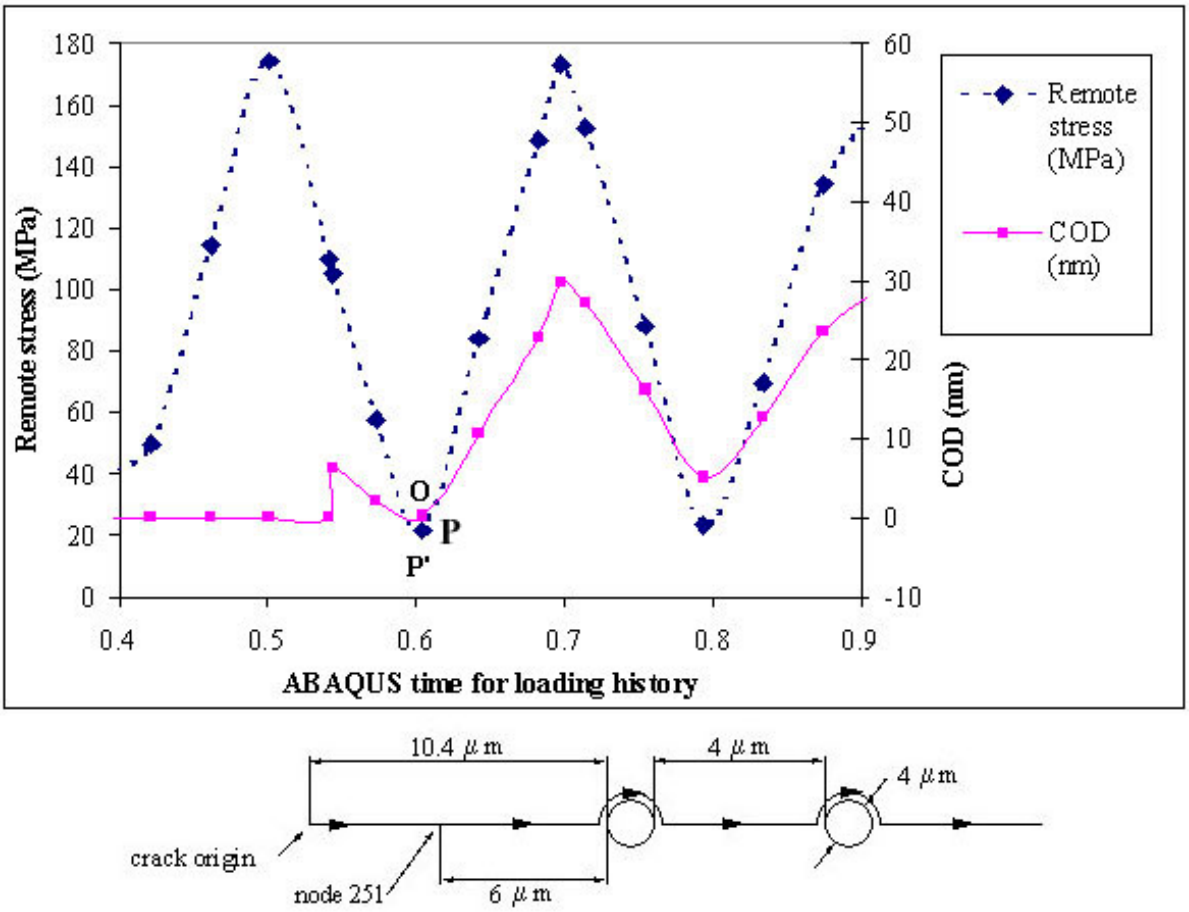

Figure 4.70. Crack opening displacement with effects of crack closure at node 251 for a stress amplitude of 133 MPa (R=0.2, D=B=4 μm, ε_a =0.2%).

4.3.1.2.9. DENDRITE CELL SIZE EFFECTS ON THE CYCLIC CRACK TIP DISPLACEMENT AND CRACK CLOSURE

The finite element mesh used to simulate the growth of a microstructurally short crack in a cast Al-Si alloy is presented in Figure 4.71. Initially, the study considered five dendrite cells created by rows of Si particles embedded in an Al-1%Si dendritic material. We note that the mesh in Figure 4.71 is symmetric about the left face, thus creating five dendrite cells. A section of the fine mesh region is highlighted in Figure 4.71, and the element size is about 1/4 the silicon particle diameter. An isotropic linear elastic constitutive model was used to model the silicon particles, while a nonlinear elasto-plastic constitutive model was used to model the Al-1%Si dendritic material. In this section, as a first approximation, the growth of the fatigue crack was modeled by allowing the crack to grow incrementally along a prescribed crack plane without considering a criterion for crack extension, or the residual deformation fields caused by a traversing fatigue crack. As such, only monotonic loading conditions were considered with different predetermined crack lengths, a. The purpose of such an analysis is to obtain a first order approximation of the effects of silicon particle rich dendritic cell walls on fatigue crack growth. The crack path was assumed to follow a Mode I route unless it encountered a silicon particle, in

which case the crack grew around the particle matrix interface, as experimentally observed for microstructurally small cracks (Gall *et al*., 1999b).

Contour plots of the maximum plastic shear strain are shown in Figures 4.72 and 4.73. The overall crack lengths in Figures 4.72 and 4.73 are 24 μm and 36 μm, respectively. Furthermore, Figures 4.72a and 4.73a present plastic strain contours for pure Al-1%Si materials and Figures 4.72b and 4.73b are plastic strain contours for Al-1%Si materials containing Si particles. An overlay of the finite element mesh is included in Figure 4.72, but the mesh is removed from Figure 4.73 for clarity of the plastic strain contours. By comparing the contour plots in the (a) pure Al-1%Si and (b) Al-1%Si with Si particles, it is clear that the presence of the Si particles alters the overall shape of the crack tip plastic zone. In general, the plasticity is forced to find paths around the particles, as evident in Figures 4.72b and 4.73b. Although the shape of the crack tip plastic zone is altered by the presence of the particles, the constraint of the particles has a minimal influence on the local crack tip plasticity and crack opening displacement. Note in Figure 4.73 that the size of the intense zone of plasticity near the crack tip is the same (b) with or (a) without the surrounding Si particles. Furthermore, Figure 4.74 presents the crack opening displacement for the materials with and without Si particles for the (a) 24 μm crack and (b) 36 μm crack. At both crack lengths, the crack tip is somewhat blunted by the presence of the silicon particles. However, the degree of crack tip blunting is minimal compared to the severe decrease in surface crack growth rates when a crack tip impinges upon a silicon particle (Shiozawa *et al*. 1997).

A summary of the crack tip opening displacement for materials with and without Si particles, as a function of crack tip position, is shown in Figure 4.75. A schematic section of the finite element mesh from Figure 4.71 is inset in Figure 4.76 to allow correlation of the crack tip position with the location of the Si particles. Essentially, as the crack traverses through the pure Al-1%Si material and the Al-1%Si material with silicon particles, the crack opening displacements are nearly identical. The only noticeable difference between the crack opening displacements in the two materials occurs when the crack is forced to change its local path and move around a Si particle. Even when the crack tip node is at the boundary of the silicon particle and the Al-1%Si matrix, the crack opening displacement is not significantly decreased by the presence of the Si particle (Figure 4.76). The crack opening displacement is only lowered when the crack is allowed to change direction and locally forced into an unfavorable mode of growth (Figure 4.76).

With the results from the present section, we assert that the overall constraint of the surrounding silicon particles does not have a strong *relative* influence on the growth of a microstructurally small fatigue crack in cast Al-Si alloys in the matrix phase. Instead, the local interaction and forced path change of the cracks when encountering silicon particles is the dominant cause for the severe decrease in growth rates experimentally observed in cast Al-Si alloys (Shiozawa *et al*. 1997). Appropriately, it is not imperative to consider the surrounding silicon particles, and the remainder or this paper will focus on the local interaction of cracks with silicon particles directly in-line with the crack plane.

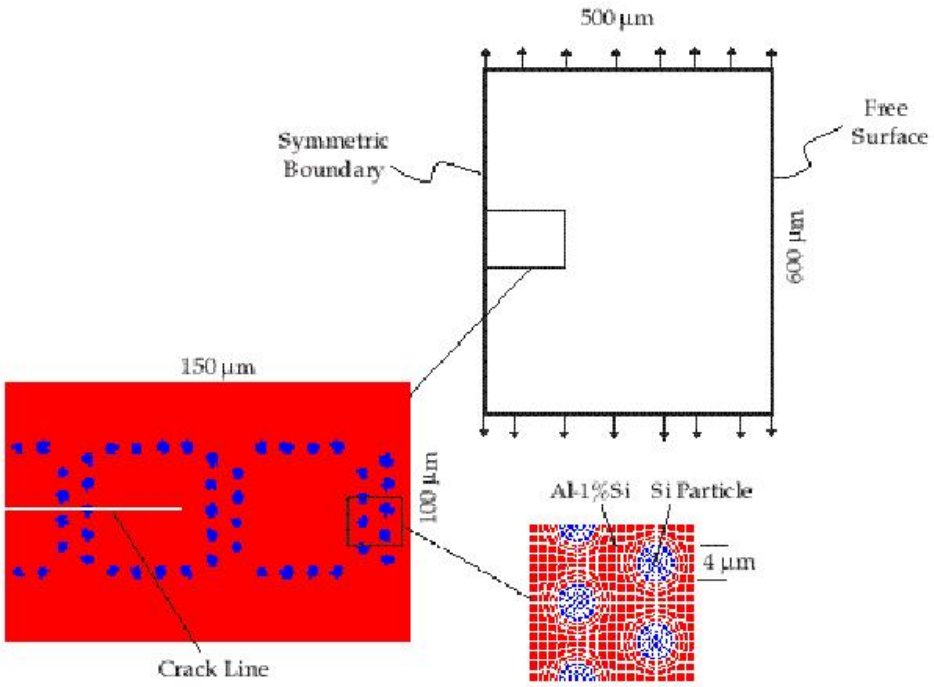

Figure 4.71. Finite element mesh design used for simulating crack growth through a 2-D dendrite cell structure in a cast Al- Si alloy.

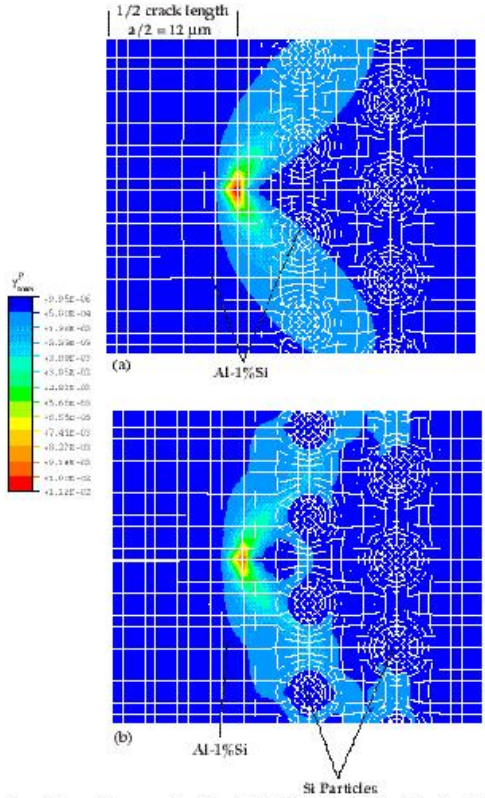

Figure 4.72. Plastic zones for a 24 µm long crack subjected to 0.2% far-field strain for (a) pure Al-1% Si and (b) Al-1%Si containing Si particles. The two meshes were identical except for the designation of the rounded regions as pure Si.

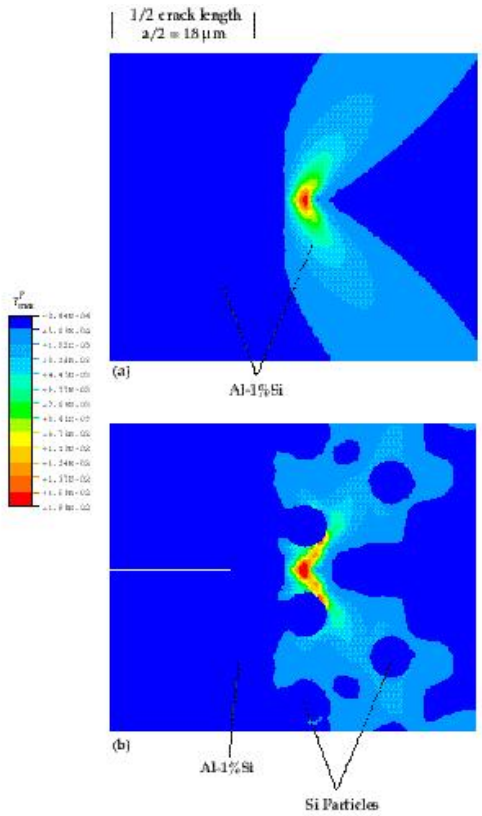

Figure 4.73. Plastic zones for a 36 μm crack subjected to 0.2% far-field strain for (a) pure Al-1% Si and (b) Al-1%Si containing Si particles. The two meshes were identical except for the designation of the rounded regions as pure Si.

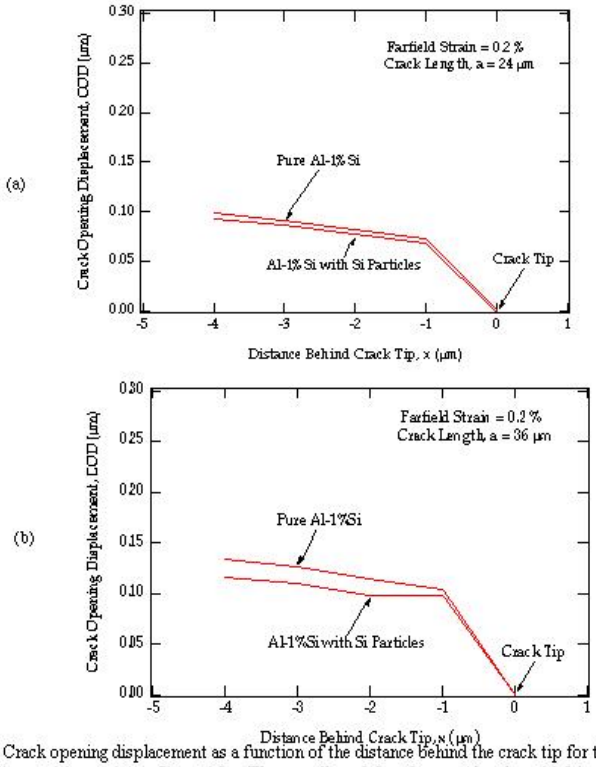

Figure 4.74. Crack opening displacement as a function of the distance behind the crack tip for the pure Al-1% Si material and the Al-1%Si material containing Si particles. The overall crack lengths considered are (a) 24 μm and (b) 36 μm.

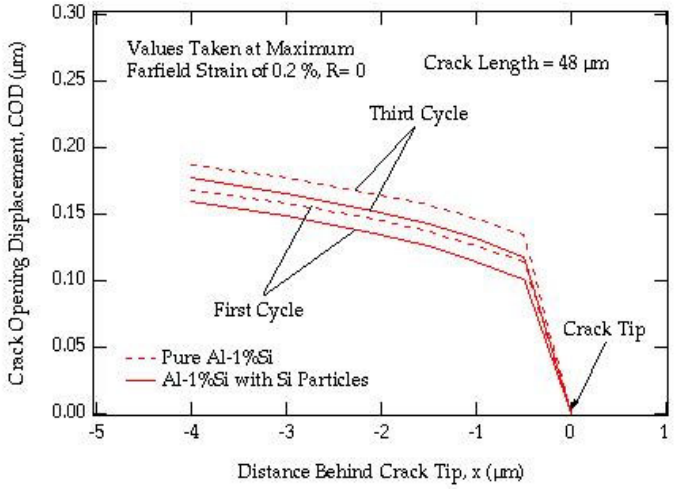

Figure 4.75. Crack opening displacement as a function of the distance behind the crack tip for the pure Al-1% Si material and the Al-1%Si material containing Si particles. The overall crack length is 48 μm.

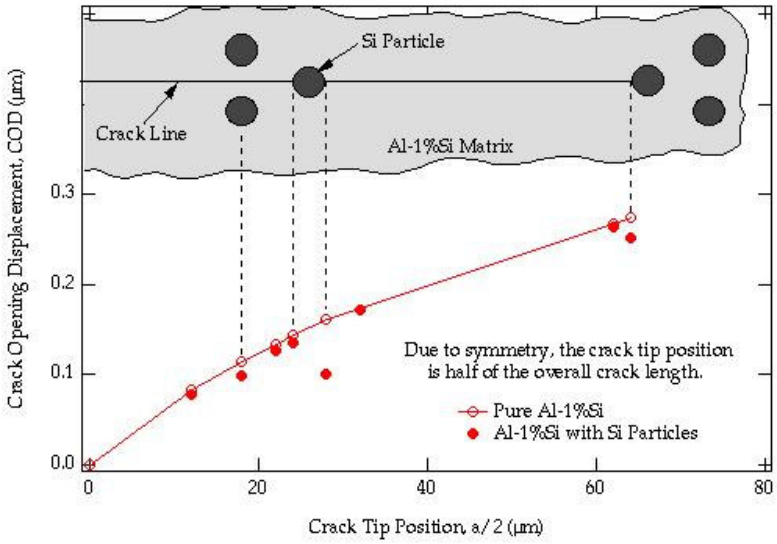

Figure 4.75. Crack opening displacement as a function of the distance behind the crack tip for the pure Al-1% Si material and the Al-1%Si material containing Si particles. The overall crack length is 48 μm.

Figure 4.77 shows the effects of dendrite cell size, DCS, on the average ΔCTD when a fatigue crack grows inside a dendrite cell at the stress amplitude of 133 MPa for a reversal cyclic tension-compression. It indicates that when the dendrite cell size is smaller, the driving force and the crack growth rate is smaller. This is consistent with the results above.

To explore the role of fatigue crack closure to help explain the above DCS effects on the average fatigue driving force, crack closure is investigated during the process of fatigue crack growth into dendrite cells. The crack path is similar to the path of Figure 4.4, i.e., the crack originates from point O, growing from left to right along the x-axis direction. The first particle that the crack meets is used to simulate the interdendritic region. After the crack grows, passing through the upper half of the particle, the crack continues to grow in the matrix of the dendrite cell. The second particle which the crack meets is also used to simulate the interdendritic region. The length of the crack before it meets the first particle is taken as 10.5 μm. The distance between the centers of the two particles is taken as the DCS. The solid line of Figure 4.78 shows the history of crack opening displacement at node 567, which is 22 μm inside a dendrite cell with DCS being 44μm. We observed that before the time 0.8 the node 567 is not fractured, and the ΔCTD is zero. After the time 0.8, this node opens, ΔCTD reaches its maximum value of 60 nm at the time 0.9, and then gradually reduces until the crack is fully closed when node 567 is on the wake of the crack tip. The crack is closed when the time equals 1.05, and the crack is re-opened at point O which is at the time of 1.15. For the case of DCS=44μm at node 567, R_{cl} =30% and R'_{cl} =100%. However, for the case of DCS=28μm at node 559 which is 8.5 μm inside the matrix region of the dendrite cell, $R_{cl}=R'_{cl}$ = 100%. This comparison indicates that as the dendrite cell size increases, the crack closure period can be found to decrease. This means that if the DCS is larger to some extent, the driving force will be larger to cause a low fatigue life.

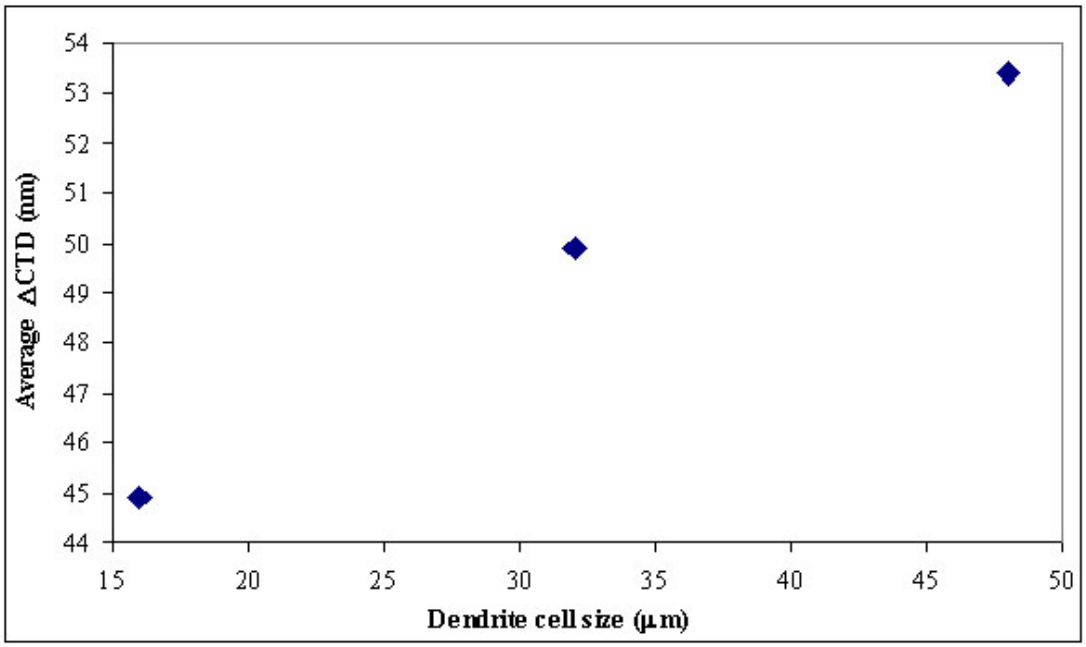

Figure 4.77. Effects of dendrite cell size on the average (over the maximum projected length) ΔCTD for fatigue crack growth across a dendrite cell at a stress amplitude of 133 MPa (R=–1, D=B=4 μm, ε_a =0.2%).

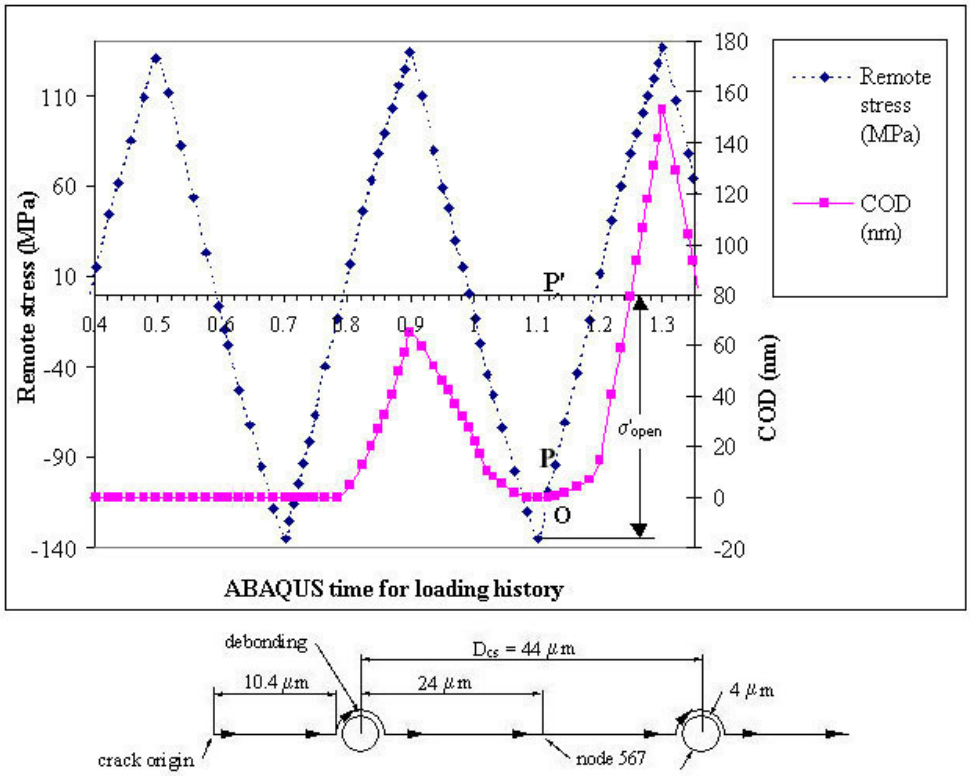

Figure 4.78. Crack opening displacement with crack closure effects at node 567 at a stress amplitude of 133 MPa (R= –1, D=4 μm, ε_a=0.2%).

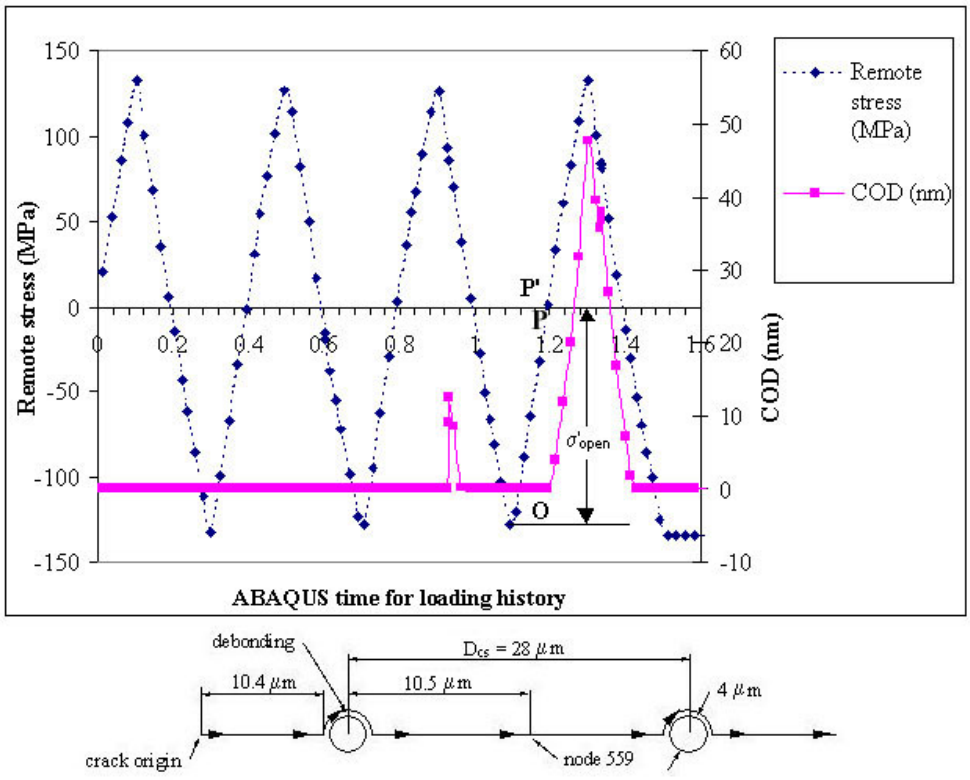

Figure 4.79. Crack opening displacement with crack closure effects at node 559 for a stress amplitude of 133 MPa (R= –1, D=4 μm, ε_a=0.2%).

5. CONTROL ARM ANALYSIS

In this computational/experimental study we use the microstructure-mechanical fatigue model to predict the response of a control arm given certain boundary conditions. Finite element simulations were performed to determine the stress/strain state. The microstructure-property fatigue model was then used with different control arms that included different microstructure/inclusion contents. Validation experiments were run at two different strain amplitudes.

In order to evaluate the predictive capability of the microstructure-property model within the context of finite element modeling, control arm experiments were designed to validate the model. Figure 5.1 shows the boundary conditions for the validation experiments of the control arm. Two different control arms, labeled later as Control Arm 1 and Control Arm 2, were cast that would ensure different levels of initial porosity. The microstructure/inclusion content was quantified by NDE using radiography and by SEM imaging and analysis in five regions of the control arm. Figure 5.2 shows the five locations. The pertinent features of interest were the spatial location of the following entities:

1. porosity volume fraction,
2. pore size distribution,
3. pore nearest neighbor distances,
4. silicon particle volume fraction,
5. silicon particle size distribution,
6. silicon particle nearest neighbor distances, and
7. dendrite cell size.

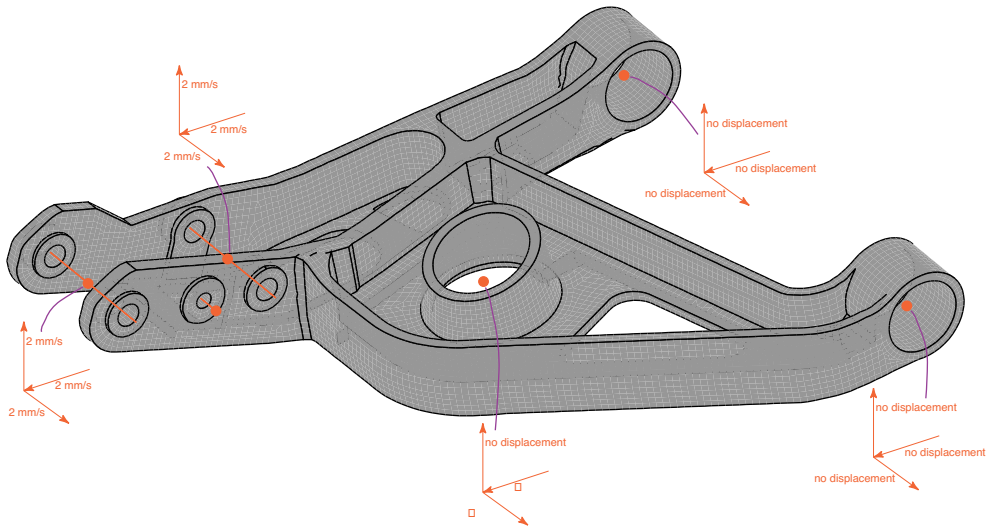

Figure 5.1. Boundary conditions for model validation tests.

In the next set of calculations we initialize the microstructure/inclusion content with data from radiography and SEM imaging. Table 5.1 summarizes the microstructure/inclusion content for the five regions on the control arm as discussed above. The results in the table are averages of the at least three measurements for two different control arms using SEM imaging (Gokhale, 2000) and radiography (Dolan, 2000).

Table 5.1. Summary of results for control arm microstructure/inclusion content from SEM images and radiography.

region	$\%V_v$	pore size (μm)	Nearest neighbor dist	3D pore size (μm)	Si particle Size (μm)	Si density (#/mm^2)	DCS (μm)
Control Arm 1 (SEM results)							
1	2.35	67.3	315	129	5.8	7088	50
2	0.30	38.9	669	54	4.8	7557	-
3	0.19	38.8	652	56	4.9	7738	-
4	0.19	45.0	402	66	4.6	6950	39
5	0.31	44.8	395	55	4.6	7659	42
Control Arm 1 (Radiography results)							
1	0.72	-	-	-	-	-	-
2	0.33	-	-	-	-	-	-
3	0.33	-	-	-	-	-	-
4	0.33	-	-	-	-	-	-
5	0.41	-	-	-	-	-	-
Control Arm 2 (SEM results)							
1	0.43	68.7	-	-	4.7	4251	-
2	-	-	-	-	5.2	5389	-
3	0.34	62.7	-	-	4.8	6318	-
4	-	-	-	-	-	-	-
5	0.32	57.8	-	-	4.7	6803	-
Control Arm 2 (Radiography results)							
1	0.48	-	-	-	-	-	-
2	0.33	-	-	-	-	-	-
3	0.33	-	-	-	-	-	-
4	0.33	-	-	-	-	-	-
5	0.33	-	-	-	-	-	-

Table 5.1 shows that the radiography and SEM results are very close for each of the control arms. One can see that the initial porosity volume fraction for Control Arm 1 is larger in certain regions than for Control Arm 2.

Figure 5.2. Lower control arm casting showing five locations from which samples are extracted for metallography and computed tomography analyses.

Finite element simulations for Control Arms 1 and 2 were performed with the bounding limits of the microstructures that were averaged in Table 5.1. Table 5.2 shows the lower and upper limits of the quantities measured by SEM in Regions 1 and 3. The other regions gave very similar results and hence were included as limiting bounds for the rest of the control arm. Fatigue analyses using the microstructure-property model were performed with the minimum and maximum values for the microstructure attributes and the stresses and strains obtained from the finite element simulations were used to predict the number of cycles for each control arm.

Because of time limitations for experimental testing, only tests that captured 0.8% local strain amplitudes were used for the finite element simulations. Figures 5.3-5.4 show the maximum principal stress results for Control Arms 1 and 2. Given these local Mises and principal stress values in Region 1, the microstructure-property fatigue model gave values for the incubation, MSC, and PSC regimes between 1000-2000 cycles for up to a 1 mm crack. Interestingly, the experimental load-cycle and displacement-cycle curves showed drops and/or bumps between 1000-2000 cycles. This change in compliance of the control arms indicate possibly indicate the onset of long crack growth as predicted by the model. The long crack model was not used because of project time limitations and complexities related to capturing a tortuous three dimensional crack growing in a finite element analysis. For specimens taken out of the control arm and then tested at 0.8% strain amplitudes, the microstructure-property fatigue model captured the general range of "small" crack sizes as the range was 5-80 cycles for the model and 4-84 for the specimen experiments.

Table 5.2. Summary of mininum/maximum SEM image results for control arms microstructure/inclusion content.

	Region 1		Region 3		Other regions	
Control Arm 1						
attribute	min	max	min	max	min	max
%Vv	0.003	0.1118	0.0001	0.0032	0	0.00061
Pores size	34	118	25	63	0	67
Particle size	4.5	7.1	4.5	5.5	4.1	5.2
DCS	49	54	40	54	40	40
Control Arm 2						
%Vv	0.00085	0.005	0.00095	0.0056	0.00015	0.0069
Pores size	29	100	43	82	31	82
Particle size	4.6	4.9	4.4	5.2	4.5	5.2
DCS	49	54	40	54	40	40

Next, we examine the connection between small specimen testing from regions within the control arm versus testing the control arm and evaluate the fatigue of production versus lightweight designs. The development of the multi-scale microstructure-property fatigue model was based upon small specimen testing in fatigue as opposed to control arm tests of the whole component. Typically, specimens are extracted from regions of a component and used for uniaxial fatigue tests. This was performed on the Control Arms 1 and 2. In particular, small specimen uniaxial fatigue tests (R=-1) were performed on material that was extracted from the five regions of the two control arms. Tables 5.3 and 5.4 summarize the results. Three specimens were tested for each section. When one considers from Table 5.2 the microstructure/inclusion content, a correlation with large pores (and volume fraction) can be made with the lowest fatigue life.

Table 5.3. Data from small specimen uniaxial tests (R=-1) of regions in Control Arm 1.

Region	*Number of cycles (min/max) at 0.2% strain amplitude*	*Number of cycles (min/max) at 0.8% strain amplitude*
1	12392-48558	12-22
2	4979-18133	22-26
4	5692- 37643	4-8
5	23806-37976	32-40

Let us now compare the small specimen data with the whole control arm tests. To relate the two, finite element simulation results must be used to determine the local stress/strain states in Region 1, for example, to the specimen tests. A completely reversed displacement boundary

condition was used. Table 5.5 summarizes this correlation. The results show one to two orders of magnitude difference between the specimen and control arm for the 0.2% strain amplitude and several orders of magnitude difference for the 0.8% strain amplitude.

Table 5.4. Data from small specimen uniaxial tests (R=-1) of regions in the Control Arm 2.

Region	*Number of cycles (min/max) at 0.2% strain amplitude*	*Number of cycles (min/max) at 0.8% strain amplitude*
1	49762-169326	7-39
2	29382	29-84
3	103931-124200	10-29
4	36339-98693	10-35
5	109200-236963	23-60

These differences exist for several reasons. First, the specimen test experienced truly uniaxial, completely reversed loading. The control arm experiences both a uniaxial loading and bending. Bending fatigue tests generally give longer fatigue lives because as the crack progresses, a lesser critical volume is stressed as it moves from tension to compression and so on. Secondly, although the uniaxial component of the stress/strain tensors are dominant, the finite element results show that shear components are significant. Hence, a multiaxial stress state exists in the control arm but did not exist in the specimen tests. Previous multiaxial tests were performed on specimens showing that at 0.8% strain amplitudes the additional shear component actually lengthens the fatigue life, approximately an order of magnitude. But at the 0.2% strain amplitudes, the additional shear component does almost nothing to the fatigue life. Hence, these explanations do account fully for the differences.

Perhaps the most important difference between the specimen results and control arm results is due to the following reason: Almost 90% of the fatigue life is dominated by the small crack regime (incubation, microstructurally small crack, and physically small crack) for small, cylindrical uniaxial specimens. The microstructure-property model has been able to model cracks in this regime for specimens taken from a wide variety of components. Furthermore, only one crack usually dominated in the specimen tests. For the control arm, Figure 5.5 shows that two cracks typically formed on each side of the support hole in the Strut 1. The fatigue life recorded for the control arm tests relates to the when the whole Strut 1 failed. In other words, when the cracks proceeded to the control arm edges as shown in Figure 5.6. The first crack started at point a in Strut 1 near support hole and propagated three dimensionally to point b near the control arm edge. Just this first crack experienced a larger volume of stressed material than the extracted specimens experienced. As such, we would expect a lesser fatigue life for the smaller specimens based upon this argument alone. As such, a few thousand more cycles would be experienced in the long crack regime in the control arm in this section, where the specimen would not experience these cycles in the long crack regime. But we are not done. The control arm experienced a second crack that went through the incubation, small crack, and long crack regimes. This second crack started at point c in Figure 5.5 and propagated to point d. The distance for the first crack to propagate was a little more than a quarter of an inch, but the second

crack must traverse at least one inch. These added distances added many cycles to the fatigue life in the long crack regime.

Table 5.5. Data comparison from small specimen uniaxial tests in Region 1 versus control arm 2 (R=-1).

	Number of cycles (min/max) at 0.2% strain amplitude	*Number of cycles (min/max) at 0.8% strain amplitude*
specimens	5×10^4-1.7×10^5	7-39
whole control arm	5×10^6	1.25×10^5

The lightweight monotonic mechanical properties were increased over the old production design (see From Atoms to Autos, A New Design Paradigm Using Microstructure-Property Modeling Part 1: Monotonic Loading Conditions). If monotonic loading trends were directly transferable to fatigue life, then one would expect that the lightweight design would have a significant improvement on the fatigue life. This was indeed true as Table 5.6 summarizes the data for the old designed control arms and the optimized, lightweight design. To analyze the microstructure-property fatigue model further, one would have to perform HCF regime testing. Because of time constraints on this project, these tests were not conducted.

Table 5.6. Data comparison from whole control arms (R=-1).

	Control Arms 1 and 2	*lightweight*
Number of cycles (min/max) at 35.6 kN applied load	22-110	550
Number of cycles (min/max) at 17.8 kN applied load	14500-19000	42000-71000

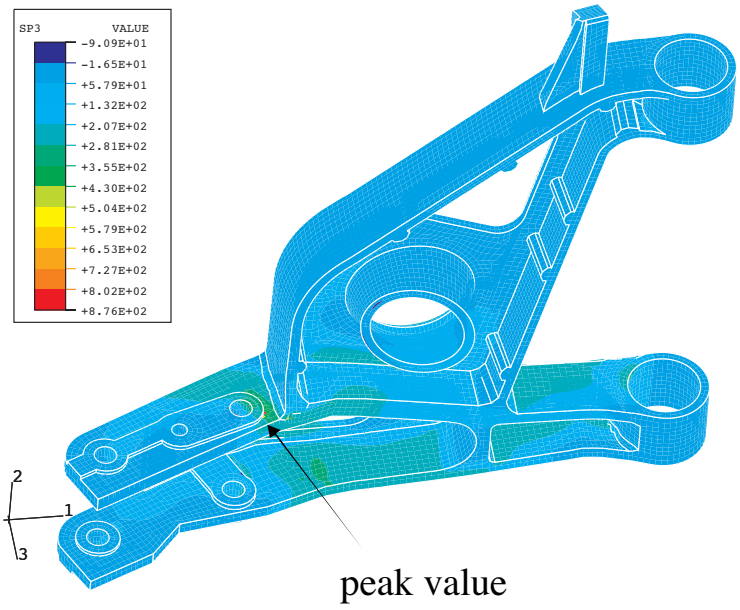

Figure 5.3. Finite element analysis showing maximum principle stress (SP3) distribution.

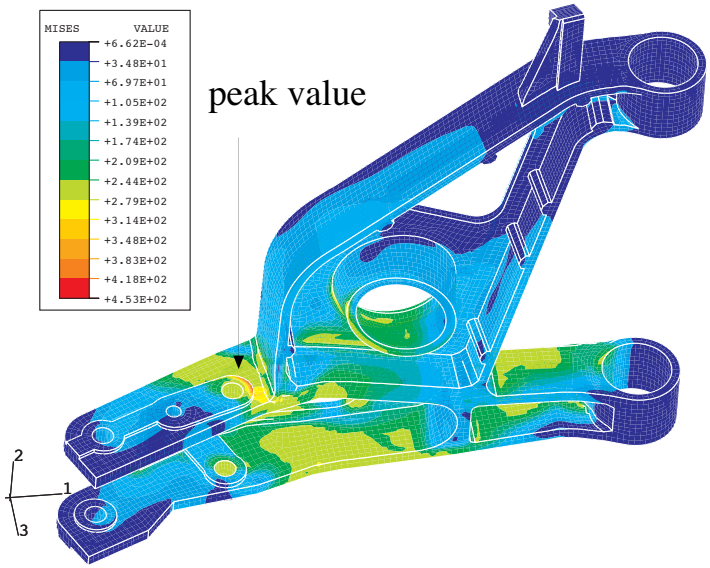

Figure 5.4. Finite element analysis showing Mises stress distribution.

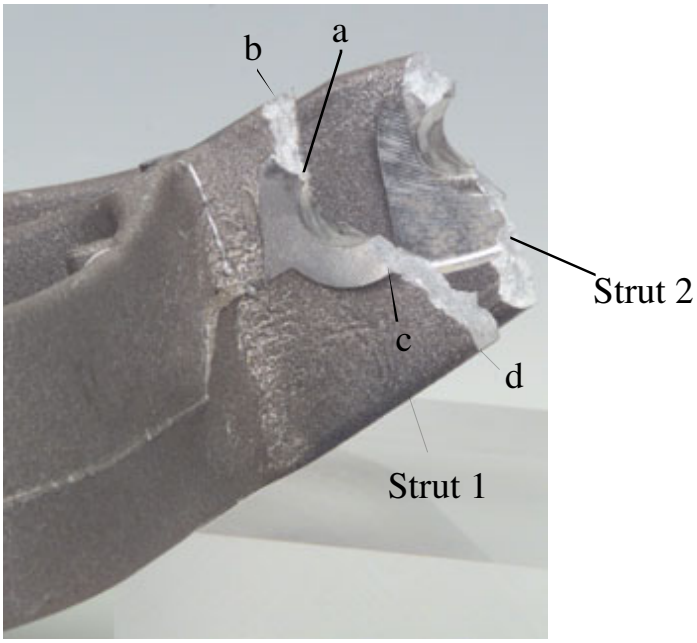

Figure 5.5. Fracture surfaces of Strut 1 in Region 1 and Strut 2. Point a is where fracture initiated and propagated to point b. After fracture of the surface from points a to b, a new crack started at point c and propagated to point d.

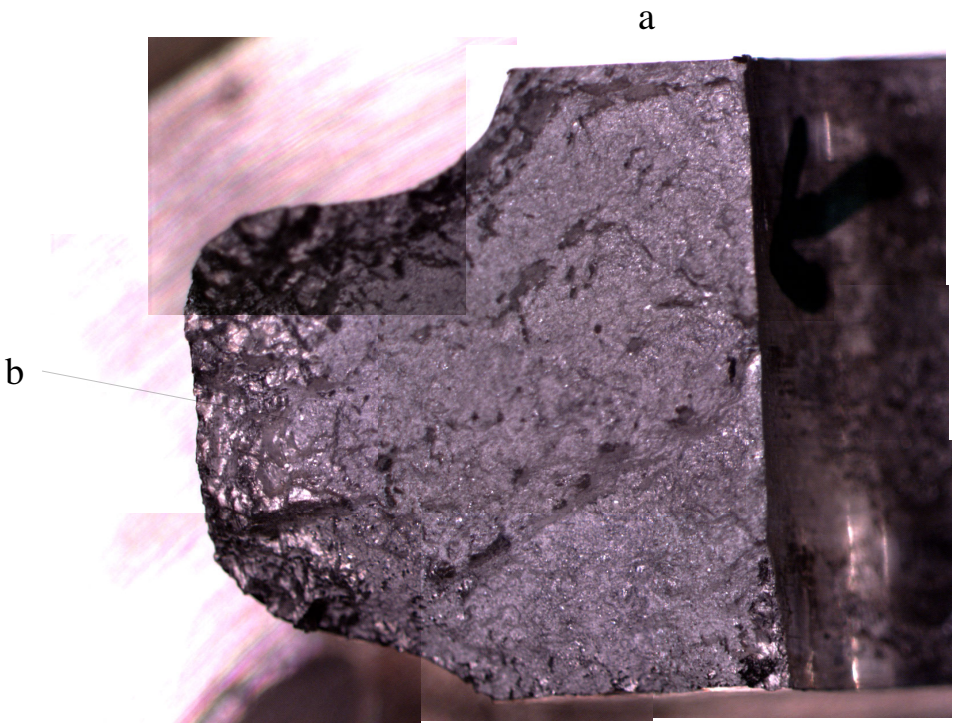

Figure 5.6. Optical image of fracture surface. Point a signifies the initial fracture point and point b signifies the final fracture point before tensile overload.

6. SUMMARY

Previous work on relating the microstructure/inclusion content on fatigue life has not received adequate treatment for cast materials. As such, we conducted a set of experiments and performed micromechanical finite element simulations to develop a database of information that was used to develop macroscale microstructure-property model for fatigue analysis. The model captures the essense of fatigue damage progression, thus enabling the promise of an accurate, predictive tool. A multi-length scale approach, from the micron scale to large structural scale analyses, was used to relate the key microstructural features to the mechanical fatigue properties.

The specific inputs to microstructure-property model include the following:

(1) silicon volume fraction
(2) silicon particle size distribution
(3) pore volume fraction
(4) pore size distribution
(5) pore nearest neighbor distance
(6) dendrite cell size distribution
(7) stress/strain state and applied amplitudes
(8) R-ratio
(9) overloads and sequence effects

The microstructure-property model for fatigue is capable of capturing the trends for other castings, such as magnesium or iron, for forgings, and for any wrought material. Experiments would be needed to determine the material constants. If some experiments are not available, the microstructure-property fatigue model can still be used without that particular feature.

List of Papers as a Result of This Study:

1. Fan, J., McDowell, D.L., Horstemeyer, M.F., and Gall, K., "Computational Micromechanics Analysis and Model Development for Fatigue Behavior of Microstructurally Small Crack Growth in Dual-Phase Materials," *Engineering Fracture Mechanics*, (2000).

2. Gall, K., Horstemeyer, M.F., McDowell, D.L., and Fan, J.H., "Finite Element Analysis of the Debonding and Fracture of Si Particle Clusters in Cast Al-Si Alloys Subjected to Cyclic Loading Conditions," *Mech. Mater.* (1999).

3. Gall, K., Yang, N., Horstemeyer, M.F., McDowell, D.L., and Fan, J., "The Influence of Modified Intermetallic and Si Particles on Fatigue Crack Paths in Commercial Cast A356 Al Alloy," *Fatigue and Fracture of Engineering Materials and Structures*, (1999).

4. Gall, K., Yang, N., Horstemeyer, M.F., McDowell, D.L., and Fan, J., "The Debonding and Fracture of Si Particles During the Fatigue of a Cast Al-Si Alloy," *Metallurgical and Materials Transactions A*, (1999).

5. Horstemeyer, M.F., "Damage Influence on Bauschinger Effect of a Cast A356 Aluminum Alloy," *Scripta Materialia*, Vol. 39, No. 11, pp. 1491-1495, (1998).

6. McDowell, D.L., Fan, J., and Horstemeyer, M.F., "Multi-Length Scale Analyses of Cyclically Loaded A356 Cast Aluminum Alloy," *AFS Transactions*, (1999).

7. Gall, K., Horstemeyer, M.F., Degner, B.W., McDowell, D.L., and Fan, J. "On the Driving Force for Fatigue Crack Formation from Inclusions and Voids in a Cast A356 Aluminum Alloy," *Int. J. Fracture*, submitted.

7. REFERENCES

ABAQUS/Standard User Manual, Hibbitt, Karlsson, & Sorensen, Inc., Vol. 1-6, (1998).

Bammann, D.J., Chiesa, M.L., and Johnson, G.C., "Modeling Large Deformation and Failure in Manufacturing Processes," *Theo. App. Mech.*, eds. Tatsumi, Wannabe, and Kambe, Elsevier Science, Vol. 259, (1996).

Bammann, D.J., Chiesa, M.L., Horstemeyer, M.F., and Weingarten, L.I., "Failure in Ductile Materials Using Finite Element Methods," *Structural Crashworthness and Failure*, eds. N. Jones and T. Weirzbicki, Elsevier Applied Science, Ch.1, 1, (1993).

Bathias, C., "A Review of Fatigue of Aluminum Matrix Reinforced by Particles of Short Fibers," *Materials Science Forum*, Vols. 217-222, pp. 1407-1412, (1996).

Bathias, C., "Relations Between Endurance Limits and Thresholds in the Field of Gigacycle Fatigue," *ASTM Fall Meeting*, Norfolk, VA, (1998).

Bazant, Z.P. and Chen, E.-P., "Scaling of Structural Failure," *ASME Applied Mechanics Reviews*, Vol. 50, No. 10, pp. 593-627, (1997).

Bowles, C.Q. and Schijve, J., "The Role of Inclusions in Fatigue Crack Initiation in an Aluminum Alloy," *Int. J. Frac.*, Vol. 9, pp. 171-179, (1973).

Broek, D., *Fracture 1969*, ed. P. L. Pratt, Chapman and Hall, p. 734, (1969).

Campbell, J., *Castings*, Butterworth Heinemann, (1991).

Cordes, T.S., Berns, H.D., Lingenselser,D.J., Mahoney, B.J. and Testin, R.A., "A SWT Fatigue Mean Stress Model for A356-T6 Cast Aluminum Alloy," *SAE Tech. Publ.* SP760, Fatigue and Fracture Toughness of A356-T6 Cast Aluminum Alloy, Vol. 881703, pp. 39-48, (1988).

Couper, M.J. and Griffiths, J.R., "Effects of Crack Closure and Mean Stress on the Threshold Stress Intensity Factor for Fatigue of an Aluminum Casting Alloy," *Fat. Frac. Eng. Mat. Struc.*, Vol. 13, pp. 615-624, (1990).

Couper, M.J., Neeson, A.E., and Griffiths, J.R., "Casting Defects and the Fatigue Behavior of an Aluminum Casting Alloy," *Fat. Frac. Eng. Mat. Struc.*, Vol. 13, pp. 213-227, (1990).

Dabayeh, A.A., Berube, A. J., and Topper, T. H. Topper, "An Experimental Study of the Effect of a Flaw at a Notch Root on the Fatigue Life of Cast Al319," *Int. J. Fat.*, Vol. 20, pp. 517-530, (1998).

Dabayeh, A.A., Xu, R.X., Du, B.P., and Topper, T. H., " Fatigue of Cast Aluminum Alloys Under Constant and Variable Amplitude Loading," *Int. J. Fat.*, Vol. 18, pp. 95-104, (1996).

DeBartolo, E.A. and Hillberry, B.M., "Effects of Constituent Particle Clusters on Fatigue Behavior of 2024-T3 Aluminum Alloy," *International Journal of Fatigue*, Vol. 20, No. 10, pp. 727-735, (1998).

Dighe, M.D. and Gokhale, A.M., "Relationship Between Microstructural Extremium and Fracture Path in a Cast Al-Si-Mg Alloy," *Scr. Mett.*, Vol. 37, pp. 1435-1440, (1997).

Dowling, N.E., "Fatigue at Notches and the Local Strain and Fracture Mechanics Approahces," *Fracture Mechanics, ASTM STP 677*, ed. C.W. Smith, ASTM Philadelphia, pp. 247-273, (1979).

Dunn, M.L., Suwoto, W., Cunningham, S., and May, C.W., *Int. J. Frac.*, Vol. 84, pp. 367-381, (1997).

Elber, W., "Fatigue Crack Closure Under Cyclic Tension," *Eng. Frac. Mech.,* Vol. 2, pp. 37-45, (1970).

Eshelby, J.D., "The Elastic Field Outside an Elliptical Inclusion," *Prc. Roy. Soc. Lond.*, Vol. A252, p. 561, (1957).

Ewalds, H.L. and Wanhill, R.J.H., *Fracture Mechanics*, Chapman and Hall, (1989).

Fan, J., McDowell, D.L., Horstemeyer, M.F., and Gall, K., "Computational Micromechanics Analysis and Model Development for Fatigue Behavior of Microstructurally Small Crack Growth in Dual-Phase Materials," *Engineering Fracture Mechanics or Mechanics of Materials*, (1999).

Fatemi, A. and Kurath, P., "Multiaxial Fatigue Life Predictions Under the Influence of Mean Stresses," *J. Eng. Mat. Tech.*, Vol. 110, pp. 380-388, (1988).

Fatemi, A. and Socie, D., "A Critical Plane Approach to Multiaxial Fatigue Damage Including Out of Phase Loading," *Fat. Frac. Eng. Mat. Struc.*, Vol. 11, pp. 145-165, (1988).

Fleck, N.A., Hutchinson, J.W., and Tvergaard, V., "Softening by Void Nucleation and Growth in Tension and Shear," *J. Mech. Phys. Solids*, Vol. 37, pp. 515-540, (1989).

Forsyth, P.J.E., "Exudation of Material From Slip Bands at the Surface of Fatigued Crystals of an Aluminum-Copper Alloy," *Nature*, Volume 171, pp. 172-173, (1953).

Gall, K., Horstemeyer, M.F., McDowell, D.L., and Fan, J.H., "Finite Element Analysis of the Debonding and Fracture Characteristics of Si Particle Clusters in Cast Al-Si Alloys Subjected to Cyclic Loading Conditions," *Mechanics of Materials*, (1999).

Gall, K., Yang, N., Horstemeyer, M.F., McDowell, D.L., and Fan, J., "The Influence of Modified Intermetallic and Si Particles on Fatigue Crack Paths in Commercial Cast A356 Al Alloy," *Fatigue and Fracture of Engineering Materials and Structures*, (1999).

Gall, K., Yang, N., Horstemeyer, M.F., McDowell, D.L., and Fan, J., "The Debonding and Fracture of Si Particles During the Fatigue of a Cast Al-Si Alloy," *Metallurgical and Materials Transactions A*, (1999).

Gokhale, A.M., Patel, G., and Dighe, M., "Quantitative Characterization of Cast Microstructures of A356 Alloy," USCAR Project Review Meeting, Sandia National Laboratory, Livermore, CA, (1998).

Grosskreutz, J.C., and Shaw, G.G., "Critical Mechanisms in the Development of Fatigue Cracks in 2024-T4 Aluminum", *Fracture 1969, Proc. 2nd Int. Conf. Frac., Brighton, pp. 620-629* (1969).

Gundlach, R.B., Ross, B., Hetke, A., Valtierra, S., and Mojica, J.F., "Thermal Fatigue Resistance of Hypoeutectic Aluminum-Silicon Alloys. *AFS Trans.*, Vol. 102, pp. 205-223, (1994).

Gungor, S. and Edwards, L., "Effect of Surface Texture on Fatigue Life in a Squeeze Cast 6082 Aluminum Alloy," *Fat. Frac. Eng. Mat. Struc.*, Vol. 16, No. 4, pp. 391-403, (1993).

Harkegard, G., "A Finite Element Analysis of Elastic-Plastic Plates Containing Cavities and Inclusions with Reference to Fatigure Crack Initiation," *Int. J. Frac.,* Vol. 9, pp. 437-447, (1973).

Harvey, S.E., Marsh, P.G., and Gerberick, W.W., "Atomic Force Microscopy and Modeling of Fatigue Crack Initiation in Metals," *Acta. Metall. Mater.,* Vol. 42, pp. 3493-3502, (1994).

Hayhurst, D.R., Leckie, F.A., and McDowell, D.L., "Damage Growth Under Nonproportional Loading," ASTM STP 853, Philadelphia, pp. 688-699, (1985).

Horstemeyer, M.F. and McDowell, D.L. "Using Statistical Design of Experiments for Parameter Study of Crystal Plasticity Modeling Features under Different Strain Paths," Sandia National Laboratories Report SAND96-8683 (1997).

Horstemeyer, M.F., "Damage Influence on Bauschinger Effect of a Cast A356 Aluminum Alloy," *Scripta Materialia*, Vol. 39, No. 11, pp. 1491-1495, (1998).

Horstemeyer, M.F. and Gokhale, A.M., *Int. J. Solid Struc.*, (1999).

Horstemeyer, M.F., McDowell, D.L., and McGinty, R.D., "Design of Experiments for Constitutive Model Selection: Application to Polycrystal Elastoviscoplasticity," Modell. Simul. Mater. Sci. Eng., Vol. 7, pp. 253-273 (1999).

Hoshide, T. and Socie, D.F., "Crack Nucleation and Growth Modeling In Biaxial Fatigue", *Engineering Fracture Mechanics*, Vol. 29, No. 3, pp. 287-299, (1988).

Hoskin, G.A., Provan, J.W., and Gruzleski, J.E., "The In-Situ Fatigue Testing of a Cast Aluminum-Silicon Alloy," *Theor. Appl. Frac. Mech*., Vol. 10, pp. 27-41, (1988).

Hyzak, J.M. and Bernstein, "The Effect of Defects on the Fatigue Crack Initiation Process in Two P/M Superalloys: Part I. Fatigue Origins," *Metall. Trans.*, Vol. 13A, pp. 33-43, (1982).

Inguanti, P.C., "Cast Aluminum Fatigue Property/Microstructure Relationships," *17th SAMPE Conf.*, Oct. 22-24, pp. 61-72, (1985).

Katagiri, K., Omura, A., Koyanagi, K., Awatani, J., Shiraishi, T., and Kaneshiro, H., "Early Stage Crack Tip Morphology in Fatigued Copper," *Metall. Trans.*, Vol. 8A, pp. 1769-1773, (1977).

Kearney, A. and Rooy, E.L., "Aluminum Foundry Products," *ASM Handbook*, Vol. 2, pp. 123-151, (1990).

Kennerknecht, S., Dumant, R., Tombari, and Van Biljon, *Journal of Minerals, Metals, and Materials Society*, Vol. 49, No. 11, pp. 22-281, (1997).

Kim, W.H. and Laird, C., "Crack Nucleation and Stage I Propagation in High Strain Fatigue – II. Mechanism," *Acta. Metall.*, Vol. 26, pp. 789-799, (1978).

Kung, C.Y. and Fine, M.E., "Fatigue Crack Initiation and Microcrack Growth in 2024-T4 and 2124-T4 Aluminum Alloys," *Metall. Trans.*, Vol. 10A, pp. 603-610, (1979).

Kuo, A.S. and Liu, H.W., "An Analysis of Unzipping Model for Fatigue Crack Growth," *Scripta Metallurgica*, Vol. 10, pp. 723-728, (1976).

Lalor, P.L. and Sehitoglu, H., "Fatigue Crack Closure Outside a Small-Scale Yielding Regime," *Mechanics of Fatigue Crack Closure*, Eds. J.C. Newman, Jr. and W. Elber, ASTM STP 982, Philadelphia, pp. 342-360, (1987).

Lankford, J. and Kusenberger, F. N., "Initation of Fatigue Cracks in 4340 Steel," *Mett. Trans.*, Vol. 4, pp. 553-559, (1973).

Lankford, J., "Inclusion-Matrix Debonding and Fatigue Crack Initiation in Low Alloy Steel," *Mett. Trans.,* Vol. 4, pp. 155-157, (1976).

Lankford, J., Davidson, D., and Chan, K.S., "The Influence of Crack Tip Plasticity in the Growth of Small Cracks," *Metallurgical Transactions A*, Volume 4A, pp. 1459-1588, (1984).

Lankford, J., *Fat. Frac. Engn. Mat Struct.*, Vol. 5, pp. 233-248, (1982).
Lankford, J., *Fat. Frac. Engn. Mat Struct.*, Vol. 8, pp. 161-175, (1985).
Laz, P.J. and Hillberry, B.M., "Fatigue Life Prediction from Inclusion Initiated Cracks," *Int. J. Fat.*, Vol. 20, pp. 263-270, (1998).
Lee, F.T., Major, J.F., and Samuel, F.H., "Effect of silicon Particles on the Fatigue Crack Growth Characteristics of Al-12 Wt Pct Si-0.35 Wt Pct Mg-(0 to 0.02) Wt Pct Sr Casting Alloys," *Metall. Mater. Trans.,* Vol. 26A, pp. 1553-1570, (1995).
Lee, F.T., Major, J.F., and Samuel, F.H., "Fracture Behavior of Al12wt%Si0.35wt%Mg(0-0.02)wt%Sr Castings Under Fatigue Testing," *Fat. Frac. Engn. Mat Struct.,* Vol. 18, pp. 385-396, (1995).
Li, C., "Vector CTD Analysis for Crystallographic Crack Growth," *Acta Metall. Mater.*, Vol. 38, No. 11, pp. 2129-2134, (1990).
Liu, A.F., "Behavior of Fatigue Cracks in a Tension Bolt," *Structural Integrity of Fasteners*, ASTM STP 1236, pp. 124-140, (1995).
Lukas, P., "Fatigue Crack Nucleation and Microstructure," *ASM Handbook,* Vol. 19, *Fatigue and Fracture, ASM International,* pp. 96-109, (1996).
Mackay, T.L. and Alperin, B.J., "Stress-Intensity Factors for Fatigue Cracking in High Strength Bolts," *Eng. Frac. Mech.*, Vol. 21, pp. 391-397, (1995).
Major, J.F., "Porosity Control and the Fatigue Behavior in A356-T61 Aluminum Alloy," *AFS Trans.*, Vol. 102, pp. 901-906, (1994).
McClintock, F.A., "Considerations for Fatigue Crack Growth Relative to Crack Tip Displacement," *Engineering Against Fatigue*, Eds. J.H. Beynon, M.W. Brown, T.C. Lindley, R.A. Smith and B. Tomkins, Balkema Press, Chapter 24, pp. 227-241, (1999).
McClung, R.C. and Sehitoglu, H., *Eng. Frac. Mech.*, Vol. 33, pp. 237-271, (1989).
McClung, R.C., Chan, K.S., Hudak, S.J., and Davidson, D.L., *ASM Handbook*, Vol. 19, pp. 153-158, (1996).
McDowell, D.L. "Multiaxial Effects in Metallic Materials," *Symposium on Durability and Damage Tolerance, ASME AD-Vol. 43*, ASME Winter Meeting, Chicago, IL, pp. 2131-267, (1994)
McDowell, D.L. and Bennett, V., "Micromechanical Aspects of Small Multiaxial Fatigue Cracks," Proc. 5th Int. Conf. on Biaxial/Multiaxial Fatigue & Fracture, Cracow, Poland, pp. 325-348, (1997).
McDowell, D.L., "Stress State Dependence of the Cyclic Ratchetting Behavior of Two Rail Steels," *International Journal of Plasticity*, Vol. 11, No. 4, pp. 397-421, (1995).
McDowell, D.L., "Basic Issues in the Mechanics of High Cycle Metal Fatigue," *Int. J. Frac.,* Vol. 80, pp. 103-145, (1996-b).
McDowell, D.L., "Multiaxial Fatigue Strength," *ASM Handbook,* Vol. 19, pp. 263-273, (1996-a).
McDowell, D.L., Fan, J., and Horstemeyer, M.F., "Multi-Length Scale Analyses of Cyclically Loaded A356 Cast Aluminum Alloy," *AFS Transactions*, (1999).
Morris, W.L., "The Effects of Intermetallics Composition and Microstructure on Fatigue Crack Initiation in A1 2219-T851," *Metall. Trans.,* Vol. 9A, pp. 1345-1348, (1978).

Morris, W.L., Buck, O., and Marcus, H.L., “Fatigue Crack Initiation and Early Propagation in A1 2219-T851,” *Metall. Trans.,* Vol. 9A, pp. 1345-1348, (1976).

Murakami, Y. and Endo, M., "Effects of Defects, Inclusions, and Inhomogeneities on Fatigue Strength," *Fatigue*, Vol. 16, pp. 163-182, (1994).

Murakami, Y., *Stress Intensity Factors Handbook*, Vols. 1 and 2, Pergamon Press, Oxford, (1987).

Murali, S., Arvind, T.S., Raman, K.S., and Murthy, K.S.S., "Fatigue Properties of Sand Cast, Stircast and Extruded Al-7Si-0.3Mg Alloy with Trace Additions of Be and Mn," *Mat. Trans. JIM*, Vol. 38, pp. 28-36, (1997).

Murali, S., Trivedi, A., Shamanna, K.S., and Murthy, K.S.S., "Effect of Iron and Combined Iron and Beryllium Additions on the Fracture Toughness and Microstructures of Squeeze Cast Al-7Si-0.3Mg Alloy," *J. Mat. Eng. Perform.,* Vol. 5, pp. 462-468, (1996).

Needleman, A., "A Continuum Model for Void Nucleation by Inclusion Debonding," *J. Appl. Mech.,* Vol. 109, pp. 525-531, (1987).

Neumann, P., "New Experiments Concerning the Slip Processes at Propagating Fatigue Cracks-I.," *Acta. Metall.*, Vol. 22, pp. 1155-1165, (1974).

Newman, J.C. Jr., “FASTRAN II-A Fatigue Crack Growth Structural Analysis Program,” *NASA-TM-104159, NASA Langley Research Center*, (1992).

Newman, J.C., Jr., "A Review of Modelling Small-Crack Behavior and Fatigue-Life Predictions for Aluminum Alloys," *Fatigue and Fracture of Engineering Materials and Structures*, Vol. 17, No. 4, pp. 429-439, (1994).

Nisitani, H., "Behavior of Small Cracks in Fatigue and Relating Phenomena," Current Research on Fatigue Cracks, T. Tanaka, M. Jono and K. Komai, Eds., Current Japanese Materials Research, Vol. 1, *Elsevier*, pp. 1-26, (1987).

Padkin, A.J., Brereton, M.F., and Plumbridge, W.J., "Fatigue Crack Growth in Two Phase Alloys," *Mater. Sci. Tech.*, Vol. 3, pp. 217-223, (1987).

Paris, P.C. and Erdogan, F., "A Critical Analysis of Crack Propagation Laws," *Trans. ASME, J. Basic Eng.,* Vol. D85, pp. 528-534, (1963).

Pearson, S., *Eng. Frac. Mech.*, Vol. 7, pp. 235-247, (1975).

Pelloux, R.M.N. , "Mechanisms of Formation of Ductile Fatigue Striations," *Trans ASME*, Vol. 62, pp. 281-285, (1969).

Plumtree, A. and Schafer, S., "Initiation and Short Crack Behavior in Aluminum Alloy Castings," *The Mechanical Behavior of Short Fatigue Cracks*, Eds. K. J. Miller and E. R. de los Rios, EGF Publication 1, Suffolk, UK, pp. 215-227, (1997).

Repetto, E.A. and Ortiz, M., “A Micromechanical Model of Cyclic Deformation and Fatigue-Crack Nucleation in f.c.c. Single Crystals,” *Acta Materialia*, Vol. 45, No. 6, pp. 2577-2595, (1997).

Sadananda, K. and Vasudevan, A.K., “Analysis of Fatigue Crack Closure and Thresholds,” ASTM STP 1220, Fracture Mechanics: 25th Volume, Ed. F. Erdogan, ASTM, Philadelphia, pp. 484-501, (1995).

Samuel, A.M., and Samuel, F.H., "A Metallographic Study of Porosity and Fracture Behavior in Relation to the Tensile Properties in 319.2 End Chill Castings," *Metall. Mater. Trans.,* Vol. 26A, pp. 2359-2372, (1995).

Schaefer, M. and Fournelle, R.A., "Effect of Strontium Modification on Near-Threshold Fatigue Crack Growth in an Al-Si-Cu Die Cast Alloy," *Metall. Mater. Trans.*, Vol. 27A, pp. 1293-1302, (1996).

Sehitoglu, H. and Sun, W., "Modeling of Plane Strain Fatigue Crack Closure," *ASME Journal of Engineering Materials and Technology*, Vol. 113, pp. 31-40, (1991).

Shiozawa, K., Tohda, Y., and Sun, S.M., "Crack Initiation and Small Fatigue Crack Growth Behavior of Squeeze-Cast Al-Si Aluminum Alloys," *Fat. Frac. Eng. Mat. Struc*., Vol. 20, pp. 237-247, (1997).

Skallerud, B., Iveland, T., and Harkegard , G., "Fatigue Life Assessment of Aluminum Alloys With Casting Defects," *Eng. Frac. Mech.,* Vol. 44, pp. 857-874, (1993).

Smith, R.A. and Miller, K.J., "Fatigue Cracks at Notches*," International Journal of the Mechanical Sciences*, Vol. 19, pp. 11-22, (1977).

Socie, D.F., "Critical Plane Approaches for Multiaxial Fatigue Damage Assessment," *Advances in Multiaxial Fatigue*, ASTM STP 1191, D.L. McDowell and R. Ellis, Eds., American Society of Testing and Materials, Philadelphia, pp. 7-36, (1993).

Sonsino, C. M. and Ziese, J., "Fatigue Strength and Applications of Cast Aluminum Alloys with Different Degrees of Porosity," *Int. J. Fat.*, Vol. 15, pp. 75-84, (1993).

Stanzl-Tschegg, S.E., Mayer, H.R., Tschegg, E.K., and Beste, A., "In-Service Loading of AlSi11 Aluminum Cast Alloy in the Very High Cycle Regime," *Int. J. Fat.*, Vol. 15, pp. 311-316, (1993).

Stephens, R.I., Berns, H.D., Chernenkoff, R.A., Indig, R.L., Koh, S.K., Lingenfelser, D.J., Mitchell, M.R., Testin, R.A., and Wigant, C.C., "Low-Cycle Fatigue of A356-T6 Cast Aluminum Alloy Wheels," *Fatigue and Fracture Toughness of A356-T6 Cast Aluminum Alloy*, SAE Tech. Publ. SP760, Vol. 881701, pp. 1-28, (1988).

Stephens, R.I., Mahoney, B.J. and Fossman, R.G., "Low Cycle Fatigue of A356-T6 Cast Aluminum Alloy Wheels," *Fatigue and Fracture Toughness of A356-T6 Cast Aluminum Alloy*, SAE Tech. Publ. SP760, Vol. 881707, pp. 93-102, (1988).

Sundstrom, B., "An energy Condition for Initiation of Interfacial Microcracks at Inclusions," *Eng. Frac. Mech.,* Vol. 6, pp. 483-492, (1974).

Suresh, S., *Fatigue of Materials*, Cambridge University Press, Cambridge, UK, (1991).

Tan, Y.H., Lee, S.L., and Lin, Y.L., "Effects of Be and Iron Content on Plane Strain Fracture Toughness in A357 Alloys," *Metall. Mater. Trans. A,* Vol. 26A, pp. 2937-2945, (1995).

Tanaka, K. and Mura, T., "A Theory of Fatigue Crack Initiation at Inclusions," *Metall. Trans.,* Vol. 13A, pp. 117-123, (1982).

Tanaka, K., *Fracture Mechanics: Perspectives and Directions (20th Symposium)*, ASTM STP 1020, R. P. Wei and R. P. Gangloff, Eds., pp. 151-183, (1989).

Ting, J.C. and Lawrence, F.V., "Modeling the Long-Life Fatigue Behavior of a Cast Aluminum Alloy," *Fat. Frac. Eng. Mat. Struc*., Vol. 16., No. 6, pp. 631-647, (1993).

Tynelius, K.E., Major, J F., and Apelian, D., "A Parametric Study of Microporosity in the A356 Casting Alloy System," *AFS Trans.*, Vol. 101, pp. 401-413, (1993).

Venkataraman, G., Chung, Y.M., and Mura, T., "Application of Minimum Energy Formalism in a Multiple Slip Band Model for Fatigue-I. Crack Nucleation and Derivation of a Generalized Coffin-Manson Law," *Acta. Metall. Mater.*, Vol. 39, No. 11, pp. 2631-2638, (1991).

Venkataraman, G., Chung, Y-W, and Mura, T., “Application of Minimum Energy Formalism in a Multiple Slip Band Model For fatigue-I. Calculation of Slip Band Spacings,” *Acta. Metall. Mater.,* Vol. 39, pp. 2621-2629, (1991).

Venkataraman, G., Chung, Y-W, and Mura, T., “Free Energy Formulation of Fatigue Crack Initiation Along Persistent Slip Bands: Calculation of S-N Curves and Crack Depths,” *Acta. Metall. Mater.,* Vol. 38, pp. 31-40, (1990).

Voigt, R.C. and Bye, D.R., "Microstructural Aspects of Fracture in A356," *AFS Trans.*, Vol. 99, pp. 33-50, (1991).

Wang, C.H. and Miller, K.J., “The Effects of Mean and Alternating Shear Stresses on Short Fatigue Crack Growth Rates, " *Fatigue and Fracture of Engineering Materials and Structures*, Vol. 15, No. 12, pp. 1223-1236, (1992).

Wang, Q.G., Apelian, D. and Griffiths, J.R., “Microstructural Effects on the Fatigue Properties of Aluminum Castings,” Proc. 1st Int. Aluminum Casting Tech. Symp., Rosemont, Illinois, (1998).

Wang, Z. and Zhang, R.J., “Microscopic Characteristics of Fatigue Crack Propagation in Aluminum Alloy Based Particulate Reinforced Metal Matrix Composites,” *Acta Metall. Mater.*, Vol. 42, No. 4, pp. 1433-1445, (1994).

Weinacht, D.J. and Socie, D.F., “Fatigue Damage Accumulation in Grey Cast Iron,” *International Journal of Fatigue*, Vol. 9, No. 2, pp. 79-86, (1987).

Wickberg, A., Gustafsson, G., and Larsson, L.E., "Microstructural Effects on the Fatigue Properties of a Cast A17SiMg Alloy," *SAE Trans.*, Vol. 840121, pp. 1.728-1.735, (1984).

Wigant, C.C. and Stephens, R.I., *Fatigue and Fracture Toughness of A356-T6 Cast Aluminum Alloy-SAE SP 760,* Warrendale, PA, pp. 1-100, (1988).

Yeh, J.W and Liu, W.P., "The Cracking Mechanism of silicon Particles in an A357 Aluminum Alloy," *Metall. Mater. Trans.,* Vol. 27A, pp. 3558-3568, (1996).

This page intentionally blank

A. APPENDIX: CYCLIC PLASTICITY MODELS AND CONSTANTS

In this work, two slightly different internal state variable plasticity models were used in the micromechanical finite element simulations to model the elastic-plastic response of A356 aluminum alloy and the Al-1%Si matrix. Both of these materials were assumed to be plastically incompressible elastoplastic materials, and the silicon particles were assumed to be elastic.

A.1. MCDOWELL MATERIAL MODEL DISCUSSION AND MATERIAL CONSTANTS USED

The constitutive behavior of the matrix and the alloy is described by a simplified nonlinear kinematic hardening law (McDowell, 1995). The yield surface is described as follows:

$$\frac{3}{2}(s_{ij}-\alpha_{ij})(s_{ij}-\alpha_{ij})-\rho^2=0 \qquad \text{Equation A.1}$$

$$d\alpha_{ij}=\sum_{r=1}^{n} d\alpha_{ij}^{(r)} \qquad \text{Equation A.2}$$

$$d\alpha_{ij}^{(r)}=c^{(r)}[b^{(r)}n_{ij}-\alpha_{ij}^{(r)}]dp \qquad \text{Equation A.3}$$

where σ_{ij} is the deviatoric stress, ρ an isotropic hardening parameter, α_{ij} the back stress, n_{ij} a unit vector, and dp is the increment of cumulative plastic strain. The latter two are defined as follows:

$$n_{ij}=\frac{(s_{ij}-\alpha_{ij})}{\left\|(s_{ij}-\alpha_{ij})\right\|} \qquad \text{Equation A.4}$$

$$dp=\sqrt{d\varepsilon_{ij}^{p}d\varepsilon_{ij}^{p}} \qquad \text{Equation A.5}$$

Since the material saturates quickly, the effect on fatigue life of the transient process before the cyclic steady state on fatigue life is minimal. Therefore, isotropic hardening is not considered in the work and ρ is taken as a constant. It is found that two terms (n=2) in the back stress expression are sufficient to describe the cyclic hysteresis loops for A356 aluminum alloy and the Al-1%Si matrix. In this case, there are only five material constants for the cyclic plastic response of each material. To determine these constants, two cyclic stress-strain tests were conducted. One is the cyclic test of A356 aluminum alloy of Al-7%Si, and the other is for the Al-1%Si (the Al-rich matrix). From the obtained stress-strain curves, these material constants and elastic constants are determined and listed in Table A.1. Figures 4.1 and 4.2 compare the stress/strain curves showing the cyclic experimental data and the calculated curve, which uses these material constants for A356 Al alloy and for the Al-1%Si matrix. Satisfactory agreement is found using only five constants to describe the nonlinear behavior. This constitutive law was embedded into a UMAT, a user-defined subroutine in the ABAQUS finite element code (1998).

Table A.1: Material parameters of constitutive laws for both A356 aluminum alloy and Al-1%Si matrix.

	Al-1%Si matrix	A356 Al alloy	Particle
ρ (MPa)	91.5	92.9	-
$b^{(1)}$ (MPa)	73	90	N/A
$b^{(2)}$ (MPa)	27.2	27.2	N/A
$C^{(1)}$	1500	1700	N/A
$C^{(2)}$	839	839	N/A
E (MPa)	70	73.8	112.7
ν	0.3	0.3	0.3

A.2. MODIFIED BCJ MATERIAL MODEL DISCUSSION AND MATERIAL CONSTANTS USED

For the micromechanical finite element simulations using the BCJ material model. The inclusions are assumed to behave in an isotropic, linear elastic manner with an elastic modulus of E_s = 130 GPa and a Poisson's ratio of 0.28 (representative of pure silicon). The matrix material is described using an internal state variable cyclic plasticity model (Bammann *et al.*, 1993 and 1996), except that the isotropic hardening parameter was changed to another kinematic hardening parameter. The cyclic stress-strain model captures the dependence of plastic flow on strain rate, temperature, and large strain deformation. However, in the present work for cyclic fatigue, the temperature and strain rate dependence of the model are not utilized. A thorough analysis of the relevant equations, assumptions, and predictive capability of the model is found in a previous publication (Bammann *et al.*, 1993). However, for the sake of completeness, the important equations are summarized below. The constants for the model were determined by fitting the predicted stress-strain response to the uniaxial experimental stress-strain response using a least squares data fit to the experimental data in Figures 4.1 and 4.2. In both the model and the experiment, the evolution of the stress-strain response saturates after 10 cycles at this strain amplitude.

The constitutive model assumes a hyperelastic stress rate of the form,

$$\overset{o}{\underline{\sigma}} = \left(k - \frac{2}{3}G\right) tr\left(\underline{D}^e\right)\underline{I} + 2G\underline{D}^e \qquad \text{Equation A.6}$$

where $\underline{\sigma}$ and $\overset{o}{\underline{\sigma}}$ are the Cauchy stress and the co-rotational (Jaummann) rate of the Cauchy stress respectively, and k = 67.6 GPa and G = 25.9 GPa are the room temperature elastic bulk and shear moduli, respectively. The deviatoric plastic deformation tensor, $\underline{D}^p$, is given by the following relationship:

$$\underline{D}^p = f \sinh\left[\frac{\left\|\underline{\sigma}' - \frac{2}{3}\underline{\alpha}\right\| - Y}{V}\right]\frac{\underline{\sigma}' - \frac{2}{3}\underline{\alpha}}{\left\|\underline{\sigma}' - \frac{2}{3}\underline{\alpha}\right\|} \qquad \text{Equation A.7}$$

where Y = 147 MPa is the initial uniaxial yield strength of the material at room temperature. The values f = 1 x 10^{-5} 1/s, and V = 0 MPa are material constants also related to the yielding, and $\underline{\sigma}'$ is the deviatoric Cauchy stress. The terms $\underline{\alpha}$ are an additive term that includes two internal state variable kinematic hardening terms. The elastic rate of deformation tensor, $\underline{D}^v$, is given by the following relationship:

$$\underline{D}^e = \underline{D} - \underline{D}^p \qquad \text{Equation A.8}$$

The rate equations for the two internal state variables $\underline{\alpha}_1$ and $\underline{\alpha}_2$ are given as follows,

$$\overset{o}{\underline{\alpha}}_1 = h\underline{D}^p - r\tfrac{2}{3}\underline{D}^p\left\|\underline{\alpha}_1\right\|\underline{\alpha}_1 \qquad \text{Equation A.9}$$

$$\overset{o}{\underline{\alpha}}_2 = H\underline{D}^p - R\tfrac{2}{3}\underline{D}^p\left\|\underline{\alpha}_2\right\|\underline{\alpha}_2 \qquad \text{Equation A.10}$$

where the constants h = 2,503 MPa and H = 1,000 MPa specify hardening rates and r = 8.45 MPa and R = 2.00 MPa relate to dynamic recovery rates for the Al-1.0%Si-0.3%Mg matrix material. The capability of the cyclic constitutive model to accurately capture the nonlinear effects of reversed yielding and plastic flow are critical to the present analysis of plastic deformation near inhomogeneities. Moreover, the flow rules and evolution equations for the present constitutive model have physical meaning since they are motivated by dislocation based arguments (Bammann *et al*., 1993 and 1996). Simple elastic and elastoplastic constitutive relationships may give erroneous predictions owing to the unphysical nature of their modeling and inability to accurately predict complex multidimensional stress-strain paths.

This page intentionally blank

B. APPENDIX: Al-Si interface strength calculations using atomistic calculations

Predicting the monotonic or cyclic mechanical properties of materials containing incoherent inclusions requires knowledge of the local misfit stress and strain distributions near such particles when a material is subjected to far-field boundary conditions. For pristine and perfectly bonded inclusions, an Eshelby based approach (Eshelby, 1957) can be used to obtain a relationship between local and far-field stresses and strains. However, second phase inclusions within a ductile matrix are not always pristine, but rather can be fractured or debonded (Puttick, 1959; Grosskreutz and Shaw, 1969; Broek, 1973; Lankford and Kusenberger, 1973; Hahn and Rosenfield, 1975). For example, Figure B.1 is a duo of scanning electron microscope (SEM) images taken from a fracture surface of cast A356 aluminum alloy, subjected to cyclic loading conditions (Gall *et al.*, 1999). The SEM images demonstrate that pure silicon inclusions within a ductile aluminum matrix may (a) fracture or (b) debond depending on the fatigue crack tip driving force (striation spacing) and inclusion morphology. Predicting whether an inclusion will fracture versus debond for different particle shapes and loading conditions is difficult without information on the relative strength of the particle versus its interface with the matrix material.

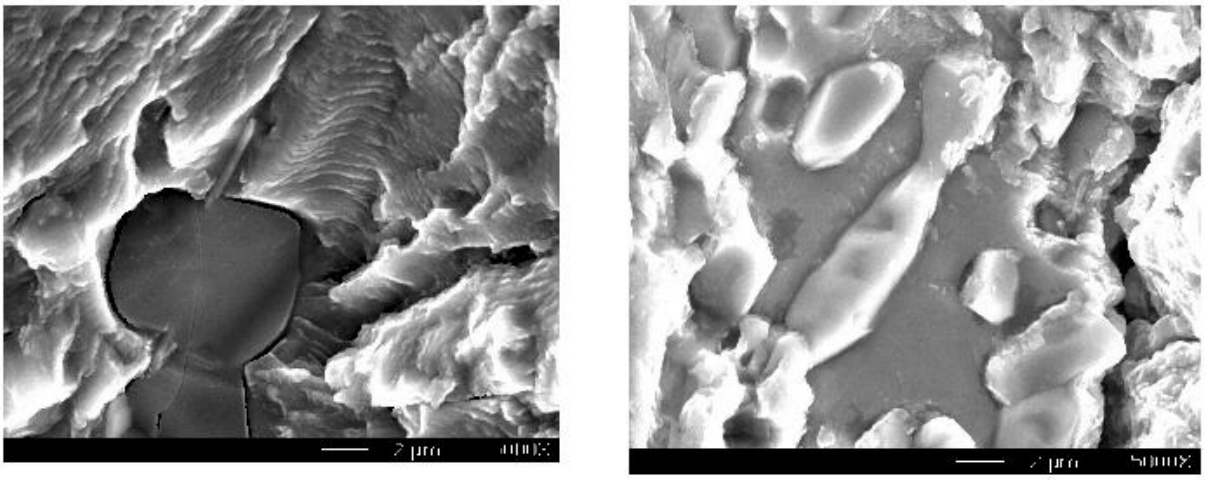

(a) (b)

Figure B.1. Scanning electron microscope images of the fracture surface of a cast A356-al alloy subjected to cyclic loading conditions. The images demonstrate that pure silicon inclusions are observed to both (a) fracture and (b) debond.

As second phase particles fracture or debond, finite element calculations can be used to obtain the evolution of local stress and strain distributions with respect to the far-field boundary conditions (Harkegard, 1973; Gall *et al*., 1999). One consideration in the finite element modeling of interface debonding, and crack propagation in general, is modeling the generation of free surfaces. Previous finite element studies have used cohesive zone approaches (Dugdale, 1960; Barenblatt, 1962) to model, for example, fracture in rocks (Boone *et al*., 1986), inclusion debonding in ductile materials (Needleman, 1987; Xu and Needleman, 1993) dynamic crack propagation in brittle materials (Camacho and Ortiz, 1996), failure of adhesive joints (Tvergaard and Hutchinson 1994, 1996), and various other interfacial crack growth problems (Needleman, 1990a,b; Suo *et al.*, 1992; Tvergaard and Hutchinson 1992; Needleman, 1992; Xu and Needleman, 1993, 1995, 1996; Needleman, 1997; Bigoni *et al.*, 1997; Siegmund *et al.*, 1997; Xu *et al.*, 1997). The mathematical forms for cohesive zone equations are motivated (Needleman, 1990a) from metallic atomic binding energy relationships (Rose *et al.*, 1981; Rose *et al.*, 1983; Ferrante and Smith, 1985).

Given this background we proceed first with atomistic simulations to determine an understanding of silicon fracture and silicon-aluminum interface debonding. Second, we perform microscale finite element analyses to determine the parameters of interest for macroscale microstructure-mechanical property model.

The present atomistic study will consider the deformation characteristics of the interface between pure FCC aluminum (Al) and diamond cubic silicon (Si). Al-Si interfaces have technological importance in cast Al-Si alloys and electronics packaging applications. We will use the semi-empirical Modified Embedded Atom Method (MEAM) (Baskes, 1992) to model the Al-Si interfaces under imposed tensile boundary conditions. The MEAM (Baskes, 1992) differs from the standard EAM (Daw and Baskes, 1984) in that the angular dependence of the electron density is included in the MEAM. With exception to one MEAM simulation, which was deformed under static loading conditions at 0 K, all models were deformed in the molecular dynamics framework at high strain rates (1×10^9 1/s). The MEAM is a powerful tool for analyzing local interfacial failure mechanisms since the structure and/or strength of the interface need not be assumed *a priori*. Consequently, the predictions of the MEAM simulations provide insight into the underlying physics of interfacial decohesion and fracture.
/
Previous MEAM simulations on the characteristics of Ni-Si interfaces (Baskes *et al.*, 1994) have provided insightful results. In general, the work of Baskes *et al.*, (1994) determined the structure and adhesion energy of a thin layer of Ni on a Si substrate. However, such MEAM studies on Ni-Si interfaces have not considered the effects of different MEAM models on the strength of the interface. In order to draw accurate comparisons with continuum based debonding models, a more thorough study of the effects of MEAM model geometry, loading, and displacement measurement conditions should be undertaken. The current MEAM simulations consider the stress-strain and traction-displacement responses of Al and Si blocks of various size, attached at a flat interface, and subjected to tensile boundary conditions applied parallel to the interface normal. The effect of randomly dispersed point vacancy defects on the strength of the interface is investigated. In addition, the effect of crack-like vacancy defect size on the competing failure mechanisms of Al-Si interface debonding versus isolated fracture in the Al or Si is considered.

Finally, different locations for measuring opening displacement are discussed in the framework of a continuum based cohesive zone approach. This preliminary study will not consider the effects of pertinent metallurgical factors such as interface misorientations (Kurtz and Hoagland, 1998), dislocations (Kurtz and Hoagland, 1998), or impurities (Rice and Wang, 1989; Olson, 1997). We attempt here to determine the overall applicability of atomistic simulations to study interfacial decohesion in the context of current continuum based modeling approaches. Once the task at hand has been accomplished, the effects of the aforementioned metallurgical factors can be more effectively studied.

The results of the present study augment the findings of different experimental techniques used to characterize the structure, strength, and fracture behavior of bi-material interfaces. For example, the properties of material interfaces have been studied using a wide range of mechanical testing methods such as: peel tests (Yoshino and Shibata, 1992), laser spallation tests (Gupta *et al.*, 1993), zero-creep tests (Josell and Spaepen, 1993-a, b), push-through tests (Warren *et al.*, 1992; Mackin *et al.*, 1992; Izawa *et al.*, 1996), pull-out tests (Lamon *et al.*, 1995), normal tension tests (He *et al.*, 1996), transverse compression tests (Turner and Evans, 1996), and bending tests (Reimanis *et al.*, 1990; Reimanis *et al.*, 1991; Bartlett and Evans, 1993; Leung *et al.*, 1995). The particular conclusions of the aforementioned collection of experimental studies are dependent on the material studied. However, the interface between two adjoining materials almost always serves as the weak link for failure for all material systems and loading conditions considered. In addition to the experimental studies, numerous analytical approaches (Erdogan, 1963; Rice and Sih, 1965; Comninou, 1990; Loboda, 1998) have been used to study the stress and strain fields near interfacial cracks in dissimilar materials, analogous to fracture mechanics based approaches for homogeneous materials. Energy based criteria have also been utilized to study the competing modes of interface debonding versus fracture into the bulk materials (Evans *et al.,* 1989; He *et al.,* 1994).

Atomistic calculations, starting from atomic pair potentials or some related modification, have been used for a wide variety of materials. Brenner (1996) summarized the class of bond order formalism that has proven valuable for covalently bonded systems. Stoneham *et al.* (1996) summarized the shell model, which is a modification of a pair potential, used for ceramics. For metals, Daw and Baskes (1984) developed the MEAM, which employs a pair potential augmented by a function of another pair-wise sum based on the electron density. We use the MEAM in the atomistic simulations for the study of finite deformations of single crystal aluminum and silicon and the interface between the two materials.

Figure B.2 is a representative example of the response of the interface model to applied far-field velocity boundary conditions. The center figure is a plot of the average uniaxial stress versus the true uniaxial strain for the aggregate shown in Figure B.2. The average stress is calculated using for the entire aggregate of atoms. Upon initial application of the end velocities, the average axial stress in the model is compressive (negative). The initial negative stresses, which exist even in a statically relaxed model, is caused by the attempted contraction of the Al and Si due to the presence of the free surfaces. Moreover, the lattice constants of the materials are not exact (.5 % error) since their ratio must be an integer to properly enforce periodicity. During continued movement of the end atoms, the average axial stresses become tensile, and the stresses continue increasing until a critical stress level is reached. At the critical stress level, the failure of the

interface between the Al and the Si atoms begins to nucleate (Figure B.2). The nucleation of interfacial failure occurs spatially at the location where the Al and Si atoms are displaced (rippled) in the relaxed and undeformed state. In fact, aside from differences in the bonding potentials between Al and Si atoms, the rippled nature of the interface is one reason that the interface is weak compared to the pristine bulk material. The rippling facilitates local stress concentrations and failure through local damage nucleation and a subsequent unzipping of the interface atoms rather than simultaneous bond breakage. Such a failure mechanism is analogous to the severe decrease in strength for the movement of a single dislocation versus the simultaneous failure of all adjacent atomic bonds.

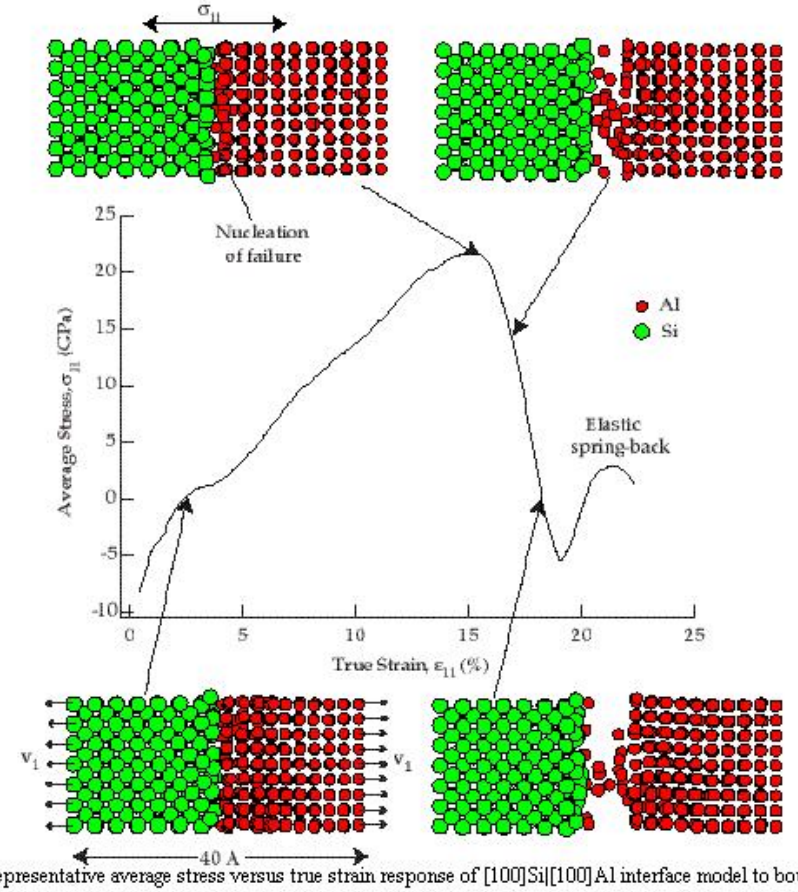

Figure B.2. Representative average stress versus true strain response of [100]Si[100]Al interface model to boundary velocities, v_1, At the far ends of the blocks in the [100] and [-100] directions. The model is periodic in the [010] and [001] directions.

As the interface debonds, the average stresses in the atomistic model decrease over a finite strain increment (Figure B.2). Moreover, during interfacial debonding, the Si atoms are slightly distorted from their elastic positions, however the Al atoms undergo gross permanent changes in position, revealing that plastic dissipation occurs in the Al. Owing to the highly constrained and pristine state of the present lattice, it is difficult to envision any explicit dislocation emission or movement near the fracturing interface. When the average stress in the block reaches approximately 0 GPa, the interfacial separation is complete and several Al atoms are still attached to the Si (Figure B.2). After separation, the two blocks experience elastic springback in an oscillatory manner as indicated in Figure B.2. For the remaining figures, the elastic springback portion of the stress-strain curve is removed since it is not pertinent to understanding the local debonding mechanisms. We note that the predicted debonding stress levels (~20 GPa)

in the present study are elevated compared to, for example, the ultimate tensile strength (~200 MPa) of cast Al-Si alloys where debonded and fractured Si particles are observed (Dighe and Gokhale, 1997; Samuel and Samuel, 1995). The high attainable stress levels are due to the pristine state of the interface (defect and impurity free), the highly constrained (relatively thin and periodic) nature of the interface model, and the dynamic loading conditions. The periodic nature and relatively high applied strain rates are inherent to practical MEAM simulations, thus revealing a limitation of current atomistic modeling efforts. The addition of defects such as point vacancies will slightly lower the strength of the "perfect" incoherent interface, as will be demonstrated in Section 5. Interface misorientations, dislocations (Kurtz and Hoagland, 1998), and impurities (Rice and Wang, 1989; Olson, 1997) will further lower the strength of the interface as much as several orders of magnitude. We also note that under some stress states other than pure tension, a size scale effect, which is the basis of strain gradient plasticity, will also cause the local stresses to be much higher than experimental observations on large scale samples (Fleck *et al*., 1994; Horstemeyer and Baskes, 1999).

The stress distributions across the interface, predicted by the MEAM simulations, provide insight into the local failure mechanisms. Figure B.3 is a distribution of average uniaxial stresses just before interfacial failure. The stresses were averaged in the [010] and [001] directions, and the average stress in the entire volume is also indicated in Figure B.3 as a straight line. The distributions predicted by both the molecular dynamics and static simulations are presented in Figure B.3. The average stresses in the stiffer silicon material are higher for an equivalent dynamic displacement of both model ends. The different stress levels in the two materials are artifacts of the dynamic nature of the simulations. However, in the static case, the stresses away from the interface are comparable in both materials, consistent with static stress equilibrium concepts. Very close to the interface, the stresses in both materials are higher than the nominal values away from the interface, under both static and dynamic loading conditions. The magnification of stresses is due to the rippled nature of the interface and the local balance of forces. In other words, owing to the different crystal structures and lattice parameters of the two phases, some atoms cannot interact strongly with immediate neighbors across the interface. The low interaction force levels between certain atoms promotes high forces between other atoms which are attempting to keep the interface intact. Thus, extremely close to the interface, several atoms are equilibrated under relatively higher forces as evident in Figure B.3. This microscopic disturbance of stresses near the interface facilitates the nucleation and propagation of debonding failure. We note that such a local disturbance in the stress fields is produced by the heterogeneous nature of the interface as caused by the lattice structure of the two materials. Of course, in a homogeneous continuum based model, no stress intensification would be predicted for the given periodicities and boundary conditions.

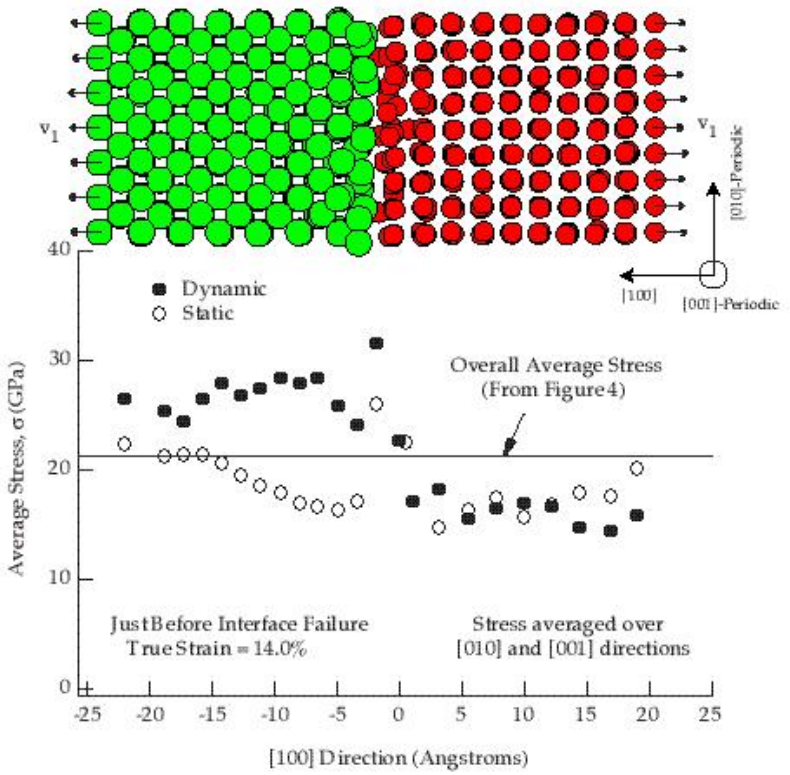

Figure B.3. Stress distribution along the [100] direction for the [100]Si|[100]Al interface model. The atomistic image corresponds directly to the different positions indicated along the lower axis of the plot. The model is periodic in the [010] and [001] directions, and the stresses are averaged in these directions.

The strength of material interfaces will invariably be degraded by the presence of metallurgical defects such as dislocations, vacancies, and chemical impurities. Although chemical impurities (Rice and Wang, 1989; Olson, 1997) and interface dislocations (Kurtz and Hoagland, 1998) are expected to have a significant influence on the strength of an interface, the present MEAM simulation will exclusively consider the effects of vacancy-type defects on interface debonding. The incorporation of impurity atoms in MEAM simulations requires the development of atomic potentials for such materials and is beyond the scope of the present study. Moreover, a thorough study of different interface dislocations and misorientations is a separate topic altogether and can be attacked once the present framework is set forth. Figure B.4 illustrates the dependence of the strength of the interface on the number fraction of defects near the interface. The point vacancy defects in the simulations in Figure B.4 were distributed randomly throughout the two atomic planes adjacent to the interface in (a) just the Al, (b) just the Si, and (c) both the Al and Si. In all three situations (Figures B.4) the incorporation of vacancy defects at the interface lowers the fracture strength of the interface. In the range of defect number fractions considered, the decrease in the interfacial strength scales nearly linearly with the number fraction of defects (Figure B.4a). The small reductions in strength due to the randomly dispersed vacancies (Figures B.4) are absolutely negligible given the small overall concentration (<< 1%) of vacancies traditionally found in metals (Meyers and Chawla, 1984).

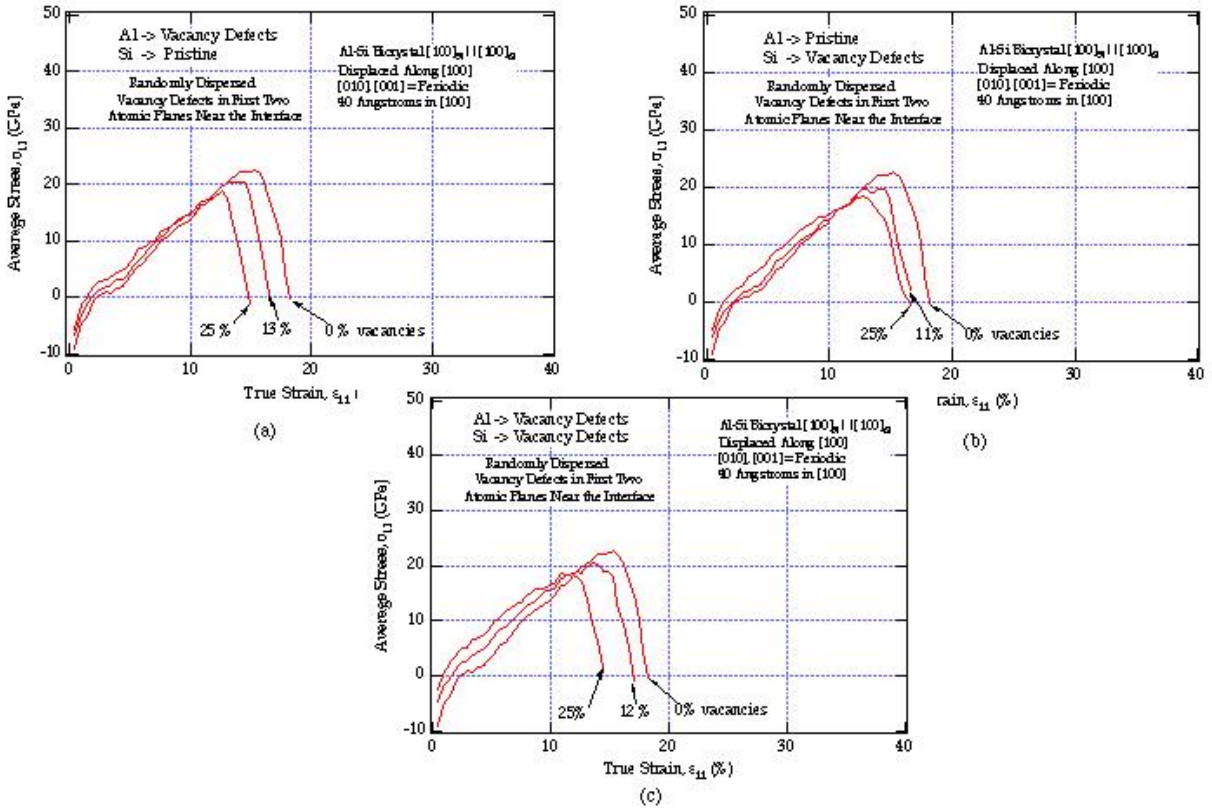

Figure B.4. Effect of randomly distributed point vacancy defects on the stress-strain response of the 40 Angstrom [100]Si||[100]Al interface model. The vacancy defects are distributed within the first two atomic layers near the interace in (a) the aluminum, (b) the silicon, and (c) both the aluminum and silicon.

We have established that the Al-Si interface with and without point vacancy defects is a weak link for failure under tensile loading parallel to the $[100]_{Al}||[100]_{Si}$ interface normal. Now we investigate the role of microscopic crack like defects in the bulk materials on the competing mechanisms of fracture in the pure Al, pure Si, or at the Al-Si interface. Figures B.5 and B.6 are compilations of the initial damaged state and final failure mode of four different MEAM simulations with different sized and spaced flaws in the Si or Al, respectively. Before conducting the MEAM simulations, atomic rows along the [001] direction were removed to create a crack-like vacancy defect in the silicon (Figure B.5) or aluminum (Figure B.6). Since the model is periodic in the [010] direction, the models in Figures B.5 and B.6 simulate a periodic array of evenly spaced cracks rather than a single defect. As the initial flaw size is increased (periodic flaw spacing is concurrently decreased) in both materials, failure in the pure materials is favored over interfacial failure. Flaws in the Si do not distract the failure from occurring at the interface until the flaw area projected onto a plane normal to the tensile axis is nearly 30% (Figure B.5). Flaws in the Al are even less effective in moving the failure away from the interface since it takes a larger flaw area projected on a plane normal to the tensile axis (about 50%) to accomplish bulk failure in the Al (Figure B.6) versus the interface. These values are only valid for pristine materials with defects on this size scale.

Figure B.5. Effect of initial defect size in the pure silicon material on the failure mode of the 40 Angstrom [100] Si|[100]Al interface model. All models have equivalent geometries, and they are periodic in the [010] and [001] directions.

Figure B.6. Effect of initial defect size in the pure aluminum material on the failure mode of the 40 Angstrom [100] Si|[100]Al interface model. All models have equivalent geometries, and they are periodic in the [010] and [001] directions.

Figure B.7 demonstrates that the periodic size scales of the model in the [010] and [001] directions have an influence on the fracture behavior of the material in the presence of defects. The lower model in Figure B.7 has double periodicity in both directions and a flaw size that is also double compared to the model at the top of the figure. Recall that changing the transverse periodic lengths had a negligible influence on the tensile stress-strain behavior of the model without defects. However, the size of the periodic lengths has an influence when flaws within the materials are introduced. The dependence of the fracture mode of the model on the flaw size is consistent with fracture mechanics notions where the intrinsic flaw size is related to the driving force for fracture. However, in the present simulations, the larger flaw in the Si does not promote earlier fracture in the Si compared to the smaller flaw, which is not entirely consistent with static fracture mechanics concepts. One reason that the smaller flaw could promote earlier failure is due to the propagation of elastic waves in the dynamic MEAM model. Such elastic waves can promote premature fracture in the smaller model since the ligament between the cracks is smaller than in the larger model, and shorter time is required for spatial movement of the waves. As such, the probability that the local stress field that initiates fracture will be augmented by an elastic stress wave is increased in the smaller scale MEAM model. Moreover, we note that the interaction between the different flaw sizes and the interface, which is a flaw itself, may also provide some rational for the qualitative disagreement with static fracture mechanics flaw size concepts. In either case, caution must be exercised when extending static fracture mechanics based ideas to dynamic debonding problems since complex local stress states may develop due to interactions with the flaws, elastic waves, and the interface. Moreover, extending fracture mechanics based ideas to atomistic size scales is not trivial due to the small flaw and geometry size scale inherent to atomistic simulations.

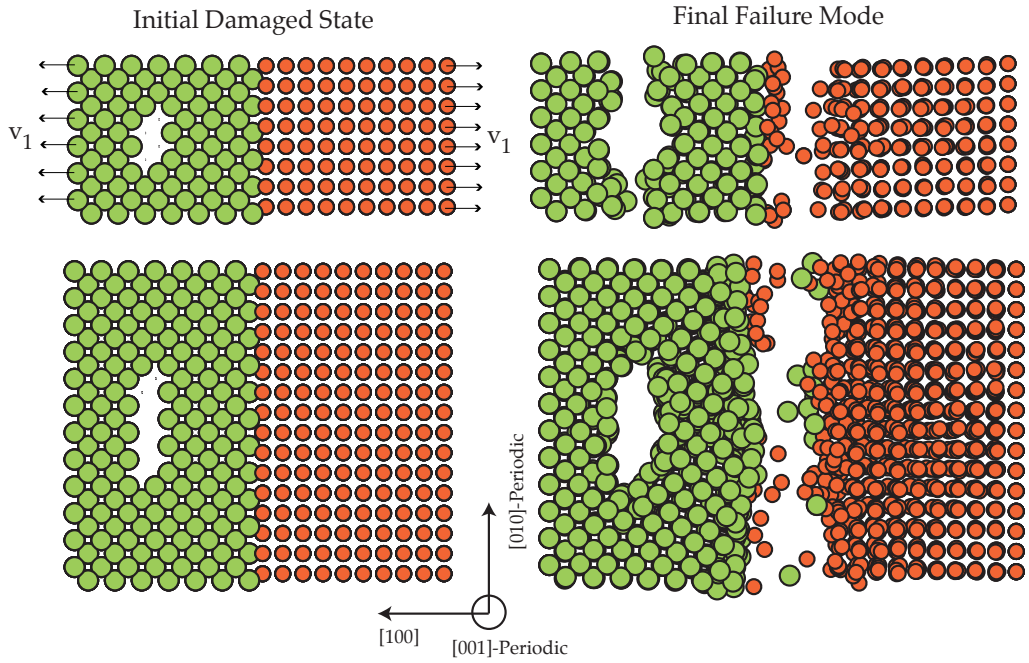

Figure B.7. Effect of initial defect size in the pure silicon material on the failure mode of the 40 Angstrom [100]Si||[100]Al interface model. The two models are periodic in the [010] and [001] directions and have periodicities scaled equivalently with the two different initial flaw sizes.

This page intentionally blank

DISTRIBUTION

1 Kola Agagu
GM Powertrain Group
General Motors Corporation
Casting Technology Center
Mail Code 486-077-034
77 West Center Street
Saginaw, MI 48605-5073

1 Richard Andriano
Stahl Specialty Co.
111 E. Pacific
P. O. Box 6
Kingsville, MO 64061-0006

1 Diran Apelian
Metal Processing Institute
Worcestor Polytechnic Institute
100 Institute Road
Worcester, MA 01609-2280

1 Mike I. Baskes
MST-8, MS G755
Los Alamos National Laboratory
Los Alamos, NM 87545

1 John Bassani
University of Pennsylvania
Dept. of Mechanical Engineering and Applied Mechanics
297 Towne Bldg.
Philadelphia, Pa 19104-6315

1 Armand Beaudoin
Dept. of Mechanical and Industrial Engineering
University of Illinois at Urbana-Champaign
140 Mechanical Engineering Building, MC-244
1206 West Green Street
Urbana, IL 61801

1 Richard Becker
Lawrence Livermore National Laboratory
7000 East Ave
L-228
Livermore, Ca 94450

1 Richard Berkmortel
Global Technolgy Centre
Meridian Technologies, Inc.
25 MacNob Avenue
Strathroy, Ontario
Canada N7G 4H6

1 John T. Berry
Mississippi State University
Department of Mechanical Engineering
210 Carpenter Engineering Building
P. O. Box ME
Mississippi State, MS 39762-5925

1 Mary Boyce
Dept. of Mechanical Engineering
Massachusetts Institute of Technology
Cambridge, MA 02139-4307

1 John Brockenbrough
100 Technical Drive
Alcoa Center PA 15069

1 Robert J. Bucci
Engineering Design Center
Aluminum Company of America
Alcoa Technical Center
100 Technical Drive
Alcoa Center, PA 15069-0001

1 James T. Burg
Aluminum Company of America
Alcoa Technical Center
100 Technical Drive
Alcoa Center, Pennsylvania 15069-0001

1 Carloa H. Caceres
Department of Mining, Minerals and Materials Engineering
The University of Queensland
Brisbane Qld 4072
Australia

1 Joseph A. Carpenter, Jr.
Office of Transportation Technolgies
U. S. Department of Energy
EE-32, Room 5G-045
1000 Independence Ave., SW
Washington, DC 20585

1 Weinong Wayne Chen
Aerospace & Mechanical Engineering
The University of Arizona
Tucson, AZ 85721

1 Xiaoming Chen
Safety Research and Development Department, FRL
2101 Village Road, P.O. Box 2053
MD 2115, Rm 2626
Dearborn, MI 48124

1 Yang-Tse Cheng
Engineered Surfaces and Tribology
Material and Processes Laboratory
General Motors
Research and Development
Mail Code 480-106-224
30500 Mound Road
P. O. Box 9055
Warren, MI 48090

1 Gerald S. Cole
Manufacturing Systems Department
Ford Research Laboratory
20000 Rotunda Drive
P. O. Box 2053
MD 3135, Rm. 2170, SRL
Dearborn, MI 48121, 2053

1 Bruce M. Cox
Cast Metals Laboratory
Daimer Chrysler Corporation
CIMS 481-01-41
800 Chrysler Drive
Auburn Hills, MI 48326-2757

1 Paul Creapeau
General Motors
6595 Joslyn Rd
Pontiac, MI 48340

1 Louis Desrosiers
InTerMag Technologies Inc.
357 rue Franquet Sainte-Foy
Quebec, Canada QCGIP 4N7

1 Sara Dillich
Energy Efficiency and Renewable Energy
Office of Industrial Technologies, EE-20
1000 Independence Avenue SW
Washington DC 20585-0121

1 Ken Dolan
Lawrence Livermore National Laboratory
7000 East Ave
L-333
Livermore, CA 94550

1 Ray Donahue
Mercury Marine
W 6250 Pioneer Rd.
Fond DuLac, Wi 54936-1939

1 L. Donay
Alchem Aluminum Inc.
368 West Garfield P.O. Box 139
Coldwater, Mi. 49036

1 Mike Evans
Gibbs Did Casting Corporation
369 Community Drive
Henderson, KY 82420

10 Jinghong Fan
Division of Mechanical Engineering,
Alfred University
Saxon Drive
Alfred, NY, 14802

1 Ken Fischer
Consolidated Metco, Inc
13940 N. Rivergate Blvd
Portland, OR 97203

1 Joseph Foster
Wright Laboratory/ Armament Directorate
Eglin AFB, FL 32548

1 George N. Frantziskonis
Department of Civil Engineering & Engineering Mechanics
The University of Arizona
Tucson, AZ 85721-0072

1 Kenneth Gall
University of Colorado
Department of Mechanical Engineering
Campus Box 427
Boulder, CO 80309

1 H. Gao
Dept. of Mechanical Engineering
Stanford University
Stanford, CA 94305

1 Gerald Gegel
740 S. Columbus Ave.
Morton, IL 61550

1 Vincent J. Genise
Product Engineering and Development
Citation
27730 Franklin Road
Southfield, MI 48034

1 Dale A. Gerard
General Motors Corporation
GM Powertrain
Mail Code 480-723-624
30003 Van Dyke
Building 2-7
Warren, MI 48090-9060

1 Bill Gerberich
University of Minnesota
Chemical Engineering and Materials Science
151 Amund H
421 Washington Ave SE
Minneapolis, MN 55455

1 Arun Gokhale
School of Materials Sciences Engineering
Georgia Tech
Atlanta, Ga 30332-0405

1 Nasr M. Ghoniem
Mechanical and Aerospace Engineering Department
46-147G Engr IV
University of California Los Angeles
420 Westwood Plaza
Box 951597
Los Angeles, CA 90095-1597

1 Leo Ghuzhoy
Advance Materials Technology
Caterpillar Inc.
Technical Center – E/854
P. O. Box 1875
Peoria, IL 61656-1875

1 Kasi K. Goundan
GMNA Materials & Fastening Engineering Center
General Motors
Mail Code 480-205-314
30007 Van Dyke
Warren, MI 48090-9065

1 David Hall
Louisiana Tech
Mechanical Engineering Dept
PO Box 10348
Ruston, LA 71272

1 Yanyao Jiang
Department of Mechanical Engineering
College of Engineering/312
University of Nevada
Reno, NV 89557-0154

1 Peggy E. Jones
Advanced Materials Development Center
GM Powertrain
1629 N. Washington
P. O. Box 5073
Saginaw, MI 48605-5073

1 George Johnson
Mechanical Engineering
University of California
Berkeley, CA 94720-1740

1 J.W. Ju
Civil & Environmental Engineering
UCLA
Los Angeles,CA 90024-1593

1 J. G. Kaufman
Daufman Associates, Ltd.
3662 Pevensey Drive
Columbus, OH 43220-4821

1 Akhtar Khan
The University of Maryland Balt. County
ECS 234
Baltimore, MD 21250

1 Chung-Whee Kim
EKK, Inc.
100 North Pond Drive
Suite A
Walled Lake, MI 48390

1 Tom Lacy
Department of Aerospace Engineering
Wichita State University
1845 Fairmount
Wichita, Kansas 67260-0044

1 Joe LaRoche
Alcan Ingot
Division of Alcan Aluminum Corporation
6060 Parkland Boulevard
Cleveland, OH 44124-4185

1 Naiyi, Li
Manufacturing Systems Department
Ford Research Laboratory
22101 Village Road
P. O. Box 2053
MD 3135, Rm. 3011, SRL
Dearborn, MI 48121-2053

1 Hiumin Liu
Product Engineering and Development
Citation Corporation
27730 Franklin Road
Southfield, MI 48034

1 W. K. Liu
Mechanical Engineering Dept.
Northwestern University
Evanston, IL 60208-3109

1 Mike Lovell
University of Pittsburgh
Mechanical Engineering
Pittsburgh, PA

1 D. Scott MacKenzie
Failure Analysis & NDT
The Boeing Company
P. O. Box 516 MC S102-2152
St. Louis, MO 63166-0516

1 Hans U. Mair
Operational Evaluation Division
Institute for Defense Analysis
1801 N. Beauregard Street
Alexandria, VA 22311-1772

1 J. Fred Major
Alcan International Limited
Kingston Research and Development Centre
P. O. Box 8400, 945 Princess Street
Kingston, Ontario K7L 5L9 Canada

1 Antoinette Maniatty
MEAEM
RPI
110 8th St.
Troy, NY 12180-3590

1 Peter Matic
Naval Research Lab
Code 6303
Washington DC 20375-5343

1 Paul J. Maudlin
MST-8, MS G755
Los Alamos National Laboratory
Los Alamos, NM 87545

10 Dave McDowell
GWW School of Mech. Engng.
Georgia Tech
Atlanta, GA 30332-0405

1 John Mckirgan
Code 614
Naval Surface Warfare Center
Carderock Division
9500 MacArthur Blvd
West Bethesda, MD 20817-5700

1 Matt Miller
Sibley School of Mechanical Engineering
194 Rhodes Hall
Cornell University
Ithica, NY 14853

1 Roger Minich
Lawrence Livermore National Laboratory
7000 East Ave
L-097
Livermore, CA 94450

1 Kyran D. Mish
Lawrence Livermore National Laboratory
7000 East Ave
L-151
Livermore, CA 94450

1 Dan Mosher
UTRC MS129-73
411 Silver Lane East
East Hartford, CT 06108

1 Sia Nemat-Nasser
University of California, San Diego
Department of AMES
La Jolla, CA 92093-0416

1 A. Needleman
Brown University
Division of Engineering
Providence, RI 02912-9104

1 Sam Noboulsi
Air Force Institute of Technology
Department of Aeronautics and Astronautics
AFIT/ENY BLDG 640
2950 P Street
Wright-Patterson AFB, OH 45433-7765

1 Bill Nix
Stanford University
Department of Materials Science & Engineering
Stanford, CA 94305

1 Mike Ortiz
Graduate Aeronautical Laboratories
Mail Code 105-50
California Institute of Technology
Pasadena, CA 91125

1 Mark A. Osborne
Advanced Materials Development Center
GM Powertrain
1629 N. Washington
P. O. Box 5073
Saginaw, MI 48605-5073

1 Richard J. Osborne
GMNA Materials & Fastening Engineering Center
General Motors
Mail Code 480-205-314
30007 Van Dyke
Warren, MI 48090-9065

1 Donald D. Penrod
Manufacturing Services and Development, Inc.
4665 Arlington Drive
Cape Haze, FL 33946

1 David Poirior
Aerospace and Mechanical Engineering
University of Arizona
Tucson, AZ 85721

1 Pete Pollack
The Aluminum Association
900 19th. Street N.W.
Washington, D.C. 20006-2168

1 Bob. R. Powell
Research & Development Center
General Motors
Mail Code 480-106-212
30500 Mound Road
P. O. Box 9055
Warren, MI 48090-9055

1 Vincent C. Prantil
Mechanical Engineering Department
Milwaukee School of Engineering
1025 North Broadway
Milwaukee, WI 53202-3109

1 Thomas Prucha
Intermet Corporation
5445 Corporate Drive
Suite 200
Troy, Michigan 48098

1 A. Rajendran
US Army Research Office
4600 South Miami Blvd
PO Box 2211
RTP, NC 27709-2211

1 S. Ramaswamy
General Electric Company
Corporate R&D
Niskayuna, NY 12309

1 K.T. Ramesh
Johns Hopkins University
Department of Materials Science & Engineering
3499 N Charles St.
Baltimore, MD 21218

1 Mark Rashid
Department of Civil and Environmental Engineering
University of California at Davis
Davis, CA 95616-5294

1 Jim Rossi
Westmoreland Mechanical Testing & Research
P.O. Box 388
Youngstown, Pa 15696—0388

1 Sunil Saigal
Civil and Environmental Dept.
Carnegie Mellon University
Pittsburgh, Pa 15123-3890

1 Mark T. Samonds
UES Software, Inc.
175 Admiral Cochrane Drive, Suite 110
Annapolis, MD 21401

1 Carlos Sanday
Naval Research Lab
Code 6303
Washington DC 20375-5343

1 Gregory Sanders
Entelechy
42325 E. Ann Arbor Road
Suite 220
Plymouth, MI 48170-4356

1 Joseph S. Santner
American Foundry Society
505 State Street
Des Plaines, IL 60016-8399

1 Scott Schoenfeld
Army Research Laboratory
AMSRL-WT-TD
Aberdeen Proving Ground, MD 21005-5066

1 Robert G. Seese
KBAlloys, Inc.
P. O. Box 14927
Reading, PA 19612-4927

1 Vijey Shende
Amcast Automotive
300 Galleria Office Center Suite 208
Southfield, Mi. 48034

1 Yih-Chyun Sheu
General Motors Truck Group
General Motors
Truck Product Center – Central
Mail Code 483-510-2F2
Cube #113E6
2000 Centerpoint Parkway
Pontiac, MI 48341-3147

1 Donald A. Shockey
SRI International
333 Ravenswood Avenue
Menlo Park, CA 94025

1 G. Shulke
Chrysler Corporation
800 Chrysler Dr.
Auburn Hills, MI 48326-2757

1 G. Sigworth
116 Derby Street
Johnstown, Pa. 15905

1 Jerry H. Sokolowski
Mechanical And Material Engineering
University of Windsor
RM 209 Essex Hall
401 Sunset Avenue
Windor, Ontario
Canada N9B3P4

1 Al Torok

Kaiser Aluminum
6909 Thornwood St. NW
Canton, Ohio 44718

1 Dan Tortorelli
Dept. of Mechanical and Industrial Engineering
University of Illinois at Urbana-Champaign
140 Mechanical Engineering Building, MC-244
1206 West Green Street
Urbana, IL 61801

1 S. Viswanathan
Oak Ridge National Laboratory
PO BOX 2008, Bldg 4508
Oak Ridge, TN 37831-6983

1 Shaupoh Wang
AEMP Corporation
2404 Dr. F.E. Wright Drive
Jackson, TN 38305

1 Qigui Wang
Advanced Materials Development Center
GM Powertrain
1629 N. Washington
P. O. Box 5073
Saginaw, MI 48605-5073

1 David Weiss
ECK Industries
P.O. Box 967
Manitowoc, WI 54221-0967

1 Hussein Zbib
Washington State University
Dept. of Mechanical and Materials Engineering
Pullman, WA 99164-2920

1 Mohammed Zikry
Dept. of Mechanical and Aerospace Engineering
North Carolina State University
Raleigh, NC 27695-7910

1 MS 0310 P. Yarrington, 9230

1	MS 0316	S.S. Dosanjh, 9233
1	MS 0316	G.S. Heffelfinger, 9209
1	MS0321	W.J. Camp, 9200
1	MS0513	A.D. Romig, 1000
1	MS0820	P.A. Taylor, 9232
1	MS 0826	W.L. Hermina, 9113
1	MS0841	T.C. Bickel, 9100
1	MS 0847	H.S. Morgan, 9123
1	MS 0847	R.A. May, 9126
1	MS 0847	T. Hinnerichs, 9126
1	MS 1111	S.J. Plimpton, 9233
1	MS 1111	H. P. Hjalmarson, 9235
1	MS 1111	M. J. Stevens, 9235
1	MS 1411	J. M. Philips, 1802
1	MS 1411	H.E. Fang, 1834
1	MS 9001	M. E. John, 8000
		Attn: R. C. Wayne, 2200, MS 9005
		J. Vitko, 8100, MS 9004
		W. J. McLean, 8300, MS 9054
		D. R. Henson, 8400, MS 9007
		P. N. Smith, 8500, MS 9002
		K. E. Washington, 8900, MS 9003
1	MS 9221	C. M. Hartwig, 8510
1	MS 9405	R. Stulen, 8700
		Attn: R. Q. Hwang, 8721, MS 9161
		J.M. Hruby, 8702, MS 940
		K. L. Wilson, 8724, MS 9402
		J. C. F. Wang, 8723, MS 9403
		W. A. Kawahara, 8725, 9042
		J. L. Handrock, 8727, 9042
1	MS 9161	D. L. Medlin, 8721
1	MS 9161	M. van Schilfgaarde, 8721
1	MS 9405	D. J. Bammann, 8726
1	MS 9161	E. P. Chen, 8726
1	MS 9405	B. Somerday, 8724
1	MS 9405	N. Moody, 8725
1	MS 9405	P.M. Gullett, 8726
1	MS 9405	Y. Hammi, 8726
10	MS 9405	M. F. Horstemeyer, 8726
1	MS 9405	D. A. Hughes, 8726
1	MS 9405	R. E. Jones, 8726
1	MS 9161	P. A. Klein, 8726
1	MS 9161	J. Zimmerman, 8726

1	MS 9405	E. B. Marin, 8726
1	MS 9405	R. A. Regueiro, 8726
1	MS 9042	M. L. Chiesa, 8727
1	MS 9042	J. J. Dike, 8727
1	MS 9012	P. E. Nielan, 8920
1	MS 0188	D. Chavez, LDRD Office, 4001
1	MS 0899	Technical Library, 4916
1	MS 9021	Technical Communications Department, 8511/ Technical Library, MS 0899, 4916
1	MS 9021	Technical Communications Department, 8511 for DOE/OSTI
3	MS 9018	Central Technical Files, 8940-2

This page intentionally blank